Technische Universität München
Institut für Energietechnik

Professur für Thermofluiddynamik

Scale-resolved and stochastic approaches for noise prediction in duct singularities

Ugur Karban

Vollständiger Abdruck der von der Fakultät für Maschinenwesen der Technischen Universität München zur Erlangung des akademischen Grades eines

DOKTOR – INGENIEURS

genehmigten Dissertation.

Vorsitzender:
apl. Prof. Dr.-Ing. habil. Christian Breitsamter
Prüfer der Dissertation:
Prof. Wolfgang Polifke, Ph.D.
Prof. Dr.-Ing. Hans-Jakob Kaltenbach

Die Dissertation wurde am 03.07.2017 bei der Technischen Universität München eingereicht und durch die Fakultät für Maschinenwesen am 25.10.2017 angenommen.

Foreword

It is a historical debate between the academic world and the industry, that academic works are usually considered to be too much isolated from the real-life problems. After mentioning my PhD topic in friendly chats, I might have been exposed more than a hundred times to the question: 'So, what is it gonna be used for?' With all my regards to the owners of this question, I have to confess that even I had to force my imagination to think of the possibility of my work in PhD affecting someone else's life at a certain point. And from time to time, I had to question my decision on starting a PhD and working on an idealized problem instead of dealing with real-life challenges. Well, at this exact moment when I come to the point of finishing my PhD, I know by heart that devoting such a time and effort on a single problem, no matter how idealized the problem is, helps to better understand an unknown point, and together with other individual contributions to solve different problems, serves to a 'strictly' positive change in the world. Besides, doing a PhD, itself is a very tough real-life challenge causing a change not only in one's area of expertise, but also in his/her personality. It is now time to do the accounting of what I gained, and what I lost (item # 1: some of my hair :/) throughout this period, and take the chance to thank to the ones whom I am indepted a lot.

Firstly, I would like to express my sincere gratitude to my advisors Prof. Christophe Schram, and Prof. Wolfgang Polifke. It was such an enlightening and great experience to work with them. I specially thank Christophe for his very friendly attitude towards me starting from the very first day we met. He showed a great interest in all my questions and problems throughout this period, no matter what those problems were related to. He also made a priceless contribution to my socialization with my colleagues by inviting me to the salsa courses he gave and to the holy ritual of von Karman named the 'beer meetings', which he organized. I also eagerly thank Prof. Polifke for accepting me as an external PhD student and offering me an extension at the end of my contract at VKI, which gave me the vital time to capitalize my research. He was always extremely motivating, and positive towards me, and towards his other students as well, which is something that a PhD student definitely needs to keep his/her energy level up.

I am grateful to every member of the FlowAirS project, for which I was recruited, and to European Commission in a broader sense for offering such a grant. Meeting with so many great people on a regular basis made being part of the project a unique experience for me to be remembered life-through.

I would like to show my gratitude to all VKI family, with special thanks to the dream team of 'Aeroacoustics'. I also owe a sincere thank to Dr. Raimondo Giammanco for solving any problem I had with computers and doing his best to help me even off the working hours.

I thank my dearest friend Eda Doğan for her invaluable support in the writing period of this

thesis. Her efforts to revise my writings within such a short time interval can not be repaid.

I am specially thankful to all my closest friends in Brussels, Bayındır Saracoğlu, Çiğdem Taş, Ertan Ümit, Nil Atmaca, Özge Çetin, Onur Şaylan and Sibel Güçlü Şaylan, who made Belgium no different than my home. My un-finishing PhD was a common problem to them as well :) and I wholeheartedly know that they look forward to seeing me as a PhD even more than I do. Thanks to them, my experience of living abroad went much beyond my imagination.

Talking about the friends, very special thanks go to every single member of 'ıssız adam': Ceyhan Çiçek, Merve Gümüşlü and Onat Güneş. They were always right next to me whenever I needed, although living in another country. It is simply priceless, and a great honor to be a member of this tiny gang.

My deepest thanks go to my beloved Rana Ceylandağ. Her existence in my life is just priceless and this thesis would never be possible without her support and love.

And finally, I am deeply grateful beyond any words to my Mom Şükran Karban, my Dad Murat Karban, and my Brother Kazım Karban for their endless support in all my decisions. It is my honor to devote this study to them.

Abstract

This study focuses on the numerical investigation of the broadband noise generated by a low-Mach-number flow passing through ducted diaphragms. The goal of the study is to develop a fast and accurate tool based on a stochastic noise prediction method. Various noise prediction techniques including a direct approach and different hybrid approaches were implemented and were compared against experimental data. The experimental data was acquired performing in-duct aeroacoustic measurements on the test campaign installed in the anechoic chamber of the von Karman Institute for Fluid Dynamics. The measured data was post-processed using a multi-port method to identify the active source.

The scale-resolved flow data is provided from compressible Large Eddy Simulation. The applicability and the accuracy of a hybrid approach that combines Lighthill's analogy and Green's function for sound generation and radiation, respectively, are investigated. A tailored Green's function is proposed using the mode-matching technique to account for the scattering of single and tandem diaphragms in cylindrical ducts. Unsteady flow data required for the noise prediction approach is provided using the LES data, and alternatively through a stochastic method. The latter, namely 'Stochastic Noise Generation and Radidation' (SNGR) method, synthesizes turbulent velocity field satisfying the two-point statistics of a target mean flow. A grouping scheme for the noise sources based on the octree structure is introduced to minimize the memory requirements and further to reduce the computational cost. Comparison of the SNGR results and the LES predictions and measured data revealed that promising noise predictions can be achieved using the SNGR method given a proper anisotropy model and the spectral decay rate.

Contents

1 Introduction

1.1 Motivation and goal

Flow generated noise is an important problem encountered in almost every area of daily life. Especially for environments where high velocity flows are of concern, such as aircrafts, the noise generated by the flow itself and its interaction with the surrounding structures, can significantly reduce human comfort, and even be hazardous in particular conditions, unless measures are taken. Although it is a conventional problem that has existed for a long time throughout history, it has been less than a century since substantial explanations were developed for the underlying mechanism of flow noise generation. Today, it remains as a challenging research problem to predict the noise generated by complex flows in real engineering applications, and there are many ongoing research projects focusing on different application areas. Among these, flow noise in aircrafts is of particular concern due to reaching substantially high levels.

There are various noise mechanisms in an aircraft, generating different levels of noise during different phases of the flight. The noises coming from the sources like the engines, high-lift devices, landing gear etc., which can be grouped under aircraft *exterior noise*, has been extensively investigated both in the past and in ongoing research projects. There exist, on the other hand, a noticeable gap in the literature for the studies investigating the *interior noise* which is mainly due to the Environmental Conditioning Systems (ECS), also known as the Heating, Ventilation and Air Conditioning (HVAC) systems. Two particular examples of aircraft noise to which HVAC noise has a significant contribution are the 'ramp noise' and the 'cockpit noise'. For example, it was reported in [32] that the cockpit noise in an F16 jet aircraft is weighted by around 10 dB when maximum defog is switched on. As it will be discussed later in the thesis, a source causing a 10 dB increase in the noise spectrum can easily be considered to be dominant.

This HVAC system noise problem is not only studied in aircraft research, but indeed, is of high concern to the research related to transportation in general. With the increasing trend to use more and more electric vehicles in public and private transportation, HVAC noise problem has gained even more importance: in the absence of combustion engine noise, the noise coming from the HVAC systems simply became more audible. A significant contributor to the HVAC noise is the flow noise generated by various flow restrictions installed in the HVAC systems.

Flow restrictions are typical elements of HVAC systems and ECS for building, automotive, railway and aircraft applications. They can be fixed in position, i.e. diaphragms and orifices, or variable, i.e valves, and are mainly used to balance the mass flow rates between different branches of a ventilation network. Diaphragms and orifices offer an easy and efficient solution to this problem. However, they can also generate substantial broadband noise due to the turbulence they generate and/or interact with, and can even whistle in some particular conditions. Since *a posteriori* mitigation solutions aimed at ensuring passenger satisfaction or quiet workplaces

may be quite expensive, it is often preferable to perform an acoustic analysis at design stage in order to predict whether the system will meet the desired noise targets. The noise generation mechanisms associated with the interaction of the flow with solid surfaces are rather complex. Therefore, designing an HVAC system to achieve a target noise level is not possible without optimization, which makes having a fast and reliable tool essential to predict flow generated noise in ducted systems.

The goal of this PhD study was determined as developing a numerical tool to predict the broadband noise in ducted flows, which can be used in HVAC noise problems. The complex geometry of a typical HVAC system was simplified to a model problem which still reproduces most of the aeroacoustic installation effects observed in a real system while redundant complexities are avoided, which could cause losing the focus. The main focus here is placed on the stochastic approaches for being a significantly cheaper, but less accurate alternative to the scale-resolved prediction methods.

The details of the model problem designed for the PhD study, and an overview of the existing approaches for flow noise prediction are presented in the next two sections.

1.2 Problem definition

A configuration with tandem diaphragms installed in a cylindrical duct was selected to represent the HVAC noise. The schematic representation of the ducted diaphragms is provided in Figure 1.1. Given the two diaphragms, the upstream diaphragm induces a detached turbu-

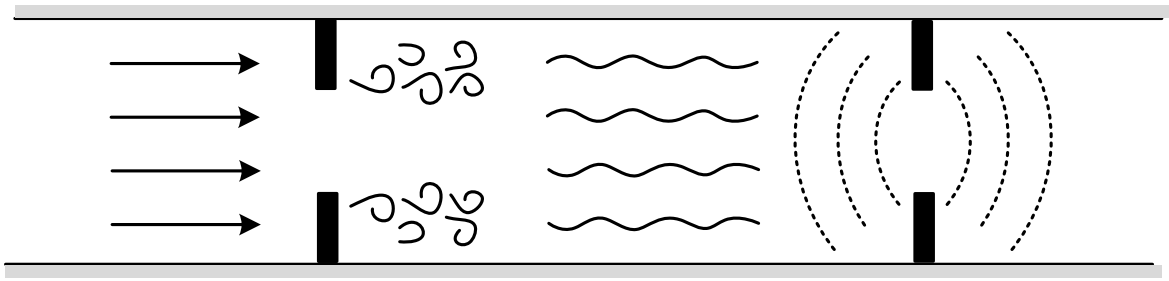

Figure 1.1: Shematic representation of the model problem for HVAC noise.

lent flow, convected through the downstream diaphragm. This mechanism is known to generate significant noise, above the level that would be emitted by the diaphragms if they were not interacting (Sengissen *et al.* [82]). The diaphragms are designed to be identical, offering a circular centered opening with a blockage ratio of $\tilde{0}.68$. Use of such a simple geometry allowed handling the noise propagation problem analytically, without making any apparent sacrifice from the complexity of the resulting interaction of the turbulence with solid surfaces. The duct inner diameter, D, is 0.15 m and the separation length of the two diaphragms is set to be $2D$. The reasoning behind setting this separation length is discussed in Section 3.3.2. To better understand the installation effects of the downstream diaphragm, a single diaphragm configuration, which is obtained by removing the downstream diaphragm, is also investigated.

1.3 An overview of the numerical noise prediction approaches

Use of Computational Fluid Dynamics (CFD) to predict noise generated by flows is a relatively recent concept, dating back to mid 1980s, while CFD for turbulence prediction has been available for more than half a decade. Such a slow evolution is due to the significantly higher costs for predicting the acoustic fluctuations of a given flow field compared to predicting its turbulent fluctuations. The discipline investigating the flow noise prediction using unsteady computational data is called 'Computational Aeroacoustics' (CAA). The name was introduced in the work of Hardin *et* Lamkin [25]. This initial study aimed at computing the sound generation by uniform flow over a cylinder at extremely low Reynolds numbers (around 200). They computed the cylinder noise using some integral solutions valid at low Mach numbers (Crow [17]). Later on, many different applications were reported in the literature, using a number of approaches for noise prediction. A classification of existing CAA approaches is depicted in Figure 1.2, where the basic distinction is made regarding the noise prediction method being 'direct' or 'hybrid'.

Direct approaches simply solve the compressible 'Navier-Stokes' equations, which describe both the flow and the acoustic fields. The unsteady flow field is obtained using one of the unsteady flow simulation techniques: Large Eddy Simulation (LES), Detached Eddy Simulation (DES), or Unsteady Reynolds Averaged Navier-Stokes (U-RANS) if only large scales are needed. Although the idea is straightforward, the applicability of such approaches are very limited due to their excessive computational costs. Even with today's computers, it is not possible to simulate, within an acceptable time-range, a commercial flow accurately enough to resolve the acoustic field inside.

Hybrid approaches offer a relatively cheaper solution to flow noise prediction albeit introducing some simplifications over the nonlinearity of the problem. The fundamental assumption of this type of approaches is that sound propagation in flow is a linear process, and therefore can be treated separately from the generation of noise, which is highly nonlinear. This assumption allows solving the incompressible flow first to generate the source data, and calculating the propagation afterward. There are different methodologies to achieve this based on an incompressible LES, or alternatively a RANS simulation. Note that semi-empirical methods are usually not counted among CAA methods. However, they are added in this classification to indicate that there exists methods in the literature relating RANS solutions to noise spectrum data through semi-empirical formulations [55]. A method based on LES is called *Split-based* method, in which a reduced set of compressible equations are solved using the incompressible unsteady pressure data to predict density fluctuations. Alternatively, 'aeroacoustic analogies' provide a powerful tool to predict sources of noise based on the unsteady incompressible flow data. Once the sources are calculated, the propagation problem is solved either using Green's functions, or linearized equations of motions such as *Linearized Euler Equations* (LEE) and *Acoustic Perturbation Equations* (APE). The unsteady incompressible solutions are usually obtained performing an LES. An alternative is called the *stochastic approaches*, in which the unsteady turbulent velocity field is synthesized based on a RANS solution such that the resulting field satisfy the two point statistics of the mean turbulent flow. The resulting synthetic velocity field is again used to predict noise sources based on aeroacoustic analogies. This study focuses on evaluation the applicability of a stochastic approach in ducted diaphragm flows. To solve the

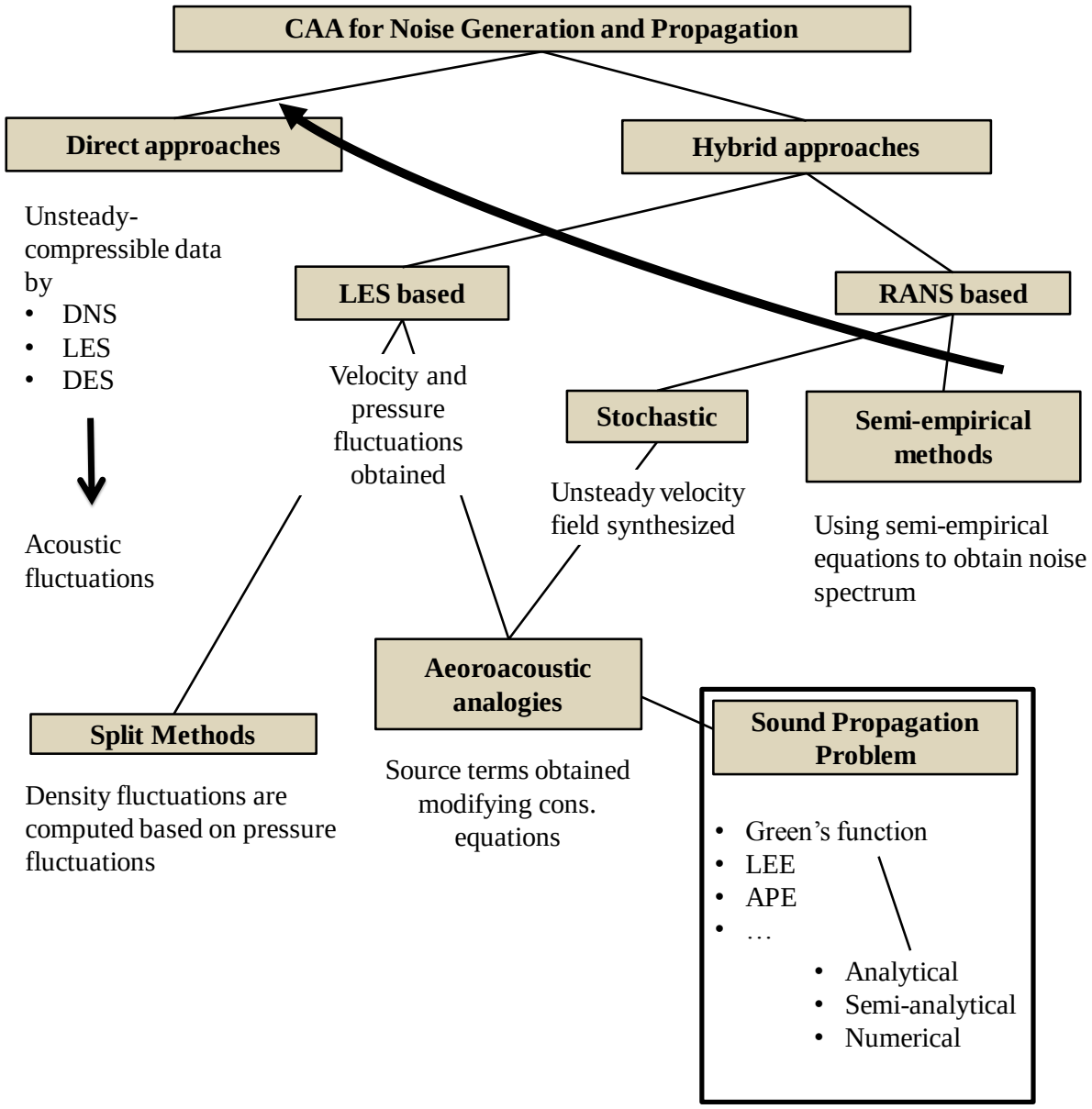

Figure 1.2: Classification of CAA methods. Arrow direction show increasing accuracy.

propagation problem, the Green's function approach is adopted, and an analytical formulation for ducted diaphragm cases is introduced. The organization of the analyses and the discussions provided in the thesis is explained in the next section.

1.4 Organization of the thesis

The theoretical concepts required for a better understanding of the thesis work are presented in Chapter 2. Fundamental theory of acoustics, some applied methods, and methods to relate turbulence and flow noise generation are discussed here. The details of the experimental setup

used in the study, and the calibration procedures are explained in Chapter 3. In Chapter 4, the post-processing methods implemented for the identification of the scattering characteristics of various components on the test rig, and the flow noise source are discussed and the results are presented. The details of the numerical flow simulations performed in the thesis study are given in Chapter 5. The numerical analysis included the investigation of a compressible LES for unsteady flow prediction, and axisymmetric RANS computations for prediction of the mean flow properties. Derivation of an analytical Green's function to solve sound propagation problem taking into account the scattering from the single and tandem diaphragms is presented in Chapter 6. The validation of the resulting analytical functions against a commercial numerical solver is also provided in this chapter. Various noise prediction approaches are discussed and the predictions from these approaches obtained using the unsteady LES data are compared in Chapter 7. The noise prediction approaches discussed in this chapter include both direct and hybrid approaches. In Chapter 8, the stochastic approach adopted in this study is discussed in detail. The implementations involved using mean LES data, and alternatively the RANS solutions to define the target flow parameters. The comparison of the noise predictions using the stochastic approach, and the unsteady LES based predictions are also presented here. And finally, some concluding remarks about the study are discussed in Chapter 9.

1.5 Published work

The study discussed in this thesis is based on several publications. The chronological order of these publications are as follows. A first attempt to apply SNGR method in ducted diaphragm noise problem was investigated in a conference paper presented in *20^{th} AIAA/CEAS Aeroacoustics Conference* [35]. Derivation of tailored Green's function for ducted diaphragms, together with implementation of Lighthill's analogy for flows in such configurations were discussed in a journal paper published in *Acta Acustica Unites with Acustica* [36]. The methods developed for system identification of ducted diaphragms was presented in a journal paper published in *The Journal of Acoustical Society of America* [34]. Finally, implementation of SNGR method with modified time filter was submitted to the *International Journal of Aeracoustics* [37].

2 Theory

A summary of the theoretical basis used in this study is provided in this chapter. The concepts discussed include fundamental acoustic equations, acoustic field inside cylindrical ducts, modal decomposition and aeroacoustic analogies. Further analyses can be found in Rienstra and Hirschberg [72], Jacobsen [31], Schram [80] on duct acoustics, and in [80] on aeroacoustic analogies.

2.1 Fundamental relations of acoustics

2.1.1 Governing equations of fluid motion

The fundamental assumption made for analyzing a fluid flow is the continuum assumption. The discrete structure of the fluid molecules is neglected, and fluid is assumed to consist of infinitesimally small elements called 'fluid particles' which contain sufficient amount of molecules to show average molecular characteristics. Once the continuum assumption is made, a given fluid flow can be described in terms of a number of variables which are well-defined everywhere inside the fluid. This subsection briefly discusses the governing equations for fluid motion. No derivations for governing equations are provided since fluid dynamics is not the focus of this thesis. A detailed discussion can be found in the books of Kundu *et al* [43] and Pope [66].

Applying the laws of conservation on a fluid particle, the conservation equations in differential form are obtained as follows:

$$\frac{\partial \rho}{\partial t} + \nabla \cdot (\rho \mathbf{u}) = 0, \tag{2.1}$$

$$\rho \frac{Du_i}{Dt} = \rho g_i + \frac{\partial \tau_{ij}}{\partial x_i}, \tag{2.2}$$

where ρ denotes the fluid density, $\mathbf{u}$ is the flow velocity, and $\mathbf{g}$ and τ_{ij} are the body and the surface forces per unit volume, respectively. Eq. (2.1) is called the continuity equation, and Eq. (2.2) is called the momentum conservation equation. D/Dt represents the material derivative, i.e. the time rate of change of a fluid particle on a frame following the particle and is defined as;

$$\frac{D}{Dt} = \frac{\partial}{\partial t} + \mathbf{u} \cdot \nabla. \tag{2.3}$$

For most of the engineering applications, the fluid is assumed to be 'Newtonian', which implies a linear relation between the stress and the rate of strain. Considering that the fluid is Newtonian

and Stokes assumption is valid, a linear relation for τ_{ij} can be defined as;

$$\tau_{ij} = -\left(p + \frac{2}{3}\mu(\nabla \cdot \mathbf{u})\right)\delta_{ij} + 2\mu e_{ij}, \tag{2.4}$$

where p is pressure, μ is the fluid viscosity, and e_{ij} is the strain rate tensor given as;

$$e_{ij} \equiv \frac{1}{2}\left(\frac{\partial u_i}{\partial x_j} + \frac{\partial u_j}{\partial x_i}\right).$$

Eq. (2.4) is called the 'constitutive equation' for a Newtonian fluid. Substituting the constitutive equation in momentum conservation equation as follows;

$$\rho\frac{Du_i}{Dt} = -\frac{\partial p}{\partial x_i} + \rho g_i + \frac{\partial}{\partial x_j}\left[2\mu e_{ij} - \frac{2}{3}\mu(\nabla \cdot \mathbf{u})\delta_{ij}\right], \tag{2.5}$$

the general form of the Navier-Stokes equation is obtained.

2.1.2 Wave equations

Acoustic waves in a fluid medium occur in the form of pressure fluctuations which propagate along the medium through the exchange of energy among particles next to each other. Such an energy exchange also induces a fluctuation in the fluid density. Assuming ideal gas and adiabatic process, i.e. no heat exchange, the isentropic relation between the pressure and density of a fluid is written as;

$$p = C\rho^{\gamma}, \tag{2.6}$$

where C is a constant and γ is the specific heat ratio, which is also a constant given a homogenous fluid at a constant temperature. The mean and the fluctuating parts of pressure, $p(t)$ and density $\rho(t)$ can be separated as follows:

$$p(t) = p_0 + p'(t), \tag{2.7}$$
$$\rho(t) = \rho_0 + \rho'(t), \tag{2.8}$$

where the subscript 0 and the prime denote the mean and fluctuating parts, respectively. Replacing Eqs. (2.7) and (2.8) into Eq. (2.6) and taking the time derivative as;

$$\begin{aligned}
\frac{\partial\left(p_0 + p'\right)}{\partial t} &= C\frac{\partial\left(\rho_0 + \rho'\right)^{\gamma}}{\partial t}, \\
\frac{\partial p'}{\partial t} &= C\gamma\rho^{\gamma-1}\frac{\partial \rho'}{\partial t}, \\
\frac{\partial p'}{\partial t} &= c^2\frac{\partial \rho'}{\partial t},
\end{aligned} \tag{2.9}$$

the pressure and density fluctuations can be related through a constant $c \equiv \sqrt{C\gamma\rho^{\gamma-1}} = \sqrt{\gamma p/\rho}$, which is defined as the 'speed of sound'.

The acoustic wave propagation equation is obtained by linearizing and reorganizing the continuity and the momentum conversation equations. Assuming that $\rho' \ll \rho_0$ and the medium is at rest, the continuity equation given in Eq. (2.1) can be reduced to the following expression:

$$\rho_0 \nabla \cdot \mathbf{u} + \frac{\partial \rho'}{\partial t} = 0. \tag{2.10}$$

Replacing time derivative of the density fluctuation in Eq. (2.10) using Eq. (2.9) yields

$$\rho_0 \nabla \cdot \mathbf{u} + \frac{1}{c^2} \frac{\partial p'}{\partial t} = 0. \tag{2.11}$$

Euler's equation of motion for a fluid particle (conservation of momentum) is given as;

$$\rho \frac{D\mathbf{u}}{Dt} + \nabla p = 0. \tag{2.12}$$

Inserting Eq. (2.7) and (2.8) into Eq. (2.12), assuming homogeneous medium and neglecting higher order terms, linearized Euler equation is obtained as follows:

$$\begin{aligned} \left(\rho_0 + \rho'\right)\left(\frac{\partial}{\partial t} + \mathbf{u} \cdot \nabla\right)\mathbf{u} + \nabla\left(p_0 + p'\right) = 0, \\ \rho_0 \frac{\partial \mathbf{u}}{\partial t} + \nabla p' = 0, \end{aligned} \tag{2.13}$$

Taking the time derivative of Eq. (2.11) and the divergence of Eq. (2.13), the two expressions are merged to yield

$$\begin{aligned} \rho_0 \nabla \cdot \frac{\partial \mathbf{u}}{\partial t} + \nabla^2 p' = \rho_0 \frac{\partial \nabla \cdot \mathbf{u}}{\partial t} + \frac{1}{c_0^2} \frac{\partial^2 p'}{\partial t^2}, \\ \nabla^2 p' - \frac{1}{c_0^2} \frac{\partial^2 p'}{\partial t^2} = 0. \end{aligned} \tag{2.14}$$

Eq. (2.14) is called the 'linearized wave equation'. c_0 denotes the uniform speed of sound in the homogeneous and isentropic medium. In a time harmonic-system, any unsteady variable, $\xi(\mathbf{x}, t)$ is defined as;

$$\xi = \hat{\xi}(\mathbf{x}) e^{i\omega t + \phi}, \tag{2.15}$$

where $\hat{\xi}$ is the complex amplitude dependent on the position, and ω and ϕ denote the frequency and the phase, respectively. For physical quantities such as the acoustic pressure fluctuation, only the real parts of the complex amplitude and the exponential term are taken into account as follows:

$$p' = \Re\left\{\hat{p} e^{i\omega t + \phi}\right\} = \left|\hat{p}\right| \cos\left(i\omega t + \phi\right). \tag{2.16}$$

The second time derivative of the acoustic pressure fluctuation then becomes

$$\frac{\partial^2 p'}{\partial t^2} = -\omega^2 \left|\hat{p}\right| \cos\left(i\omega t + \phi\right). \tag{2.17}$$

Inserting Eqs. (2.16) and (2.17) into Eq. (2.14) yields

$$\nabla^2 \hat{p} \cos\left(i\omega t + \phi\right) + \frac{\omega^2}{c_0^2} \hat{p} \cos\left(i\omega t + \phi\right) = 0, \tag{2.18}$$

which can be easily reduced to the 'Helmholtz equation':

$$\nabla^2 \hat{p} + \omega_*^2 \hat{p} = 0, \tag{2.19}$$

where $\omega_* \equiv \omega / c_0$ is called the free-field wavenumber. $|\hat{p}|$ is denoted as $\hat{p}$ in Eq. (2.19) for better readability. Note that Eq. (2.19) holds also true for the complex variable p'. The Laplacian operator, ∇^2 takes the form

$$\nabla^2 = \frac{\partial^2}{\partial x^2} + \frac{\partial^2}{\partial y^2} + \frac{\partial^2}{\partial z^2}, \tag{2.20}$$

in a Cartesian coordinate system, while in a spherical coordinate system, it is written as;

$$\nabla^2 = \frac{1}{r^2}\frac{\partial}{\partial r}\left(r^2 \frac{\partial}{\partial r}\right) + \frac{1}{r^2 \sin\vartheta}\frac{\partial}{\partial \vartheta}\left(\sin\vartheta \frac{\partial}{\partial \vartheta}\right) + \frac{1}{r^2 \sin^2\vartheta}\frac{\partial^2}{\partial \varphi^2}, \tag{2.21}$$

and in a cylindrical coordinate system, it becomes

$$\nabla^2 = \frac{1}{r}\frac{\partial}{\partial r}\left(r \frac{\partial}{\partial r}\right) + \frac{1}{r^2}\frac{\partial^2}{\partial \vartheta^2} + \frac{\partial^2}{\partial x^2}. \tag{2.22}$$

2.2 Duct acoustics

The acoustic field inside the duct illustrated in Figure 2.1 which has constant cross-section and x-independent linear boundary conditions can be obtained as an infinite summation of special solutions called 'acoustic modes'. For simple duct geometries such as rectangular, circular, and in particular cases elliptic, those acoustic modes can be analytically calculated using separation of variables.

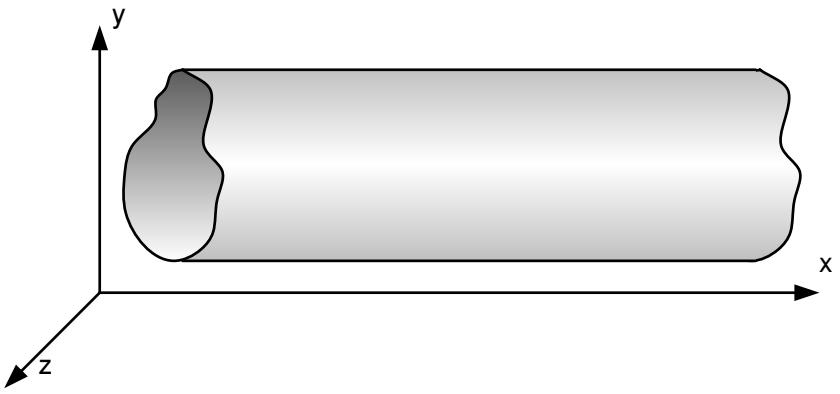

Figure 2.1: A duct with constant cross-section.

Considering the hard-walled cylindrical duct case of the this study, Helmholtz equation for the complex variable p' is given as;

$$\frac{\partial^2 p'}{\partial r^2} + \frac{1}{r}\frac{\partial p'}{\partial r} + \frac{1}{r^2}\frac{\partial^2 p'}{\partial \vartheta^2} + \frac{\partial^2 p'}{\partial x^2} + \omega_*^2 p' = 0, \tag{2.23}$$

with the boundary condition for the rigid duct wall

$$\left.\frac{\partial p'}{\partial r}\right|_{r=a} = 0, \tag{2.24}$$

where a is the duct radius. A solution for Eq. (2.23) can be assumed of the form

$$p' = F(x)G(r)H(\vartheta)e^{i\omega\vartheta}. \tag{2.25}$$

Inserting Eq. (2.25) in Eq. (2.23) yields

$$\frac{1}{G}\frac{\mathrm{d}^2 G}{\mathrm{d}r^2} + \frac{1}{rG}\frac{\mathrm{d}G}{\mathrm{d}r} + \frac{1}{r^2 H}\frac{\mathrm{d}^2 H}{\mathrm{d}\vartheta^2} + \underline{\frac{1}{F}\frac{\mathrm{d}^2 F}{\mathrm{d}x^2}} + \omega_*^2 = 0. \tag{2.26}$$

The underlined term in Eq. (2.26) depends only on x and is the only x-dependent term, which is possible only if it equals a constant, $-k^2$:

$$\frac{1}{F}\frac{\mathrm{d}^2 F}{\mathrm{d}x^2} = -k^2, \tag{2.27}$$

$$\frac{\mathrm{d}^2 F}{\mathrm{d}x^2} + k^2 F = 0. \tag{2.28}$$

Eq. (2.28) has a general solution of the form

$$F(x) = Ae^{-ikx} + Be^{+ikx}. \tag{2.29}$$

Replacing the underlined term in Eq. (2.26) using Eq. (2.27) and multiplying the resulting expression by r^2,

$$\frac{r^2}{G}\frac{\mathrm{d}^2 G}{\mathrm{d}r^2} + \frac{r}{G}\frac{\mathrm{d}G}{\mathrm{d}r} + \underline{\frac{1}{H}\frac{\mathrm{d}^2 H}{\mathrm{d}\vartheta^2}} + r^2\left(\omega_*^2 - k^2\right) = 0 \tag{2.30}$$

is obtained. The underlined term in Eq. (2.30) is again to be equal to a constant, $-m^2$ similar to the case in Eq. (2.26):

$$\frac{1}{H}\frac{\mathrm{d}^2 H}{\mathrm{d}\vartheta^2} = -m^2, \tag{2.31}$$

$$\frac{\mathrm{d}^2 H}{\mathrm{d}\vartheta^2} + m^2 H = 0. \tag{2.32}$$

Once again, a general solution is available for Eq. (2.32) as follows:

$$H(\vartheta) = Ce^{\pm im\vartheta}. \tag{2.33}$$

Note that H should be periodic with a period 2π due to the axisymmetry of the duct:

$$H(\vartheta) = H(\vartheta + 2\pi). \tag{2.34}$$

Replacing ϑ in Eq. (2.33) with $(\vartheta+2\pi)$ is then to give the same solution, which is only achievable if m is an integer. The only function in Eq. (2.25) for which a general solution is yet to be found is $G(r)$. Inserting Eq. (2.31) into Eq. (2.30), and multiplying it by G/r^2 gives the following expression:

$$\frac{\mathrm{d}^2G}{\mathrm{d}r^2} + \frac{1}{r}\frac{\mathrm{d}G}{\mathrm{d}r} + G\left(\alpha^2 - \frac{m}{r^2}\right) = 0, \tag{2.35}$$

where α is defined in the following relation:

$$\alpha^2 = \omega_*^2 - k^2. \tag{2.36}$$

Eq. (2.35) is called the 'Bessel equation' and a general solution is provided as;

$$G(r) = DJ_m(\alpha r) + EY_m(\alpha r), \tag{2.37}$$

where J_m and Y_m are Bessel functions of the first and second kind, respectively. J_m and Y_m are plotted for different m values in Figure 2.2. It is seen that for $r = 0$, only J_m has a finite

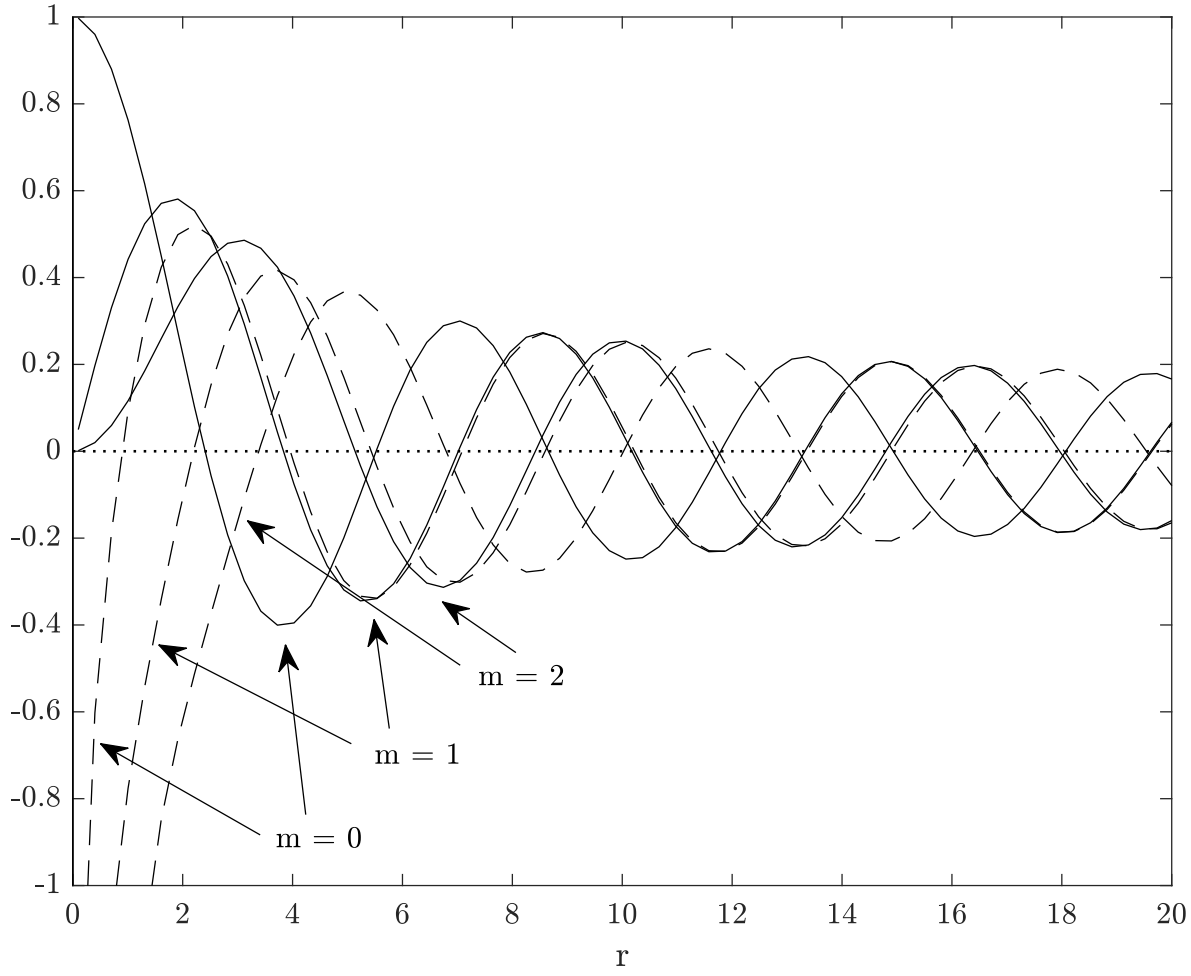

Figure 2.2: Bessel functions of the first and the second kind.

value while all Y_m functions tend to $-\infty$ which is obviously not physical. To eliminate the

non-physical part, E is to be zero, yielding

$$G(r) = DJ_m(\alpha r). \tag{2.38}$$

Since G is the only r-dependent function, the boundary condition given in Eq. (2.24) reduces to the following expression:

$$\left.\frac{\mathrm{d}G}{\mathrm{d}r}\right|_{r=a} = D\alpha J'_m = 0, \tag{2.39}$$

where J'_m is the derivative of the J_m with respect its argument. For Eq. (2.39) to be true, $\alpha a = \alpha_{m\mu} a$ should be satisfied where $\alpha_{m\mu} a$ corresponds to the μ^{th} non-trivial, non-negative zero of J'_m. Note that k was related to α in Eq. (2.36). Therefore for α taking only particular values, $\alpha_{m\mu}$, k becomes

$$k_{m\mu} = \sqrt{\omega^2 - \alpha_{m\mu}^2}. \tag{2.40}$$

The solutions given by Eqs. (2.29), (2.33) and (2.38) are called the 'duct modes', and the corresponding eigenvalues, $k_{m\mu}$, m and $\alpha_{m\mu}$ are called the 'axial', 'azimuthal', and 'radial' wavenumbers, respectively. It should be noted that all $\alpha_{m\mu}$ values are real, while it is the case for only a finite number of $k_{m\mu}$. Figure 2.3 presents the axial wavenumbers distributed in the complex plane for a given (m, ω_*) pair, where it is seen that only four of the wavenumbers lie on the real axis. The importance of the axial wavenumbers being real or complex will be discussed below.

The radial modes given in Eq. (2.38) satisfying the boundary condition in Eq. (2.39) are not normalized. A more convenient form can obtained by scaling each mode to satisfy the orthonormality condition given as;

$$\int_0^a r U_{m\mu}(r)^2 \mathrm{d}r = 1, \tag{2.41}$$

where

$$U_{m\mu}(r) \equiv N_{m\mu} J_{m\mu}(\alpha_{m\mu} r). \tag{2.42}$$

Using the integration formula given as;

$$\int x \mathscr{C}_m(\beta x) \tilde{\mathscr{C}}_m(\beta x) = \frac{1}{2}\left(x^2 - \frac{m^2}{\beta^2}\right) \mathscr{C}_m(\beta x) \tilde{\mathscr{C}}_m(\beta x) + \frac{1}{2} x^2 \mathscr{C}'_m(\beta x) \tilde{\mathscr{C}}'_m(\beta x),$$

Eq. (2.41) becomes

$$\begin{aligned} \int_0^a r U_{m\mu}(r)^2 \mathrm{d}r &= \frac{1}{2}\left(r^2 - \frac{m^2}{\alpha_{m\mu}^2}\right) U_{m\mu}^2 + \frac{1}{2} r^2 U'_{m\mu} U'_{m\mu} \Big|_{r=0}^{a} \\ &= 1. \end{aligned} \tag{2.43}$$

The term $U'_{m\mu}$ equals 0 by definition, as $\alpha_{m\mu}$ is selected to make J'_m zero, causing the last term in Eq. (2.43) to be dropped. The right hand side of Eq. (2.43) becomes zero at $r = 0$, since either

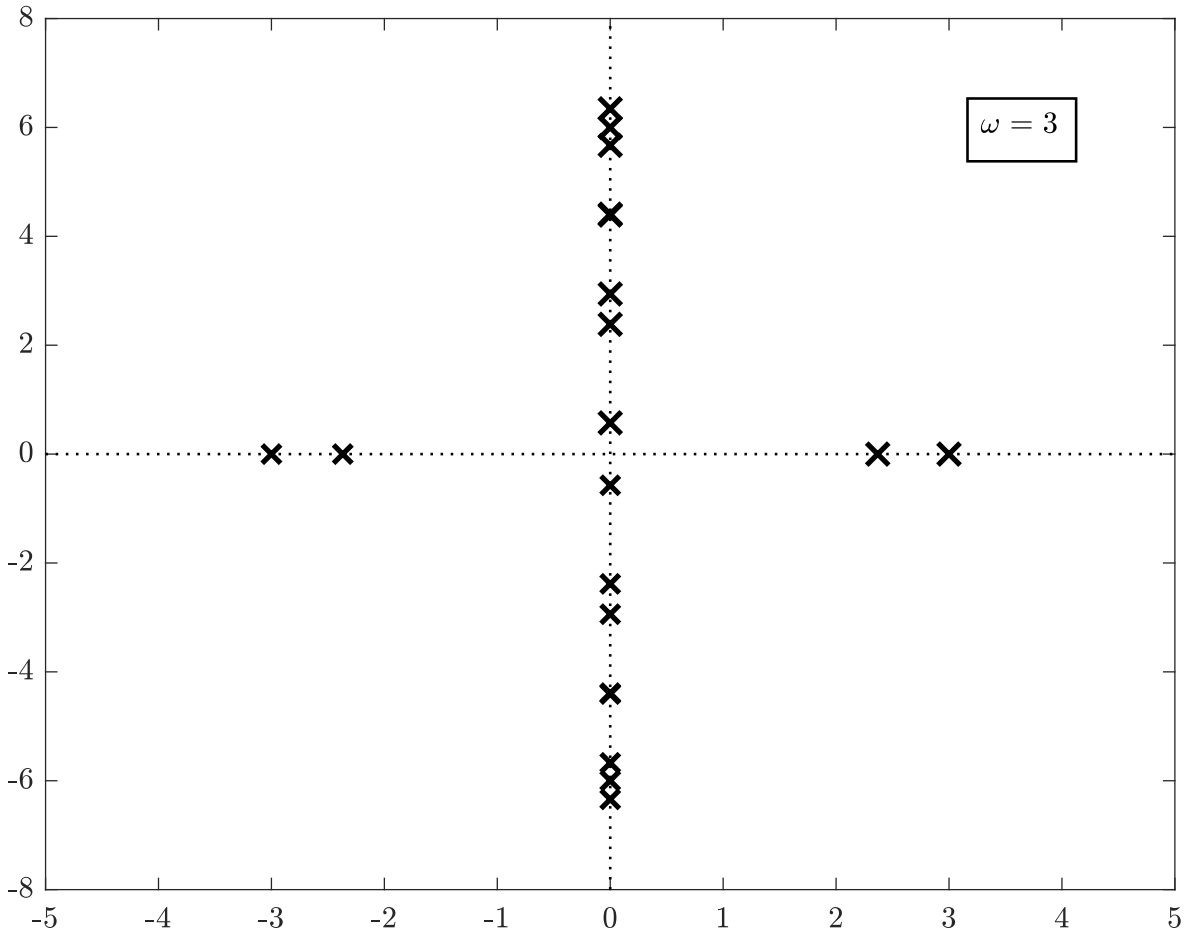

Figure 2.3: The axial wavenumbers for a given $\omega = 3$.

m or $J_m(0)$ is zero. The normalization factor $N_{m\mu}$ is then obtained as follows:

$$\frac{1}{2}\left(a^2 - \frac{m^2}{\alpha_{m\mu}^2}\right) N_{m\mu}^2 J_m(\alpha_{m\mu}a)^2 = 1,$$

$$N_{m\mu} = \left[\frac{1}{2}\left(a^2 - \frac{m^2}{\alpha_{m\mu}^2}\right) J_m(\alpha_{m\mu}a)^2\right]^{-1/2}. \tag{2.44}$$

This completes the analysis to obtain a general solution to define the acoustic field inside a cylindrical duct. The acoustic field is given as a summation of the duct modes in the following form:

$$p'(x,r,\vartheta) = \sum_{m=-\infty}^{\infty}\sum_{\mu=1}^{\infty}\left(A_{m\mu}e^{-ik_{m\mu}x} + B_{m\mu}e^{+ik_{m\mu}x}\right)U_{m\mu}(r)e^{-im\vartheta}, \tag{2.45}$$

where $A_{m\mu}$ and $B_{m\mu}$ are the mode amplitudes. It was mentioned above that only a finite number of axial wavenumbers are real although the summation given in Eq. (2.45) is infinite. For the axial wavenumbers which are complex, the power term in the axial mode turn into a negative real, causing the mode to exponentially decay. This means that only the modes with real axial wavenumbers can propagate inside a duct. For the axial mode to be real, inside of the square

root given in Eq. (2.40) should be positive:

$$\omega^2 > \alpha_{m\mu}^2. \tag{2.46}$$

This leads to the following expression which represents the frequency limit f_c for a given mode to be real:

$$f_c = \frac{\alpha_{m\mu} c_0}{2\pi a}. \tag{2.47}$$

Eq. (2.47) gives the minimum frequency for an acoustic mode (m, μ) to start propagating inside the duct. The propagative modes at a given frequency are called 'cut-on modes', and similary, the frequency limit given in Eq. (2.47) is called the 'cut-on frequency'. A special case is obtained for the frequency below the limit obtained for $(m, \mu) = (0, 1)$, where only a single mode can propagate along the duct. Substituting the corresponding values for (m, μ) in Eq. (2.45), it reduces to a simple expression:

$$p' = \left(A_{01} e^{-ik_{m\mu}x} + B_{01} e^{+ik_{01}x} \right). \tag{2.48}$$

The acoustic wave obtained using Eq. (2.48) is called a 'plane wave' since p' depends only on the axial component x. From the physical point of view, $e^{\mp ik_{m\mu}x}$ correspond to the right- and left-going waves, respectively. This implies for an acoustic wave traveling inside a duct that either $A_{m\mu}$ or $B_{m\mu}$ is zero.

2.2.1 Effect of uniform mean flow

The solution given in Eq. (2.45) can be extended to the case where the acoustic field is convected with a uniform mean flow. Defining the axial flow velocity, $\mathbf{u}_0 = [u_0, 0, 0]^\top$, the linearized continuity equation given in Eq. (2.11) becomes

$$\begin{aligned} \rho_0 \nabla \cdot \mathbf{u} + \frac{1}{c_0^2} \frac{\partial p'}{\partial t} + \frac{1}{c_0^2} \mathbf{u}_0 \cdot \nabla p' = 0, \\ \rho_0 \nabla \cdot \mathbf{u} + \frac{1}{c_0^2} \frac{\partial p'}{\partial t} + \frac{1}{c_0^2} u_0 \frac{\partial p'}{\partial x} = 0. \end{aligned} \tag{2.49}$$

Similarly, the momentum conservation equation given in Eq. (2.13) turns into

$$\begin{aligned} \rho_0 \frac{\partial \mathbf{u}}{\partial t} + \rho_0 \left(\mathbf{u}_0 \cdot \nabla \right) \mathbf{u} + \nabla p' = 0, \\ \rho_0 \frac{\partial \mathbf{u}}{\partial t} + \rho_0 u_0 \frac{\partial \mathbf{u}}{\partial x} + \nabla p' = 0. \end{aligned} \tag{2.50}$$

Assuming time harmonic pressure and velocity fluctuations, Eqs. (2.49) and (2.50) can be written as;

$$\frac{1}{c_0^2} \left(i\omega + u_0 \frac{\partial}{\partial x} \right) p' + \rho_0 \nabla \cdot \mathbf{u} = 0, \tag{2.51}$$

$$\rho_0 \left(i\omega + u_0 \frac{\partial}{\partial x} \right) \mathbf{u} + \nabla p' = 0. \tag{2.52}$$

The term $\rho_0\mathbf{u}$ can be eliminated from Eqs. (2.51) and (2.52) to yield the convected wave equation:

$$\frac{1}{c_0^2}\left(i\omega + u_0\frac{\partial}{\partial x}\right)^2 p' - \nabla^2 p' = 0. \tag{2.53}$$

Note that

$$\frac{1}{c_0^2}\left(i\omega + u_0\frac{\partial}{\partial x}\right)^2 = \left(i\omega_* + M\frac{\partial}{\partial x}\right)^2, \tag{2.54}$$

where the parameter $M \equiv u_0/c_0$ is called the Mach number. Similar to the no-flow case, a solution in Fourier-Bessel modes can be obtained for the above eigenvalue problem as;

$$p'(x,r,\vartheta) = \sum_{m=-\infty}^{\infty}\sum_{\mu=1}^{\infty}\left(A_{m\mu}e^{-ik^+_{m\mu}x} + B_{m\mu}e^{+ik^-_{m\mu}x}\right)U_{m\mu}(r)e^{-im\vartheta}, \tag{2.55}$$

where the relation between the radial and axial wavenumbers are given as follows:

$$\alpha^2_{m\mu} = \left(\omega - Mk_{m\mu}\right)^2 - k^2_{m\mu}, \tag{2.56}$$

$$k^{\pm}_{m\mu} = \frac{-\omega M \pm \sqrt{\omega^2 - \left(1-M^2\right)\alpha^2_{m\mu}}}{1-M^2}. \tag{2.57}$$

Since the flow has only the axial component and separation of variables apply, the mean flow is expected to effect only the axial modes. Therefore, the normalization of the radial modes remains the same for the no-flow and uniform mean flow cases.

2.2.2 Sound propagation due to a point source inside a cylindrical duct

When there is a point source inside a cylindrical duct, the acoustic field generated by the source located at $\mathbf{x}_0$ can be obtained solving the inhomogeneous convected wave equation:

$$\nabla^2 G - \left(i\omega_* + M\frac{\partial}{\partial x}\right)^2 G = \delta(\mathbf{x}-\mathbf{x}_0), \tag{2.58}$$

where $G(\mathbf{x}|\mathbf{x}_0)$ is the Green's function representing the pressure field due to a unit point source, δ. The Dirac function can be represented as;

$$\delta(\mathbf{x}-\mathbf{x}_0) = \frac{\delta(r-r_0)}{r}\frac{1}{2\pi}\int_{-\infty}^{\infty} e^{-i\kappa(x-x_0)}\mathrm{d}\kappa \int_{-\infty}^{\infty} e^{-im(\vartheta-\vartheta_0)}\mathrm{d}m, \tag{2.59}$$

which immediately reduces to

$$\delta(\mathbf{x}-\mathbf{x}_0) = \frac{\delta(r-r_0)}{r}\frac{1}{2\pi}\int_{-\infty}^{\infty} e^{-i\kappa(x-x_0)}\mathrm{d}\kappa \sum_{-\infty}^{\infty} e^{-im(\vartheta-\vartheta_0)} \tag{2.60}$$

since the solution should be periodic in azimuthal direction restricting m to take integer values only. The solution to the inhomogeneous equation given in Eq. (2.58) is predicted to be of the form

$$G(x,r,\vartheta|x_0,r_0,\vartheta_0) = \sum_{m=-\infty}^{\infty} e^{-im(\vartheta-\vartheta_0)}G_m(r,x) = \sum_{m=-\infty}^{\infty} e^{-im(\vartheta-\vartheta_0)}\int_{-\infty}^{\infty}\hat{G}_m(r,\kappa)e^{-i\kappa(x-x_0)}\mathrm{d}\kappa. \tag{2.61}$$

Inserting Eqs. (2.60) and (2.61) into Eq. (2.58) yields

$$\frac{\partial^2 \hat{G}_m}{\partial r^2} + \frac{1}{r}\frac{\partial \hat{G}_m}{\partial r} + \left(\alpha^2 - \frac{m^2}{r^2}\right)\hat{G}_m = \frac{\delta(r-r_0)}{4\pi^2 r_0}, \tag{2.62}$$

where α is defined as;

$$\alpha^2 = \Omega^2 - \kappa^2, \tag{2.63}$$

and $\Omega = \omega_* - \kappa M$. The solution of Eq. (2.62) is obtained by extending the homogeneous solution to handle the source term on the right hand side as follows:

$$\hat{G}_m(r,\kappa) = A(\kappa)J_m(\alpha r) + \frac{1}{8\pi}H(r-r_0)\big(J_m(\alpha r_0)Y_m(\alpha r) - Y_m(\alpha r_0)J_m(\alpha r)\big), \tag{2.64}$$

where $H(r-r_0)$ is the Heaviside function. The boundary condition for the hard-wall duct is once again given as;

$$\hat{G}'_m\big|_{r=a} = 0, \tag{2.65}$$

where the prime denotes derivative with respect to the argument. The amplitude $A(\kappa)$ can be calculated substituting Eq. (2.64) into the boundary condition equation as follows:

$$\begin{aligned}
\hat{G}'_m\big|_{r=a} &= \alpha A J'_m + \frac{1}{8\pi}H\left(\alpha J_{m0}Y'_m - \alpha Y_{m0}J'_m\right) + \frac{1}{8\pi}\delta\left(\alpha J_{m0}Y'_m - \alpha Y_{m0}J'_m\right)\big|_{r=a} = 0,\\
AJ'_{ma} &= -\frac{1}{8\pi}\left(J_{m0}Y'_{ma} - Y_{m0}J'_{ma}\right),\\
A &= \frac{1}{8\pi}\left(Y_{m0} - J_{m0}\frac{Y'_{ma}}{J'_{ma}}\right).
\end{aligned} \tag{2.66}$$

Note that since the point source is inside the duct, the condition $r_0 < a$ is always true, making $H = 1$ and $\delta = 0$. The terms J_{m0}, Y_{m0}, J_{ma}, Y_{ma} are short-hand notations for the Bessel functions of the first and second kind calculated at (αr_0) and (αa), respectively. Substituting the value of A in Eq. (2.64), $\hat{G}_m$ can be written as;

$$\hat{G}_m = \begin{cases} \dfrac{1}{8\pi}\left(Y_{m0} - J_{m0}\dfrac{Y'_{ma}}{J'_{ma}}\right)J_m, & \text{for } r < r_0 \\ \dfrac{1}{8\pi}\left(Y_m - J_m\dfrac{Y'_{ma}}{J'_{ma}}\right)J_{m0}, & \text{for } r > r_0 \end{cases}$$

which can be given in a shorter form as;

$$\hat{G}_m = \frac{1}{8\pi}\left(\frac{Y_m(\alpha r_>)J'_{ma} - J_m(\alpha r_>)Y'_{ma}}{J'_{ma}}\right)J_m(\alpha r_<), \tag{2.67}$$

where $r_> = \max(r, r_0)$ and $r_< = \min(r, r_0)$. In Eq. (2.67), both the numerator and denominator can be written as α^m times an analytical function, making $\hat{G}_m$ a meromorphic function with isolated poles at $\alpha = \alpha_{m\mu}$ satisfying $J_m(\alpha_{m\mu}a)' = 0$. The integral given in Eq. (2.61)

$$\int_{-\infty}^{\infty} \hat{G}_m(r,\kappa)e^{-i\kappa(x-x_0)}\mathrm{d}\kappa \tag{2.68}$$

can then be calculated using the residue theorem. Given a meromorphic function $f(z)$ with isolated poles $b_1, \ldots, b_n$ in the complex plane enclosed in a simple contour γ, residue theorem indicates that the line integral of f around γ can be evaluated as;

$$\oint_\gamma f(z)dz = 2\pi i \sum \mathrm{Res}(f, b_k), \tag{2.69}$$

where $\mathrm{Res}(f, b)$ is a residue of f. If $f(z)$ can be expressed as a quotient of two functions, $f(z) = g(z)/h(z)$, where $h(b) = 0$ and $h'(b) \neq 0$, and if b is a simple pole, the residue equals;

$$\mathrm{Res}(f, b) = \frac{g(b)}{h'(b)}. \tag{2.70}$$

In Eq. (2.68), the integration contour is closed around the lower half-plane for $x < x_0$ to enclose the right-propagating modes, and around the upper half-plane for $x > x_0$ to enclose the left-propagating modes. Following Eq. (2.70), the derivative of the denominator of $\hat{G}_m$ with respect to κ is given as;

$$\frac{\mathrm{d}J'_{ma}}{\mathrm{d}\kappa}\Big|_{\kappa=\kappa_{m\mu}} = J_m(\alpha_{m\mu}a)Q_{m\mu}, \tag{2.71}$$

where

$$Q^{\pm}_{m\mu} = \pm a^2\left(\kappa_{m\mu} + \Omega_{m\mu}M\right)\left(1 - \frac{m^2}{\alpha^2_{m\mu}}\right). \tag{2.72}$$

The $\pm$ sign refer to the right- and left-going modes, respectively. For $\alpha = \alpha_{m\mu}$, the Wronskian given as;

$$J_m(x)Y'_m(x) - Y_m(x)J'_m(x) = \frac{2}{\pi x} \tag{2.73}$$

reduces to

$$J_m(\alpha_{m\mu}a)Y'_m(\alpha_{m\mu}a) = \frac{2}{\pi x}. \tag{2.74}$$

Similarly the numerator of the term in parentheses in Eq. (2.67) reduces to $-J_m(\alpha_{m\mu}r_>)Y_m(\alpha_{m\mu}a)'$ which can further be treated as;

$$\begin{aligned} -J_m(\alpha_{m\mu}r_>)Y_m(\alpha_{m\mu}a)' &= -J_m(\alpha_{m\mu}r_>)Y_m(\alpha_{m\mu}a)'\frac{J_m(\alpha_{m\mu}a)}{J_m(\alpha_{m\mu}a)}, \\ &= \frac{2}{\pi x}\frac{-J_m(\alpha_{m\mu}r_>)}{J_m(\alpha_{m\mu}a)}. \end{aligned} \tag{2.75}$$

Calculating the residue using Eqs. (2.71) and (2.75) and substituting in the residue theorem, $G_m(r, x)$ is derived as;

$$G_m(r, x) = \frac{i}{2\pi}\sum_{\mu=1}^{\infty}\frac{J_m(\alpha_{m\mu}r_<)J_m(\alpha_{m\mu}r_>)}{Q_{m\mu}J_m(\alpha_{m\mu}a)^2}e^{-i\kappa(x-x_0)}. \tag{2.76}$$

Having $r_<$ and $r_>$ in pair, the distinction can now be removed, and the Green's function for a point source inside a cylindrical duct can be written as follows:

$$G(\mathbf{x}, \mathbf{x}_0) = \frac{i}{2\pi}\sum_{m=-\infty}^{\infty}\sum_{\mu=1}^{\infty}\frac{J_m(\alpha_{m\mu}r)J_m(\alpha_{m\mu}r_0)}{Q_{m\mu}J_m(\alpha_{m\mu}a)^2}e^{-i\kappa(x-x_0)-im(\vartheta-\vartheta_0)}. \tag{2.77}$$

2.2.3 Modal decomposition of the acoustic field inside a cylindrical duct

So far in the analyses provided in this section, finding the acoustic pressure at a given listener point inside the duct was aimed at by performing a summation over the acoustic modes. In this subsection, the problem will be reversed: given the acoustic pressure data at various points inside the duct, the modal components will be calculated. The method is called 'modal decomposition' and was devised by Åbom [3] as a higher order mode extension to the two-microphone method of Chung *et* Blaser [15] which was valid only for the plane wave region. A revisit of the method is provided below.

Following the analysis in Section 2.2.1, the pressure field at a point inside a cylindrical duct is given as;

$$p'(x,r,\vartheta) = \sum_{m=-\infty}^{\infty}\sum_{\mu=1}^{\infty} p^{+}_{m\mu}U_{m\mu}(r)e^{-ik^{+}_{m\mu}x-im\vartheta} + p^{-}_{m\mu}U_{m\mu}(r)e^{+ik^{-}_{m\mu}x-im\vartheta}, \tag{2.78}$$

where $p^{\pm}_{m\mu}$ correspond to the right-/left-going waves. Considering more than one listener points, a system of equations can be constructed based on Eq. (2.78). Assuming Q cut-on modes, $m_i\mu_i$ where $(i = 1,2,\ldots,Q)$ and P listener points, x_j where $(y = 1,2,\ldots,P)$, a linear system is obtained as;

$$\mathbf{p}' = \mathbb{J}\mathbf{p}^{\pm}, \tag{2.79}$$

where $\mathbf{p}'_{(P\times 1)} = [p'_{x_1}\ \cdots\ p'_{x_P}]^{\top}$ and $\mathbf{p}^{\pm}_{(2Q\times 1)} = [p^{+}_{m_1\mu_1}\ p^{-}_{m_1\mu_1}\ \cdots\ p^{+}_{m_Q\mu_Q}\ p^{-}_{m_Q\mu_Q}]^{\top}$. The transfer matrix between the measurements and right-/left-going waves, $\mathbb{J}$, is constructed in the form of a block matrix as;

$$\mathbb{J}_{(P\times 2Q)} = \begin{bmatrix} \mathscr{J}_{1,1} & \cdots & \mathscr{J}_{1,Q} \\ \vdots & \ddots & \vdots \\ \mathscr{J}_{P,1} & \cdots & \mathscr{J}_{P,Q} \end{bmatrix}, \tag{2.80}$$

where the generic block, $\mathscr{J}_{p,q}$ is defined as;

$$\mathscr{J}_{p,q} \equiv \begin{bmatrix} U_{m_q\mu_q}(r)e^{-ik^{+}_{m_q\mu_q}x_p-im_q\vartheta_p} & U_{m_q\mu_q}(r)e^{ik^{-}_{m_q\mu_q}x_p-im_q\vartheta_p} \end{bmatrix}. \tag{2.81}$$

It is obvious from Eq. (2.79) that the modal components of any sound field can be calculated by taking the inverse of the transfer matrix, $\mathbb{J}$ as follows:

$$\mathbf{p}^{\pm} = \mathbb{J}^{-1}\mathbf{p}'. \tag{2.82}$$

For $\mathbb{J}$ to be invertible it should be non-singular, i.e. it should contain at least $2Q$ linearly independent rows, which immediately implies $P \geq 2Q$. The matrix, $\mathbb{J}$ depends only on the listener positions meaning that a proper positioning of the listeners is required to satisfy such a criterion. Note that, it is possible to obtain an overdetermined system by setting $P > 2Q$ with proper positioning of listeners yielding a linearly independent system. In such a case, a direct inversion is not possible. Moore-Penrose inversion (also called a 'pseudo-inverse') should be used instead as follows:

$$\mathbb{J}^{\dagger} = (\mathbb{J}^{\top}\mathbb{J})^{-1}\mathbb{J}^{\top}. \tag{2.83}$$

Eq. (2.82) is then to be updated as;

$$\langle \mathbf{p}^{\pm} \rangle = \mathbb{J}^{\dagger} \mathbf{p}', \tag{2.84}$$

where $\langle \mathbf{p}^{\pm} \rangle$ denotes the least square estimate of $\mathbf{p}^{\pm}$. Constructing an overdetermined system is of high practical importance. For real applications, either numerical or experimental, the pressure data recorded at the listeners usually include non-acoustic content, i.e. error, as well. The pseudo-inverse gives a least square estimation, which eliminates to a certain extent the error in the input data.

2.3 Flow noise prediction through aeroacoustic analogies

The governing equations of the acoustic perturbations and the fluid flow are the same. The fluctuation data obtained using an unsteady compressible set of flow equations also contain the acoustic field induced by the flow. Flow noise prediction approaches making use of numerical solvers which take into account this compressibility effects are named 'direct approaches'. The acoustic field is not explicitly modeled in direct approaches. The compressible equations inherently include a two-way coupling mechanism with the flow and the acoustic field. This allows the direct approaches to solve any aeroacoustic problem: tonal, broadband, combustion etc. noise. However, due to the disparity of scales and amplitudes between the hydrodynamic and acoustic perturbations, the accuracy of the numerical simulations are to be very high to be able the resolve the acoustic field properly. Such a demand for high accuracy results in excessive computational costs making direct approaches infeasible for many engineering flows. Hybrid approaches as an alternative can provide satisfactory noise predictions at significantly lower costs. The fundamental assumption of the hybrid approaches is that a one way coupling is considered between the flow and the acoustic fields. The prediction of the flow and the acoustic field are treated sequentially, ignoring the effect of the acoustic field on the flow. There are various noise prediction methods counted as hybrid. Among them, aeroacoustic analogies take an important place for low Mach number noise prediction problems. The noise prediction strategies adopted in the present study are mainly based on the aeroacoustic analogies of Lighthill and Curle. Therefore, a detailed revisit is provided in the following subsections.

2.3.1 Lighthill's aeroacoustic analogy

Lighthill [51] introduced the idea of reformulating the equations of fluid motion to allow a distinction between the sound generation and propagation parts, which are called the 'source' and 'reference' regions. Lighthill's derivation of such a formulation starts with the conservation equations of mass and momentum. The conservative form of the momentum equation is given as;

$$\frac{\partial \rho u_i}{\partial t} + \frac{\partial \rho u_i u_j}{\partial x_j} = -\left(\frac{\partial p}{\partial x_i} - \frac{\partial \sigma_{ij}}{\partial x_j} \right) + f_i, \tag{2.85}$$

where **f** is the density of the force field. Taking the time derivative of the continuity equation (2.1) as;

$$\frac{\partial^2 \rho}{\partial t^2} + \frac{\partial}{\partial t}\frac{\partial \rho u_i}{\partial x_i} = 0, \tag{2.86}$$

and the divergence of Eq. (2.85) as;

$$\frac{\partial}{\partial x_i}\frac{\partial \rho u_i}{\partial t} + \frac{\partial^2 \rho u_i u_j}{\partial x_i \partial x_j} = -\left(\frac{\partial^2 p}{\partial x_i^2} - \frac{\partial^2 \sigma_{ij}}{\partial x i \partial x_j}\right) + \frac{\partial f_i}{\partial x_i}, \tag{2.87}$$

Eq. (2.87) is subtracted from Eq. (2.86) to obtain;

$$\frac{\partial^2 \rho}{\partial t^2} = \frac{\partial^2 (\rho u_i u_j - \sigma_{ij})}{\partial x_i \partial x_j} + \frac{\partial^2 p}{\partial x_i^2} - \frac{\partial f_i}{\partial x_i}. \tag{2.88}$$

A term $c_0^2(\partial^2 \rho / \partial x_i^2)$ where c_0 is a velocity is subtracted from both sides of Eq. (2.88) to obtain the wave propagation operator of d'Alembert on the left hand side as follows:

$$\frac{\partial^2 \rho}{\partial t^2} - c_0^2 \frac{\partial^2 \rho}{\partial x_i^2} = \frac{\partial^2 (\rho u_i u_j - \sigma_{ij})}{\partial x_i \partial x_j} + \frac{\partial^2 p - c_0^2 \rho}{\partial x_i^2} - \frac{\partial f_i}{\partial x_i}. \tag{2.89}$$

Splitting the flow variables (ρ, p) into a uniform reference state (ρ_0, p_0) and a fluctuating part (ρ', p'), assuming stagnant flow, and following an analysis similar to the one given in Section 2.1.2, Eq. (2.89) can be written in terms of the fluctuating variables to obtain Lighthill's analogy:

$$\frac{\partial^2 \rho'}{\partial t^2} - c_0^2 \frac{\partial^2 \rho'}{\partial x_i^2} = \frac{\partial^2 T_{ij}}{\partial x_i \partial x_j} - \frac{\partial f_i}{\partial x_i}, \tag{2.90}$$

with T_{ij}, the so-called Lightill's stress tensor defined as;

$$T_{ij} \equiv \rho u_i u_j + (p' - c_0^2 \rho')\delta_{ij} - \sigma_{ij}. \tag{2.91}$$

An important notice to be made here is that Eq. (2.91) is the exact equation defining all the mechanisms generating acoustic waves in a uniform stagnant fluid. This implies that an attempt to predict the noise generated inside flow using Eq. (2.91) requires the knowledge of all the non-linear interactions among the flow variables, and therefore is not necessarily better than directly solving the compressible Navier-Stokes equation. On the other hand, it allows evaluating the relative importance of different noise generation mechanisms given a flow condition, so that simplifications are easy to make.

The term f_i drops if there are no external forces exerted on the fluid elements. For typical industrial flow where high-Reynolds number assumption can be made, the contribution of the viscous term, σ_{ij} to noise generation with respect to the $\rho u_i u_j$ term can be neglected. Moreover, for isentropic flows, the second term on the right hand side of Eq. (2.91) can also be dropped. And finally, for low-Mach number flows, the compression effects can be considered to be very small so that the following simplification holds true:

$$\rho u_i u_j \simeq \rho_0 u_i u_j. \tag{2.92}$$

2.3.1.1 Integral formulation of Lighthill's analogy

Assuming causality and initially silent medium, the integral formulation of Eq. (2.90) is given as;

$$\rho'(\mathbf{x},t) = \int_{-\infty}^{t} \iiint_{V} \frac{\partial^2 T_{ij}}{\partial y_i \partial y_j} G \mathrm{d}^3\mathbf{y}\mathrm{d}\tau - c_0^2 \int_{-\infty}^{t} \iint_{\partial V} \left(\rho' \frac{\partial G}{\partial y_i} - G \frac{\partial \rho'}{\partial y_i} \right) n_i \mathrm{d}^2\mathbf{y}\mathrm{d}\tau, \tag{2.93}$$

where $\mathbf{x}$ and $\mathbf{y}$ denote the listener and source positions, respectively. The volume integral on the right hand side of Eq. (2.93) correspond to the incident sound field generated by volumetric sources, and the surface integral represents the scattering of the incident field over the boundaries, ∂V. This form of integral representation of Lighthill's analogy is highly prone to numerical issues, as any error contained in the stress tensor data is severely amplified by double differentiation. Integration by parts can be applied two times on the volume integral in Eq. (2.93) to provide a more robust formulation as follows:

$$\begin{aligned}
\int_{-\infty}^{t} \iiint_{V} \frac{\partial^2 T_{ij}}{\partial y_i \partial y_j} G \mathrm{d}^3\mathbf{y}\mathrm{d}\tau &= \int_{-\infty}^{t} \iint_{\partial V} \frac{\partial T_{ij}}{\partial y_i} G n_j \mathrm{d}^2\mathbf{y}\mathrm{d}\tau - \int_{-\infty}^{t} \iiint_{V} \frac{\partial T_{ij}}{\partial y_i} \frac{\partial G}{\partial y_j} \mathrm{d}^3\mathbf{y}\mathrm{d}\tau, \\
&= \int_{-\infty}^{t} \iint_{\partial V} \left(\frac{\partial T_{ij}}{\partial y_i} G n_j - T_{ij} \frac{\partial G}{\partial y_j} n_i \right) \mathrm{d}^2\mathbf{y}\mathrm{d}\tau \\
&+ \int_{-\infty}^{t} \iiint_{V} T_{ij} \frac{\partial^2 G}{\partial y_i \partial y_j} \mathrm{d}^3\mathbf{y}\mathrm{d}\tau.
\end{aligned} \tag{2.94}$$

Substituting Eq. (2.94) in Eq. (2.93) yield;

$$\begin{aligned}
\rho'(\mathbf{x},t) &= \int_{-\infty}^{t} \iiint_{V} T_{ij} \frac{\partial^2 G}{\partial y_i \partial y_j} \mathrm{d}^3\mathbf{y}\mathrm{d}\tau \\
&+ \int_{-\infty}^{t} \iint_{\partial V} \left(\frac{\partial T_{ij}}{\partial y_i} G n_j - T_{ij} \frac{\partial G}{\partial y_j} n_i \right) \mathrm{d}^2\mathbf{y}\mathrm{d}\tau \\
&- c_0^2 \int_{-\infty}^{t} \iint_{\partial V} \left(\rho' \frac{\partial G}{\partial y_i} - G \frac{\partial \rho'}{\partial y_i} \right) n_i \mathrm{d}^2\mathbf{y}\mathrm{d}\tau.
\end{aligned} \tag{2.95}$$

The double differentiation in the volume integral in Eq. (2.93) is now shifted to the Green's function, G for which a more robust differentiation, if not analytical, can be achieved. Assuming free-field without any boundaries, the scattering terms vanish from Eq. (2.94). Note that, to be able to impose this condition, the Green's function should satisfy the Sommerfeld boundary condition:

$$\lim_{r\to\infty} r \left(\frac{\partial G}{\partial t} + c_0 \frac{\partial G}{\partial r} \right) = 0. \tag{2.96}$$

2.3.2 Curle's aeroacoustic analogy

Lighthill's analogy does not provide any solution to treat the scattering from the boundaries. Therefore it is applicable only in free-field. Curle extended Lighthill's analogy to take into

account the interaction of the incident field with steady surfaces. The analysis starts with finding an expression to replace $\partial T_{ij}/\partial y_i$;

$$\frac{\partial T_{ij}}{\partial y_i} = \frac{\partial}{\partial y_i}\big(\rho u_i u_j + (p' - c_0^2\rho')\delta_{ij} - \sigma_{ij}\big). \tag{2.97}$$

Thanks to the symmetry of T_{ij}, change of indices do yield the same result for the expression

$$\left(\frac{\partial T_{ij}}{\partial y_i}\right) n_j = \left(\frac{\partial T_{ij}}{\partial y_j}\right) n_i. \tag{2.98}$$

Inserting the conservation of momentum equation (2.85) in the absence of external forces in Eq. (2.97) and using Eq. (2.98), the following expression is obtained:

$$\frac{\partial T_{ij}}{\partial y_i} = -\frac{\partial \rho u_i}{\partial \tau} - c_0^2 \frac{\partial \rho'}{\partial y_i}. \tag{2.99}$$

Substituting Eq. (2.91) and Eq. (2.99) in Eq. (2.95) gives the following expression:

$$\begin{aligned}\rho'(\mathbf{x},t) = &\int_{-\infty}^{t}\iiint_V T_{ij}\frac{\partial^2 G}{\partial y_i \partial y_j}\mathrm{d}^3\mathbf{y}\mathrm{d}\tau \\ &+\int_{-\infty}^{t}\iint_{\partial V}\left\{\left(-\frac{\partial \rho u_i}{\partial \tau} - c_0^2\frac{\partial \rho'}{\partial y_i}\right)G - \big(\rho u_i u_j + (p' - c_0^2\rho')\delta_{ij} - \sigma_{ij}\big)\frac{\partial G}{\partial y_j}\right\} n_i \mathrm{d}^2\mathbf{y}\mathrm{d}\tau \\ &- c_0^2\int_{-\infty}^{t}\iint_{\partial V}\left(\rho'\frac{\partial G}{\partial y_i} - G\frac{\partial \rho'}{\partial y_i}\right) n_i \mathrm{d}^2\mathbf{y}\mathrm{d}\tau.\end{aligned} \tag{2.100}$$

Note that there are terms canceling each other in Eq. (2.100). When all the cancellations are performed, the following expression is obtained:

$$\begin{aligned}\rho'(\mathbf{x},t) = &\int_{-\infty}^{t}\iiint_V T_{ij}\frac{\partial^2 G}{\partial y_i \partial y_j}\mathrm{d}^3\mathbf{y}\mathrm{d}\tau \\ &-\int_{-\infty}^{t}\iint_{\partial V}\left(\frac{\partial \rho u_i}{\partial \tau}G + \big(\rho u_i u_j + p'\delta_{ij} - \sigma_{ij}\big)\frac{\partial G}{\partial y_j}\right) n_i \mathrm{d}^2\mathbf{y}\mathrm{d}\tau.\end{aligned} \tag{2.101}$$

There exists again a term in Eq. (2.101) where velocity is differentiated. Integrating this term by parts as follows;

$$\int_{-\infty}^{t}\iint_{\partial V}\frac{\partial \rho u_i}{\partial \tau} G n_i \mathrm{d}^2\mathbf{y}\mathrm{d}\tau = \iint_{\partial V}\big[\rho u_i n_i G\big]_{-\infty}^{t}\mathrm{d}^2\mathbf{y} - \int_{-\infty}^{t}\iint_{\partial V}\rho u_i n_i \frac{\partial G}{\partial \tau}\mathrm{d}^2\mathbf{y}\mathrm{d}\tau. \tag{2.102}$$

The first integral on the right hand side of Eq. (2.102) vanishes due to the virtue of causality, and the second integral vanishes for impermeable fixed boundaries due to the no-slip condition. Eq. (2.101) then reduces to the following:

$$\rho'(\mathbf{x},t) = \int_{-\infty}^{t}\iiint_V T_{ij}\frac{\partial^2 G}{\partial y_i \partial y_j}\mathrm{d}^3\mathbf{y}\mathrm{d}\tau - \int_{-\infty}^{t}\iint_{\partial V}(p'\delta_{ij} - \sigma_{ij})\frac{\partial G}{\partial y_i} n_i \mathrm{d}^2\mathbf{y}\mathrm{d}\tau. \tag{2.103}$$

Eq. (2.103) is valid for any Green's function. Curle's analogy uses the free-field Green's function which is not discussed here since a tailored Green's function for cylindrical ducts is used instead in the this study. The discussion of implementation of a tailored Green's function in Eq. (2.103) is left to the Section 7.2.

3 Experimental study on ducted diaphragm flows

3.1 Introduction

The experimental investigation of the diaphragm flows include the determination of the configurations to be numerically investigated by means of some preliminary measurements, and providing reference flow and noise field data for the numerical analyses. All the experimental analyses were carried out using the test rig installed in the anechoic chamber of the von Karman Institute for Fluid Dynamics (VKI). Flow field measurements were conducted using hot-wire anemometry. The aeroacoustic measurements included various campaigns to measure the noise field inside and outside the duct, and to identify the active flow noise and the scattering characteristic of the diaphragms. This chapter is devoted *i*) to provide detailed information about the anechoic chamber and the test rig together with the instrumentation used, and *ii*) to discuss the preliminary investigations conducted to determine the details of the test cases investigated in the study.

3.2 Experimental setup

3.2.1 Anechoic chamber

The anechoic chamber installed in VKI was designed for studying and certifying low speed cooling and ventilation fans (ducted or unducted) [11]. It is split into two rooms by a wall partition in which flow elements of various types, such as fans, ducts etc. can be perpendicularly fitted. A schematic depicting the anechoic room is presented in Figure 3.1. The rooms are constructed in the shape of a trapezoid to reduce the number of pressure nodes inside the room. An external blower is connected to the Room II through acoustic mufflers, which damp out the noise emitted by the blower itself (see Figure 3.2-a). The blower permits controlling the pressure difference, and thereby the mass flow rate along the flow element. It operates in suction mode and induces, from the inlet plenum, a flow, which is discharged to Room II through the flow element. This mode of operation ensures a minimized level of incoming turbulence for the flow element. The instrumentation used for aeroacoustic measurements are installed in Room I. It is also possible to make wake measurements in Room II. The instrumentation in the anechoic chamber is controlled via a Data Acquisition (DAQ) system placed outside the chamber. An opening on the ground of the anechoic chamber served as a passage for the harness coming from the DAQ system. The rotational speed of the blower is controlled from an electronic

control unit shown in Figure 3.2-b, located next to the DAQ system.

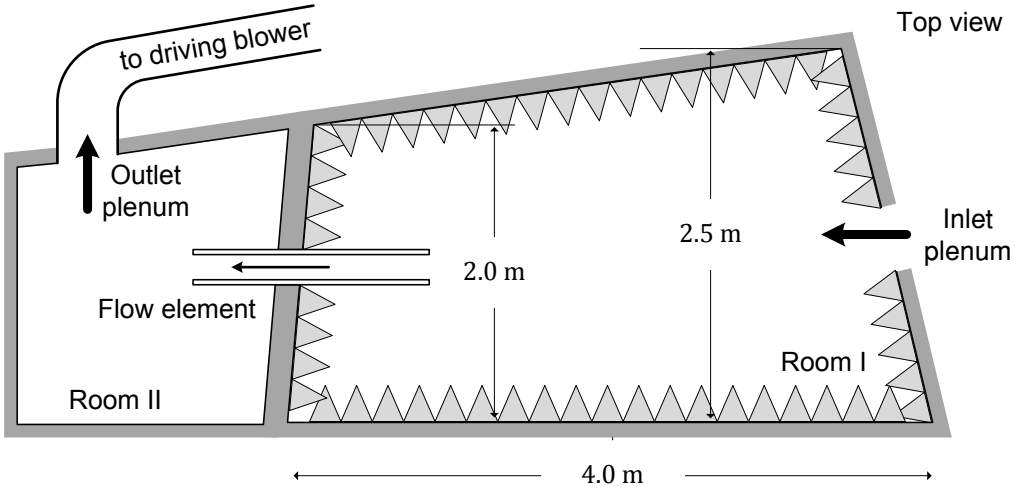

Figure 3.1: Schematic representation of the anechoic chamber installed in VKI.

Figure 3.2: (a) Acoustic mufflers connecting the blower to the anechoic chamber. (b) Electronic control unit of the blower.

3.2.2 Test rig

The test rig used in the thesis study was designed and manufactured within the scope of the IDEALVENT project, to investigate ducted fan noise. It consists of a modular duct system traversing the wall partition as shown in Figure 3.3. The duct system contains fans, non-air-moving devices, i.e. diaphragms, and various instrumented sections hosting static pressure probes, radial and azimuthal hot-wire traversing mechanisms, microphone multi-ports and loudspeaker arrays. A bell-mouth is installed at the inlet of the duct to provide clean inflow. At the outlet, which is behind the wall-partition, an anechoic termination is used to reduce the contamination of the noise field inside the duct due to the duct-end reflections. The modules in between were designed to be interchangeable, bringing a flexibility to investigate different configurations. They

are made of Plexiglass to have visual access for Particle Image Velocimetry (PIV) measurements. The duct inner diameter, D equals 0.15 m. To generate flow noise, diaphragm sections are attached to the duct, obstructing the duct flow. The diaphragm sections are constituted of single/tandem diaphragm(s) with a wall thickness of 0.008 m, and a circular opening at the center offering a blockage ratio equal to 0.68.

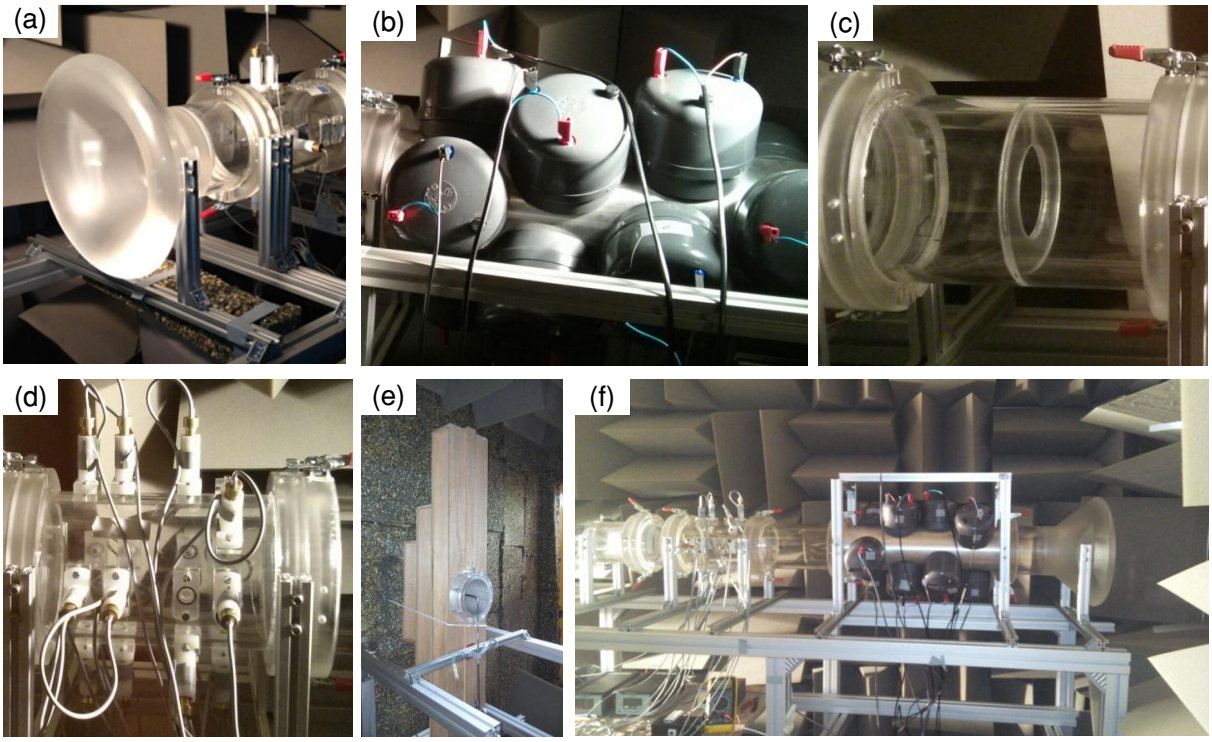

Figure 3.3: Test rig installed in the anechoic chamber. (a) Bell-mouth. (b) Loudspeaker array. (c) Diaphragm module. (d) Microphone array. (e) Anechoic termination. (f) Duct assembly.

3.2.2.1 Instrumentation

The flow and noise field measurements involved the use of hotwire anemometry, microphone and loudspeaker arrays, and calibration of these devices. The technical details of the instrumentation used in the experimental analyses and the calibration procedures followed are explained below:

Hotwire Anemometry: Velocity measurements were conducted using a constant temperature single-wire anemometry made of 9 μm tungsten wire. The 9 μm wire allowed to capture eddy frequencies up to 10 kHz. The hotwire anemometry was calibrated using a converging calibration nozzle, and a water manometer, as shown in Figure 3.4. The calibration was achieved by placing the hotwire within the potential core of the nozzle. The velocity at the potential core is calculated through Bernoulli principle, by measuring the pressure drop between the core and the nozzle stagnation chamber, using a water manometer. The hotwire anemometry was supported by a traversing mechanism depicted in Figure 3.4, which can be attached to the

modules of the duct. The traversing mechanism was automated by two electric servo motors, moving the hotwire anemometry in radial and azimuthal directions to span the cross-section at which it is located.

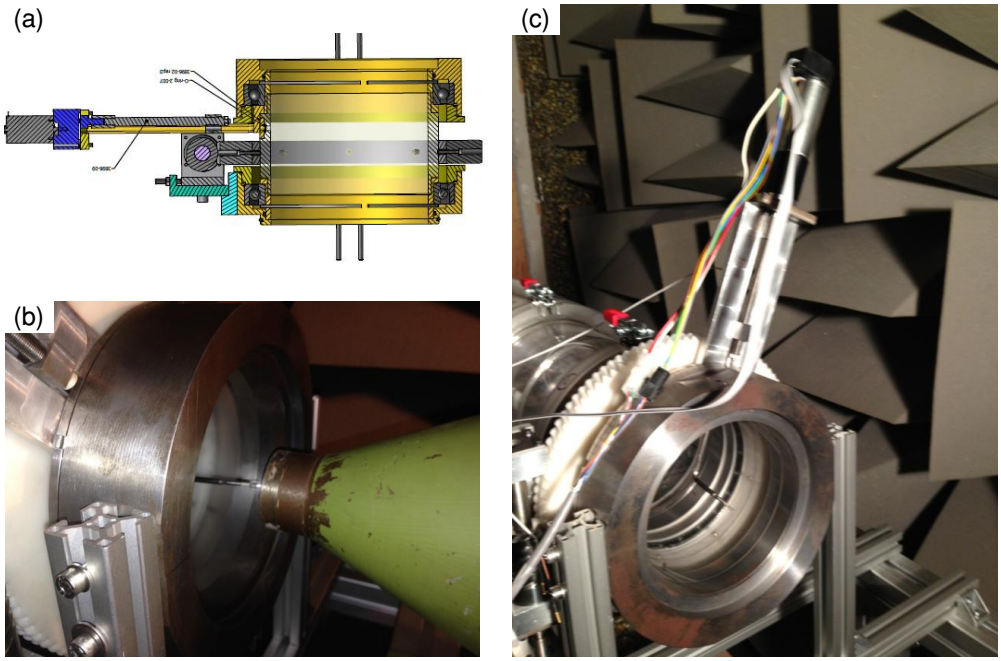

Figure 3.4: (a) Technical drawing of the hotwire traversing mechanism. (a) Use of the calibration nozzle. (b) Hotwire traversing mechanism attached to the duct.

Loudspeakers: External acoustic excitation of the duct was achieved by using 4-inch Morel type EM428 loudspeakers (see Figure 3.5-a). Type E428 loudspeakers give 150W nominal output with a nearly constant sensitivity between 200 Hz and 5 kHz. Three 8-channel multiplexers shown in Figure 3.5-b were used to simultaneously control the loudspeaker arrays, and to amplify the input signal.

Microphones: To measure the acoustic field inside the duct, 1/4-inch Bruel & Kjaer (B&K) type 4938 microphones were used with B&K type 2670 preamplifiers (see Figure 3.6). Type 4938 microphones have a dynamic range of 30-172 decibels (dB), and a frequency range of 4 Hz-70 kHz. The change of the pressure-field response of the microphone remains within ± 2 dB for this frequency range. The microphones were individually calibrated at 94 dB - 1 kHz using a B&K type 4231 sound calibrator.

Conditioning amplifier: To increase the quality of the acoustic measurements, the microphones are used together with conditioning amplifiers, which supply powering to the transducer, provide electrical isolation, and filter and amplify the signal measured by the transducer. In our test rig, B&K Nexus type 2690 conditioning amplifiers shown in Figure 3.7 were used. Type 2690 amplifier supports 4-channel amplification and provides a gain of -20 to $+80$ dB with a gain linearity within ± 0.02 dB. It has built-in analog filters at 0.1, 1, 10, and 20 Hz for

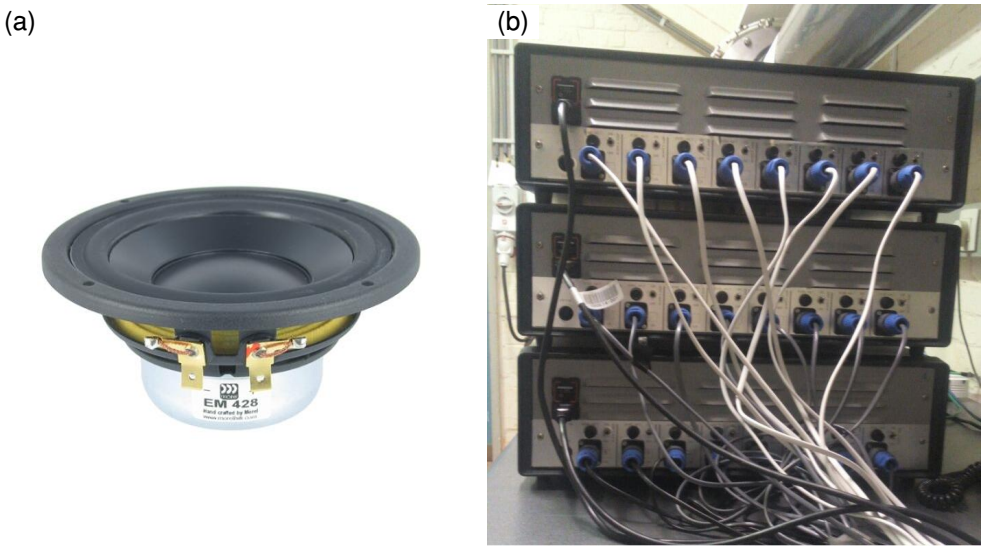

Figure 3.5: (a) Loudspeaker. (b) Multiplexers connected in parallel.

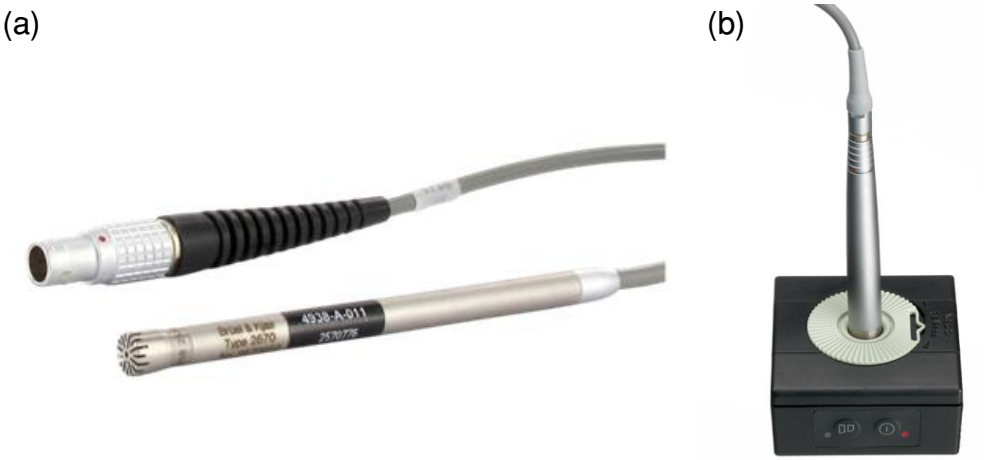

Figure 3.6: (a) Microphone attached to preamplifier. (b) Sound calibrator.

high-pass, and at 100 Hz, 1, 3, 10, 22.4, 30, and 100 kHz for low-pass with a decay value of 40 dB/decade. A low-pass filter at 22.4 kHz was selected for all the aeroacoustic measurements. The gains were re-adjusted for each test configuration to maximize the measurement sensitivity.

DAQ system: The control of the loudspeakers and the acquisition of the measurement data were managed using a DAQ system. The DAQ system consists of a NI PXI 1045 chassis, carrying a NI PXI 8105 embedded controller, and 8 NI PXI 6143 multifunction I/O modules used with NI TB 2706 termination blocks. Each I/O module has 8 analog input channels (16 bit resolution and 250 kS/s sampling rate), 8 digital I/O channels, a digital trigger, and an internal clock operating at 10 MHz. The overall configuration of the data acquisition setup used for the acoustic measurements is depicted in Figure 3.8.

Figure 3.7: Conditioning amplifier.

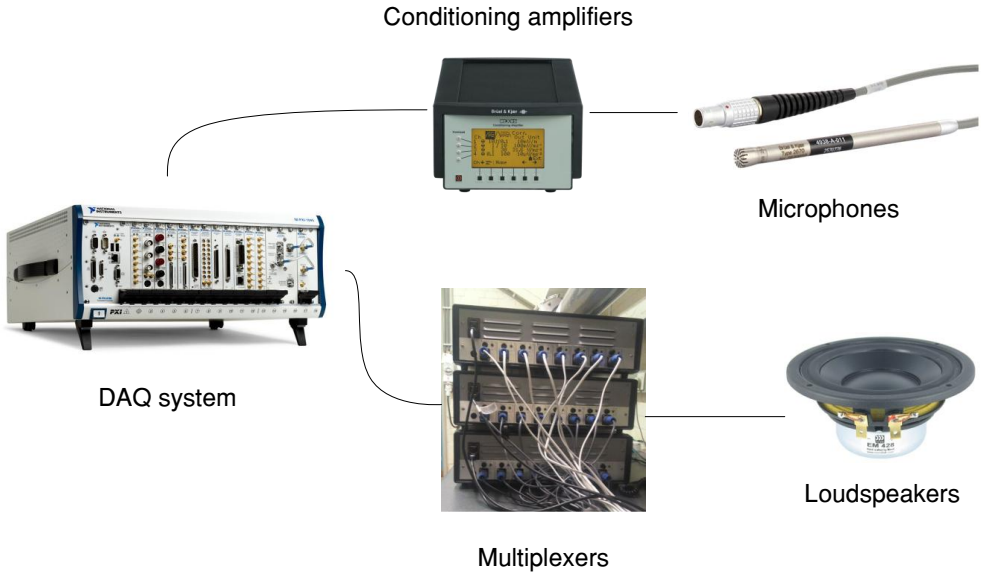

Figure 3.8: The setup used for data acquisition.

3.3 Preliminary investigations about the test cases

3.3.1 Inflow velocity

The noise generated by diaphragm flows is proportional to some power of the inflow velocity. For a clear distinction of the acoustic installation effects of diaphragms from the background noise of the empty duct, the inflow velocity should be above a certain value. However, computational costs of the numerical analysis, which is based on LES also increases with the inflow velocity, meaning that there should be a trade-off between the level of noise generated by diaphragm(s) and the computational costs. Outside-duct measurements were carried out to determine the minimum inflow velocity inducing distinguishable noise generation by the diaphragm(s). Two free-field microphones both facing towards the center of the bell-mouth

were located at the positions depicted in Figure 3.9. The microphones are used in pair with

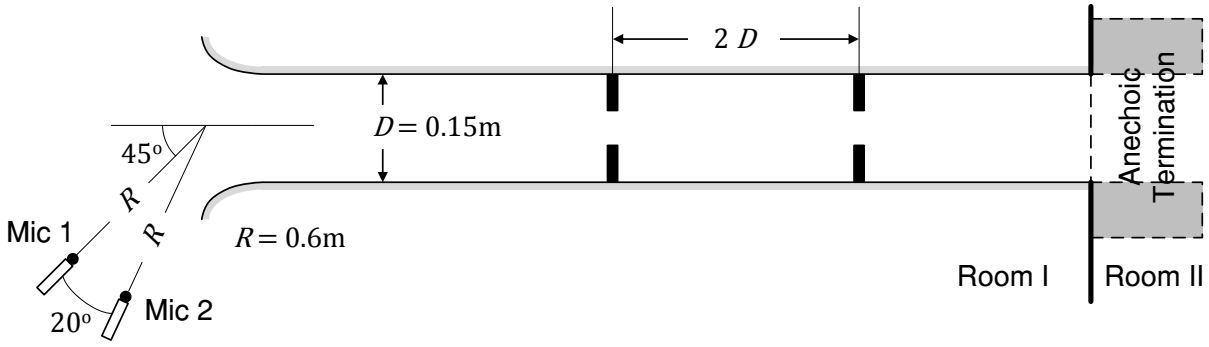

Figure 3.9: Schematic representation of the experimental setup for the outside-duct measurements.

an azimuthal separation of 20 degrees to avoid directivity issues. The microphone readings were sampled at 25,600 Hz for the outside-duct measurements, and for the rest of the thesis study as well. The frequency analysis of the measured noise field was performed using the Fast Fourier Transform (FFT) normalized with respect to the number of FFT points equal to 2^{15}, and presented in Sound Pressure Levels (SPL) calculated as SPL [dB] = $20\log_{10}(P/P_{ref})$ where $P_{ref} = 2 \times 10^{-5}$ Pa. The SPLs corresponding to the empty duct, single and tandem diaphragm cases are presented in Figure 3.10 for an inflow bulk velocity of 6 m/s. The spectra measured in both single and tandem diaphragm configurations were observed to be sufficiently higher than the background noise, with a minimum difference of 15 dB at 5 kHz in the single diaphragm case.

3.3.2 Separation distance of the tandem diaphragms

The experimental part of the thesis study focuses on characterization of broadband noise generated by ducted singularities. When installed closer than a critical value for a given flow condition, tandem diaphragms are known to generate a non-linear acoustic interaction, namely whistling [94], which is outside the scope of this study. Therefore, avoiding any whistling was of primary concern in deciding the distance between the tandem diaphragms. Positioning the diaphragms well apart from each other, on the other hand, increases the computational cost of LES, which was also undesirable. The rig design allowed to set the distance between the diaphragms as multiples of $1D$. It was observed that a $1D$ separation between the two diaphragms triggered whistling for a similar flow case. Therefore, the separation distance of the tandem diaphragms were set as $2D$, and the resulting noise field was measured using a wall-flush microphone positioned at the upstream far-field. Figure 3.11 presents the result of the measurement, where no tonal peaks as a sign of whistling are observed for the frequency range of interest.

3.3.3 Positioning of the modules along the duct axis

In determining the overall configuration of the duct, three criteria were observed: *i*) not locating any listeners in the source region downstream of the diaphragm(s), *ii*) having a sufficiently

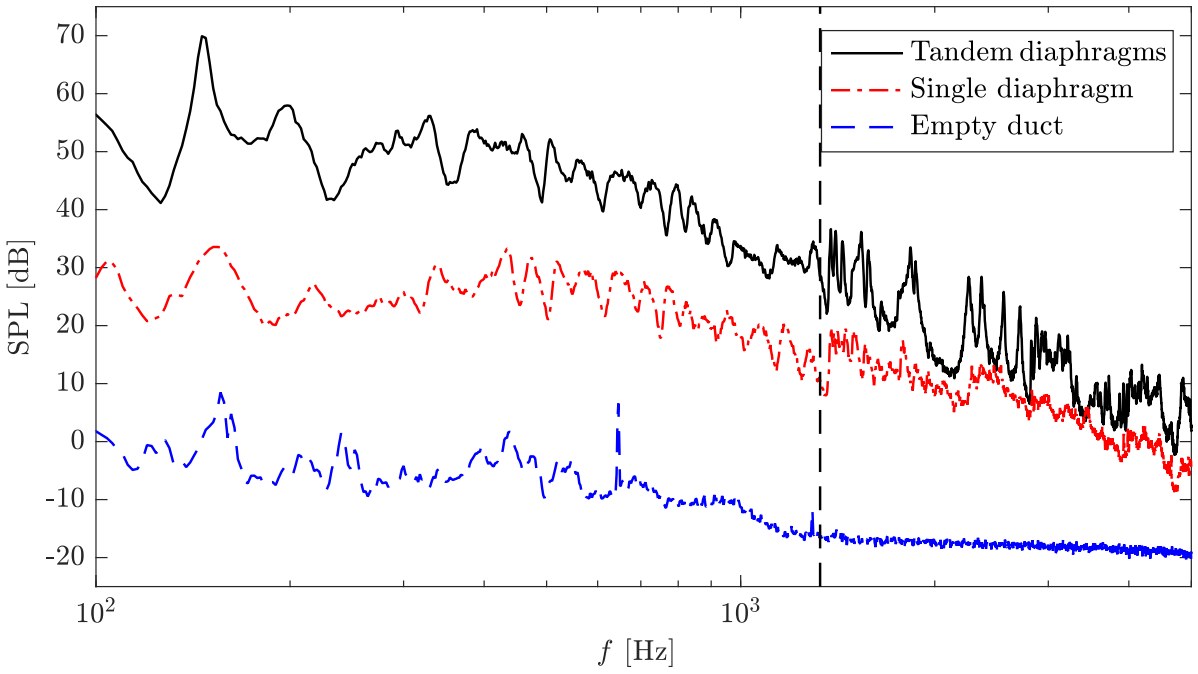

Figure 3.10: Noise spectra obtained for the empty duct, the single diaphragm, and the tandem diaphragm configurations for an inflow bulk velocity of 6 m/s. The vertical dashed line indicates the first cut-on.

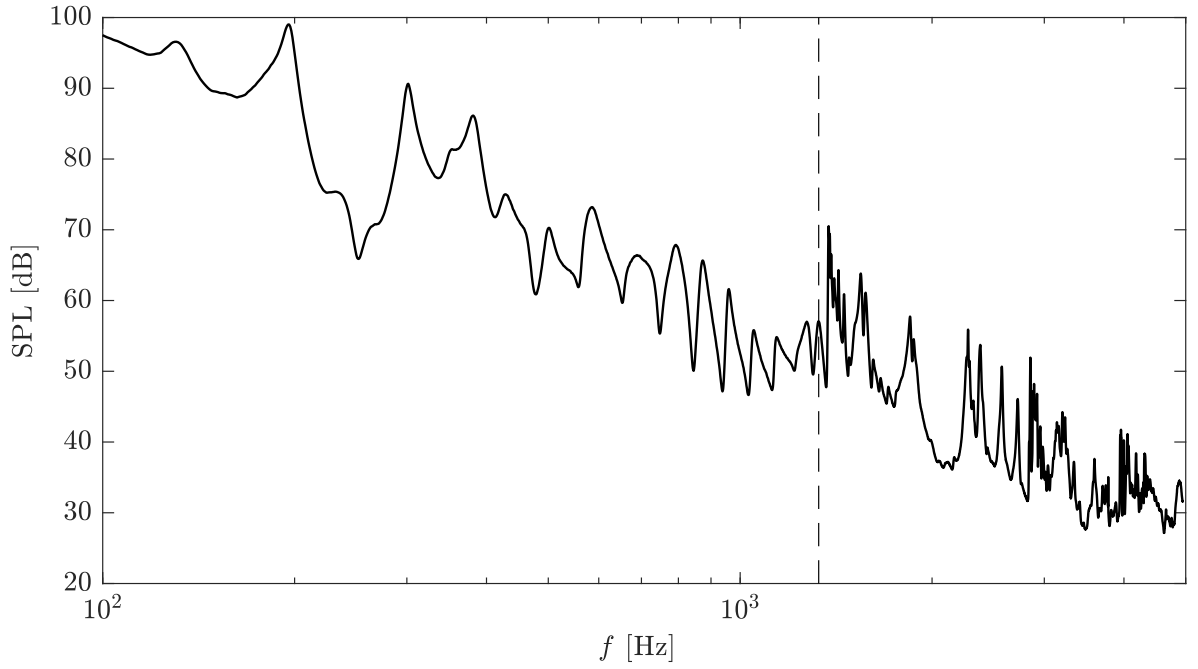

Figure 3.11: In-duct noise spectrum for the tandem diaphragm case measured at upstream far-field. The vertical dashed line indicates the first cut-on.

long inlet section to obtain a fully developed boundary layer before the flow reaches the di-

aphragm(s), and *iii*) leaving adequate distance between the microphone and loudspeaker arrays to eliminate the effect of the evanescent modes emitted from the loudspeakers. These criteria simply imply better measurements with longer duct. However, the duct must fit in the anechoic chamber with sufficient clearance before the inflow plenum to ensure axisymmetric inflow conditions. Regarding the dimensions of Room I, the part of the duct contained in this room was extended to be $21D$ long leaving a $5D$ gap between the bell-mouth and the inflow plenum. The rest of the duct configurations were determined investigating the influence of the aforementioned three criteria as discussed below.

While applying the modal decomposition method, only the cut-on modes were taken into account. Therefore, the contribution of the higher order modes to the acoustic pressure was to be avoided. Besides, the zone of listeners should be free of sources, even if the sources emit only the cut-on modes, not to modify the acoustic waves as they pass through the listener zones. These two conditions imply keeping sufficient distance between the microphones and the sources of sound, i.e. the loudspeakers and the turbulence itself.

The two-port method expects the microphone arrays to be in between the source region and the loudspeaker array, for both upstream and downstream sections. According to Lighthill's analogy, noise sources are scaled with the level of turbulence. As a corollary, dominant sources are distributed close to the downstream side of the diaphragm. This brings the necessity for a longer downstream section, leaving sufficient gap between the source region and the downstream microphone array. To obtain the longest downstream section, the minimum length of inlet section yielding converged downstream flow conditions was to be known. The decay-out distance of the evanescent modes up to the 2^{nd} azimuthal mode was also needed to minimize the distance of the microphones from the loudspeakers, and eventually to maximize the distance from the source region.

A parametric study based on axisymmetric RANS simulations was conducted to determine the shortest inlet section where the inflow had a fully developed boundary layer before reaching the diaphragm, and therefore yielded converged downstream conditions. The RANS simulations were computed for various single diaphragm cases with different diaphragm positions: $4D$, $5D$ and $6D$ apart from the duct starting position. To have more realistic inflow conditions for the duct, the bell-mouth and a simplified version of the inflow plenum were also modeled as shown in Figure 3.12. The solutions are obtained using the baseline $k-\omega$ model of ANSYS Fluent 15.0

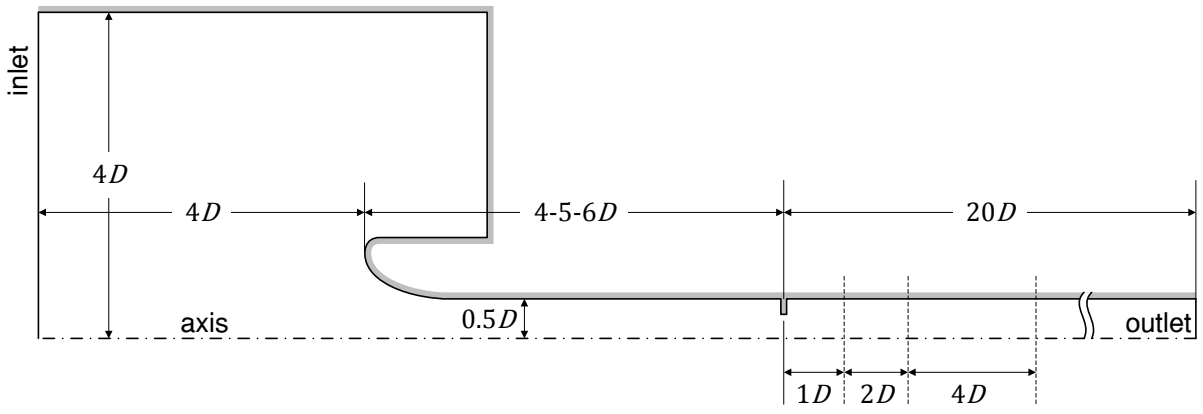

Figure 3.12: Model geometry for the RANS simulation.

[CITE]. Constant inlet velocity of 0.093 m/s with 5% turbulence intensity was imposed on the opening to ensure a bulk velocity of 6 m/s inside the duct. Pressure outlet boundary condition was imposed on the duct-end cross-section with zero gauge pressure. The effect of the length of the inlet section on the downstream flow field was investigated by comparing the velocity magnitude and the turbulent kinetic energy on the downstream cross-sections denoted by vertical dashed lines in Figure 3.12. The resulting downstream flow field of $4D$, $5D$, and $6D$ long inlet configurations are presented in Figure 3.13. No significant difference in the downstream flow

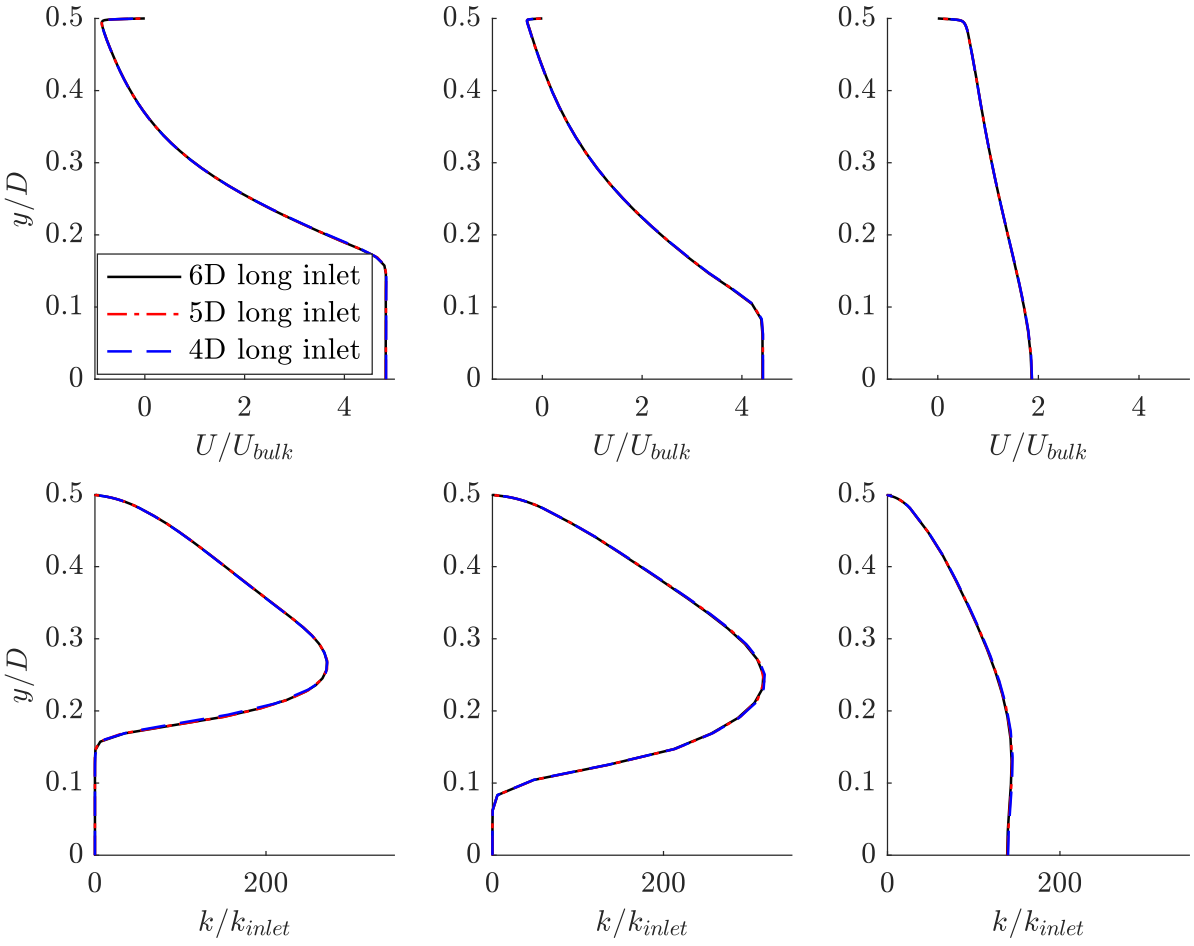

Figure 3.13: Mean velocity field (top) and turbulent kinetic energy (bottom) distribution for different inlet configurations on cross-sections 1D (left), 2D (middle), and 4D (right) downstream of the diaphragm.

field was observed between the three configurations as seen in Figure 3.13.

The bell-mouth and the modules hosting the microphone and loudspeaker arrays already sum up to a duct portion of $6D$ length, for which converged downstream flow conditions are verified by the above CFD analysis. The minimum length of the duct was then determined based on the distance left between the loudspeaker and microphone arrays. To observe the decaying behavior of the evanescent modes, a configuration with a test source and two listener arrays were devised as shown in Figure 3.14. The sound field emitted from a loudspeaker was considered to be of monopolar form. Therefore a monopole was used as the test source. The number and the

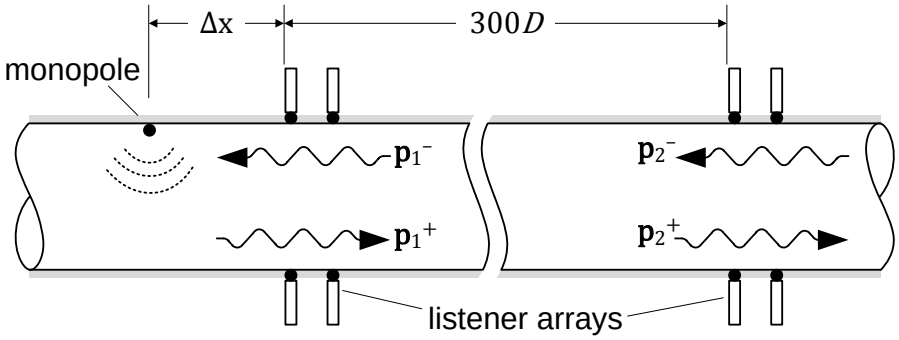

Figure 3.14: Configuration used for testing the effect of the evanescent modes in the near-field.

relative positions of listeners within the listener arrays were determined to be the same with those of the microphone arrays installed in the test rig. The source was positioned near one of the microphone arrays. The other microphone array was positioned well apart ensuring the far-field conditions. The modal decomposition of the acoustic field generated by the test source was conducted at each of the listener sections to obtain $\mathbf{p}_1^{\pm}$ and $\mathbf{p}_2^{\pm}$. The acoustic field at a reference position was then calculated twice by reconstructing the acoustic modes, $\mathbf{p}_1^{\pm}$ and $\mathbf{p}_2^{\pm}$ respectively. The entire process was repeated for different Δx values. The duct configuration allows the distance between the closest loudspeaker-microphone pair to be $0.73D$ or more with a step increase of $1D$. The acoustic field, which is obtained by reconstructing the acoustic modes predicted in the far-field is given at the top of Figure 3.15. At the bottom of the figure, the difference in the resulting acoustic field, which occurs when the acoustic modes are predicted using the near-field listener array is presented for different source positions. It is observed in Figure 3.15 that the effect of the evanescent modes on modal decomposition is more apparent close to the cut-on frequencies. The evanescent modes decay more slowly at frequencies close to cut-on, causing such a behavior. Better prediction of the acoustic modes were obtained as the separation between the source and the listener increased up to $2.73D$, while no significant improvement was observed for longer separation distances.

3.3.4 Microphone arrays

The upper limit for the acoustic modes to be investigated in the thesis is the 2$^{\text{nd}}$ azimuthal mode, which corresponds to 5 cut-on modes ranging from $(m,\mu) = (-2,0)$ to $(m,\mu) = (2,0)$ implying 10 unknowns in total. To isolate these modes, the number of listener points, N_L at a given duct section should satisfy $N_L \geq 10$, as discussed in Section 2.2.3. To increase the robustness of the measurements by having an overdetermined system, the microphone arrays are constructed of 12 microphones, for both the upstream and the downstream sections. The relative positions of the microphones with respect to the (upstream) diaphragm are listed in Table 3.1. The minimum distance of 0.04 m between the axial stations of each of the microphone arrays allows a modal decomposition up to 4,250 Hz, which is calculated by a version of Nyquist theorem based on the sampling distance of wavenumber. The upper limit of modal decomposition in the thesis is

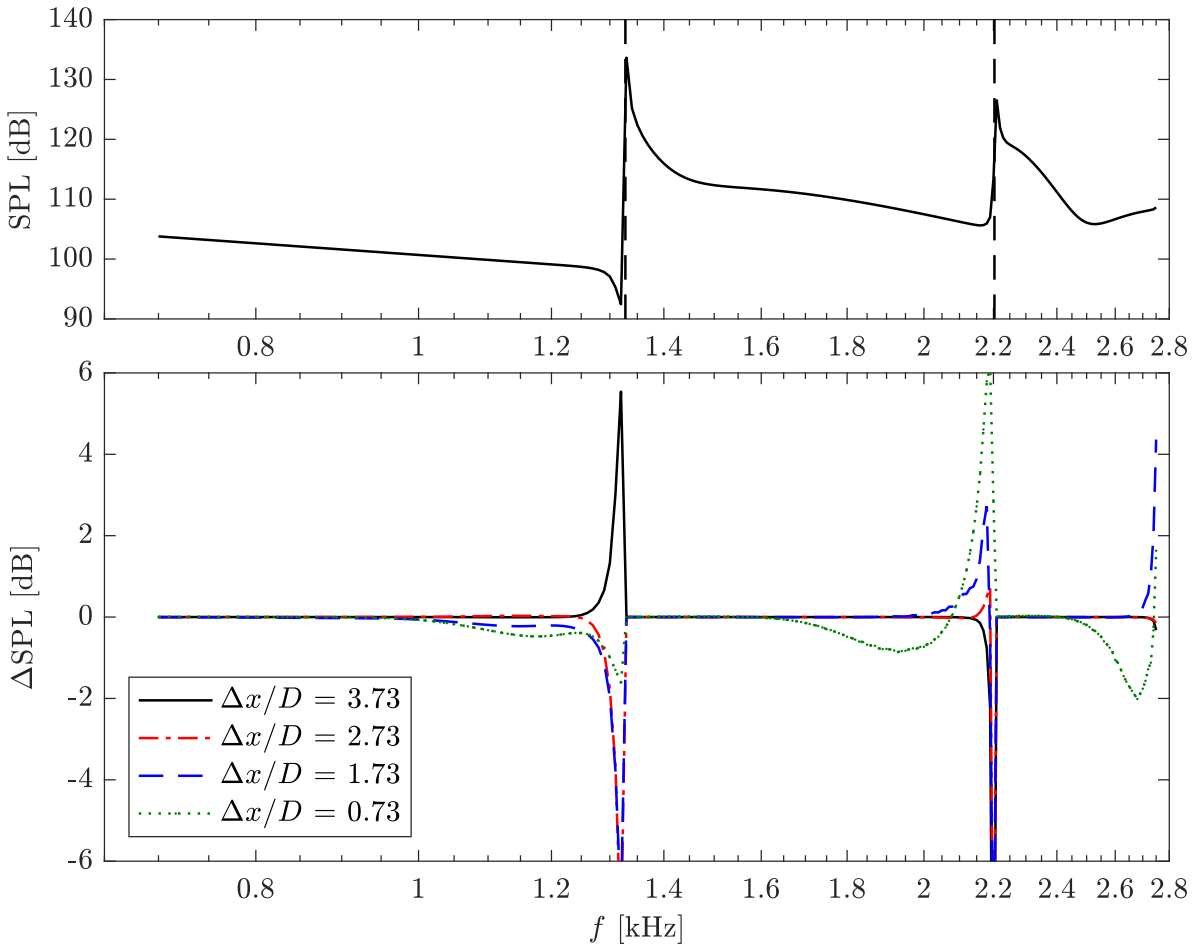

Figure 3.15: (Top) SPL of the acoustic field obtained reconstructing the modes computed in the far-field. Vertical dashed lines indicate the first and the second cut-on frequencies. (Bottom) Difference in the resulting SPL, observed when the near-field data is used to predict to acoustic modes. The curves shown in the plot correspond to different source positions.

the cut-on frequency, f_c subsequent to the 2nd azimuthal mode, which is found as follows:

$$f_c = \frac{\alpha_{m\mu} c_0}{2\pi a}. \tag{3.1}$$

Using Eq. 3.1, the upper frequency limit is calculated to be 2,764 Hz, which is lower than the Nyquist limit mentioned above.

It was discussed in Section 2.2.3 that the transfer matrix between the left- and right-going waves, $\mathbb{J}$ has to be invertible, i.e. non-singular. The $\mathbb{J}$ matrix is dependent only on the listener positions. Therefore, its level of singularity can be checked at the design stage. As an inverse measure of singularity, the conditioning number of $\mathbb{J}$ is computed through the following equation:

$$\kappa(\mathbb{J}) = \|\mathbb{J}\| \|\mathbb{J}^{-1}\| \tag{3.2}$$

Note that Eq. 3.2 cannot be applied to overdetermined systems since the resulting matrix is not square, and thus not invertible. The inverse of an overdetermined matrix can be estimated by

Table 3.1: Positions of the microphones. The axial coordinate is relative with respect to the (upstream) diaphragm.

Upstream section		Downstream section	
Microphone No.	(Δx [m], ϑ [deg])	Microphone No.	(Δx [m], ϑ [deg])
Mic 1	(-0.52, 0)	Mic 13	(1.00, 90)
Mic 2	(-0.52, 135)	Mic 14	(1.00, 180)
Mic 3	(-0.52, -90)	Mic 15	(1.00, -45)
Mic 4	(-0.48, 45)	Mic 16	(1.04, 45)
Mic 5	(-0.48, 90)	Mic 17	(1.04, 90)
Mic 6	(-0.48, 180)	Mic 18	(1.04, 180)
Mic 7	(-0.41, 0)	Mic 19	(1.11, -90)
Mic 8	(-0.41, 90)	Mic 20	(1.11, 0)
Mic 9	(-0.41, -90)	Mic 21	(1.11, -90)
Mic 10	(-0.37, 0)	Mic 22	(1.15, 0)
Mic 11	(-0.37, 90)	Mic 23	(1.15, 180)
Mic 12	(-0.37, 180)	Mic 24	(1.15, -90)

computing the Moore-Penrose inverse (pseudo-inverse) as follows:

$$\mathbb{J}^{\dagger} = (\mathbb{J}^{\top}\mathbb{J})^{-1}\mathbb{J}^{\top}. \tag{3.3}$$

Eq. 3.2 can then be reformulated as

$$\kappa(\mathbb{J}) = \|\mathbb{J}\|\,\|\mathbb{J}^{\dagger}\| \tag{3.4}$$

to compute the conditioning number of an overdetermined system. The κ data computed for the given microphone arrays is plotted in Figure 3.16. It is observed that the microphone arrays used in both sections yield a non-singular linear system for the given modal range.

3.3.5 Phase calibration of the microphones

When recording an acoustic signal by a microphone, depending on the impedance of the microphone and the cabling used in data acquisition, a constant phase is added to the recorded signal. The modal decomposition technique is based on detecting the phase change of the acoustic field at different measurement positions. To properly capture this phase data, the unknown phase contribution of each of the microphones has to eliminated. For this purpose, the phase calibration of the microphones was done using a calibration tube. The calibration tube shown in Figure 3.17 consists of a cylindrical tube with an inner diameter of 0.042 m, attached at one end to a MONACOR type KU-516 loudspeaker with a frequency range of 160 Hz-6.5 kHz. On the other end

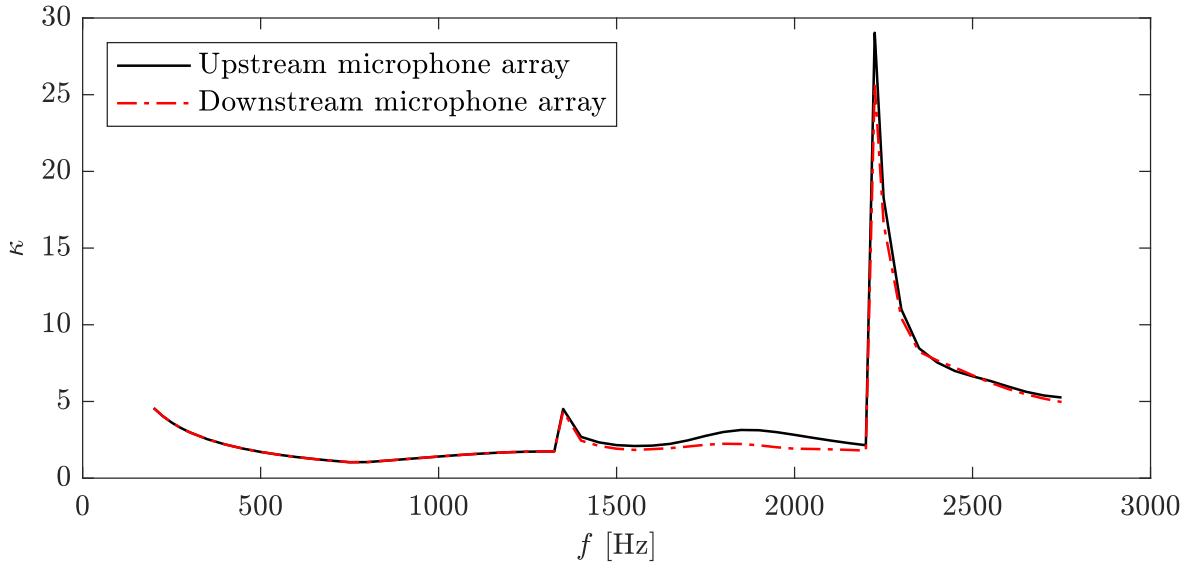

Figure 3.16: The conditioning numbers for the upstream and downstream microphone arrays.

of the tube, 8 axially aligned openings exist to mount the microphones. When excited by the loudspeaker at a given frequency lower than the first cut-off, which is at 4,750 Hz, the phase of the resulting acoustic field depends only on the axial position along the tube. Therefore, the microphones, sharing the same axial position, are exposed to the same phase. The phase calibration can then be achieved by computing the phase differences in the signals measured by different microphones.

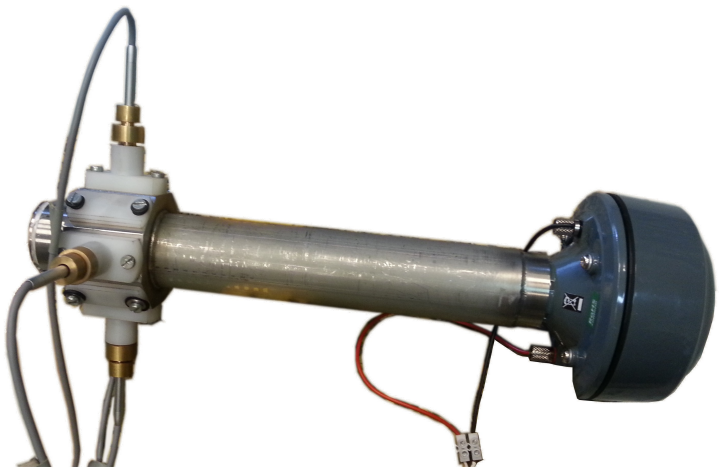

Figure 3.17: Calibration tube with microphones installed.

Since the calibration tube has a fixed length, the acoustic field inside the tube contains various pressure nodes. The positions of these nodes change with frequency, and may thereby match the position of microphone openings, degrading the microphone measurements. To investigate the existence of such a degradation, the coherence between microphone measurements is calculated

through the following expression:

$$C_{xy}(f) = \frac{\|G_{xy}(f)\|^2}{G_{xx}(f)G_{yy}(f)}, \tag{3.5}$$

where G_{xy} is the cross-spectral density between the signals x and y, and G_{xx} and G_{yy} are the auto-spectral density of x and y, respectively. The expected value of C_{xy} is 1 if x and y are causal, and is 0 if there exist no causality in between. In Figure 3.18, the phase difference between a reference microphone and 7 other microphones are plotted together with the corresponding coherence data. The coherence value is observed to be less than 1 for the frequency

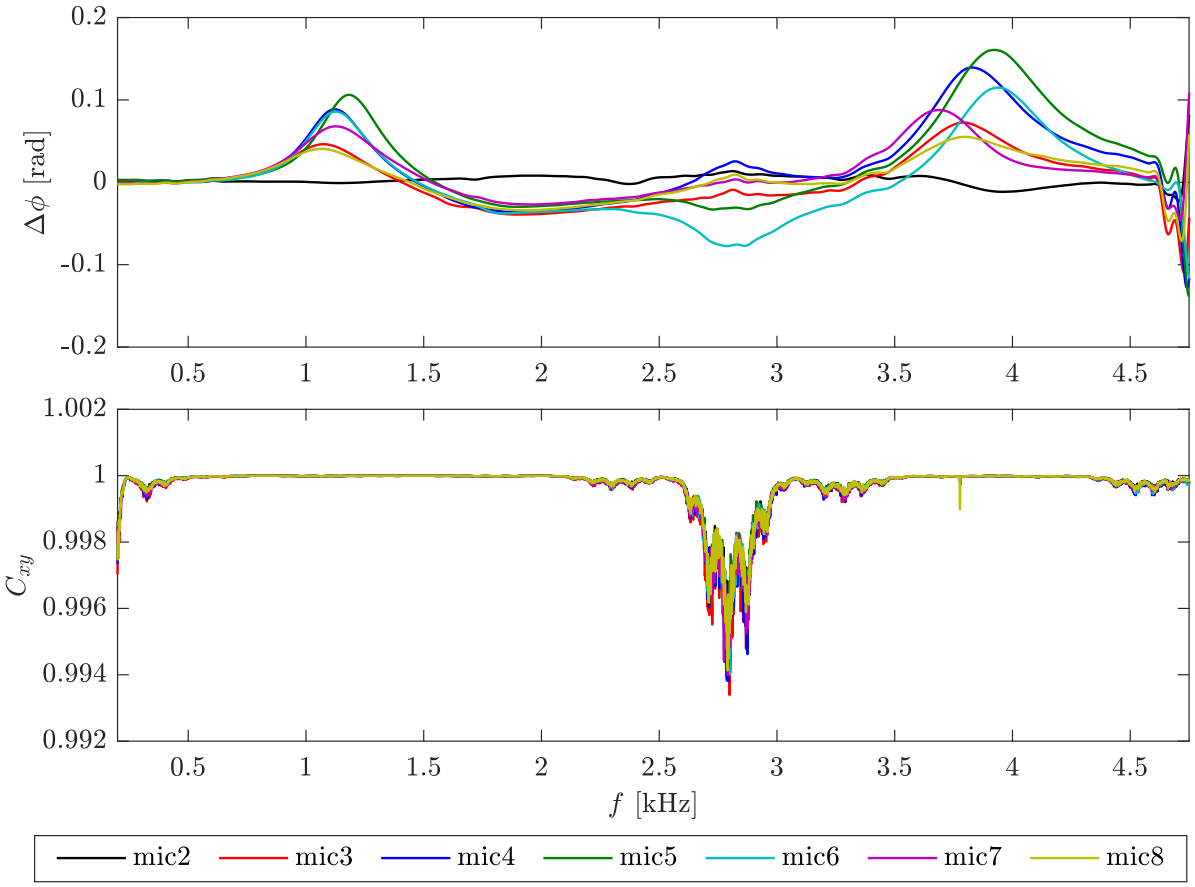

Figure 3.18: Phase difference (top) and coherence (bottom) data between a reference microphone (mic 1) and 7 other microphones (mic 2-8).

range 2-3.5 kHz, indicating certain level of non-causality in the measurements due to a possible pressure node around the microphones. A deviation in the phase difference is also observed in the same range of frequency. As a remedy, the phase difference data for the frequency range 2-3.5 kHz was regenerated using a spline function which takes the remaining part as input. The regenerated phase difference used in calibration of the microphones is plotted in Figure 3.19.

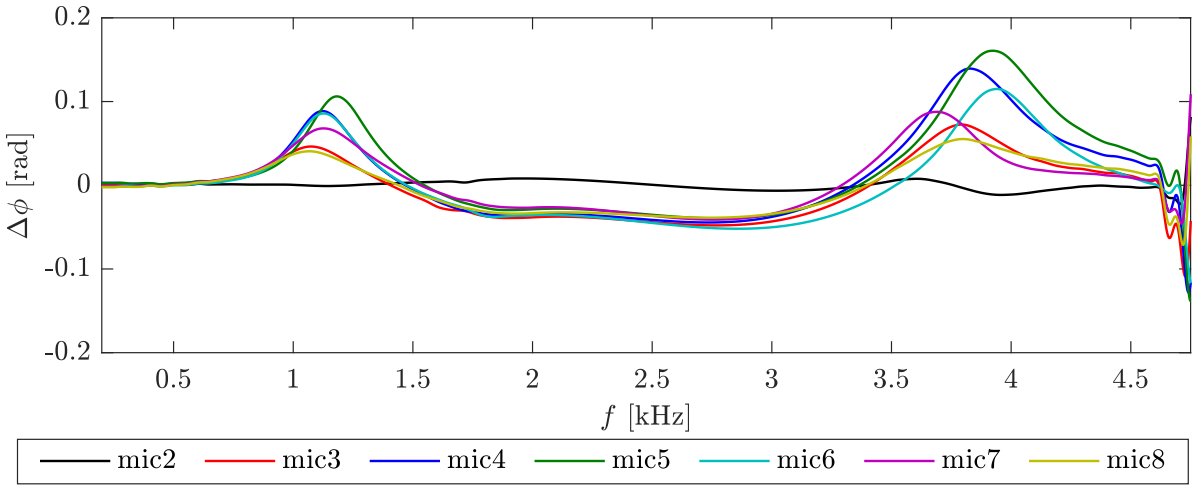

Figure 3.19: Phase calibration updated using a spline function between 2 kHz and 3.5 kHz.

3.3.6 Loudspeaker arrays

The exact positions of the loudspeakers are not needed for the experimental analyses. However, as in the case of the microphone arrays, the set of load cases obtained by the excitation of each of the loudspeakers should be linearly independent, i.e. non-singular. Therefore, a similar conditioning number analysis is performed for the loudspeaker arrays and the result is plotted in Figure 3.20. The trend observed in Figure 3.20 is similar to the one seen in Figure 3.16, although

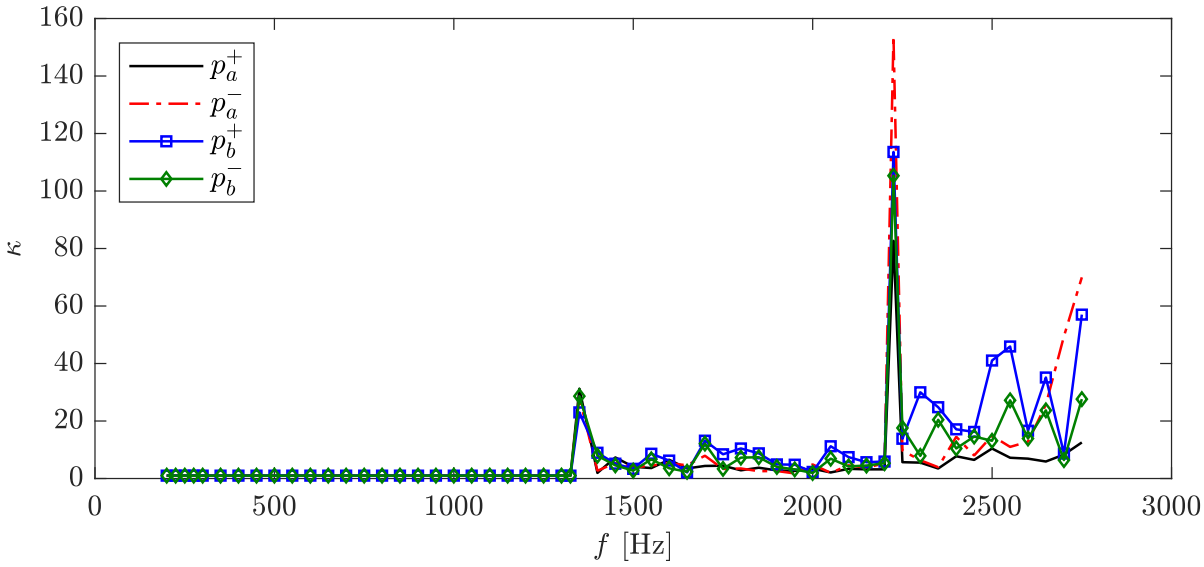

Figure 3.20: The conditioning numbers for the load cases obtained by excitation of the upstream and the downstream loudspeaker arrays.

being less smooth. And the κ values are around 5 times higher compared to the conditioning number of the microphone arrays, for the frequency range beyond the first cut-off. This implies a higher level of singularity in the source excitations.

3.3.7 Configuration of the duct for single and tandem diaphragm cases

A schematic is presented in Figure 3.21 depicting the finalized configurations for the single and the tandem diaphragm cases: an inlet bell-mouth providing a clean inflow is followed by the loudspeaker module containing an array of 12 loudspeakers. Leaving a $2.73D$ distance with the loudspeaker module, the upstream microphone section is installed comprising 12 wall-flush microphones at 4 consecutive sections. At a distance of $2D$ downstream of the last microphone is the diaphragm section. A second set of 12-microphone and 12-loudspeaker modules are located $6D$ downstream of the diaphragm(s) section, again leaving a $2.73D$ distance in between. The distance between the microphone array and the closest diaphragm reduces to $4D$ in the tandem diaphragms case. The dominant sources in this case are contained between the two diaphragms, leaving thereby sufficient distance between the loudspeaker array. A detailed analysis to determine the effective source regions is provided in Section 7.3.2. Traversing the wall-partition, the duct is terminated with an anechoic module to reduce the contamination in the in-duct noise field due to the duct termination reflections.

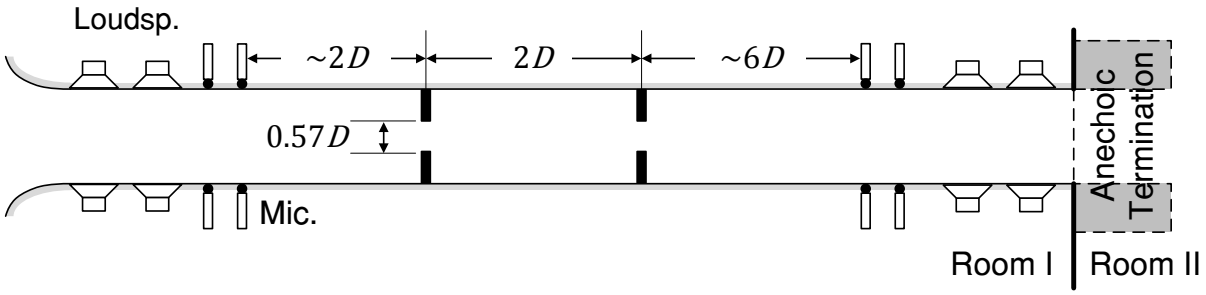

Figure 3.21: Schematic of the experimental rig for the tandem diaphragm configurations. The single diaphragm configuration is obtained by removing the downstream diaphragm.

3.4 Flow field measurements using hotwire anemometry

The hotwire measurements were conducted to provide reference mean flow field to compare with the numerical simulations. The hotwire traversing mechanism was attached to the duct at various cross-sections shown in Figure 3.22.

Each cross-section was spanned from the center to the surface at two azimuthal positions perpendicular to each other. The hotwire measurements were taken for 10 seconds at each radial position. The hotwire orientation yielded a measurement direction equal to the sum of the axial and radial velocity components. The flow data was obtained by averaging the measurements taken at different azimuthal positions. The resulting mean velocity field is presented in Figure 3.23.

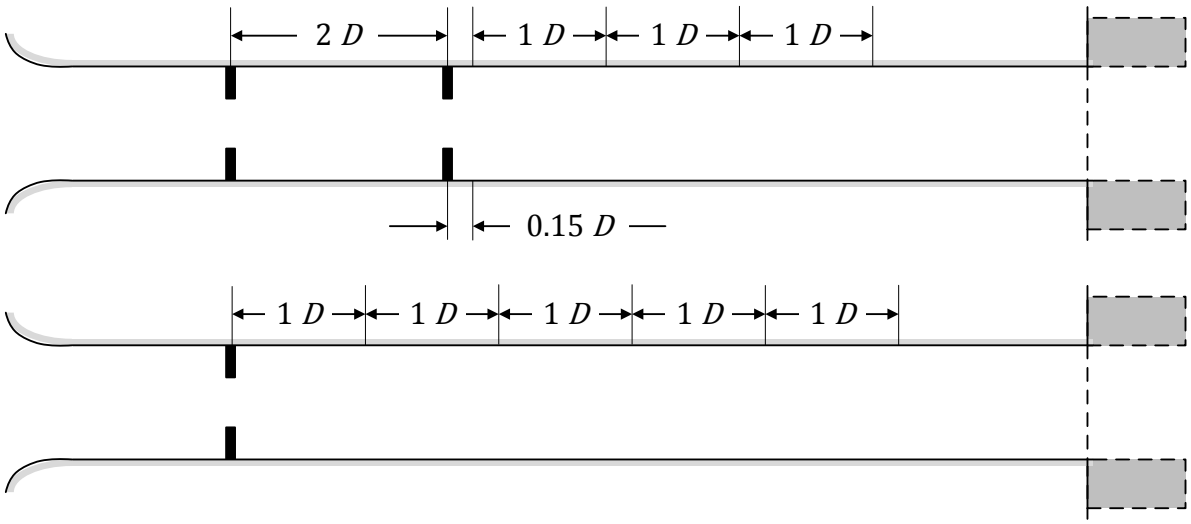

Figure 3.22: Schematic depicting the hotwire measurement cross-sections downstream the diaphragm(s) for the tandem (top) and the single (bottom) diaphragm cases.

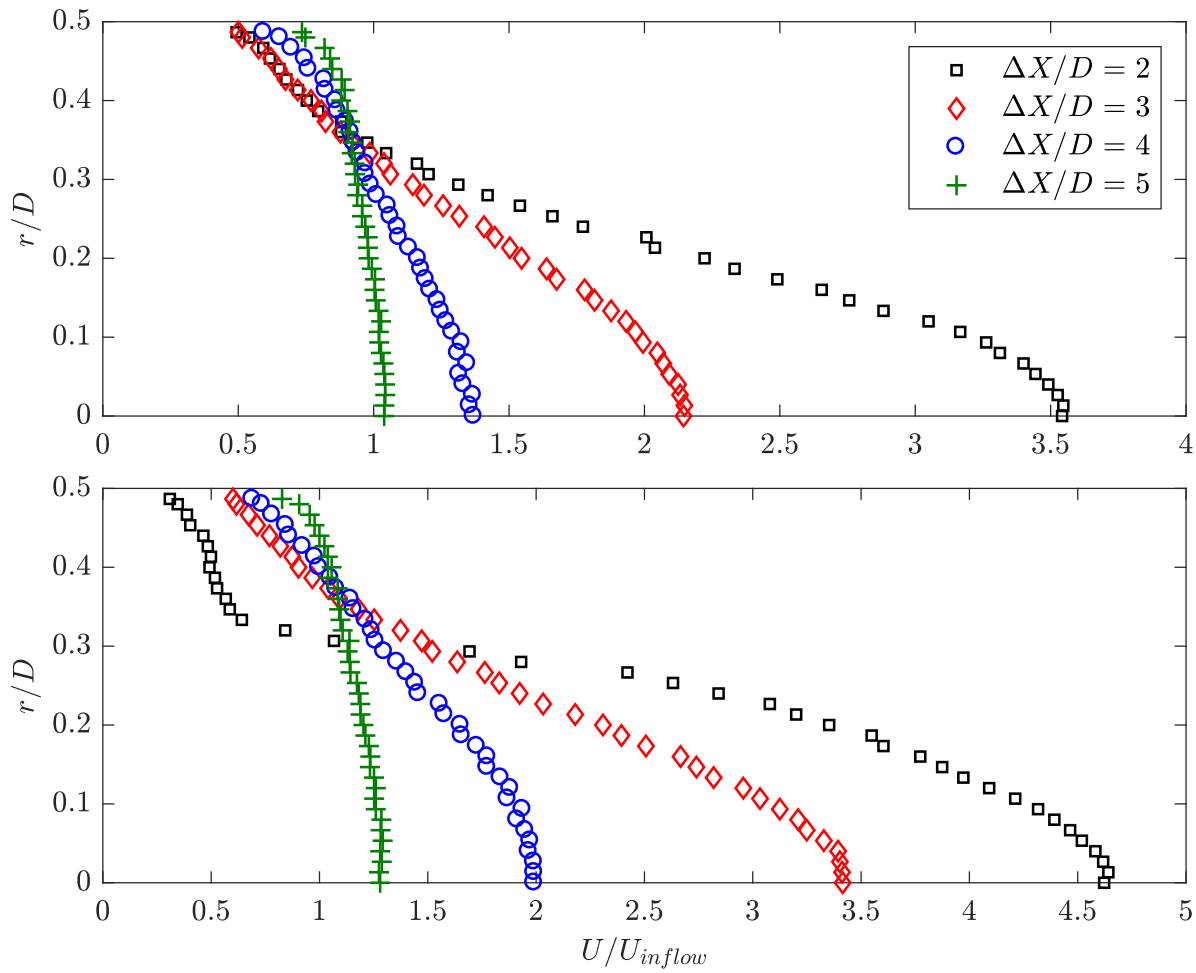

Figure 3.23: Mean velocity measurement data for the single (top) and tandem (bottom) diaphragms cases

4 Active source identification using the two-port method

4.1 Introduction

Designing ventilation systems for building, automotive and public transportation vehicle applications involves integrating various fans, flow restrictions, silencers, etc. into a complex duct system. Upfront flow noise prediction for such complex systems is required for optimized design and to avoid *a posteriori* corrective measures which are usually expensive, if possible at all. The acoustic network modeling approach offers an attractive fast framework for this purpose. It consists in isolating, characterizing and recombining the sub-components of a complex system, with an overall computational cost below the effort associated with the modeling of the whole system at once. The process can produce results with good accuracy as long as the interactions between different noise-generating sub-components remain linear and allow using the principle of superposition. The characterization of the isolated noise generating components, named 'source identification', constitutes a key part of this procedure.

The acoustic source identification of a component necessitates a preliminary identification of the acoustic scattering properties of the system in which it is tested. To this end, different methods were proposed in the literature, which often rely on an external known acoustic source, with large enough amplitude to consider the unknown component source field as negligible in comparison and remove that unknown from the system of equations. The earliest method in this field is the classical standing wave tube method, introduced by Taylor [93] in the early 20^{th} century, in which a microphone is traversed on a tube attached to an acoustic driver at one end, and to the system under investigation on the other end. A bit later, Johnston and Schmidt [33] developed the two-microphone method, showing an easier implementation as no scanning of the duct with the microphone was required. In their method, the microphone readings were correlated to the excitations at discrete frequencies from the external source to obtain incident, reflected and transmitted waves. Since then, the concept of using two or more microphones for source and impedance prediction became a standard for the methods using external source. Seybert and Ross [83] developed a two-microphone method with band-limited random excitation, and estimated the impedance via the relation between acoustic pressure and velocity. Later on, Chung and Blaser [15] introduced an alternative two-microphone method where the incident and the reflected waves are related to each other using convolution integrals based on impulsive responses calculated at, and between the microphone positions. They also implemented a sensor-switching technique for automatic phase and gain calibration of the microphones. Åbom and Bodén [68] provided a detailed investigation of possible error mechanisms in the two-microphone method of Chung and Blaser [15], which were also relevant for the other methods, and quantified their effect on the measurements. They defined the lower and upper frequency

bounds of applicability of the two-microphone method.

The source identification method implemented in the present study is based on a multi-modal decomposition technique. One of the earliest studies analyzing ducted noise sources in terms of acoustic modes was presented by Dyer [20]. Following his study, Kerschen and Johnston [39] devised a modal decomposition technique for time-variant and invariant systems where the time dependent modal amplitude is computed by combining the measured pressure data from microphones evenly distributed in the azimuthal direction. To be able to decompose the radial modes, it is normally expected to take microphone measurements at different radii inside the duct, which is intrusive and often impractical, especially in presence of flow. To overcome this problem, Yardley [100] devised a measurement technique placing microphones at different axial positions. Later on, Moore [58] used this technique to measure the radial and azimuthal modes emitted by ducted fans. All these methods somehow assume a certain source type to perform the modal decomposition. Åbom [67] introduced an alternative approach, which also constitutes the basis of the study in this chapter, capable of identifying the acoustic modes independent of the source signal type. The so-called *passive* (e.g. reflecting and scattering) properties of a circular duct are first obtained using an external source, and the *active* noise radiated by a ducted fluid machine are calculated in a second step with the external source switched off. A considerable asset of this method is that it removes the necessity of anechoic duct end terminations, which remains as a practical issue. The method was initially applied in the plane wave range (Åbom *et al.*, [69]; Lavrentjev *et al.*, [49]), but was soon extended to higher modes leading to the formulation of modal reflection and scattering matrices (Lavrentjev and Åbom, [48]), with applications to fan noise. For example, a recent identification of the first 8 propagative modes (i.e. including a radial mode) emitted by an Environmental Control System blower was performed by Sack *et al.* [78]. Sack and Åbom [77] also implemented this method for the characterization of the noise emitted by a sharp-edged orifice plate. In a recent study, Davids and Bennett [19] proposed a method combining coherence-based approaches and modal analysis to investigate the identification of separate noise sources in case of noise generation by more than one sources.

In this context, this chapter focuses on some numerical robustness issues that are associated with the above methods. The determination of the modal coefficients of a measured acoustic field and the calculation of the modal reflection scattering matrices both involve matrix inversions that can lead to measurement noise amplification if the matrices are badly conditioned. The conditioning number of the matrix can be improved by repeating the measurements with linearly-independent excitation conditions, which are usually obtained using external sources (loudspeakers). In the present study the noise emitted by the unknown source itself is used to determine the modal reflection coefficients at the duct terminations. It is shown that this approach can lead to a more robust determination of the unknown active source. Different implementations of the algorithms are compared, leading to different numerical robustness. As an illustrative application case, the aerodynamic noise generated by single and tandem diaphragms installed in a cylindrical duct is determined following two paths: *i*) by measuring the tandem diaphragms active noise at once, and *ii*) by superposing two models of the single diaphragm measured as a sub-component. The comparison is meant to assess the validity of the network model linearity principle.

4.2 Modal decomposition and filtering of non-acoustic pressure components

Microphones measure any pressure fluctuation without distinguishing between acoustic and non-acoustic perturbations. Performing acoustic measurements in a flow medium with turbulence, the measured acoustic signal is possibly contaminated by turbulent pressure fluctuations. To eliminate such a contamination in the in-duct acoustic measurements conducted in the present study, the approach mentioned Section 2.2.3 is adopted. The frequency range of interest in the present study is limited to cover up to the 2$^{\text{nd}}$ azimuthal mode, which corresponds to 5 cut-on modes ranging from $(m,\mu) = (-2,0)$ to $(m,\mu) = (2,0)$ implying 10 unknowns in total, while 12 microphones have been installed on each side of the diaphragm(s), yielding an overdetermined system. Having an overdetermined system allows a least square estimation of the propagative acoustic modes using Eq. (2.84). By re-calculating the pressure fluctuations using these modes, the parts of the recorded signal that do not propagate as acoustic modes, which we conjecture to be mainly induced by the turbulent boundary layer, are filtered out.

This is illustrated in Figures 4.1 and 4.2, showing a comparison between the acoustic spectrum directly measured at microphones 13 and 18 (corresponding to upstream and downstream sections, respectively), and the spectrum obtained by this pseudo-inversion and reconstruction procedure, for the single and tandem diaphragms cases. Significant differences are observed in the plane wave region between the measured and the reconstructed spectra for the single diaphragm case, especially in the downstream section. A contrario, the measured and reconstructed spectra match quite well for the tandem diaphragm case. The explanation stands in the level of the noise produced by the tandem diaphragm cases, where the interaction of the turbulence shed by the upstream diaphragm with the downstream one causes acoustic radiation more than 20 dB above the noise produced by the single diaphragm. It can be inferred that the microphones measure essentially pressure fluctuations of acoustic nature for the tandem configuration, while a non-negligible hydrodynamic component is present in the low frequency range for the single diaphragm.

4.3 Computing the duct terminations modal reflection matrices from active noise measurements

An outgoing wave $\mathbf{p}^+$ reaching a non-anechoic duct termination (Figure 4.3) is reflected as a wave $\mathbf{p}^-$ in proportion to the modal reflection matrix $\mathbf{R}$ [49]:

$$\mathbf{p}^- = \mathbf{R}\mathbf{p}^+ , \tag{4.1}$$

which can thus be obtained by $\mathbf{R} = \left[\mathbf{p}^-\right]\left[\mathbf{p}^+\right]^{-1}$. Similar to the above discussion, in order to permit this inversion several pairs of vectors $\mathbf{p}^+$ and $\mathbf{p}^-$ must be measured, for at least Q linearly-independent load cases if Q modes are cut-on in the frequency range of interest. Noting P the number of load cases with $P \geq Q$, the following modal matrices are constructed:

$$\mathbf{p}^{\pm}_{(Q\times P)} = \left[\mathbf{p}^{\pm}_{\mathrm{I}} \quad \mathbf{p}^{\pm}_{\mathrm{II}} \quad \cdots \quad \mathbf{p}^{\pm}_{P}\right]. \tag{4.2}$$

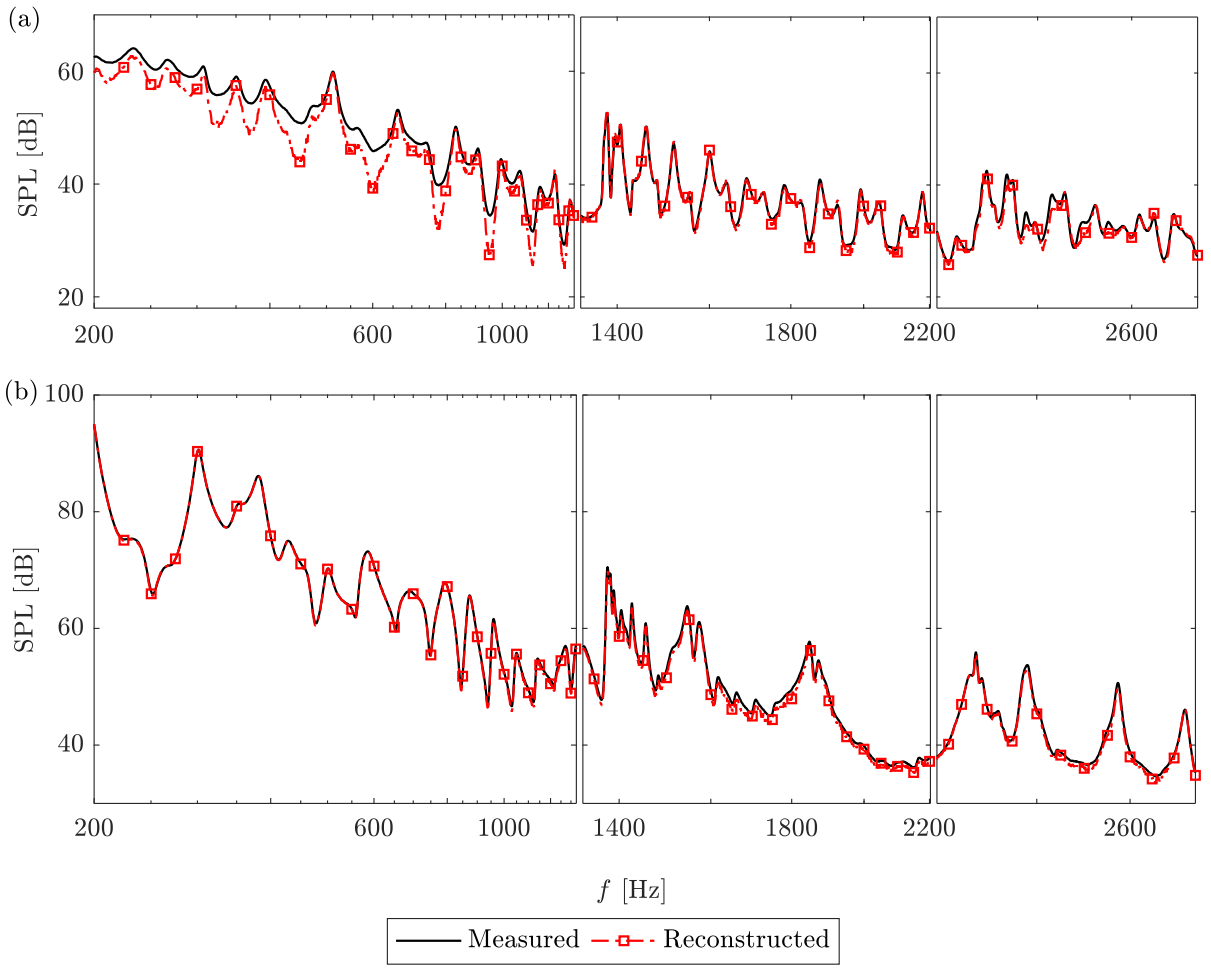

Figure 4.1: Comparison between the spectra obtained from the measured signal and the reconstructed signal at mic. #13 (upstream) for (a) the single diaphragm and (b) the tandem diaphragms cases. Left: only plane wave propagation, center: plane wave and first azimuthal mode propagative, right: plane wave, first and second azimuthal modes propagative.

The different load cases are usually obtained by means of loudspeakers as shown in Figure 3.21, used individually or in combination. However, the use of external sources in computation of the duct termination reflection coefficients may bring particular problems. The modules hosting the loudspeakers should have a perforated surface, allowing the loudspeaker sound to be transmitted inside the duct. These perforates on the duct surface influence the duct terminations reflectivity properties, sometimes in a nonlinear fashion such that the impedance value changes with the level of noise inside the duct. Moreover, since they bridge an acoustic connection between the loudspeaker and the duct, the resulting reflectivity of the duct termination becomes also dependent on the impedance of the loudspeakers. The impedance of a loudspeaker, on the other hand, may change with loudspeaker being switched on or off. This may eventually lead to different duct termination reflectivity properties for the passive and the active measurements.

Use of the loudspeaker excitations to compute the duct termination reflection coefficients gives also rise to some practical issues which increase the complexity of the measurement process. As

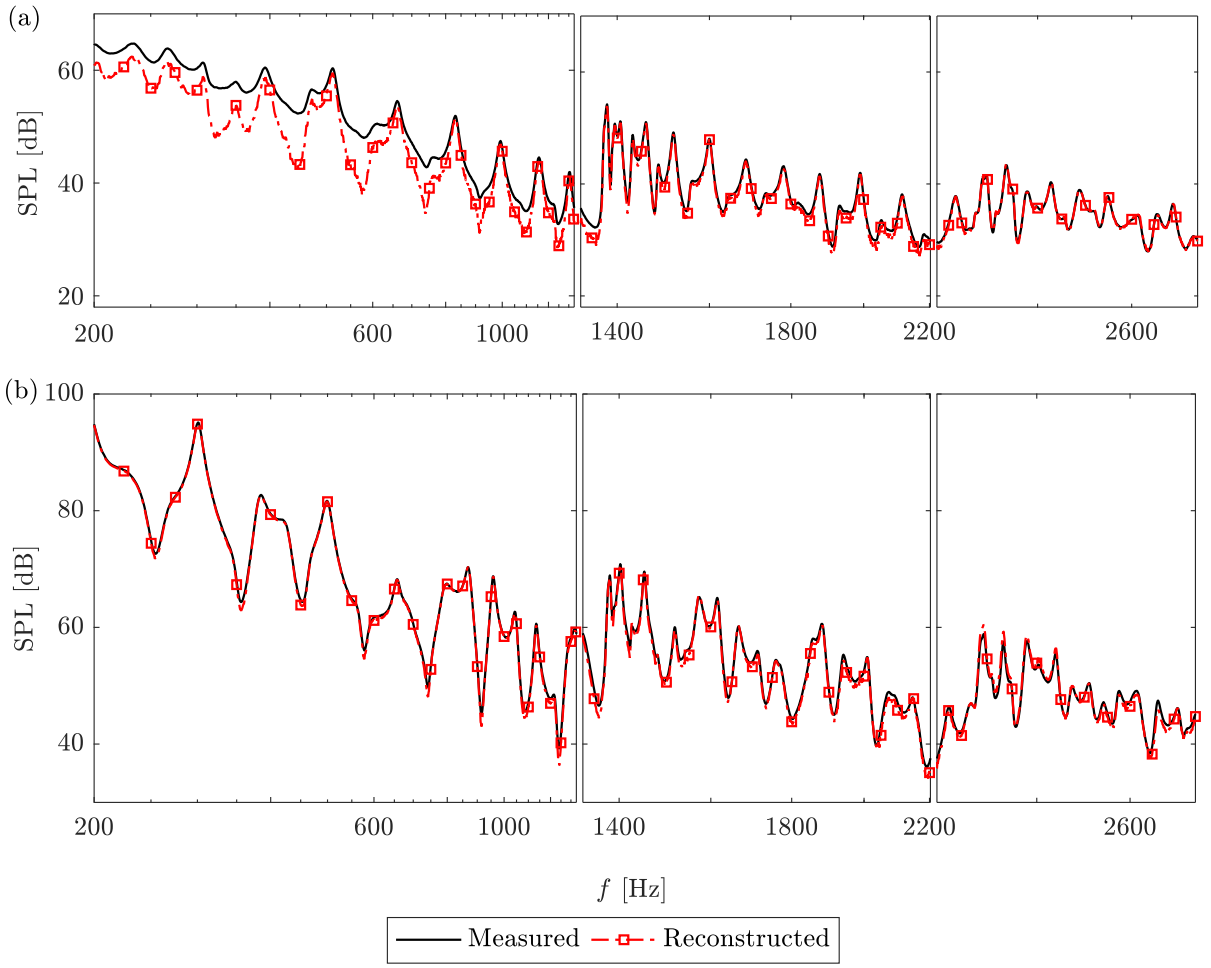

Figure 4.2: Comparison between the spectra obtained from the measured signal and the reconstructed signal at mic. #18 (downstream) for (a) the single diaphragm and (b) the tandem diaphragms cases. Left: only plane wave propagation, center: plane wave and first azimuthal mode propagative, right: plane wave, first and second azimuthal modes propagative.

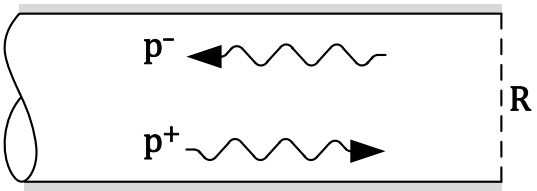

Figure 4.3: Reflection from the duct-end.

a rule, the loudspeaker must be located at the opposite side of the termination being measured, with respect to the microphone array module. Note that in order to reduce the measurement time, loudspeakers can be emitting at both sides of the test rig simultaneously to obtain the modal reflection matrices of both terminations in a single run, but in that case one must avoid emitting the same frequencies from the two sides to respect the above mentioned rule. This cannot always be guaranteed due to non-linearities or imperfections in the electro-acoustical

response of the loudspeakers. Besides, the reflection matrices should ideally be obtained in presence of the same mean flow as for the active measurements, since the flow can affect the terminations reflective properties. But in that case the loudspeakers may not have a sufficient output power to be heard over the noise of the unknown source. It then becomes simpler, and even necessary in particular conditions to use the acoustic field radiated by the source itself for the determination of the reflectivity properties of the terminations.

In case of noise produced by obstacles at large enough Reynolds numbers, the stochastic nature of turbulence ensures that *i*) the emitted sound will be relatively broadband and permit a continuous measurement of the reflection matrices across the frequency range, and *ii*) two different acquisitions are unique and linearly independent, provided the measurement is performed for a sufficiently long time. Therefore, repeating the measurements P times where $P \geq Q$ to generate P load cases, it is possible to obtain non-singular outgoing/incoming modal matrices, $\mathbf{p}^{\pm}_{(Q\times P)}$. In the present study, 90 different measurements of 30 seconds were taken for both single and tandem diaphragms configurations. The level of singularity of the resultant over-determined matrix can be inspected by calculating its conditioning number κ defined as:

$$\kappa(\mathbb{J}) = \|\mathbb{J}\|\|\mathbb{J}^{-1}\|, \tag{4.3}$$

which should remain as low as possible to minimize numerical noise amplification during the inversion process. The conditioning numbers of the incoming/outgoing fields for the single diaphragm case are depicted in Figure 4.4. The results for the tandem diaphragm case, which are very similar to the single diaphragm case, are not shown here. It can be observed that the ob-

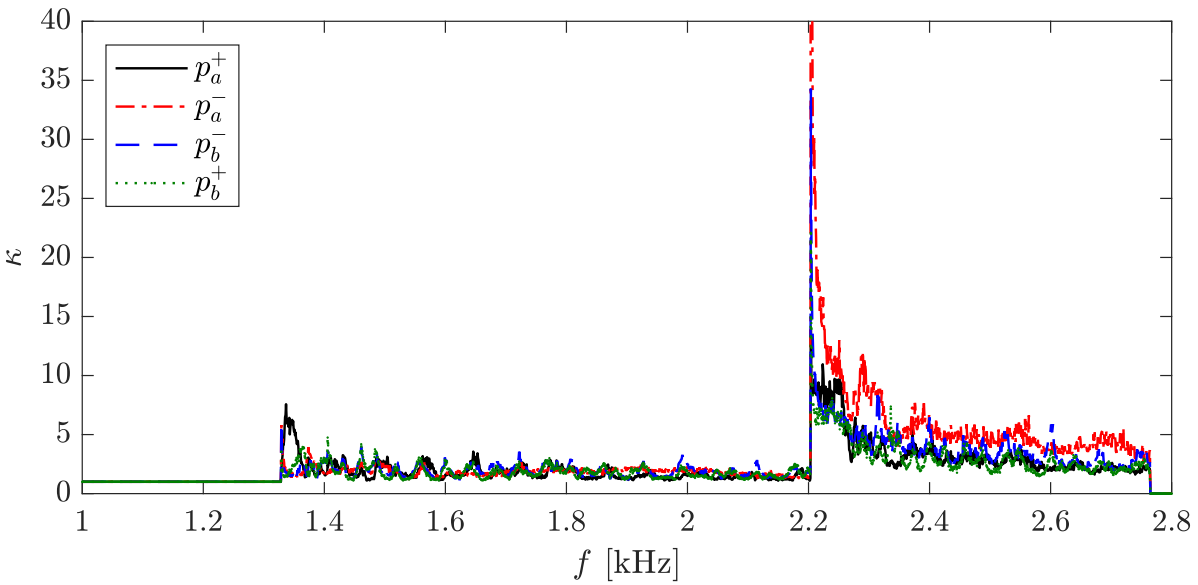

Figure 4.4: Conditioning number for the overdetermined load matrix for the single diaphragm case.

tained condition numbers remain relatively low, thereby demonstrating that the turbulent noise emitted by the component being investigated can be used to calculate the duct ends reflection matrices. To verify the convergence of the conditioning number, it is calculated for increasing number of load cases, and the resulting distribution is integrated over the frequency axis.

The integration is performed only over the frequency range corresponding to the 2nd azimuthal mode, since convergence issues, if any, are to primarily appear in this range. The resulting cumulative conditioning number, $\Sigma\kappa$ vs. the number of load cases is plotted in Figure 4.5. It can be observed that $\Sigma\kappa$ remains relatively constant for load cases greater than 20. A similar con-

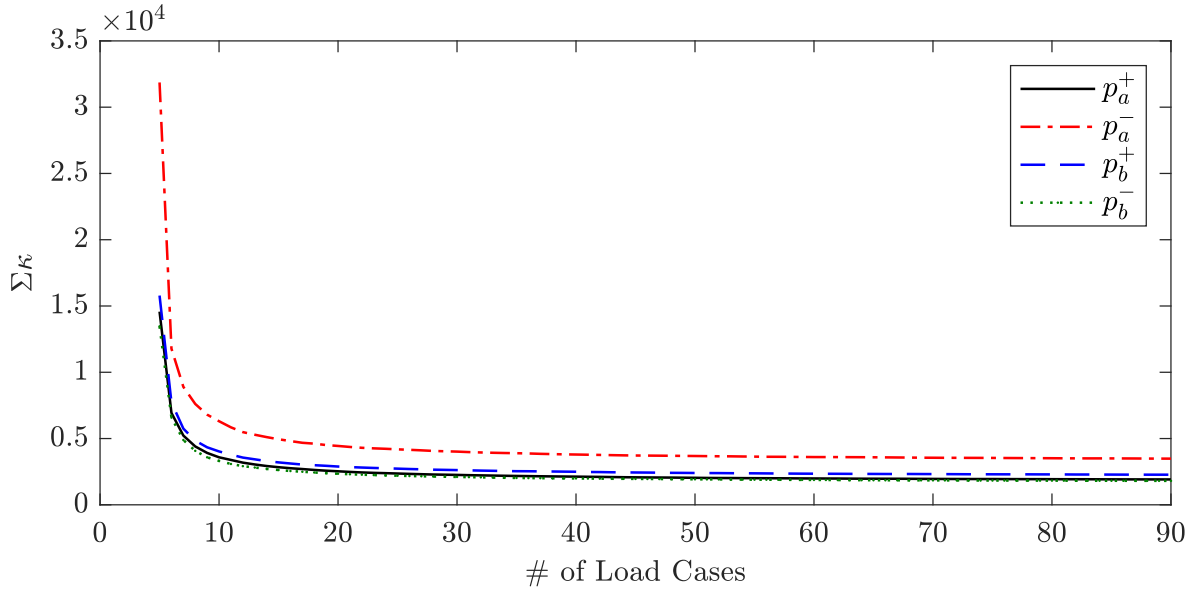

Figure 4.5: Convergence of the conditioning number for the active measurements in the single diaphragm case.

vergence analysis is performed for the passive measurements in which different load cases are obtained by exciting each of the 24 loudspeakers at a given frequency. The resulting cumulative conditioning number, $\Sigma\kappa$ corresponding to the 2nd azimuthal mode is again plotted with respect to the number of load cases, in Figure 4.6. A convergence is obtained for load cases higher than 15. The convergence value, however is observed to be two orders of magnitude higher than the value computed using the active measurement data-set. This indicates a notably higher level of singularity for the passive measurements, providing another argument for the superiority of the present approach in characterization of the duct termination reflectivity.

The reflection coefficients for the upstream and downstream duct terminations obtained following the above procedure are plotted in Figures 4.7 and 4.8 for frequencies including the first azimuthal mode. The results correspond to a configuration in which loudspeaker modules were replaced by empty duct. The off-diagonal elements of the reflection matrix for the upstream end in the first azimuthal mode are observed to be almost zero (see Figures 4.8-a, -b, and -c). This indicates very low scattering across the azimuthal modes, as expected in an axisymmetric termination [72]. On the contrary, the anechoic termination installed at the downstream end of the duct is not axisymmetric and hence induces azimuthal scattering, visible in the non-zero off-diagonal elements of the downstream termination modal reflection matrix (Figures 4.8-d, -e, and -f).

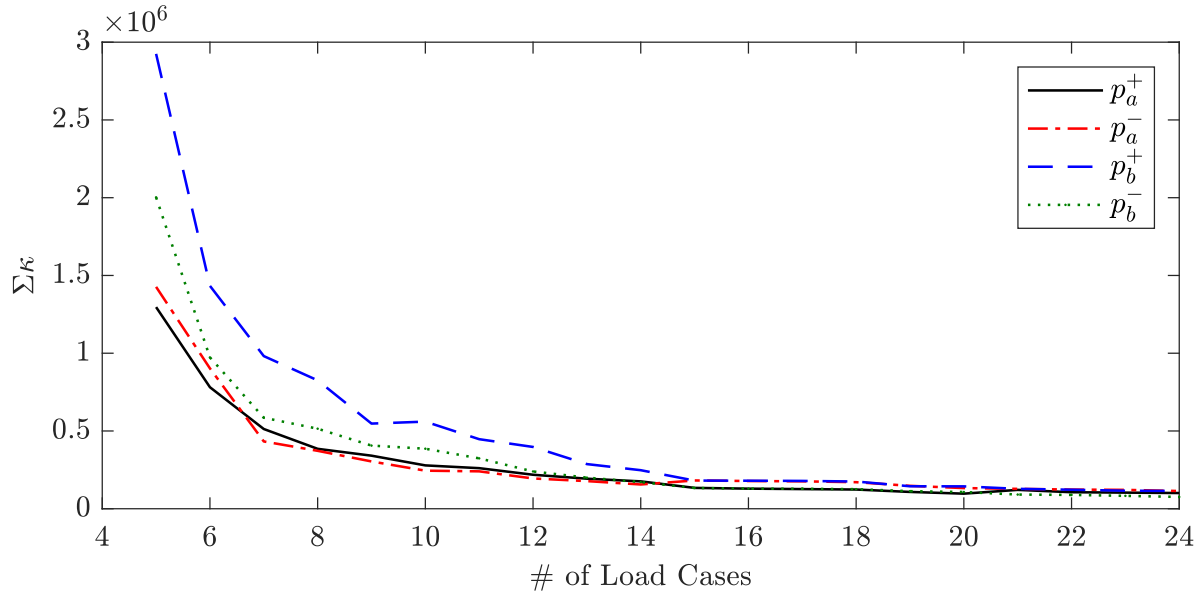

Figure 4.6: Convergence of the conditioning number for the passive measurements in the single diaphragm case.

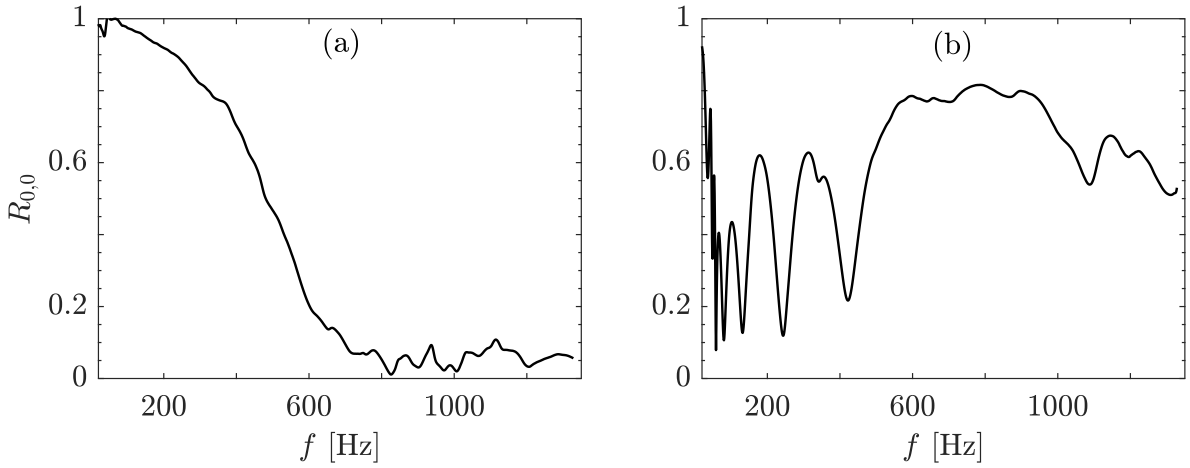

Figure 4.7: Reflection coefficient for (a) upstream and (b) downstream duct-ends in plane wave region.

4.3.1 Sensitivity of the duct termination reflectivity to the acoustic conditions

To show the validity of the above argumentation on possible drawbacks of determining the duct termination reflectivity properties by means of the loudspeakers, the dependence of these properties *i*) on the existence of the loudspeaker modules, and *ii*) on the noise level inside the duct was inspected. The reflection coefficients of the upstream and downstream duct terminations were computed within the plane wave region. The computations were done for the single and the tandem diaphragm cases, with loudspeaker modules unmounted, mounted/switched off, or mounted/switched on. For the configurations without loudspeaker modules, empty modules of

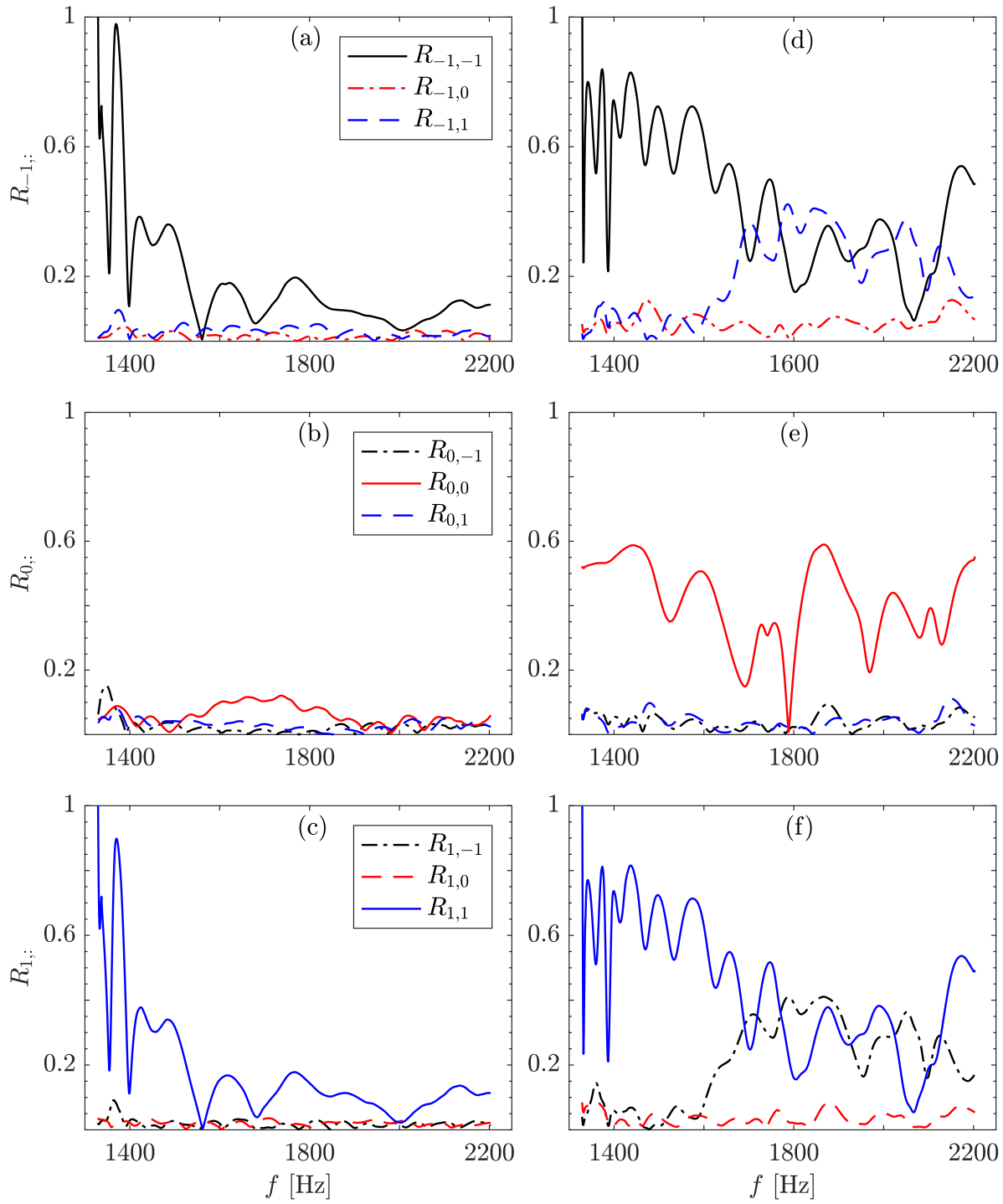

Figure 4.8: Reflection coefficient for (a,b,c) upstream and (d,e,f) downstream duct-ends for the 1st azimuthal mode.

the same length were used for replacement, to keep the duct overall length constant. The configurations with the loudspeakers switched on were obtained by completing the passive measurement campaign (see Section 4.4 for details). The reflection coefficients were then computed at the excitation frequencies only. For the rest of the test cases, termination reflection coefficients

are computed within the full range of frequency of interest, using the broadband active noise data. The comparison of all the cases is presented in Figure 4.9. It is seen that replacing the

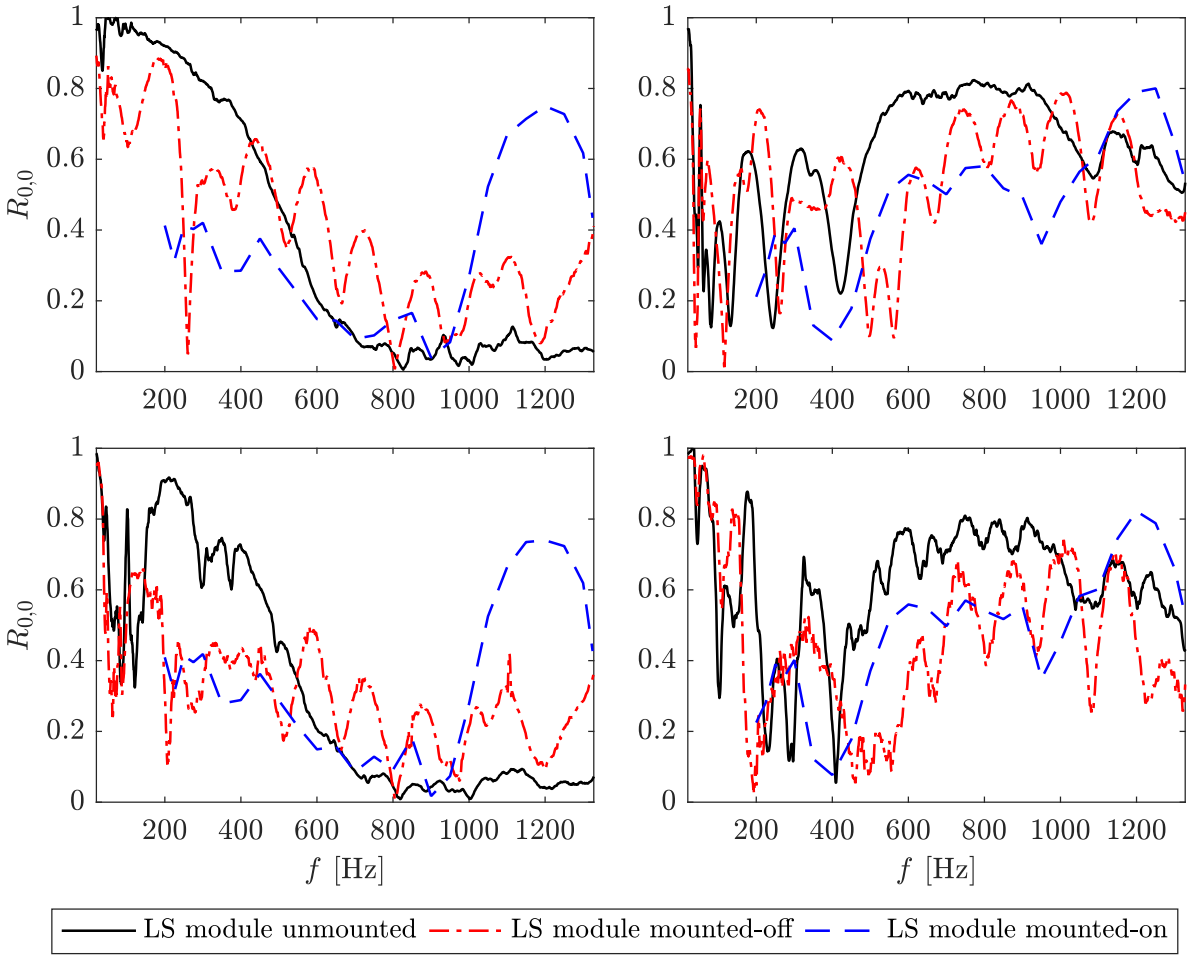

Figure 4.9: Reflection coefficients of the upstream (left) and downstream (right) terminations within the plane wave region for the single (bottom) and tandem (top) diaphragm cases.

empty modules with the perforated ones hosting the loudspeaker arrays causes a significant change in the reflection coefficients of both terminations. Moreover, switching the loudspeakers on and sending tonal excitations also remarkably affect the reflectivity. During the passive measurements, only 4 out of 24 loudspeakers were simultaneously activated. The effect is thereby expected to be even stronger in cases where more loudspeakers are used in parallel. As the reflection coefficients were computed only at the excitation frequencies for the cases with loudspeakers switched on, the possible change in the impedance of the loudspeakers for the rest of the frequency range of interest was separately investigated through the following analysis.

The same flow conditions, and thereby the same active noise data hold true for both active and the passive measurements, while the active noise in the passive measurement campaign is suppressed by tonal loudspeaker excitations. This implies the availability of the active noise data for the passive measurements within a frequency range omitting the excitation frequencies and their harmonics. Following this approach, a broadband prediction of the duct-end reflection

coefficients were obtained based on the passive measurement dataset. The predictions at the excitation frequencies were then omitted, and a pattern for the reflection coefficients was extracted for the remaining frequencies. The result is provided in Figure 4.10 in comparison to the tonal prediction of the reflection coefficients at the excitation frequencies. The broadband predictions

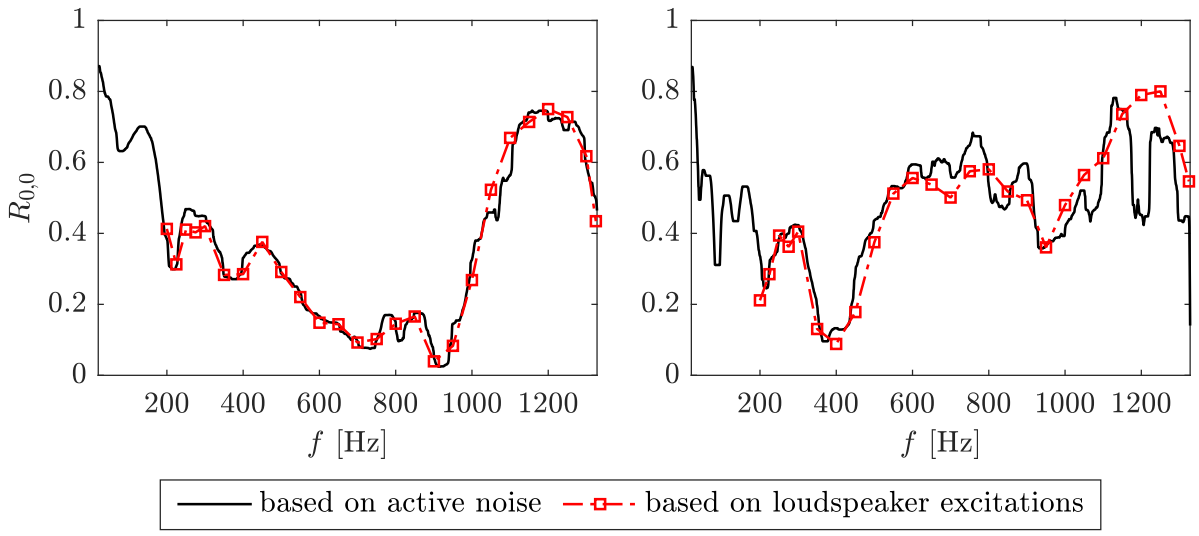

Figure 4.10: Reflection coefficients of the upstream (left) and downstream (right) terminations within the plane wave region obtained using the active (i.e. flow) and passive (i.e. loudspeaker excitations) noise data. Square markers indicate the excitation frequencies. Both computations are based on the passive measurements data-set.

seem to follow the same trend with the tonal ones, especially at the upstream termination. This verifies a broadband change in the impedance of a loudspeaker emitting tonal excitations.

The duct termination reflectivity properties may also be affected by the level of noise inside the duct. As mentioned before, the noise generated by the single and tandem diaphragms differ significantly, especially in the plane wave region. To inspect the effect of this change in the noise level on the termination reflectivity, a comparison is presented in Figure 4.11 between the two configurations with the same duct terminations. As seen in the figure, the termination reflectivity change with the level of noise for the frequency range 200-500 Hz, more evidently when the loudspeakers are installed. Beyond this frequency range, the reflection coefficient of the upstream termination remains constant at different noise levels, while a slight change can still be observed for the downstream termination.

Based on the above analyses, it can be concluded that the reflectivity properties of the duct terminations may be highly sensitive to the acoustic conditions. Therefore, the characterization of the duct termination reflectivity has to be done separately for different configurations, and the use of active noise for this purpose provides a practical solution.

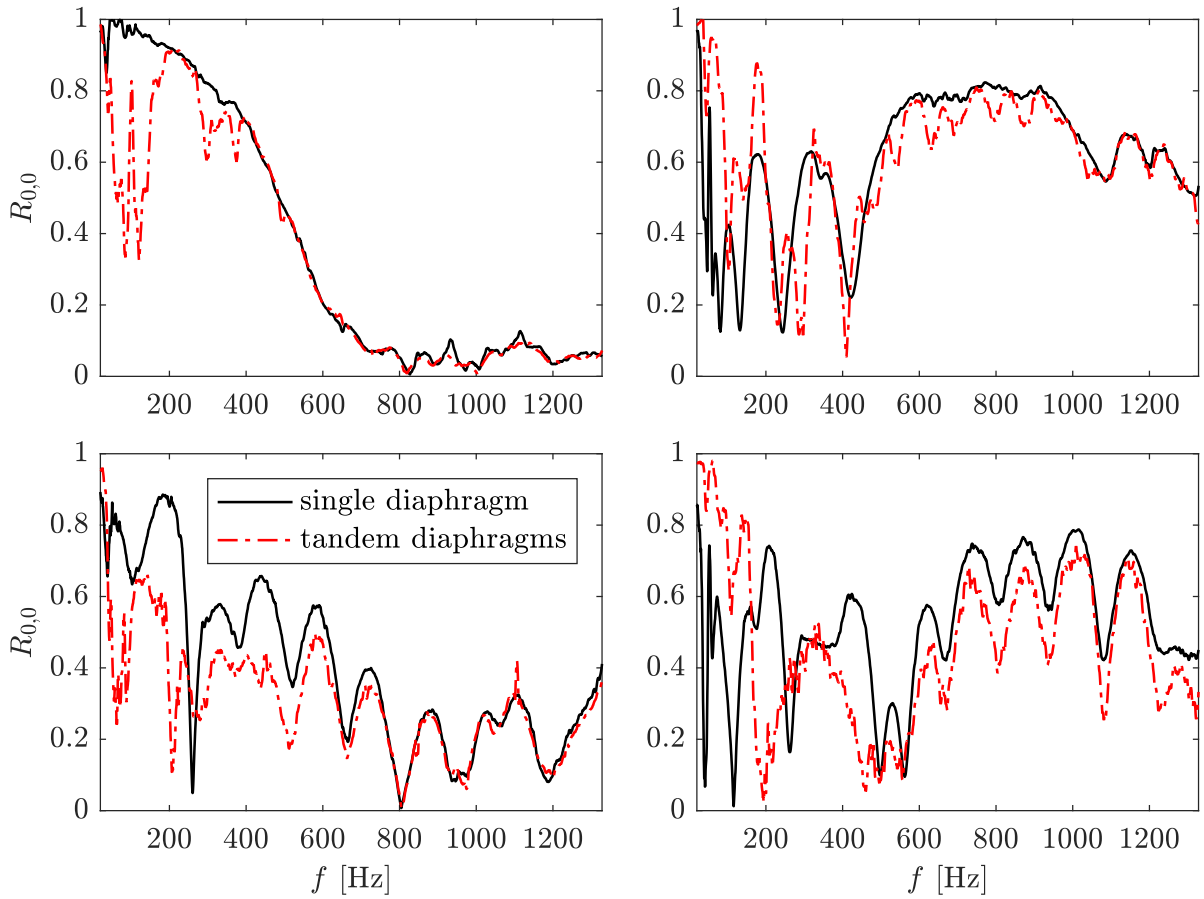

Figure 4.11: Reflection coefficients of the upstream (left) and downstream (right) terminations with (bottom) and without (top) loudspeaker modules.

4.4 Active source identification

The incoming and the outgoing waves measured at each port $\mathbf{p}^{\pm}_{a,b}$ are the sum of the source waves $\mathbf{p}^{s}_{a,b}$ and reflected waves $\mathbf{p}^{r,\pm}_{a,b}$ as illustrated in Figure 4.12:

$$\mathbf{p}^{+}_{a,b} = \mathbf{p}^{r,+}_{a,b} + \mathbf{p}^{s}_{a,b}, \tag{4.4}$$

$$\mathbf{p}^{-}_{a,b} = \mathbf{p}^{r,-}_{a,b}. \tag{4.5}$$

The source components $\mathbf{p}^{s}_{a,b}$ are the ones of interest, and the waves $\mathbf{p}^{r,\pm}_{a,b}$ result from non-anechoic terminations causing the source waves to be at least partly reflected by the duct terminations, partly-transmitted and partly-reflected at the source itself, and so forth. $\mathbf{R}_i$ and $\mathbf{R}_o$ are the inlet and outlet modal reflection matrices. $\mathbf{R}_{a,b}$ and $\mathbf{T}_{a,b}$ are the modal reflection and transmission matrices of the source for waves incident from the a and b sides, which can be grouped to form a scattering matrix

$$\mathbf{S} \equiv \begin{bmatrix} \mathbf{R}_a & \mathbf{T}_b \\ \mathbf{T}_a & \mathbf{R}_b \end{bmatrix} \tag{4.6}$$

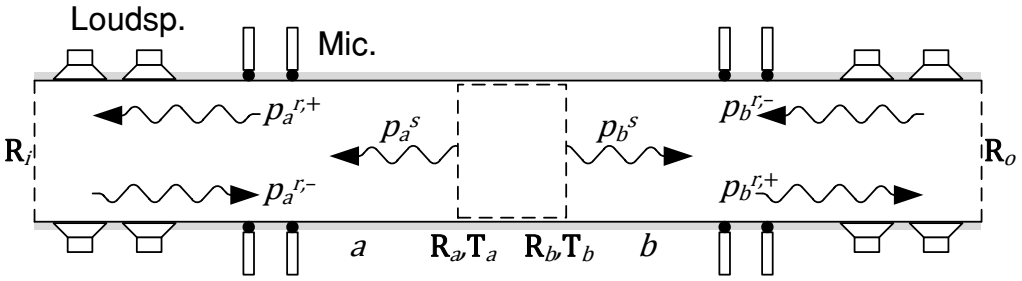

Figure 4.12: Schematic of the experimental rig for the 2-port analysis.

such that the problem can be formulated as

$$\mathbf{p}^+ = \mathbf{S}\mathbf{p}^- + \mathbf{p}^s, \tag{4.7}$$

with $\mathbf{p}^+ \equiv [\mathbf{p}_a^+ \quad \mathbf{p}_b^+]^\top$ and $\mathbf{p}^- \equiv [\mathbf{p}_a^- \quad \mathbf{p}_b^-]^\top$.

The determination of the scattering matrix $\mathbf{S}$ from Eq. (4.7) requires to invert the modal vector $\mathbf{p}^-$, and to eliminate the unknown source modal vector $\mathbf{p}^s$. The latter can be achieved by either finding the correlation between the source and the reflected waves, or using the external loudspeakers at levels high enough to render the contribution of the source to the measured sound field negligible. In that case, we have indeed

$$\mathbf{S} = \left[\mathbf{p}^+\right]\left[\mathbf{p}^-\right]^{-1}. \tag{4.8}$$

For a number Q of propagative acoustic modes, at least $2Q$ different load cases are required. In this instance, external sources are compulsory, as the acoustic field generated by the source cannot be used to determine its own scattering matrix. The elements of the scattering matrices corresponding to the single and tandem diaphragms for the plane wave region are depicted in Figure 4.13. The convective effects on the scattering matrix for both configurations are observed to be small, which is expected considering the low Mach number flow investigated.

Once the scattering matrix is determined, the source term, $\mathbf{p}_s$ can be obtained from the active measurements, i.e. loudspeakers switched off, applying first the modal decomposition and then using Eq. (4.7). The results are depicted in Figure 4.14 for the single and the tandem diaphragm cases. A quite strong contamination can be observed due to the duct end reflections for both the single and the tandem diaphragm cases. The broadband characteristic of the flow noise is much more readable in the source spectra.

An alternative formulation proposed in the literature [49] combines Eqs. (4.4), (4.1) and (4.7) to obtain:

$$\mathbf{p}^s = (\mathbf{I} - \mathbf{S}\mathbb{R})(\mathbb{J}^+ + \mathbb{J}^-\mathbb{R})^{-1}\mathbf{p}' = \mathbb{C}\mathbf{p}', \tag{4.9}$$

where $\mathbb{R} \equiv \mathrm{diag}\{\mathbf{R}_a, \mathbf{R}_b\}$, and $\mathbb{J}^\pm$ is defined such that $\mathbf{p}' = \mathbb{J}^+\mathbf{p}^+ + \mathbb{J}^-\mathbf{p}^-$. This condensed form is *a priori* more convenient than solving Eqs. (4.4), (4.1) and (4.7) in sequence since it directly relates the active source to the raw microphone measurements. In the present work this approach was however shown to exhibit numerical robustness issues, presumably due to the inversion of the matrix $(\mathbb{J}^+ + \mathbb{J}^-\mathbb{R})$. While the matrices $\mathbb{J}^\pm$ are calculated exactly, the accuracy of the reflection matrix $\mathbb{R}$ can suffer from an ill-conditioned vector $\mathbf{p}^+$ as discussed in Section 4.3. This

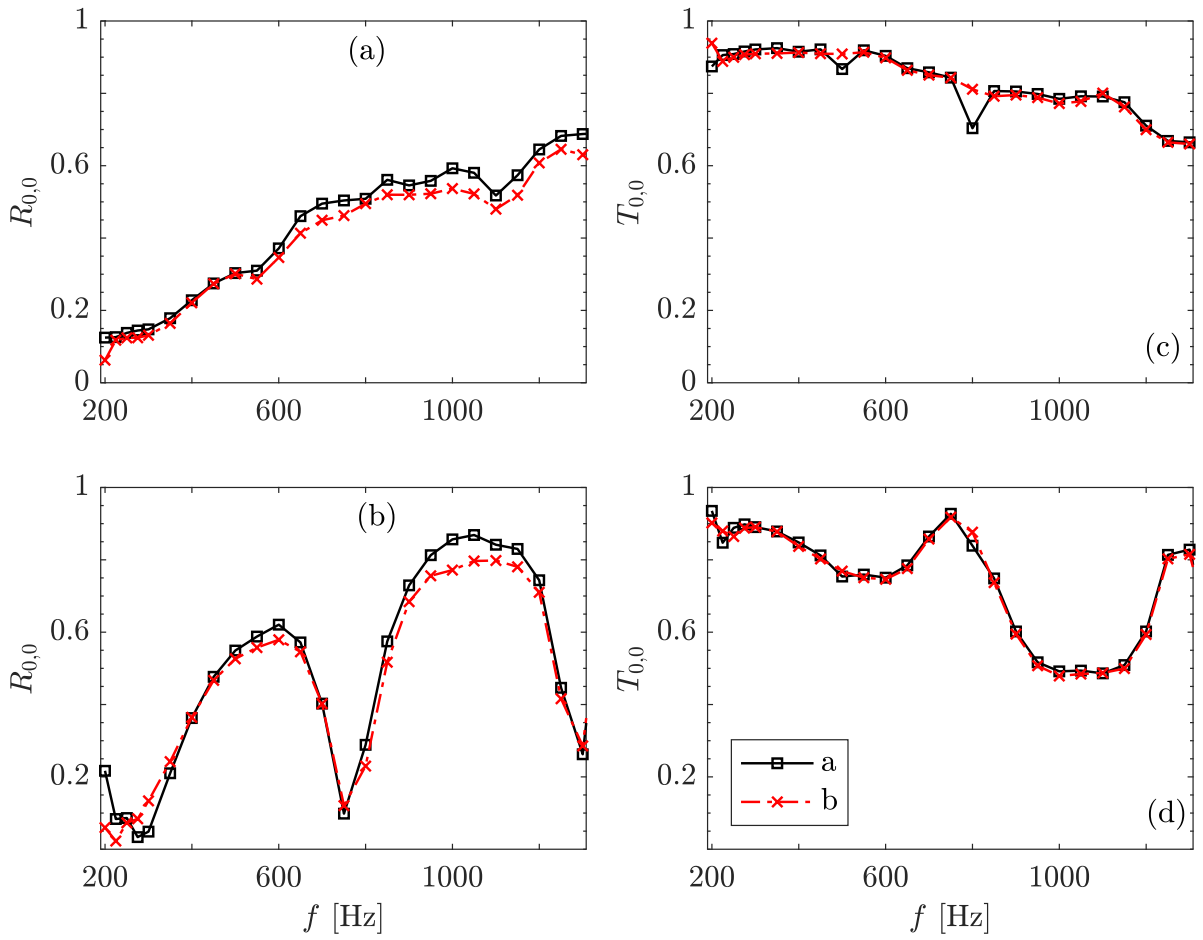

Figure 4.13: Elements of the scattering matrix of the single (a,c) and the tandem (b,d) diaphragms for the plane wave region. Markers indicate the excitation frequencies.

sensitivity is illustrated in Figure 4.15, where the source identification based on Eq. (4.9) has been performed using reflection matrices $\mathbb{R}$ obtained by two different procedures: through passive measurements using the loudspeakers, and through active measurements as proposed in this paper. The results are compared with the source identified by applying sequentially Eqs. (4.4), (4.1) and (4.7), considered here as the reference. It can be observed that the reflection matrix obtained from the active measurements yields a spectrum that is matching with the reference one, but that the reflection matrix obtained from the passive measurements induces spurious noise in the source spectrum.

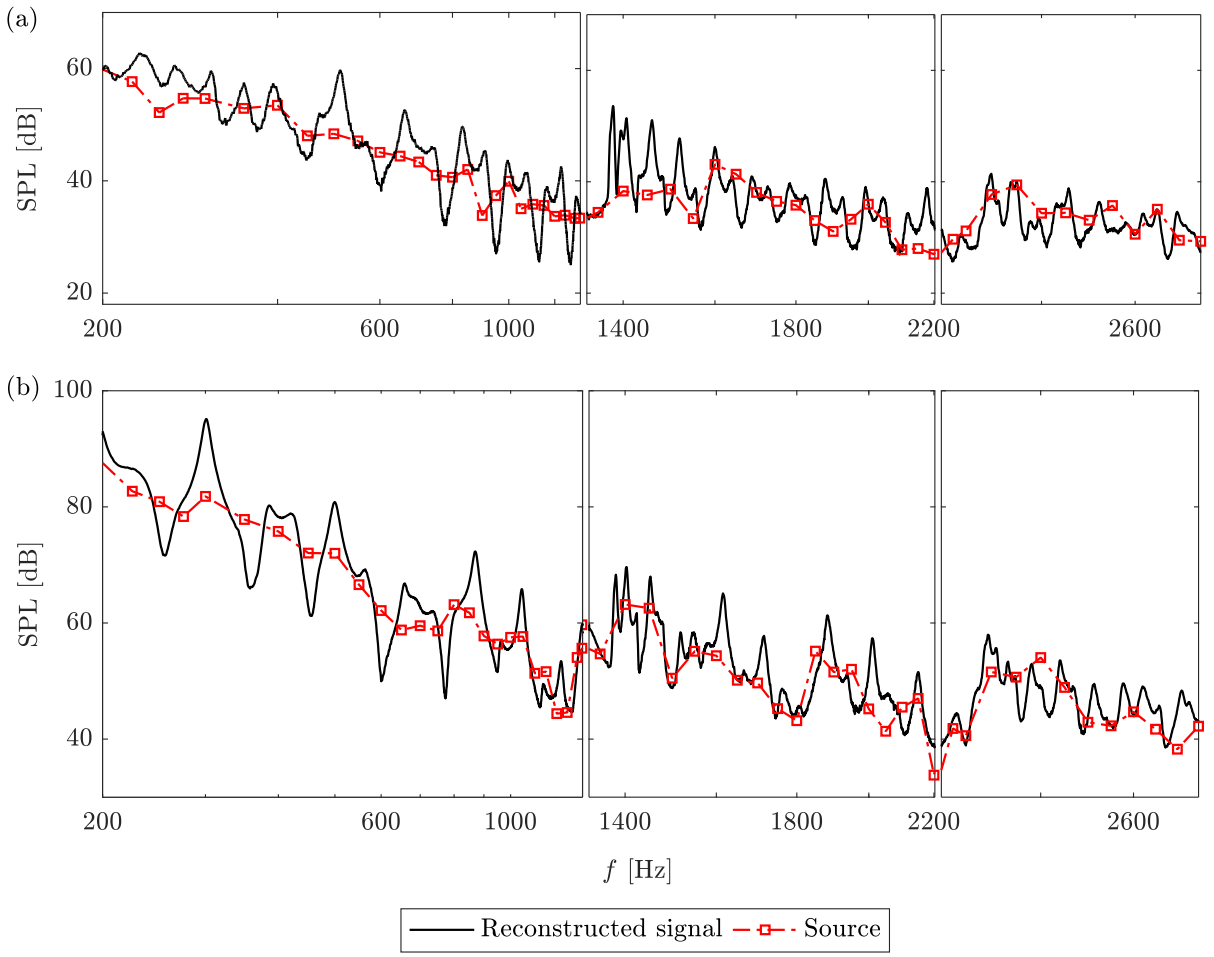

Figure 4.14: Comparison of the the source predictions obtained using the 2-port method against the reconstructed measurements for (a) single and (b) tandem diaphragm cases.

4.5 Prediction of the noise emitted by the tandem diaphragms from the active source characterization of a single diaphragm

The possibility to model a complex systems as a collection of simpler sub-components is here evaluated for the tandem diaphragms case. Given the tandem diaphragms configuration illustrated in Figure 4.16, and the $\mathbf{R}_{a,b}$ and $\mathbf{T}_{a,b}$ values calculated at $x = 0$ for the upstream diaphragm position, the equivalent scattering matrix of the tandem diaphragms can be obtained performing a recursive summation of the waves scattered between the two diaphragms. The recursive procedure described below is extensively investigated in Section 6.3. There, the single diaphragm scattering matrix is obtained by an analytical mode-matching technique neglecting convective effects, while in the present case the scattering matrix is obtained experimentally, thus including flow effects and the convective asymmetries in the upstream vs. downstream reflection / transmission coefficients that may result from it.

The relation between $\mathbf{p}_b^+$ and $\mathbf{p}_a^-$ shown in Figure 4.16 can be written in terms of the right-

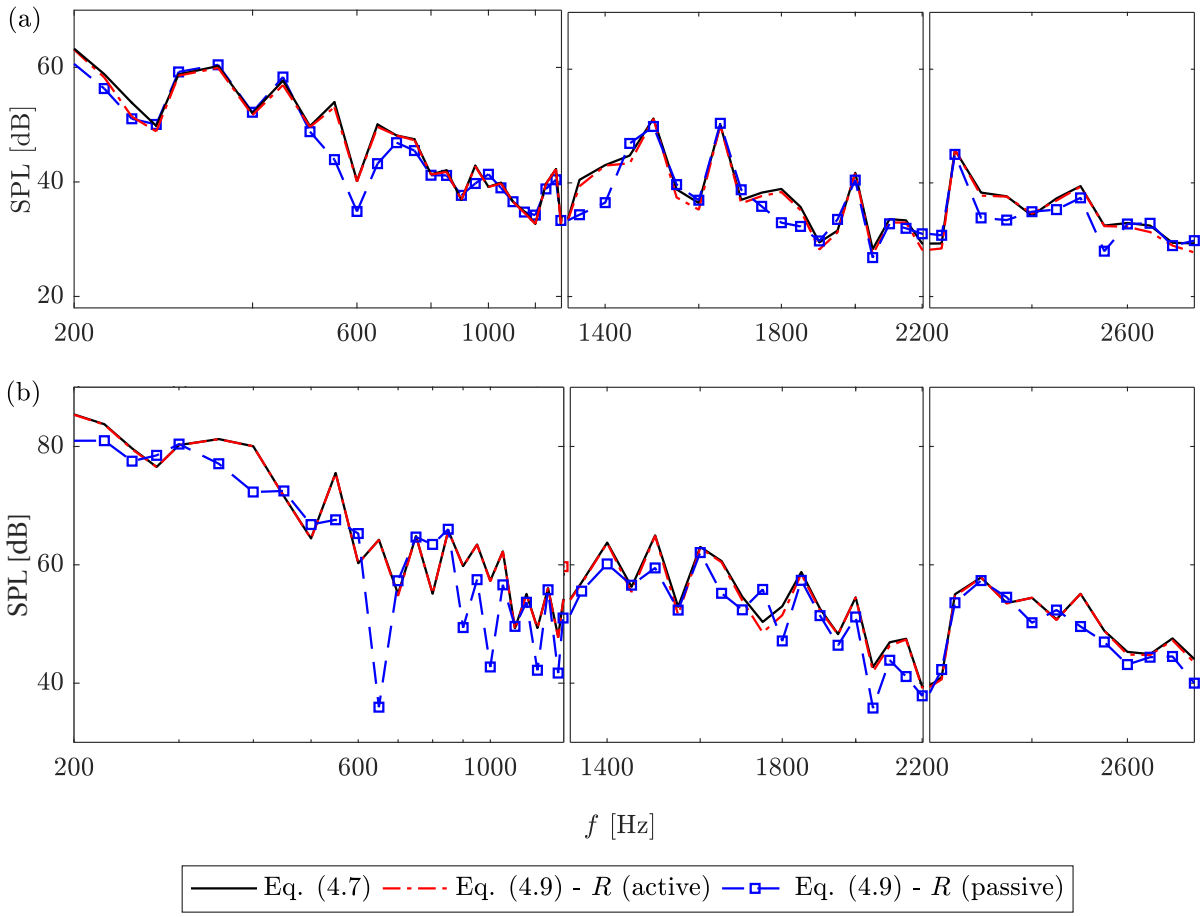

Figure 4.15: Source prediction comparison among the variants of the 2-port method for (a) single and (b) tandem diaphragm cases. Solid line: reference prediction using Eqs. (4.4), (4.1) and (4.7) in sequence; dash-dotted: source prediction using Eq. (4.9) with $\mathbb{R}$ from passive measurements; symbols: source prediction using Eq. (4.9) with $\mathbb{R}$ from active measurements.

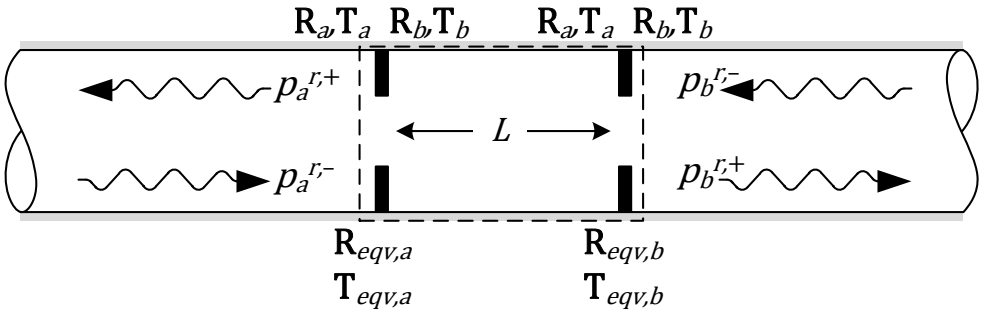

Figure 4.16: Schematic representation of the network modeling of tandem diaphragms.

going waves successively reflected between the diaphragms as shown in Figure 4.17, where

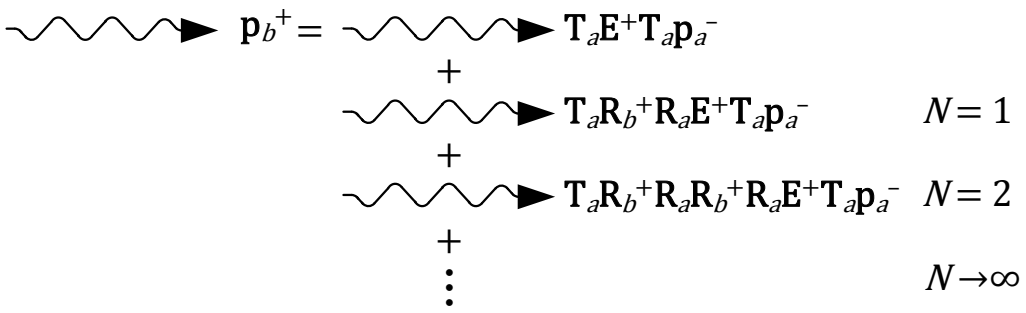

Figure 4.17: Decomposition of the outgoing wave into infinitely many right-going reflected waves.

$\mathbf{E}^{\pm} \equiv \mathrm{diag}\left\{e^{\mp \mathrm{i}\mathbf{k}^{\pm}L}\right\}$ and $\mathbf{R}^{\pm} \equiv \mathbf{E}^{\mp}\,\mathbf{R}\,\mathbf{E}^{\pm}$. This summation can be written as

$$\mathbf{p}_b^+ = (1/\mathbf{E}^+)\mathbf{T}_a(\mathbf{I} + \mathbf{R}_b^+\mathbf{R}_a + \mathbf{R}_b^+\mathbf{R}_a\mathbf{R}_b^+\mathbf{R}_a + \cdots)\mathbf{E}^+\mathbf{T}_a\mathbf{p}_a^-. \tag{4.10}$$

Please note that the term $(1/\mathbf{E}^+)$ is added in Eq. (4.10) to have $\mathbf{p}_b^+$ calculated at $x = 0$. The terms expressing the infinite sum in Eq. (4.10) can be rewritten in a recursive form:

$$\left(\mathbf{I} + \mathbf{R}_b^+\mathbf{R}_a + \cdots\right) = \left(\mathbf{I} + \mathbf{R}_b^+\mathbf{R}_a\left(\mathbf{I} + \mathbf{R}_b^+\mathbf{R}_a\,(\mathbf{I} + \cdots)\right)\right) \tag{4.11}$$

where the recursive summation can be treated using the mathematical induction method:

$$\begin{aligned} z &= \left(\mathbf{I} + \mathbf{R}_b^+\mathbf{R}_a\left(\mathbf{I} + \mathbf{R}_b^+\mathbf{R}_a\,(\mathbf{I} + \cdots)\right)\right) = (\mathbf{I} + \mathbf{R}_b^+\mathbf{R}_a z), \\ (\mathbf{I} - \mathbf{R}_b^+\mathbf{R}_a)\,z &= \mathbf{I}, \\ z &= (\mathbf{I} - \mathbf{R}_b^+\mathbf{R}_a)^{-1}. \end{aligned} \tag{4.12}$$

The infinite summation in Eq. (4.10) can be replaced by the right-hand-side of Eq. (4.12), giving the outgoing wave:

$$\begin{aligned} \mathbf{p}_b^+ &= (1/\mathbf{E}^+)\,\mathbf{T}_a\,(\mathbf{I} - \mathbf{R}_b^+\mathbf{R}_a)^{-1}\,\mathbf{E}^+\mathbf{T}_a\mathbf{p}_a^-, \\ &\equiv \mathbf{T}_{\mathrm{eqv},a}\,\mathbf{p}_a^-, \end{aligned} \tag{4.13}$$

where $\mathbf{T}_{\mathrm{eqv},a}$ is the equivalent transmission coefficient matrix for the tandem diaphragm case. Similarly, the equivalent reflection coefficient matrix can be obtained as

$$\begin{aligned} \mathbf{p}_a^+ &= \left[\mathbf{T}_b\,(\mathbf{I} - \mathbf{R}_a^-\mathbf{R}_b)^{-1}\,\mathbf{R}_a^-\mathbf{T}_a + \mathbf{R}_a\right]\mathbf{p}_a^-, \\ &\equiv \mathbf{R}_{\mathrm{eqv},a}\,\mathbf{p}_a^-. \end{aligned} \tag{4.14}$$

The equivalent scattering matrix, $\mathbf{S}_{\mathrm{eqv}}$ can be constructed:

$$\mathbf{S}_{\mathrm{eqv}} = \begin{bmatrix} \mathbf{R}_{\mathrm{eqv},a} & \mathbf{T}_{\mathrm{eqv},b} \\ \mathbf{T}_{\mathrm{eqv},a} & \mathbf{R}_{\mathrm{eqv},b} \end{bmatrix}. \tag{4.15}$$

The comparison between source predictions obtained from the network modeling and the multi-port method is given in Figure 4.18. There can be observed a very good agreement between the two source predictions.

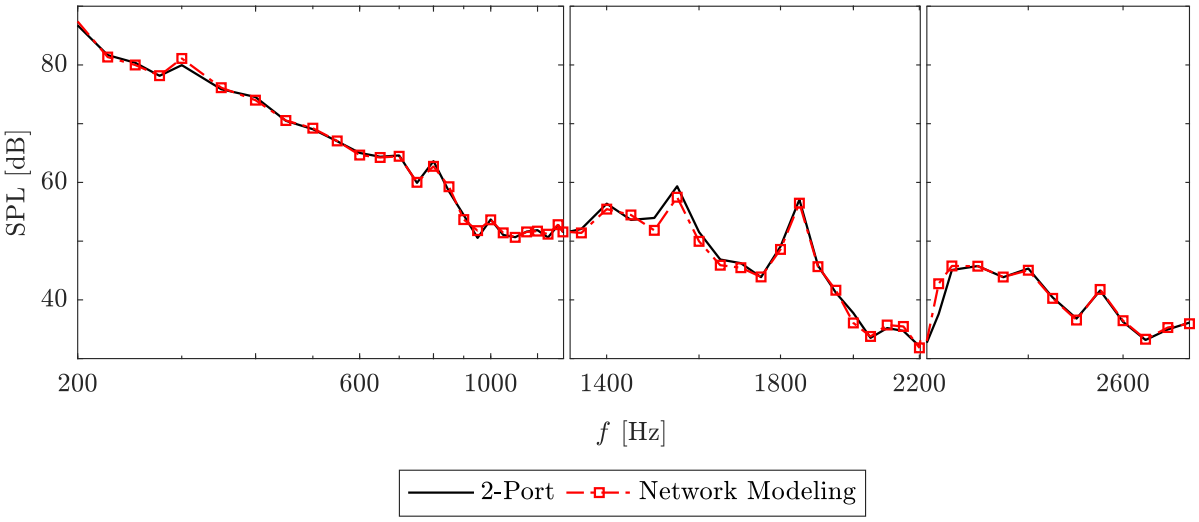

Figure 4.18: Comparison among the source predictions obtained using the 2-port method and the network modeling for (a) single and (b) tandem diaphragm cases.

To investigate the interaction of the tandem diaphragms in noise generation, the network modeling approach is implemented on the active source data obtained from the single diaphragm case. Similar to the recursive analysis introduced above, a recursive summation of the source waves $\mathbf{p}^{s}_{a,b}$ is conducted to predict the resulting active source for the tandem diaphragm case, $\mathbf{p}^{s*} = [\mathbf{p}^{s*}_{a}\mathbf{p}^{s*}_{b}]^{\top}$, using the below formulation:

$$\begin{aligned}\mathbf{p}^{s*}_{a} = \mathbf{p}^{s}_{a} + (1/\mathbf{E}^{-})\left[\mathbf{T}_{b}\left(\mathbf{I}-\mathbf{R}^{+}_{a}\mathbf{R}_{b}\right)^{-1}\mathbf{E}^{-}\mathbf{p}^{s}_{a}\right.\\ \left.+\mathbf{T}_{b}\left(\mathbf{I}-\mathbf{R}^{+}_{a}\mathbf{R}_{b}\right)^{-1}\mathbf{R}^{+}_{a}\mathbf{p}^{s}_{b}\right.. \end{aligned} \tag{4.16}$$

Eq. (4.16) can be easily re-written to obtain $\mathbf{p}^{s*}_{b}$. The active source prediction obtained from Eq. (4.16) is depicted in comparison with the source predictions obtained directly from the two-port method for the single and tandem diaphragm cases in Figure 4.19. The prediction obtained by network modeling of the active source is seen to underpredict the source for the tandem diaphragm case. Such a result indicates a non-linear mechanism is responsible for noise generation, while the interaction is observed to be linear for the scattering mechanism.

4.6 Conclusions

In this chapter, flow related noise generated by the two diaphragm configurations has been investigated up to the 2$^{\text{nd}}$ azimuthal mode using model decomposition technique. The effect of the turbulence contamination on the wall-flush microphone readings has been quantified by reconstructing the decomposed acoustic field and comparing to the raw measurements. Noticeable turbulent contamination in the acoustic measurements were observed in the single diaphragm case, while the effect was shown to be ignorable in the tandem diaphragm case. The drawbacks of the use of external sources in determination of the duct termination reflectivity properties was discussed through investigating the sensitivity of the termination reflectivity on the acoustic field and boundary conditions inside the duct. The sensitivity analysis involved comparing

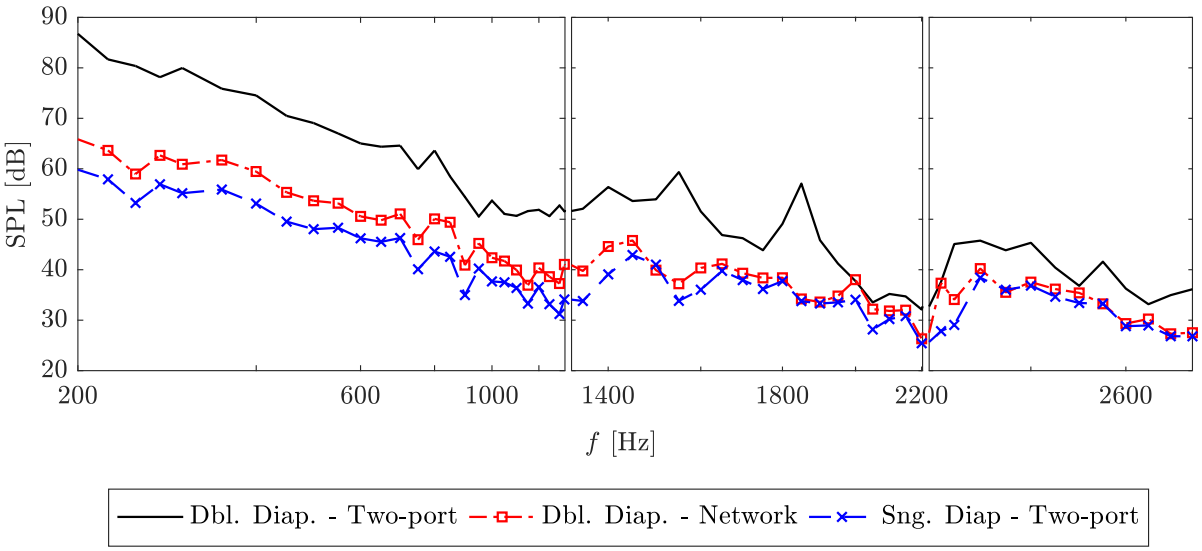

Figure 4.19: Comparison among the source predictions obtained network modeling of the active source against the predictions of the two-port method.

the single and tandem diaphragm cases with loudspeakers switched on/off or replaced by empty duct modules. Significant change in the reflection coefficients of both upstream and downstream terminations with different configurations verified the necessity to compute those coefficients separately for each test case. As a practical solution, the use of the active noise in predicting the duct termination reflection matrices was proposed. Two-port method was implemented to achieve source identification in the single and tandem diaphragm cases, using two different formulations: one with using the duct termination reflection coefficients and one without. The former was shown to suffer from robustness issues arising from the use of the reflectivity data obtained using the passive measurements. When reflection coefficients calculated based on the active noise data were used, on the other hand, the two formulations was shown to yield the same result. The linearity of the scattering and noise generation mechanisms in tandem diaphragms were also investigated. The scattering matrix and the active source for the tandem diaphragm case was predicted by network modeling of the corresponding parameters for the single diaphragm. The predictions were compared to the results of the two-port method implemented for the tandem diaphragm case. A linear interaction between the diaphragms was observed in terms of the scattering mechanism, while the interaction for noise generation was shown to be highly nonlinear.

5 Numerical investigation of ducted diaphragm flows

The noise prediction approaches investigated in the thesis required both steady and unsteady flow simulations. The unsteady flow data was obtained from a compressible LES, while axisymmetric RANS simulations were conducted for steady flow solutions. Use of LES for prediction of engineering flows became achievable only recently due to its computational costs. It was even more recent that the use of LES for direct noise computation purposes in engineering flows became possible, since proper resolution of the acoustic field, which is much smaller compared to the turbulent fluctuations in terms of the perturbation amplitudes, requires significantly enhanced refinement of mesh increasing the computational costs even more.

There are various studies in the literature attempting to solve diaphragm noise prediction problem using direct approaches based on compressible LES. The earliest attempt to the authors knowledge was made by Gloerfelt *et* Lafon [23] investigating the noise generation in a rectangular duct with a slit-shaped diaphragm at a relatively low Reynolds number ($Re_{duct} = 32,000$ and $Re_{diap} = 14,000$). Sengissen *et al.* [82] later investigated the noise generated by tandem orifices with $1D$ and $2D$ separations in a circular duct of diameter D. The Reynolds number with respect to the duct was $\tilde{1}7{,}500$ in their study. There are also studies on system identification of ducted diaphragm configurations using compressible LES. Alenius *et al.* [4] studied the scattering characteristics of a circular diaphragm installed in circular and rectangular ducts at a higher Reynolds number around 80,000, using Dynamic Mode Decomposition [79]. In a more recent study, Sovardi *et al.* [91] investigated the system identification problem in circular ducted diaphragm in the presence of a flow at $Re = 18,000$ using the 'parametric LES-SI method' in which acoustically excited flow data is used to predict the characteristics of the scattering element. The first author of that study was also responsible for conducting the compressible LES of the present study as part of his doctoral studies [90].

The RANS simulations are required to provide a reference solution for the stochastic noise prediction methods. RANS simulation for low Mach number shear flows like the present cases is a well-established research topic. There exist many studies in the literature comparing different turbulence models for this type of flows. A particular investigation of the flow through an orifice meter, which can be considered as ducted diaphragm, using CFD was done by Shah *et al.* [84]. They performed a RANS simulation using the standard $k-\epsilon$ model 3-dimensional duct geometry. Standard $k-\epsilon$ model [47], where k and ϵ denote the turbulent kinetic energy and dissipation rate respectively, is the most popular turbulence model used in many industrial CFD applications [84]. It is a two-equation model assuming linear isotropy. The model requires a wall-function to predict the boundary layer near the wall, which indeed is one of the main reasons for the popularity of the model, since the use of wall-functions reduces the requirement for a refined mesh near the wall. An important deficit of the model is that it suffers from 'stagnation

point anomaly',i.e. overestimation of turbulent kinetic energy in regions where the flow is stagnated, due to not being realizable [85]. An improved version of the standard $k-\epsilon$ model was suggested by Shih *et al.* [85]. They developed an anisotropy model satisfying the realizability constraint, therefore limiting the non-physical production of turbulent kinetic energy. There are alternative turbulence models for low Reynolds number applications in which wall-functions are not preferable due to their poor performance. Low-Re $k-\epsilon$ models again use k and ϵ equations for closure, but no wall-functions to predict the boundary layer profile. Some extra terms are added instead in the closure equations which are dominant near the wall and negligible in the free-field. The extent of the applicability of low-Re $k-\epsilon$ models is extensively investigated for many different types of flows. A detailed comparison of eight low-Re $k-\epsilon$ models was reported by Patel *et al.* in [63] where the models were tested for four different boundary layer cases. Costa *et al.* [16] tested another set of 8 low-Re $k-\epsilon$ models for internal mixed convection flows. And Hrenya *et al.* [30] performed a similar analysis for fully developed pipe flows.

In the thesis, the flow predictions obtained from the LES, and various RANS simulations using the standard $k-\epsilon$ model and six different low-Re $k-\epsilon$ models are compared against hot-wire measurement data for single and tandem diaphragm cases. The low-Re $k-\epsilon$ models investigated are Abid [2], Abe-Kondo-Nagano (AKN) [1], Chang-Hsieh-Chien (CHC) [14], Lam-Bremhorst (LB) [45], Launder-Sharma (LS) [46] and Yang-Shih (YS) [99]. The details of the numerical simulations, and the comparison of the results are given in the following subsections.

5.1 Large Eddy Simulation

The LES solver adopted in the present study is the AVBP solver [82] (developed by CERFACS and EFP), which solves the compressible Navier-Stokes equations on unstructured meshes. A second order Lax-Wendroff scheme [50] in time and space is used to discretize the temporal and spatial derivatives. The time steps of the simulations are fixed after reaching the stationary flow condition, to afford a CFL number of 0.7. The spatial discretization achieves stable simulations while granting low acoustic dissipation and dispersion errors in the domain under analysis. The large turbulent eddies (compared to the mesh elements size) are resolved, whereas the subgrid scales are resolved by means of the so called Wall-Attached-Layer-Eddy (WALE) model. The WALE model was suggested by Nicous *et* Ducros [60], who aimed at developing a turbulent eddy viscosity model, ν_t which goes naturally to zero at the wall, removing the necessity for damping functions or dynamic procedure to satisfy no-slip condition. The derived subgrid scale model was of the form;

$$\nu_t = (C_w\Delta)^2\frac{\overline{OP}_1}{\overline{OP}_2} = (C_w\Delta)^2\frac{\left(S^d_{ij}S^d_{ij}\right)^{3/2}}{\left(\overline{S}_{ij}\overline{S}_{ij}\right)^{5/2}+\left(S^d_{ij}S^d_{ij}\right)^{5/4}}, \tag{5.1}$$

where C_w is the model constant, $\Delta \equiv V^{1/3}$ is the characteristic length for a mesh element with volume V. The tensor $\hat{S}_{ij}$ is the strain rate defined as;

$$\hat{S}_{ij} = \frac{1}{2}\left(\frac{\partial\overline{u}_i}{\partial x_j}+\frac{\partial\overline{u}_j}{\partial x_i}\right), \tag{5.2}$$

where $\overline{\mathbf{u}}$ denote the resolved velocity field. The S_{ij}^d is the symmetric, traceless part of the square of the velocity gradient given as follows:

$$S_{ij}^d = \frac{1}{2}\left(\overline{g}_{ij}^2 + \overline{g}_{ji}^2\right) - \frac{1}{3}\delta_{ij}\overline{g}_{kk}, \tag{5.3}$$

where $\overline{g}_{ij} \equiv \partial\overline{u}_i/\partial x_j$ is the gradient of the resolved velocity. The model constant C_w is calculated using the following relation;

$$C_w^2 = C_s^2 \frac{\langle\sqrt{2}(\overline{S}_{ij}\overline{S}_{ij})\rangle}{\langle\overline{S}_{ij}\overline{S}_{ij}\overline{OP}_1/\overline{OP}_2\rangle}, \tag{5.4}$$

where C_s is the constant used in the Smagorinsky model [88]. The length of the domain is set as $15D$ and $17D$ for the single and tandem diaphragm cases, respectively, where the (upstream) diaphragm is located at the axial position $x = 6D$. The computational mesh shown in Figure 5.1 consists of 1.2×10^7 elements for the single diaphragm case, whereas for the tandem diaphragms case, 1.55×10^7 elements are utilized.

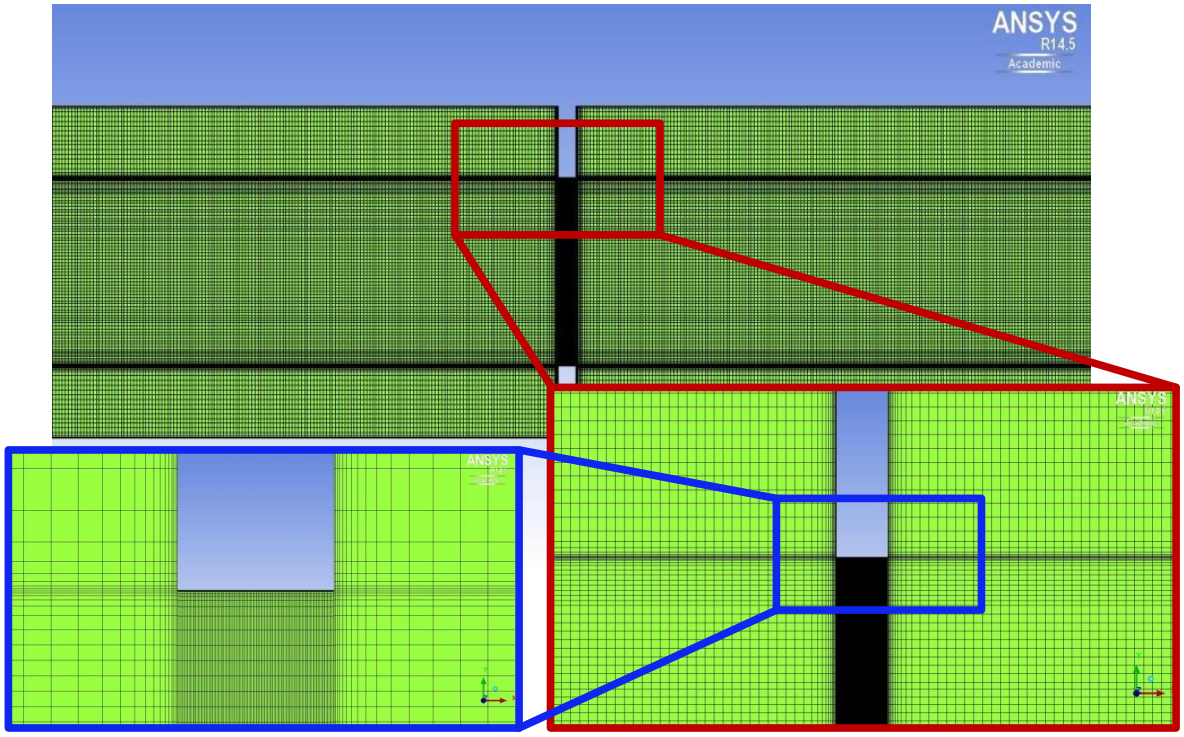

Figure 5.1: The LES mesh used in the thesis.

Both meshes consist of hexahedral elements structured according to an O-grid topology around the diaphragm. The grid is refined in radial direction with element sizes of the order of the Taylor microscale, λ which is calculated as;

$$\lambda = \sqrt{10}\eta^{2/3} l^{1/3}, \tag{5.5}$$

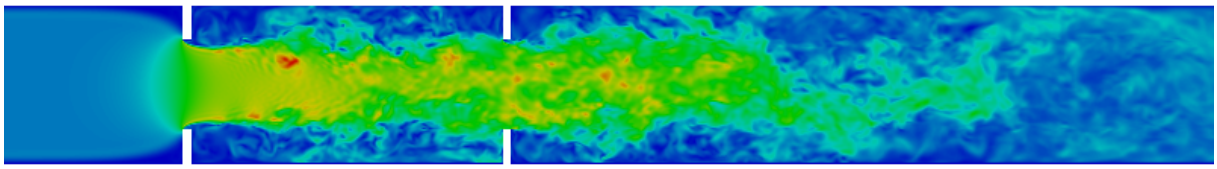

Figure 5.2: Instantaneous velocity field obtained from the LES computation.

where l is the integral length scale which can be predicted as $0.25D$ (Bailey et al. [6]) and η is the Kolmogorov length scale define as;

$$\eta = \left(\frac{\nu^3}{\epsilon}\right)^{1/4}. \tag{5.6}$$

This choice resolves the inertial turbulent scales, whereas the viscous scales are handled by means of the WALE sub-grid scale model. In order to accurately capture the turbulence generated noise, the boundary layer developed at the diaphragms is resolved. This is done by further refining the computational grid to have the first cell near the wall in the viscous sublayer; i.e. for a radial unit wall $r^+ = 5$. The simulations are carried out assuring the acoustic reflections to be as small as possible at the boundaries. Therefore the boundary conditions adopted consist of a modified version of the Navier-Stokes Characteristic Boundary Conditions (NSCBCs) [64] based on the so called Plane Wave Masking (PWM) method [65]. In PWM method, the acoustic plane waves computed in time domain using the 'characteristic based filtering' (see Section 7.1.1) are canceled out at the boundaries by imposing the opposite of the waves. The wall boundary is described by an adiabatic no-slip condition. At the inlet a constant velocity profile of $U = 6$ m/s is assumed, whereas at the outlet, a constant standard pressure $P = 101,325$ Pa is imposed. For the mean flow parameters to have converged values, the simulations were conducted throughout a one-duct-through flow. The flow data is stored with a sampling frequency of 12,500 Hz for 5,000 time steps in both single and tandem diaphragm cases. Any LES data is processed as segments of 1,000 time steps and converted to frequency domain using 1,024 FFT points. Fig. 5.2 depicts an instantaneous velocity field obtained from the LES analysis for the tandem diaphragm configuration.

5.2 Reynolds Averaged Navier-Stokes simulations

The mean flow parameters of the single and tandem diaphragm configurations were predicted with axisymmetric RANS simulations. The simulations were carried out using the commercial flow solver ANSYS Fluent v.18. The standard $k-\epsilon$ model and six low-Re $k-\epsilon$ models provided in the commercial solver were tested. The models tested in the thesis are linear, i.e. a linear relation is assumed to predict eddy viscosity:

$$\nu_t = C_\mu f_\mu \frac{k^2}{\epsilon}, \tag{5.7}$$

where c_μ is the model constant, f_μ is a damping function, and $\tilde{\epsilon} = \epsilon - D$. The generic form of transport equations for turbulent scalars are given as follows:

$$\frac{\partial k}{\partial t} + \frac{\partial k U_i}{\partial x_i} = \frac{\partial}{\partial x_j}\left[\left(\nu + \frac{\nu_t}{\sigma_k}\right)\frac{\partial k}{\partial x_j}\right] + P_k - (\epsilon - D), \tag{5.8}$$

$$\frac{\partial \epsilon}{\partial t} + \frac{\partial \epsilon U_i}{\partial x_i} = \frac{\partial}{\partial x_j}\left[\left(\nu + \frac{\nu_t}{\sigma_\epsilon}\right)\frac{\partial \epsilon}{\partial x_j}\right] + C_{\epsilon_1} f_1 \frac{\epsilon}{k} P_k - C_{\epsilon_2} f_2 \frac{\epsilon^2}{k} + E. \tag{5.9}$$

where P_k is the shear production of the turbulent kinetic energy defined as;

$$P_k = \nu_t S^2; \tag{5.10}$$

given that S is the mean strain rate tensor. The closure relations contain five model constants: C_μ, C_{ϵ_1}, C_{ϵ_2}, σ_k and σ_ϵ. The terms f_μ, f_1 and f_2 are damping functions. There are also two additional terms, D and E which do not show up in the standard formulation of $k-\epsilon$ model. The values assigned to the model constants, damping functions and additional terms differ from model to model. Model parameters are tabulated in Table 5.1. For low-Re $k-\epsilon$ models, the damping functions tend to 1, and the additional terms to zero away from the wall, recovering the standard formulation. There are a couple terms used to construct the damping functions: $Re_t = k^2/(\nu\epsilon)$, $Re_k = rk^{1/2}/\nu$, where r is the radial distance from the wall, and $y^* = u_\epsilon y/\nu$ where $u_\epsilon = (\nu\epsilon)^{1/4}$.

The 2-dimensional mesh for the single diaphragm case used in RANS simulations is shown in Figure 5.3. The domain length extends over $6D$ at the inlet section, and $13D$ at the downstream section. The mesh consisted of around 7×10^4 elements for the single diaphragm case, and around 9×10^4 elements for the tandem diaphragm case. The mesh was constructed to resolve the boundary, satisfying $y^+ < 1$ for all the duct surfaces. Uniform velocity inlet boundary condition was imposed on the inlet. The outlet boundary condition was set as pressure outlet with zero gauge pressure. Pressure and velocity equations were solved in coupled mode. Second order schemes were used for all the flow variables.

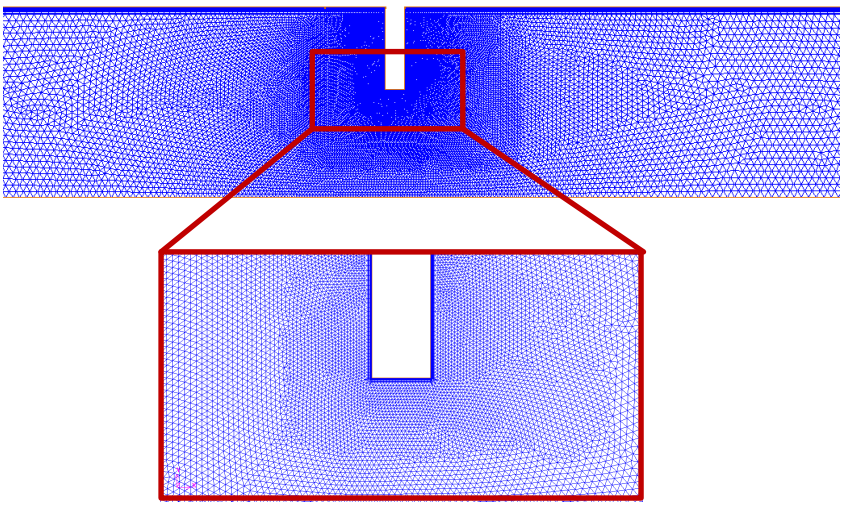

Figure 5.3: The 2D mesh used in the axiysmmetric RANS analyses.

The mean velocity fields obtained from the LES and RANS simulation are compared against the hot-wire measurements in Figures A.1, A.2, A.3 and A.4 at the measurement locations

depicted in Figure 3.22. The LES results showed good agreement with the experiments for both single and double diaphragm cases. The standard $k-\epsilon$ model failed to predict the velocity profile in both the configurations. The low-Re $k-\epsilon$ models yielded similar results except the YS model. Ab, AKN, CHC, LB, and LS models all satisfactorily predicted the velocity for the single diaphragm case, although some discrepancies were observed at tandem diaphragms case.

The turbulent kinetic distributions provided by variants of $k-\epsilon$ model are compared against the LES predictions in Figure A.5 and A.6 for the single and the tandem diaphragm configurations, respectively. The first five low-Re $k-\epsilon$ models (in alphabetical order) give similar turbulent kinetic energy distributions for both configurations, like the flow velocity predictions. All the models underpredict the turbulent kinetic energy production in the shear layer, and face 'stagnation point anomaly' at the upstream face of the downstream diaphragm. The low-Re $k-\epsilon$ models neither include production limiters, nor are realizable, and therefore are prone to produce non-physical kinetic energy. The zone where turbulent kinetic energy is maximum, on the other hand, was fairly predicted by the first five low-Re $k-\epsilon$ methods, which indicates that the transport of the kinetic energy was properly handled. The reason for YS model yielding results closer to the standard model rather than the low-Re $k-\epsilon$ models is considered to be due to the extremely small terms in the wall damping function. Probably because of stability issues, the model could be tuned to immediately behave like the standard model for not so low-Re number flows.

Table 5.1: Model constants and functions in different low-Re $k-\epsilon$ models

Model	C_μ	C_{ϵ_1}	C_{ϵ_2}	σ_k	σ_ϵ
Std	0.09	1.44	1.92	1.0	1.3
Abid	0.09	1.45	1.83	1.0	1.4
AKN	0.09	1.50	1.90	1.4	1.3
CHC	0.09	1.44	1.92	1.0	1.3
LB	0.09	1.44	1.92	1.0	1.3
LS	0.09	1.44	1.92	1.0	1.3
YS	0.09	1.44	1.92	1.0	1.3

Model	f_μ	f_1	f_2
Std	1.0	1.0	1.0
Abid	$\tanh(0.008Re_k)\left(1+\frac{4}{Re_t^{3/4}}\right)$	1.0	$1-\frac{2}{9}e^{-Re_t/36}(1-e^{-Re_t/12})$
AKN	$(1-e^{-y^*/14})^2$ $\times(1+\frac{5}{Re_t^{3/4}}e^{-(Re_t/200)^2})$	1.0	$(1-e^{-y^*/3.1})^2$ $\times(1+0.3e^{-(Re_t/6.5)^2})$
CHC	$(1-e^{-0.0215Re_k})^2$ $\times\left(1+\frac{31.66}{Re_t^{5/4}}\right)$	1.0	$(1-0.01e^{-Re_t^2})$ $\times(1-e^{-0.0631Re_k})$
LB	$(1-e^{-0.0165Re_k})^2$ $\times\left(1+\frac{20.5}{Re_t}\right)$	$1+\left(\frac{0.05}{f_\mu}\right)^3$	$1-e^{-Re_t^2}$
LS	$e^{-3/4(1+Re_t/50)^2}$	1.0	$1-0.3e^{-Re_t^2}$
YS	$(1+1/\sqrt{Re_t})(1-e^{-1.5\times10^{-4}Re_k}$ $\times e^{-5.0\times10^{-7}Re_k^3-1.0\times10^{-10}Re_k^5})$	$\frac{\sqrt{Re_t}}{1+\sqrt{Re_t}}$	$\frac{\sqrt{Re_t}}{1+\sqrt{Re_t}}$

Model	D	E	ϵ_W-B.C.
Std	0	0	Wall functions
Abid	0	0	$\nu\frac{\partial^2 k}{\partial r^2}$
AKN	0	0	$2\nu\left(\frac{\partial\sqrt{k}}{\partial r}\right)^2$
CHC	0	0	$\nu\frac{\partial^2 k}{\partial r^2}$
LB	0	0	$\nu\frac{\partial^2 k}{\partial r^2}$
LS	$2\nu\left(\frac{\partial\sqrt{k}}{\partial r}\right)^2$	$2\nu_t\nu\left(\frac{\partial^2 u}{\partial r^2}\right)^2$	0
YS	0	$\nu_t\nu\left(\frac{\partial^2 u}{\partial r^2}\right)^2$	$\nu\frac{\partial^2 k}{\partial r^2}$

6 Tailored Green's function for ducts with diaphragms

6.1 Introduction

In hybrid approaches, propagation of noise is treated subsequent to the computation of the noise sources inside the domain. The method to be used for noise propagation depends on the problem, since the noise propagation is affected by mean flow. Acoustics waves are convected with the mean flow and they go under refraction when a non-uniformity of the flow is encountered. For high-Mach number and/or highly non-uniform flows, these effects becomes non-negligible. Flow noise around/emitted by aircrafts, jet noise, etc. are examples to this type of noise problems. In such cases, it is convenient to use Linearized Euler Equations (LEE), or alternatively Acoustic Perturbation Equations (APE) [22], which account for the mean flow effects.

Contrarily, mean flow effects may be neglected for low Mach number flows, which makes methods based on wave propagation/Helmholtz equation applicable. A Green's function is used to solve the inhomogeneous equation. These approaches offer a relatively simple and significantly cheaper solution so that they are widely used in the industrial aeroacoustic applications. An important problem related to the Green's function approach is to calculate the scattering of the noise from the boundaries. For most cases, a numerical approach such as 'Finite Element' (FEM) and 'Boundary Element Methods' (BEM), is to be adopted to take into account the scattering due to the arbitrarly shaped surfaces contained in the flow domain. In some particular cases, however, an analytical solution is possible for relatively simple geometries, such as ducts with simple cross-sections, infinite planes etc. In this thesis, the noise propagation problem is solved through the derivation of a tailored Green's function including the scattering effects of the cylindrical duct and of the single/tandem diaphragm(s). While the Green's function of the cylindrical straight duct is found in classical text books (see e.g. Rienstra and Hirschberg [72] for zero and uniform mean flows, Sodha *et al.* [89] and Willatzen [97] for non-uniform mean flows), the contribution of ducted singularities to the Green's function has been more scarcely tackled in the literature. van Herpe and Crighton [28] treated the two-dimensional slit diaphragm case, but to the author's knowledge the axisymmetric solution for a tandem diaphragm was not reported at the time when this problem was investigated. A mode-matching technique proposed by Rienstra [71, 73] is here combined with a recursive summation of the reflected waves between the two diaphragms to obtain the compound duct-tandem-diaphragm Green's function. The proposed method is, of course, limited to low Mach number flows as the mean flow effects are not accounted for.

6.2 Single Diaphragm Case

The pressure at the position $\mathbf{x}(\vartheta, r, x)$ due to a right-going wave inside a cylindrical duct can be defined using a modal representation as follows:

$$p(\mathbf{x}) = \sum_{m=-\infty}^{\infty} \sum_{\mu=1}^{\infty} A_{m\mu} U_{m\mu}(r) e^{-ik_{m\mu}x - im\vartheta}, \tag{6.1}$$

where $A_{m\mu}$ denotes the amplitude of the corresponding mode, the exponential term defines the phase based on the azimuthal and the axial modes, and $U_{m\mu} \equiv N_{m\mu} J_m(\alpha_{m\mu} r)$ is the orthonormal radial component satisfying:

$$\begin{aligned} \langle U_{m\nu}, U_{m\mu} \rangle = \int_0^a U_{m\nu}(r) U_{m\mu}(r) r dr = 1, \quad \mu = \nu, \\ = 0, \quad \mu \neq \nu. \end{aligned} \tag{6.2}$$

The term J_m represents the ordinary Bessel function of the first kind and $\alpha_{m\mu}$ corresponds to the μ^{th} non-trivial zero of $J'_m(\varphi)$ where the prime denotes the first derivative with respect to φ. Please note that the initial value of α is set as 0, corresponding to the plane wave region. Calculating the integral in Eq. (6.2), the normalization constant $N_{m\mu}$ is obtained as:

$$N_{m\mu} = \left[\frac{1}{2} (a^2 - \frac{m^2}{\alpha_{m\mu}^2}) J_m^2(\alpha_{m\mu} a) \right]^{-1/2}. \tag{6.3}$$

The Green's function for cylindrical ducts given in Eq. (2.77) can be written in the form of Eq. (6.1) by defining the amplitude term $A_{m\mu}$ as:

$$A_{m\mu} = \frac{U_{m\mu}(\alpha_{m\mu} r_0) e^{ik_{m\mu}x_0 - m\vartheta_0}}{k_{m\mu}}. \tag{6.4}$$

In case of a discontinuity along the duct, the pressure wave induced by a point source is scattered as it passes through the discontinuity. Figure 6.1 schematically represents such a scattering of the incident wave, p_{inc}^{+} generated from a point source, located at the upstream position $\mathbf{x}_0$, into the reflected and transmitted waves, p_{ref} and p_{tra}.

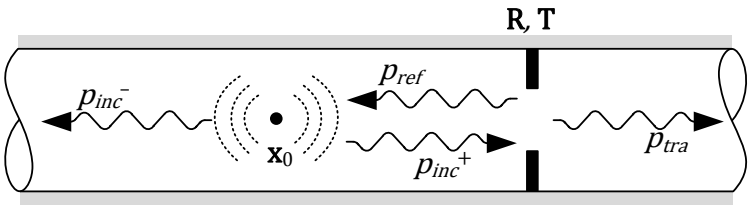

Figure 6.1: Scattering of an incident wave passing through a ducted diaphragm.

This scattering mechanism corresponds to a transfer of energy between the acoustic modes, which can be represented by a matrix with unit determinant scaling the mode amplitudes. If the discontinuity is axisymmetric, like the circular diaphragm case, the scattering occurs only

between the radial modes; i.e. no transition of energy among the azimuthal modes, which allows treating each azimuthal mode separately. In such a case, the amplitude scaling of Green's function corresponding to a single azimuthal mode can be defined on the reflection and the transmission sides by:

$$G_{\omega m,ref} = \sum_{\mu=1}^{\infty} B_{m\mu} U_{m\mu} e^{i(\pm k_{m\mu} x - m\vartheta)}, \tag{6.5}$$

$$G_{\omega m,tr} = \sum_{\mu=1}^{\infty} C_{m\mu} U_{m\mu} e^{i(\mp k_{m\mu} x - m\vartheta)}, \tag{6.6}$$

where

$$B_{m\mu} = \sum_{\nu=1}^{\infty} R_{m\mu\nu} A_{m\nu} \rightarrow \mathbf{B} = \mathbf{RA}, \tag{6.7}$$

and

$$C_{m\mu} = \sum_{\nu=1}^{\infty} T_{m\mu\nu} A_{m\nu} \rightarrow \mathbf{C} = \mathbf{TA}. \tag{6.8}$$

The matrices **R** and **T** define the scaling of the mode amplitudes on the reflection and the transmission sides, respectively. The classical mode matching technique explained in [73] for the specific case of a single diaphragm is revisited in the present study to determine these matrices. The method is based on the continuity of pressure and axial velocity; i.e. the partial derivative of pressure with respect to x, at the interface of the discontinuity which is the diaphragm in the present case. The thickness of the diaphragm is assumed to be zero as it is acoustically compact along the axial direction within the given frequency range of interest. Considering the linearity of the problem, the scattering of a single μ-mode is investigated only. Given a cylindrical duct with an infinitely thin diaphragm of radius b at the axial position $x = D$, and a point source of unit strength upstream the diaphragm, the continuity of pressure and axial velocity at the diaphragm section for the radial zone $0 < r < b$ yields respectively;

$$\sum_{\nu=1}^{\infty} (R_{m\mu\nu} A_{m\nu} e^{ik_{m\nu}D} + A_{m\nu} e^{-ik_{m\nu}D}) U_{m\nu} = \sum_{\nu=1}^{\infty} T_{m\mu\nu} A_{m\nu} U_{m\nu} e^{-ik_{m\nu}D}, \tag{6.9}$$

$$\sum_{\nu=1}^{\infty} k_{m\nu} (R_{m\mu\nu} A_{m\nu} e^{ik_{m\nu}D} - A_{m\nu} e^{-ik_{m\nu}D}) U_{m\nu} = \sum_{\nu=1}^{\infty} -k_{m\nu} T_{m\mu\nu} A_{m\nu} U_{m\nu} e^{-ik_{m\nu}D}. \tag{6.10}$$

It is not possible to derive unique expressions for **R** and **T** using Eq. (6.9) and (6.10) as no proper boundary condition is defined for the edge of the diaphragm [72]. However, considering the physical fact that the scattering should be independent of the source amplitude, a possible solution for the scattering problem can be obtained through the following equations:

$$\sum_{\nu=1}^{\infty} (R_{m\mu\nu} e^{ik_{m\nu}D} + e^{-ik_{m\nu}D}) U_{m\nu} = \sum_{\nu=1}^{\infty} T_{m\mu\nu} U_{m\nu} e^{-ik_{m\nu}D}, \tag{6.11}$$

$$\sum_{\nu=1}^{\infty} k_{m\nu} (R_{m\mu\nu} e^{ik_{m\nu}D} - e^{-ik_{m\nu}D}) U_{m\nu} = \sum_{\nu=1}^{\infty} -k_{m\nu} T_{m\mu\nu} U_{m\nu} e^{-ik_{m\nu}D}. \tag{6.12}$$

Assuming the diaphragm as a separate duct section with zero axial length, Green's function for a single μ-mode at the diaphragm location; i.e. $x = D$, can be written as;

$$G_{\omega m\mu,tr} = \sum_{\nu=1}^{\infty} T^*_{m\nu\mu} A_{m\nu} \hat{U}_{m\nu} e^{i(\mp l_{m\nu} x - m\vartheta)}, \tag{6.13}$$

where $l_{m\mu}$ and $\hat{U}_{m\mu}$ are the reduced wave number and the corresponding normalized radial component for the diaphragm section, respectively, and $T^*_{m\mu\nu}$ is the auxiliary coefficient. Then a similar relation can be established between the diaphragm and any of the duct sections based on the continuity of velocity and pressure. On the transmission side; i.e. $x = D^+$, for the radial zone, $0 < r < b$ the continuity of velocity yields;

$$\sum_{\nu=1}^{\infty} -l_{m\nu} T^*_{m\mu\nu} \hat{U}_{m\nu} e^{-il_{m\nu}D} = \sum_{\nu=1}^{\infty} -k_{m\nu} T_{m\mu\nu} U_{m\nu} e^{-ik_{m\nu}D}. \tag{6.14}$$

Please note that, using Eq. (6.11), (6.12) and (6.14), it is possible to obtain algebraic expressions for the matrices **R** and **T**, which also satisfy Eq. (6.9) and (6.10). Since the velocities on both surfaces of the diaphragm ($b < r < a$) are zero, the interval for the continuity of velocity expressed in Eq. (6.12) can be extended to the entire cross-section. Then, taking the inner product with the basis function $U_{m\lambda}$; i.e. multiplying with $U_{m\lambda} r$ and taking the integral along the duct radius as shown in Eq. (6.2), Eq. (6.12) can be reduced to the following equation in matrix form:

$$\mathbf{E}^+ \mathbf{R} - \mathbf{E}^- = -\mathbf{E}^- \mathbf{T}, \tag{6.15}$$

where $\mathbf{E}^{\pm} \equiv \delta_{\lambda\nu} e^{\pm ik_{m\lambda}D}$. Using the above expression to replace the reflection term in Eq. (6.11) and taking the inner product with the basis function $\hat{U}_{m\lambda}$, we obtain:

$$\sum_{\nu=1}^{\infty} \langle \hat{U}_{m\lambda}, U_{m\nu} \rangle_b e^{-ik_{m\nu}D} = \sum_{\nu=1}^{\infty} \langle \hat{U}_{m\lambda}, U_{m\nu} \rangle_b e^{-ik_{m\nu}D} T_{m\nu\mu}, \tag{6.16}$$

or in matrix form:

$$\mathbf{M}\mathbf{E}^- = \mathbf{M}\mathbf{E}^- \mathbf{T}, \tag{6.17}$$

where $\mathbf{M} \equiv \langle \hat{U}_{m\lambda}, U_{m\nu} \rangle_b$. Similarly, taking the inner product of Eq. (6.14) with the basis function $U_{m\lambda}$, it is obtained at $x = D^+$:

$$\sum_{\nu=1}^{\infty} \langle U_{m\lambda}, \hat{U}_{m\nu} \rangle_b l_{m\nu} e^{-il_{m\nu}D} T^*_{m\nu\mu} = k_{m\lambda} e^{-ik_{m\lambda}D} T^*_{m\lambda\mu} \quad , 0 < r < b, \tag{6.18}$$

which can again be written in matrix form as:

$$\mathbf{M}^\top \mathfrak{T}^* = \mathbf{K}\mathbf{E}^- \mathbf{T}, \tag{6.19}$$

where $\mathfrak{T}^*$ denotes all the terms related to the auxiliary coefficient and $\mathbf{K} \equiv \delta_{\lambda\nu} k_{m\lambda}$. Multiplying both sides of Eq. (6.19) with $\mathbf{M}\mathbf{K}^{-1}$ to have:

$$\mathbf{M}\mathbf{K}^{-1}\mathbf{M}^\top \mathfrak{T}^* = \mathbf{M}\mathbf{E}^- \mathbf{T}, \tag{6.20}$$

and using Eq. (6.17) to replace the right hand side of Eq. (6.20), $\mathfrak{T}^*$ is obtained as follows:

$$\mathfrak{T}^* = (\mathbf{M}\mathbf{K}^{-1}\mathbf{M}^\top)^{-1} \mathbf{M}\mathbf{E}^-. \tag{6.21}$$

Then substituting this expression in Eq. (6.19), the final expression for the transmission coefficient is derived as:

$$\mathbf{T} = \mathbf{E}^{+}\mathbf{K}^{-1}\mathbf{M}^{\top}(\mathbf{M}\mathbf{K}^{-1}\mathbf{M}^{\top})^{-1}\mathbf{M}\mathbf{E}^{-}. \tag{6.22}$$

Once the transmission matrix is derived, the reflection matrix, $\mathbf{R}$ can easily be calculated from Eq. (6.15). As mentioned before, the solution given in Eq. (6.22) is not unique; hence, may cause convergence problems while truncating the infinite series U_λ and $\hat{U}_\lambda$. To overcome this issue, it is suggested in [57] that the lengths of the truncated series should be proportional to the diameter ratio between the duct and the diaphragm; i.e. for $\mathbf{M}_{P\times Q}$, $P/Q \approx b/a$ should be satisfied.

6.3 Extension of the tailored Green's function for the tandem diaphragm case

As discussed in the previous subsection, any wave passing through a ducted diaphragm is scattered into a reflected and a transmitted wave. In case of a tandem diaphragm configuration, the acoustic wave is subjected to an infinite loop of reflections between the two diaphragms as it encounters either of them.

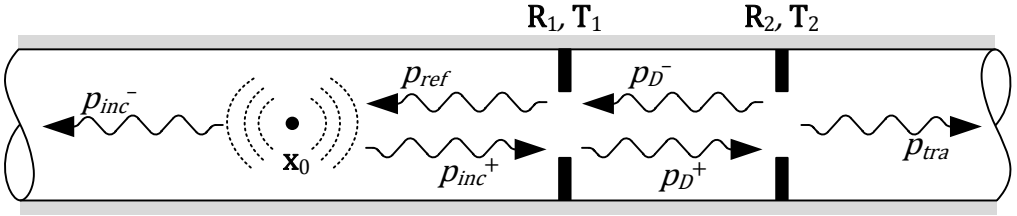

Figure 6.2: Scattering of an incident wave passing through ducted tandem diaphragms.

Considering the case shown in Figure 6.2 where the two diaphragms with reflection/transmission matrices, $\mathbf{R}_{1,2}$/$\mathbf{T}_{1,2}$, are installed in an infinite duct with a point source located upstream, these infinitely many reflections sum up to cumulative right-/left-going waves, $p_D^{\pm}$.

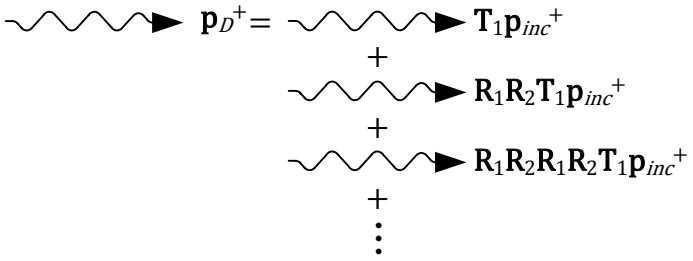

Figure 6.3: Decomposition of the cumulative right-going wave.

Taking the cumulative right-going wave, p_D^+ as an example, the summation of the infinitely many reflected waves can be described explicitly as shown in Figure 6.3. This explicit summa-

tion can be formulated as:

$$p_D^+ = (\mathbf{I} + \mathbf{R}_1\mathbf{R}_2 + \mathbf{R}_1\mathbf{R}_2\mathbf{R}_1\mathbf{R}_2 + \cdots)\mathbf{T}_1 p_{inc}^+, \tag{6.23}$$

where the infinite summation term can be reorganized to have a recursive form as follows:

$$(\mathbf{I} + \mathbf{R}_1\mathbf{R}_2 + \mathbf{R}_1\mathbf{R}_2\mathbf{R}_1\mathbf{R}_2 + \cdots) = \Big(\mathbf{I} + \mathbf{R}_1\mathbf{R}_2\big(\mathbf{I} + \mathbf{R}_1\mathbf{R}_2(\mathbf{I} + \cdots)\big)\Big). \tag{6.24}$$

Recursive summations of this kind can be treated using the mathematical induction method:

$$\begin{aligned} z &= \Big(\mathbf{I} + \mathbf{R}_1\mathbf{R}_2\big(\mathbf{I} + \mathbf{R}_1\mathbf{R}_2(\mathbf{I} + \cdots)\big)\Big), \\ z &= (\mathbf{I} + \mathbf{R}_1\mathbf{R}_2 z), \\ (\mathbf{I} - \mathbf{R}_1\mathbf{R}_2 z) &= \mathbf{I}, \\ z &= (\mathbf{I} - \mathbf{R}_1\mathbf{R}_2)^{-1}. \end{aligned} \tag{6.25}$$

Substituting Eq. (6.25) into Eq. (6.23), the following expression can be obtained for the cumulative right-going wave;

$$p_D^+ = (\mathbf{I} - \mathbf{R}_1\mathbf{R}_2)^{-1}\mathbf{T}_1 p_{inc}^+. \tag{6.26}$$

Finding an explicit expression for the cumulative waves in between the diaphragms, the reflection and the transmission matrices corresponding to the tandem diaphragm case, $\mathbf{R}_{TD}$ and $\mathbf{T}_{TD}$, respectively, can be written in terms of $\mathbf{R}_{1,2}$ and $\mathbf{T}_{1,2}$:

$$\mathbf{R}_{TD} = \mathbf{R}_1 + \mathbf{T}_1(\mathbf{I} - \mathbf{R}_1\mathbf{R}_2)^{-1}\mathbf{R}_2\mathbf{T}_1, \tag{6.27}$$

$$\mathbf{T}_{TD} = \mathbf{T}_2(\mathbf{I} - \mathbf{R}_1\mathbf{R}_2)^{-1}\mathbf{T}_1. \tag{6.28}$$

It is obvious that the reflection matrices $\mathbf{R}_{TD}$ and $\mathbf{T}_{TD}$ correspond to the listener points upstream and downstream the diaphragms, respectively for the current case where the source is located upstream. When the source is located in between the diaphragms, the same procedure should be followed for the right- and left-going incident waves, separately. Considering a listener point positioned upstream the diaphragms, the reflection matrix $\mathbf{R}_{TD}$ corresponding to the right-going incident wave, p_{inc}^+ due to a source in between the diaphragms is formulated by:

$$\mathbf{R}_{TD} = \mathbf{T}_1(\mathbf{I} - \mathbf{R}_2\mathbf{R}_1)^{-1}\mathbf{R}_2. \tag{6.29}$$

Similarly, the transmission matrix $\mathbf{T}_{TD}$ corresponding to the left-going incident wave, p_{inc}^- is written as:

$$\mathbf{T}_{TD} = \mathbf{T}_1(\mathbf{I} - \mathbf{R}_2\mathbf{R}_1)^{-1}. \tag{6.30}$$

6.4 Numerical validation of the tailored Green's function

To validate the tailored Green's function and to point out the necessity for such an analytical approach, it is compared to the commercial solver LMS Virtual Lab Rev. 13. A test quadrupole

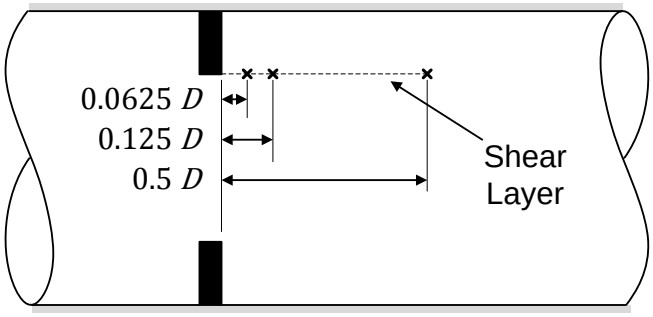

Figure 6.4: Schematic representation of the test source positions on the shear layer.

has been placed at different positions, which are selected to be within the estimated shear layer downstream the diaphragm as depicted in Figure 6.4.

The far-field acoustic pressure induced by the test quadrupole has been computed for each position, using both the numerical solver with two different meshes of 30 and 60 elements per wavelength at 1 kHz, respectively, and the tailored Green's function. In the numerical computations, the Finite Element Method option with constant second order spatial discretization scheme has been adopted to solve the Helmholtz equation. The computation time required for the numerical method per frequency is 11 CPU sec and 90 CPU sec for the fine and coarse mesh cases, respectively, while it is 0.0017 CPU sec for the analytical method.

It is observed at the top of Figure 6.5 that the analytical solution of the tailored Green's function for single diaphragm matches the numerical results with mesh convergence obtained for the source location 0.5 D. Placing the source closer to the diaphragm, the numerical solver starts overestimating the sound pressure level, especially in lower frequencies, as an indication of an insufficient mesh resolution. It should be noted that applying adaptive discretization schemes and local mesh refinement, more accurate solutions for the given source locations could have been obtained with the numerical solver. This was however not performed in this study, where the objective was mostly to validate the derivation of our specific tandem-diaphragm Green's function by means of a more general numerical approach. In the analytical method, the proximity of the sources with the diaphragm only affects the number of acoustic modes to be involved.

The verification of the tailored Green's function for tandem diaphragm is provided for a test source located in between, and downstream the diaphragms in the top and bottom plots of Figure 6.6, respectively. The test source is located off the duct axis by 0.25 D in both cases to avoid symmetry in the resulting acoustic fields. The axial positions mentioned in the figure legends have been given with respect to the upstream diaphragm.

6.5 No-flow scattering characteristics of the diaphragm

The scattering matrix of the diaphragm(s) when there is no flow is calculated using the two-port method similar to the experimental case investigated in Chapter 4. Considering the case shown in Figure 4.12 with zero flow velocity, the scattering behavior of both the single and tandem diaphragms are expected to be symmetric along the duct axis. The reflection and transmission

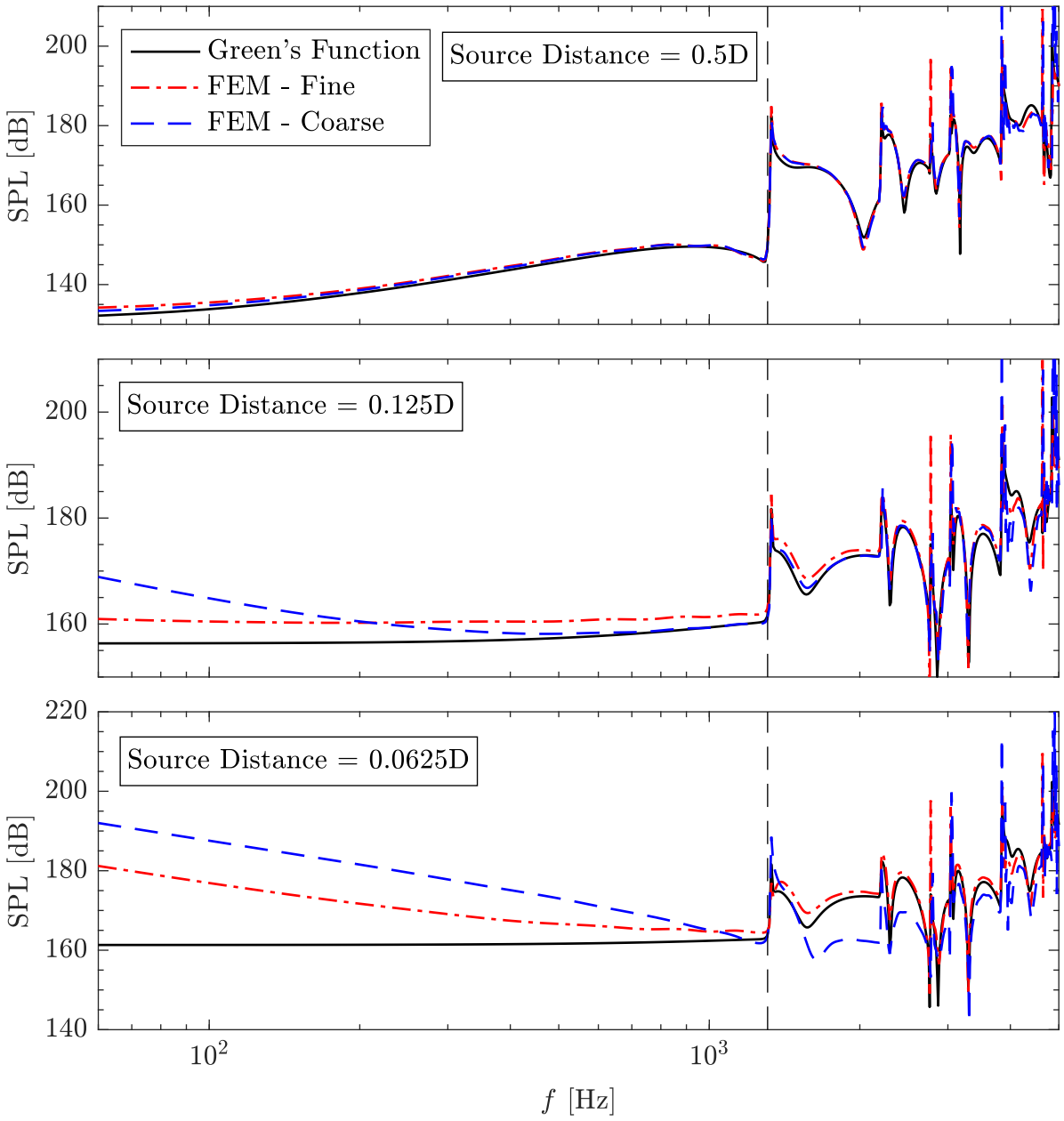

Figure 6.5: Comparison of the acoustic responses obtained from numerical solver with the tailored Green's function. The vertical dashed line indicates the first cut-off frequency.

matrices, $\mathbf{R}_{a,b}$ and $\mathbf{T}_{a,b}$ reduce to $\mathbf{R}$ and $\mathbf{T}$, respectively. Eq. (4.4) then becomes;

$$\begin{bmatrix} \mathbf{p}_a^+ \\ \mathbf{p}_b^+ \end{bmatrix} = \begin{bmatrix} \mathbf{R} & \mathbf{T} \\ \mathbf{T} & \mathbf{R} \end{bmatrix} \begin{bmatrix} \mathbf{p}_a^- \\ \mathbf{p}_b^- \end{bmatrix}. \tag{6.31}$$

The matrices $\mathbf{R}$ and $\mathbf{T}$ are calculated up to the 2$^{\text{nd}}$ azimuthal mode, which required 10 different load cases for $[\mathbf{p}_a \quad \mathbf{p}_b]^\top$ to be invertible. Different load cases are obtained by randomly placing a test source within the source zone shown in Figure 6.7, and calculating the acoustic response at the listeners on both sides of the diaphragm(s). 15 listeners are located at each of the listener zones, and the calculation is repeated for 15 different source positions, yielding an overdeter-

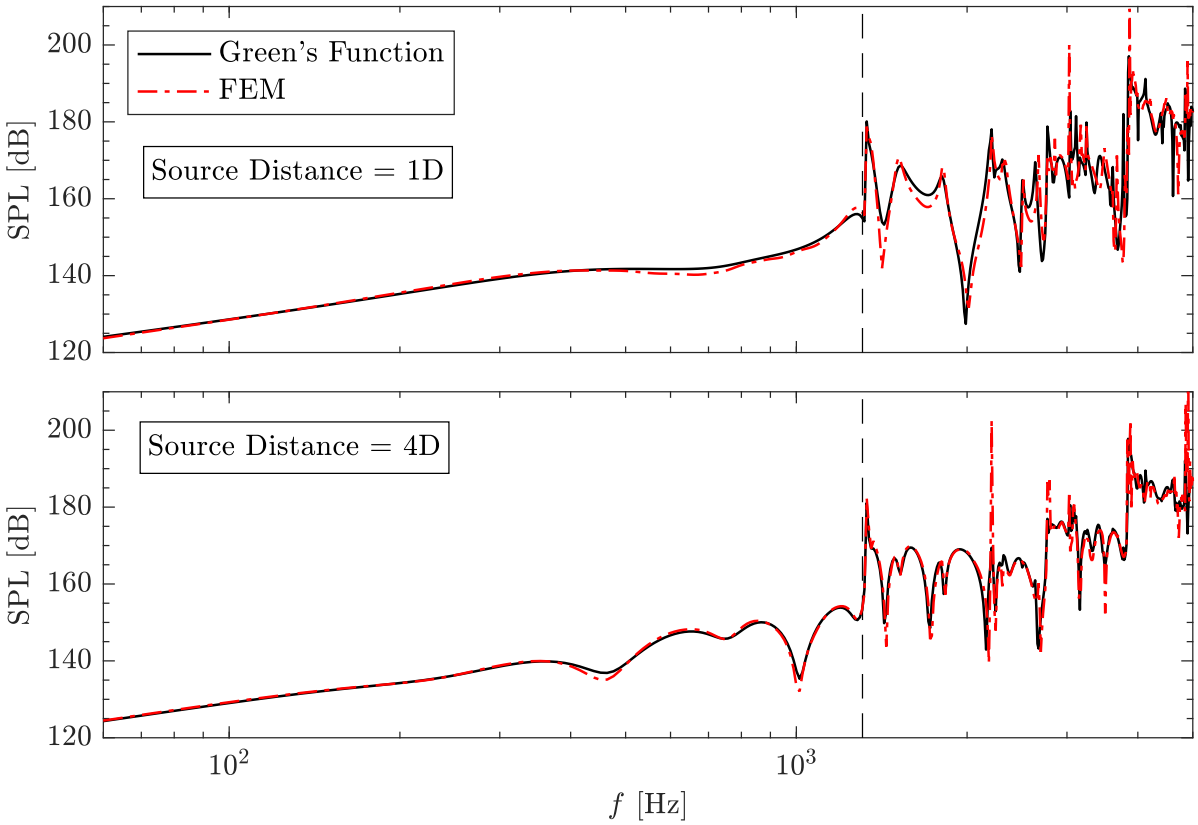

Figure 6.6: Comparison of the acoustic responses obtained from numerical solver with the tailored Green's function for tandem diaphragm case with the test source located in between (top) and downstream (bottom) the diaphragms. The vertical dashed line indicates the first cut-off frequency.

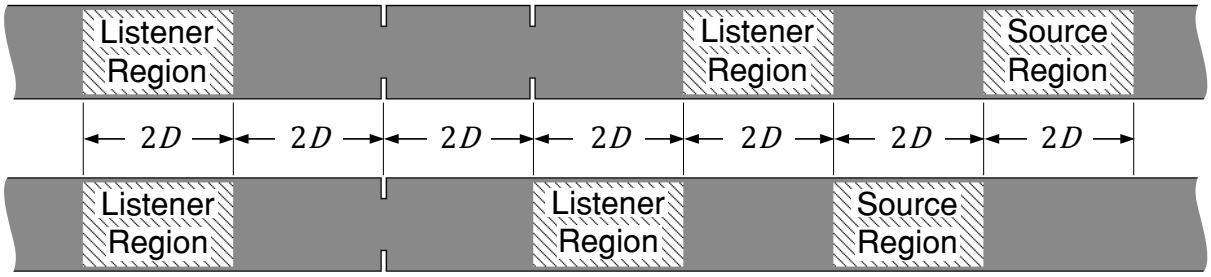

Figure 6.7: Source and listener zones defined for the system identification of the diaphragm(s).

mined system by a factor of 1.5. The source strength is defined to be constant over the frequency range with the value $1 + i1$ kg/ms^2. The acoustic response calculations are performed using the tailored Green's function for the single and tandem diaphragms. The resulting reflection and transmission coefficients up to the 1st azimuthal mode are plotted in Figures 6.8 and 6.9. The off-diagonal elements are observed to be zero as a result of the axisymmetry, and thereby are not shown in the plots.

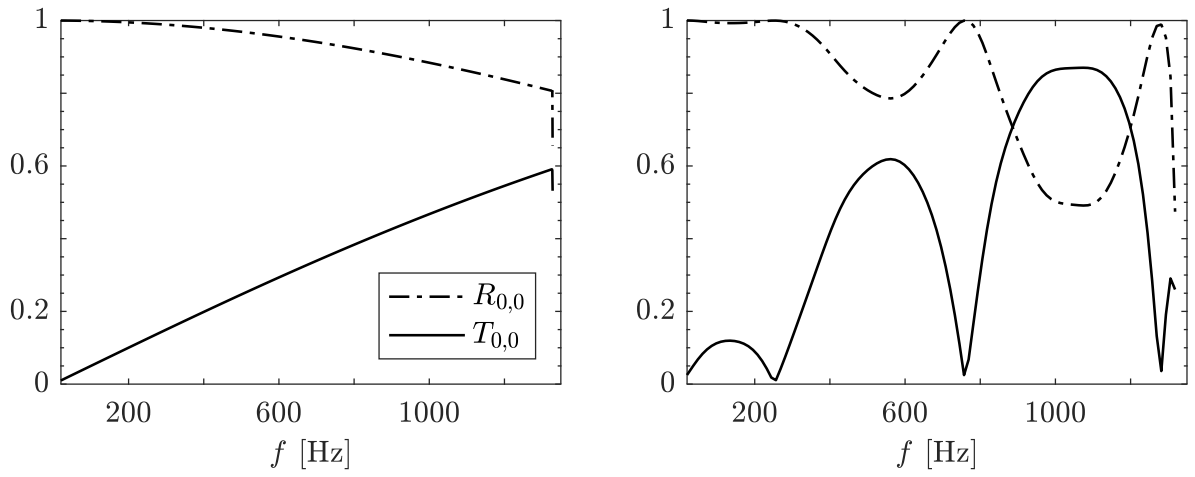

Figure 6.8: The reflection/transmission coefficient for the single (left) and the tandem (right) diaphragms for $m = 0$.

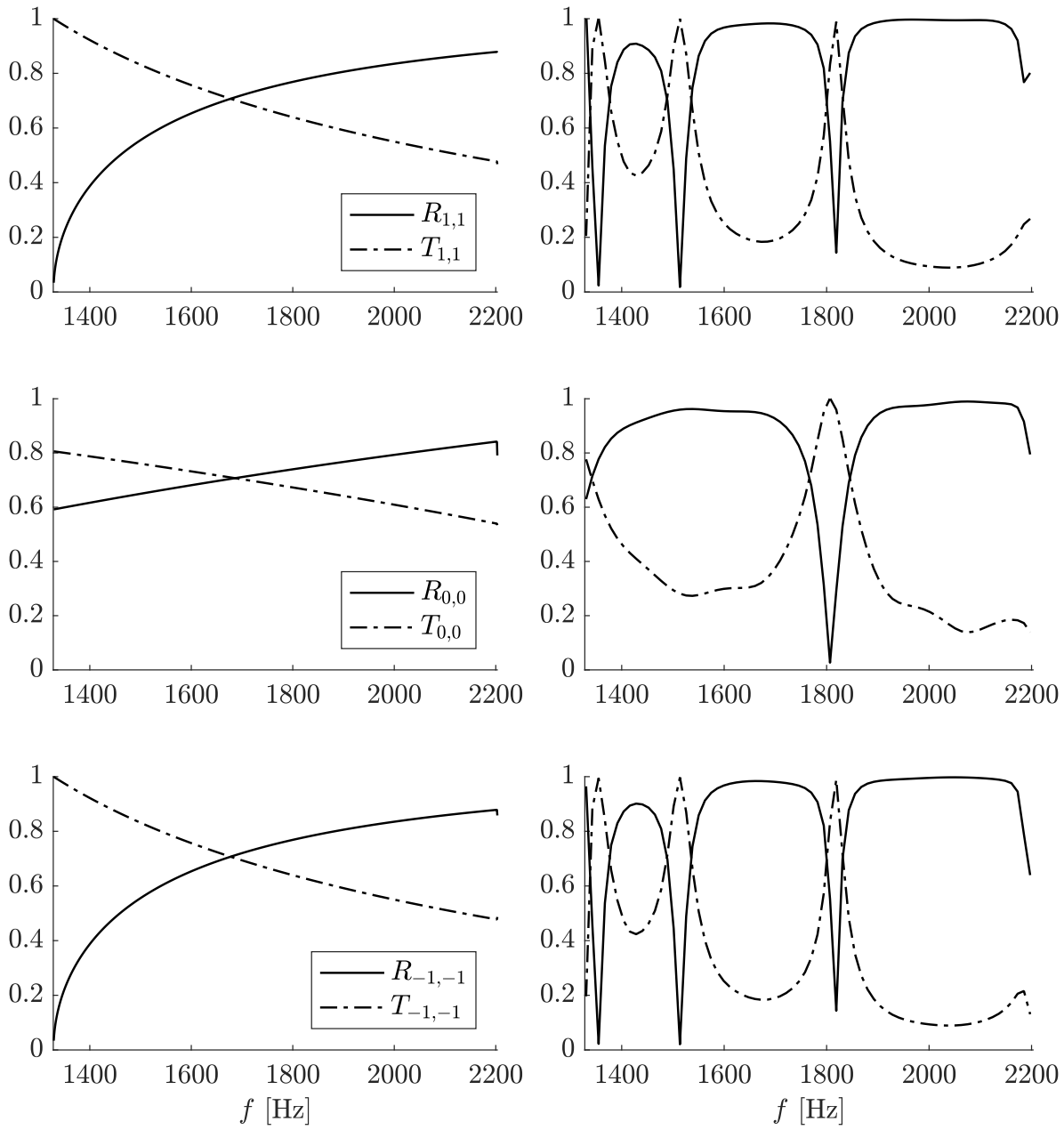

Figure 6.9: The reflection/transmission coefficient for the single (left) and the tandem (right) diaphragms for $m = 1$

7 Use of unsteady LES data for noise prediction

7.1 Noise prediction using compressible flow data

7.1.1 Characteristic Based Filtering method

To extract the acoustic field in the plane wave region from the LES calculations, a DNC method called *Characteristic Based Filtering* (CBF) is used. The method was proposed by Kopitz *et al.* [41] to provide non-reflecting boundary conditions in plane wave region for LES, and it is based on the order of magnitude difference in the correlation lengths and speed of propagation of the acoustic and the turbulent fields. The details of the method are given as follows.

In case of a left-to-right going flow with a mean velocity, U; the acoustic information is carried with the characteristic waves at a convection speed, $c_f = U + c_0$ for the right-going characteristic wave, f, and $c_g = U - c_0$ for the left-going characteristic wave, g. Considering the flow field obtained from the numerical simulation, the unsteady part which is easily computed by subtracting the mean can be written as the sum of the turbulent and the acoustic fields:

$$p = p_t + p', \tag{7.1}$$
$$u = u_t + u', \tag{7.2}$$

where p and u correspond to the unsteady pressure and velocity fields, respectively. The subindex 't' and the 'prime' denote the turbulent and the acoustic perturbations, respectively. The relations between the characteristic waves, and the acoustic perturbations are given by:

$$u' = f - g, \tag{7.3}$$
$$p' = \rho c_0 (f + g), \tag{7.4}$$

where ρ and c_0 are density and the speed of sound, respectively. The above equations can be reformulated to obtain the characteristic waves, f and g:

$$f = \frac{1}{2}\left(\frac{p'}{\rho c_0} + u'\right), \tag{7.5}$$
$$g = \frac{1}{2}\left(\frac{p'}{\rho c_0} - u'\right). \tag{7.6}$$

These waves are monitored at two different sections with axial positions, x_1 and $x_2 = x_1 + d$ (see

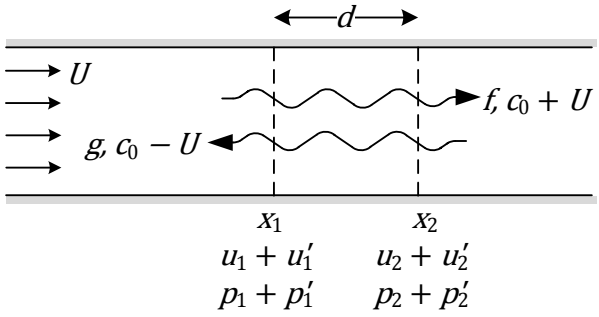

Figure 7.1: Characteristic waves traveling inside a duct with mean flow.

Figure 7.1), to have:

$$f(x_1|t) = f(x_2|t+\tau_f), \qquad \tau_f = \frac{d}{c_f}, \tag{7.7}$$

$$g(x_1|t) = g(x_2|t+\tau_g), \qquad \tau_g = \frac{-d}{c_g}. \tag{7.8}$$

At this point, two auxiliary variables in terms of the unsteady pressure, p and velocity, u are introduced in the form of the characteristic wave equation:

$$f^*(p,u) = \frac{1}{2}\left(\frac{p}{\rho c_0} + u\right), \tag{7.9}$$

$$g^*(p,u) = \frac{1}{2}\left(\frac{p}{\rho c_0} - u\right). \tag{7.10}$$

Please note that the auxiliary variables $f^*(p,u)$ and $g^*(p,u)$ can directly be obtained from the numerical flow field as they are defined in terms of the unsteady flow data. Eq. (7.1) and (7.2) implies that these auxiliary variables can also be written in terms of the acoustic and turbulent components of the unsteady flow data as $f^*(p',u',p_t,u_t)$ and $g^*(p',u',p_t,u_t)$. A time-shifted averaging of these auxiliary variables is performed over the two sections mentioned above to have $\langle f^*(x_1|t), f^*(x_2|t+\tau_f)\rangle$ and $\langle g^*(x_1|t), g^*(x_2|t+\tau_g)\rangle$. Since the characteristic wave equation is linear, this averaging can be applied to each of the arguments of f^* and g^*, separately. When the axial separation, d is sufficiently large, the turbulent components p_t and u_t become uncorrelated between the two sections. According to the statistics theory, averaging two uncorrelated signals yields a zero mean. Then, the time-shifted averaging of the auxiliary variables eliminates the turbulent contribution in the unsteady flow data, yielding approximate characteristic wave equations:

$$f \approx \langle f^*(x_1|t), f^*(x_2|t+\tau_f)\rangle, \tag{7.11}$$

$$g \approx \langle g^*(x_1|t), g^*(x_2|t+\tau_g)\rangle. \tag{7.12}$$

Once the characteristic waves are computed, the acoustic pressure and velocity can be retrieved using Eq. (7.3) and (7.4). It should be noted that the CBF method is only applicable in the plane wave region since the wave phase velocity becomes frequency dependent for the higher order modes, which prevents filtering the characteristic waves using time domain data. In the present analysis, the CBF method has been implemented locating four sections at each side

of the diaphragm(s) which are separated from each other by $0.5D$. The distance between the section planes has been selected to be greater than the integral time scale multiplied by the mean convection velocity for the turbulent structures to be uncorrelated. For the time-shifted averaging approach to be valid, the flow field enclosing the selected cross-sections is to be source-free. To ensure a source-free region, the distances between the diaphragm(s) and the nearest cross-sections at the upstream and downstream sections have been selected to be $3D$ and $5D$, respectively.

7.2 Noise prediction using the pressure distribution on the diaphragms

The dominant noise generation mechanism in ducted diaphragms is known to be the interaction between the diaphragm(s) and the turbulence around it [24, 56, 59, 81, 92]. To investigate the contribution of the diaphragms to the noise generation, a prediction method based on the surface pressure data over the diaphragms has been implemented. The method uses a variation of Curle's analogy [18] to model the noise generated by solid surfaces as dipoles, which then replace these surfaces.

Reconsidering the integral equation obtained in the derivation of Curle's analogy:

$$\rho'(\mathbf{x},t) = \int_{-\infty}^{t} \iiint_V T_{ij} \frac{\partial^2 G}{\partial y_i \partial y_j} \mathrm{d}^3\mathbf{y}\mathrm{d}\tau - \int_{-\infty}^{t} \iint_{\partial V} (p'\delta_{ij} - \sigma_{ij}) \frac{\partial G}{\partial y_j} n_i \mathrm{d}^2\mathbf{y}\mathrm{d}\tau, \tag{7.13}$$

a modification is made by choosing a tailored Green's function for cylindrical ducts, G_{cyl} instead of the free-field Green's function. Defining

$$\partial V = \partial V_{duct} + \partial V_{diap}, \tag{7.14}$$

where, V_{duct} and ∂V_{diap} denote the duct and the diaphragm surfaces, respectively, the surface integral in Eq. 7.13 can be split into two as follows:

$$\begin{aligned} \iint_{\partial V} (p'\delta_{ij} - \sigma_{ij}) \frac{\partial G_{cyl}}{\partial y_j} n_i \mathrm{d}^2\mathbf{y}\mathrm{d}\tau = &\iint_{\partial V_{duct}} (p'\delta_{ij} - \sigma_{ij}) \frac{\partial G_{cyl}}{\partial y_j} n_i \mathrm{d}^2\mathbf{y}\mathrm{d}\tau, \\ &+ \iint_{\partial V_{diap}} (p'\delta_{ij} - \sigma_{ij}) \frac{\partial G_{cyl}}{\partial y_j} n_i \mathrm{d}^2\mathbf{y}\mathrm{d}\tau. \end{aligned} \tag{7.15}$$

Since $\partial G_{cyl}/\partial n = 0$ is satisfied on the duct surface, the surface integral over ∂V_{duct} vanishes. Assuming high Reynolds number flow, the viscous term, σ_{ij} can also be dropped from Eq. (7.13) to obtain

$$\rho'(\mathbf{x},t) = \int_{-\infty}^{t} \iiint_V T_{ij} \frac{\partial^2 G_{cyl}}{\partial y_i \partial y_j} \mathrm{d}^3\mathbf{y}\mathrm{d}\tau - \int_{-\infty}^{t} \iint_{\partial V_{diap}} p'\delta_{ij} \frac{\partial G_{cyl}}{\partial y_j} n_i \mathrm{d}^2\mathbf{y}\mathrm{d}\tau. \tag{7.16}$$

On the right hand side of Eq. (7.16), the volume integral corresponds to the noise generation by the volume sources inside a cylindrical duct, and the surface integral to the scattering and noise generation by the diaphragm. To compute the surface integral in Eq. (7.16) over a discrete domain, the pressure fluctuations are integrated over the surface mesh elements, yielding acoustic

sources of dipolar form. The computations were done in the frequency domain by taking the Fourier Transform of the unsteady pressure data. The tailored Green's function at a particular frequency for a point source in a cylindrical duct, G_ω was given in Eq. (2.77) in Section 2.2.2. The derivative of the tailored Green's function with respect to the source position, $\mathbf{y}$ is calculated through the below analysis.

Defining

$$Q \equiv \frac{J_m(\alpha_{m\mu} r)}{k_{m\mu}(a^2 - \frac{m^2}{\alpha_{m\mu}^2}) J_m^2(\alpha_{m\mu} a)}, \tag{7.17}$$

$$F(r_0) \equiv J_m(\alpha_{m\mu} r_0), \tag{7.18}$$

$$H(\vartheta_0, x_0) \equiv i\big(\mp k_{m\mu}(x - x_0) - m(\vartheta - \vartheta_0)\big), \tag{7.19}$$

Eq. (2.77) can be reformatted as follows:

$$G_\omega = \frac{i}{2\pi} \sum_{m=-\infty}^{\infty} \sum_{\mu=1}^{\infty} QFe^H. \tag{7.20}$$

The tailored Green's function for a dipole placed in a cylindrical duct can then be written as;

$$G_{\omega,x_i} = \frac{i}{2\pi} \sum_{m=-\infty}^{\infty} \sum_{\mu=1}^{\infty} Q(F_{,x_i} + FH_{,x_i})e^H. \tag{7.21}$$

The derivative terms given in generic form are listed explicitly in Appendix B.1.

For the plane wave region which corresponds to $(m, \mu) = (0, 1)$, Eq. (7.21) reduces to

$$G_{\omega,x_i} = \frac{i}{2\pi} \frac{e^{\mp i\omega_0(x - x_0)}}{\omega_0 a^2} \tag{7.22}$$

for a listener in the far-field. Being r_0 and ϑ_0 invariant, Eq. (7.22) implies that for the plane wave region, the distributed dipoles at the diaphragm positions can be summed up to a single equivalent dipole for each of the diaphragms, when the listeners are located in the far-field. The noise predictions obtained from the distributed and the equivalent dipoles are compared in Figure 7.2. As expected, the two SPLs coincide for the plane wave region. The higher order modes are triggered in the distributed case due to the variation of the dipoles strengths and phases in the azimuthal and radial directions.

7.3 Noise prediction using the turbulent velocity

The acoustic density perturbation obtained using Lighthill's analogy was given in Section 2.3. When used with the tailored Green's function derived in Chapter 6 satisfying $\partial G/\partial \mathbf{n} = 0$, Eq. (2.93) reduces to

$$\rho'(\mathbf{x}, t) = \int_{-\infty}^{t} \iiint_V T_{ij} \frac{\partial^2 G}{\partial y_i \partial y_j} \mathrm{d}^3\mathbf{y}\mathrm{d}\tau, \tag{7.23}$$

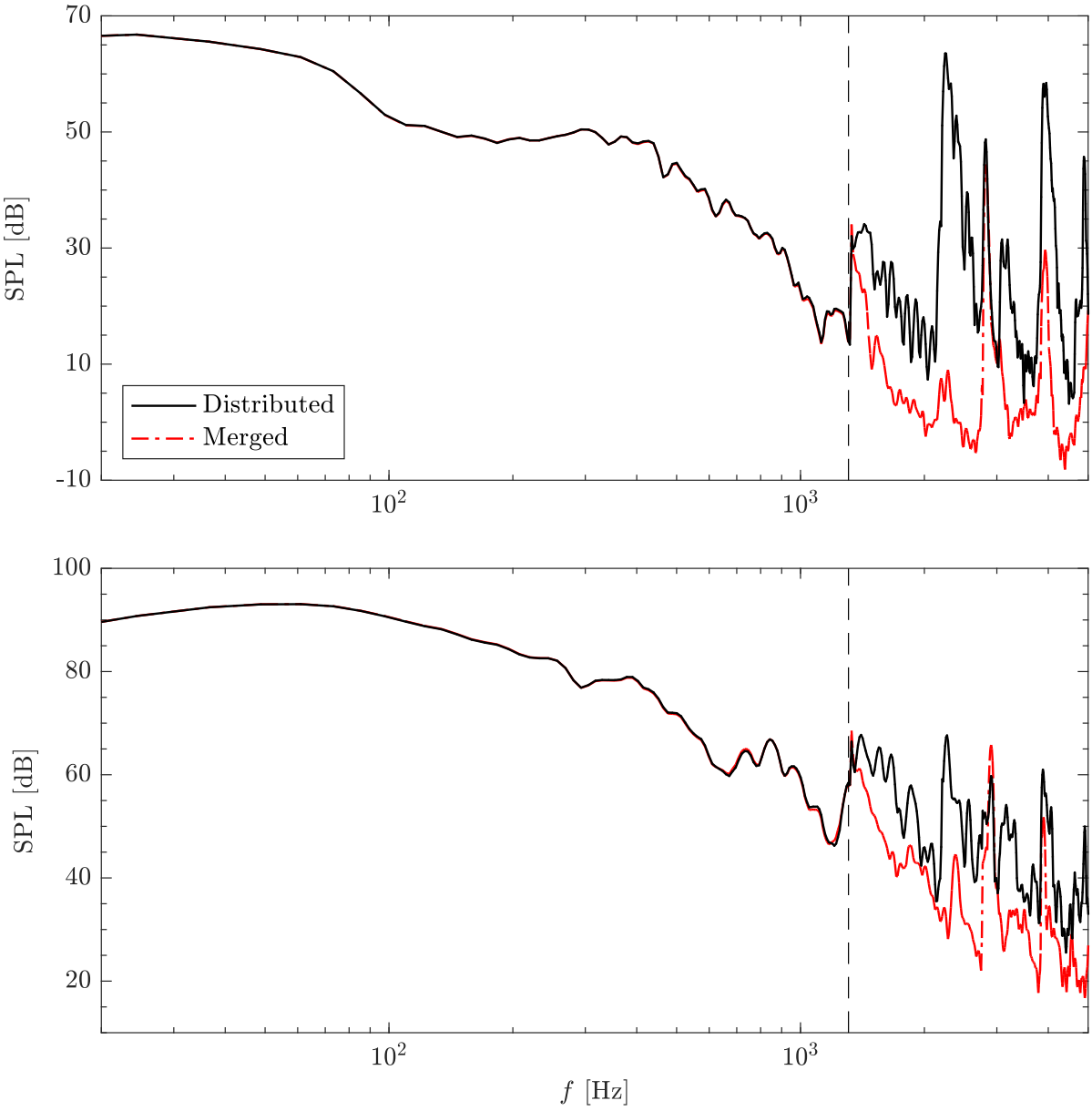

Figure 7.2: Comparison of the sound pressure level obtained from the distributed and the merged dipoles for the single (top) and the tandem (bottom) diaphragm cases. The vertical dashed line indicates the first cut-off frequency.

where

$$T_{ij} = \rho v_i v_j + (p' - c_0^2 \rho')\delta_{ij} - \sigma_{ij}. \tag{7.24}$$

For an isentropic flow, the second term in the right hand side of 7.24 becomes zero, and for a high Reynolds number flow, the viscous effects, σ_{ij} can be neglected, yielding the following expression to calculate acoustic density perturbation:

$$\rho'(\mathbf{x}, t) = \int_{-\infty}^{t} \iiint_V \rho v_i v_j \frac{\partial^2 G}{\partial y_i \partial y_j} \mathrm{d}^3\mathbf{y}\mathrm{d}\tau. \tag{7.25}$$

The source term in Eq. (7.25) is of quadrupolar form. Similar to the case of the dipolar sources, the tailored Green's function is to be differentiated twice with respect to the source position. Taking once more the derivative of Eq. (7.21), the tailored Green's function for a quadrupole inside a duct is calculated as;

$$G_{\omega,y_i y_j} = \frac{i}{2\pi} \sum_{m=-\infty}^{\infty} \sum_{\mu=1}^{\infty} Q(F_{,y_i y_j} + F_{,y_i} H_{,y_j} + F_{,y_j} H_{,y_i} + F H_{,y_i y_j} + F H_{,y_i} H_{,y_j}) e^{H}. \tag{7.26}$$

Over a discrete domain, Eq. (7.25) turns into

$$\hat{\rho}(\mathbf{x}) = \sum_{n=1}^{N} (\rho v_i v_j)_n \sum_{m=0}^{\infty} \sum_{\mu=0}^{\infty} (G_{\omega,y_i y_j})_{m\mu} \Delta_n, \tag{7.27}$$

The parameters determining the computation time of the Green's function approach per frequency and per listener are the number of sources and acoustic modes involved. A prediction with maximum accuracy is obtained when the summation in Eq. (7.27) is computed over the entire LES mesh using sufficiently high number of modes. Considering the 1.2×10^7 and 1.6×10^7 elements for the single and tandem diaphragm cases, the solution is expected to be very expensive even if an analytical approach is used. To reduce the computation time without significant loss of accuracy, a convergence analysis for the number of acoustic modes involved, and a grouping scheme for the mesh elements were applied. The details are explained in the following subsections.

7.3.1 Convergence analysis for the number of acoustic modes

The number of acoustic modes to be involved in the solution of the Green's function depends on the frequency, and the distance of the source to the listener and the diaphragms. It was discussed in Section 2.2.3 that at a given frequency, only a finite number of modes are cut-on, while the rest of the infinite series in Eq. (2.77) exhibit an exponential decay. The number of the cut-on modes at the maximum frequency of interest of the thesis study is 9. For a listener located distant to the source in a duct, accounting for only these 9 modes yields a converged acoustic response. If the source is located closer to the listener, the evanescent modes start contributing to the acoustic field. Besides, when there is a scattering surface such as a diaphragm in the near-field of the source, some of the evanescent modes may scatter into the cut-on modes, and thereby, contribute to the far-field acoustic pressure. The listener points set in the numerical cases match the microphone positions with respect to the diaphragm(s) given in Section 3.3.4. All the sources are assumed to be contained downstream of the (upstream) diaphragm. The distance between the diaphragm and the closest listener is then taken as the minimum distance between any source-listener pair. To determine the number of acoustic modes to be included in the solution is determined by calculating the acoustic response at the closest listener due to a test source for increasing number of modes until convergence. The source strength is set to be $1 + i1$ kg/ms^2 for all the frequency range. The analysis is repeated for the source positions at different distances to the diaphragm to obtain a convergence map in terms of the acoustic modes. The number of acoustic modes yielding converged acoustic response with respect to the source position is tabulated in Table 7.1.

Table 7.1: Distance to the diaphragm vs. minimum number of modes to be involved for a converged solution

$x/D <$	0.02	0.0267	0.033	0.0467	0.06	∞
Num. of Modes	40	30	25	20	15	10

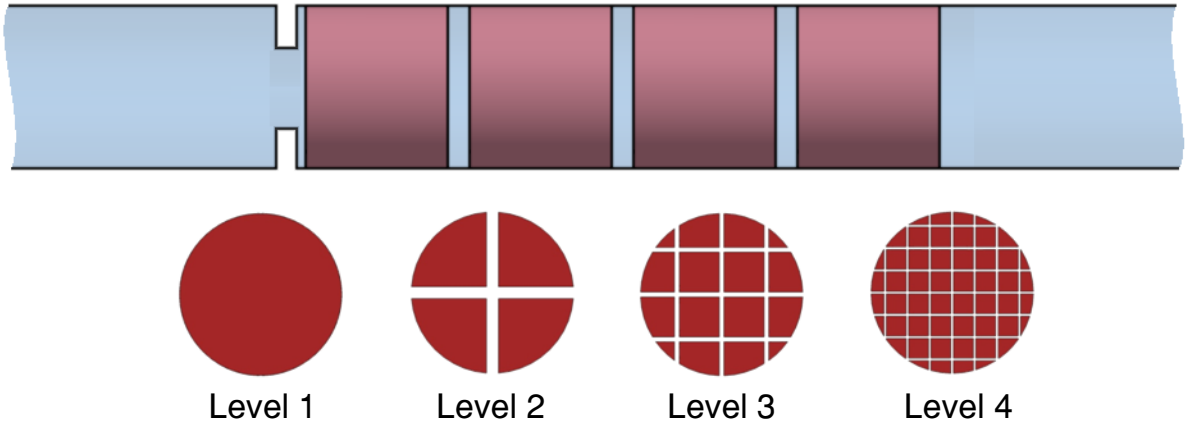

Figure 7.3: Integration of the quadrupoles using the octree structure. The red zones represent the distributed volume sources where each is integrated to an equivalent source.

7.3.2 Grouping of the sources in the flow field

The grouping scheme is introduced to decrease the number of sources, i.e. quadrupoles. This involves dividing the mesh domain into smaller subsets, and summing up the quadrupoles contained in each subset to a single equivalent source. An octree structure was used for modifying the grouping scheme in a systematical manner to see the effect of the grouping on the resultant acoustic response at the listeners. A convergence analysis, where the proximity to the diaphragm(s) is assumed to be the dominant factor was conducted to minimize this effect.

Initially, a region of dominant noise-generating sources has been defined. Considering the very low turbulence intensity upstream of the diaphragm; i.e. weak acoustic sources, and the low radiation efficiency of the quadrupolar sources away from the diaphragm, a $4D$ long region downstream of the diaphragm has been assumed to be large enough to enclose the dominant source region. Later on, it is verified that an even shorter region is sufficient for a converged acoustic response. The entire set of quadrupoles contained in the selected $4D$ long region has been divided into 4 cylindrical blocks of $1D$ length. The quadrupoles distributed in each block have been re-integrated at levels from 1 to 3, where re-integration at level 1 means summing all the quadrupoles contained in the corresponding block to a single equivalent quadrupole. At level 2, each block of quadrupoles are grouped in eight $1/2D$ long quarter-cylindrical sub-blocks. A 2D schematic is illustrated in Figure 7.3 to represent the concept of re-integration at higher levels. Each resultant point quadrupole is located at the center of gravity of its corresponding sub-block. Figure 7.4 shows the acoustic response at the far-field upstream of the diaphragm due to each of the cylindrical blocks integrated at different levels. Comparing those acoustic

responses to each other, it can be deduced that for the last block, an integration at level 1 yields sufficient convergence; i.e. an equivalent quadrupole at the volumetric center of the block can adequately represent the entire block of distributed quadrupoles. The quadrupole integration scheme described above does not depend on the turbulence correlation length, in the sense that the contributions of the integrated quadrupoles are summed in real and imaginary parts at the listener location (accounting for possible interferences), for each time segment of the CFD data, before being averaged in amplitude for all time segments (assuming time-decorrelation between segments, which was verified). For the quadrupoles upstream of the axial position $x/D = 3$, the same process has been repeated by dividing the zone into four $1/2D$ long cylindrical blocks which are re-integrated at levels from 2 to 4. It can be seen in Figure 7.5 that an integration at level 2 yields totally converged acoustic response for the cylindrical blocks downstream of $x/D = 1$. This process has been repeated for those cylindrical blocks showing discrepancy in the acoustic responses obtained at different integration levels, by halving the length of the blocks and increasing the level of integration by one, until a converged response is obtained for the entire source region. Such a methodology gradually going from integration level 1 to higher levels has been adopted to minimize the number of acoustic response computations until reaching convergence. The positional thresholds for each level in the resulting integration scheme are depicted at the top in Figure 7.6. The threshold values for the tandem diaphragm case are then directly determined regarding the results of the single diaphragm case, and are depicted at the bottom of the same figure. The convergence of the selected grouping scheme is verified for the single diaphragm case by making a comparison against a 'refined' scheme, which is obtained by increasing the level of integration by one for each axial block shown at the top of Figure 7.6. Figure 7.7 depicts that the given scheme for the single diaphragm configuration yields an acoustic response reasonably similar to one of a finer scheme, which is, again, expected to be the case for the tandem configuration as well. To verify the initial assumption of a dominant source region, the sound fields radiated from the source regions of gradually increased lengths downstream the diaphragm are compared in Figure 7.8. It is shown in the figure that the sources contained in a $0.5D$ long region, which are likely to have greater radiation efficiency due to being close to the diaphragm, are mostly responsible for the noise generation within the plane wave region. For the frequencies above the first cut-off, the sources outside this half-diameter region dominate the noise generation. Regarding the convergence of the acoustic responses, it can be verified that defining a $4D$ long region downstream the diaphragm for noise source computation provides conservative margin for a converged acoustic response at the far-field.

7.4 Comparison of the LES predictions against the in-duct aeroacoustic measurements

The noise predictions for the single and the tandem diaphragm cases obtained using the quadrupole method, the dipole method, and the CBF method, respectively are compared to the in-duct measurements. The results for the single diaphragm case are shown in Figure 7.9 where it can be seen that there is a strong contamination in the SPL obtained from the measurements especially in the plane wave region due to standing waves present along the duct, as a result of having partly reflective duct-ends in the experimental set-up. This contamination prevents a direct comparison between the measurements and the noise prediction methods, which use the

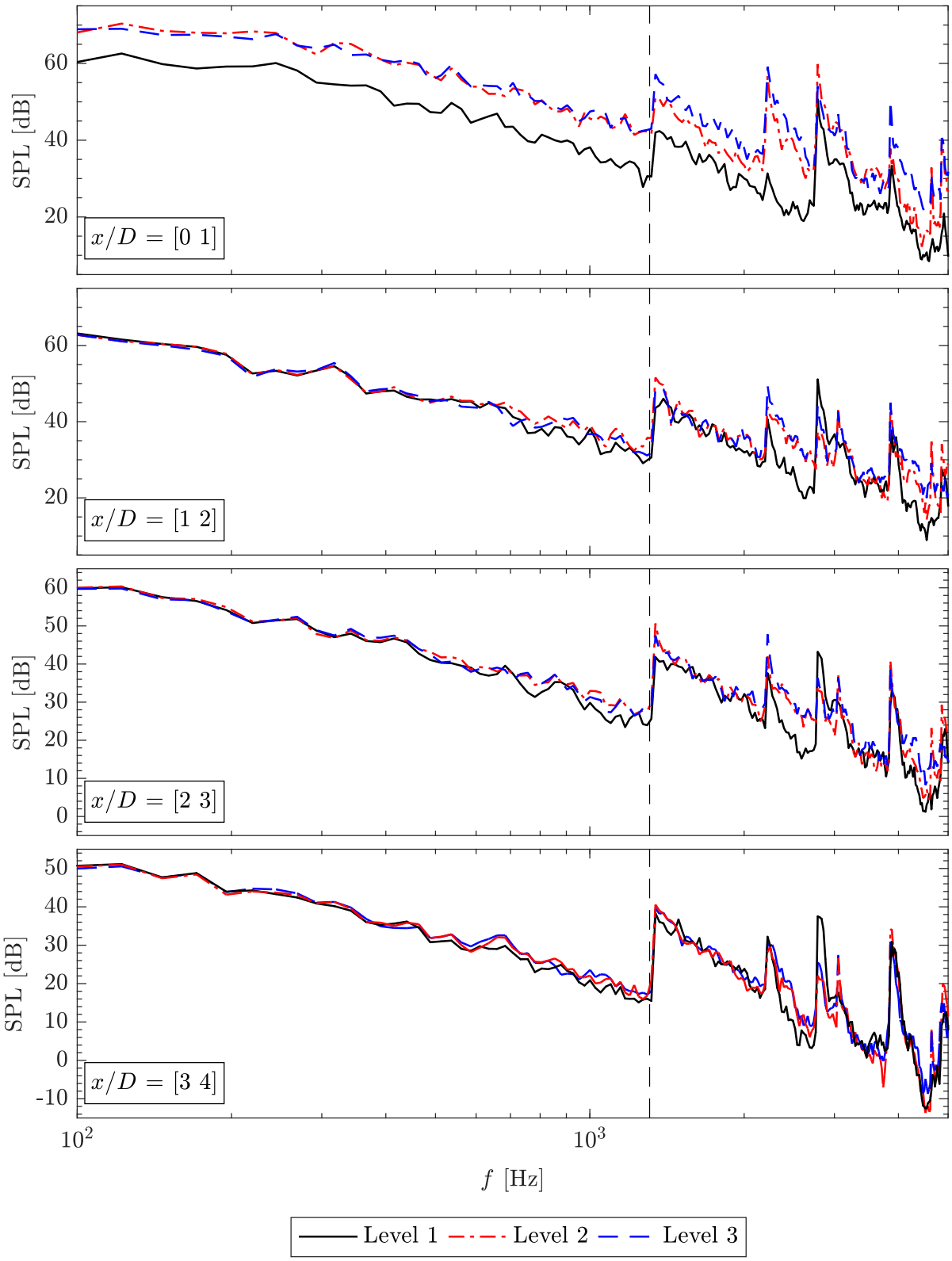

Figure 7.4: Acoustic pressure spectra at far-field induced by the quadrupoles integrated at levels from 1 to 3. Origin of x is taken on the diaphragm.

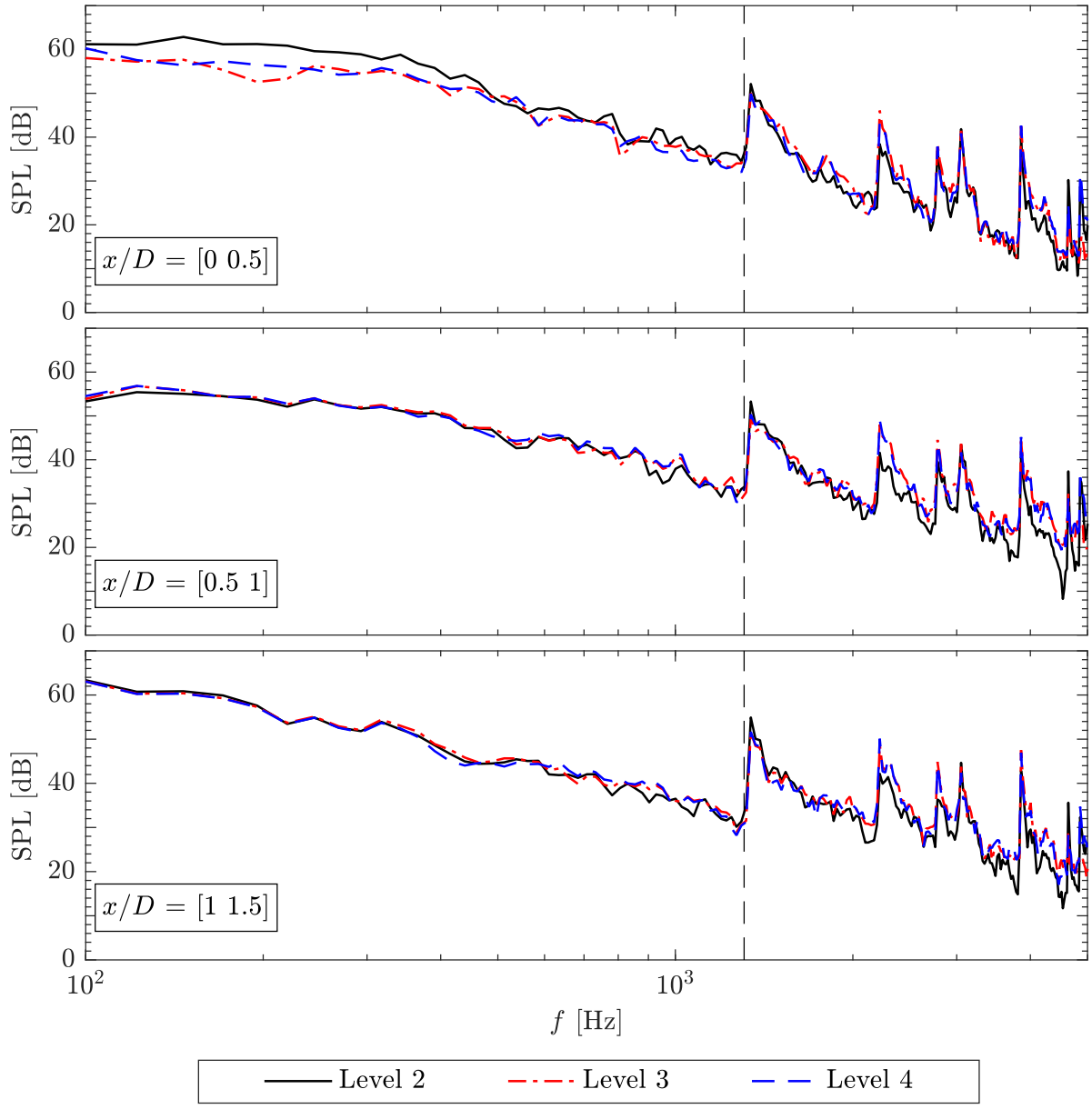

Figure 7.5: Acoustic pressure spectra at far-field induced by the quadrupoles integrated at levels from 2 to 4. Origin of x is taken on the diaphragm.

infinite duct assumption. However, it is still possible to make a general assessment of the prediction accuracies of the numerical methods, especially for the frequencies above the first cut-off. It is evident that the noise prediction obtained from the quadrupole method well matches the experiments for this frequency range. The dipole method does not provide satisfactory prediction at any part of the spectrum. However, it approaches the quadrupole method for the frequencies below 600 Hz. This indicates that isolation of the pressure fluctuations on the diaphragm surfaces as the dominant noise source is not valid for the single diaphragm case. The CBF method, which is only valid in the plane wave region, yields an SPL similar to the quadrupole method for the frequencies below 600 Hz although it inaccurately predicts a sharp decay in the SPL

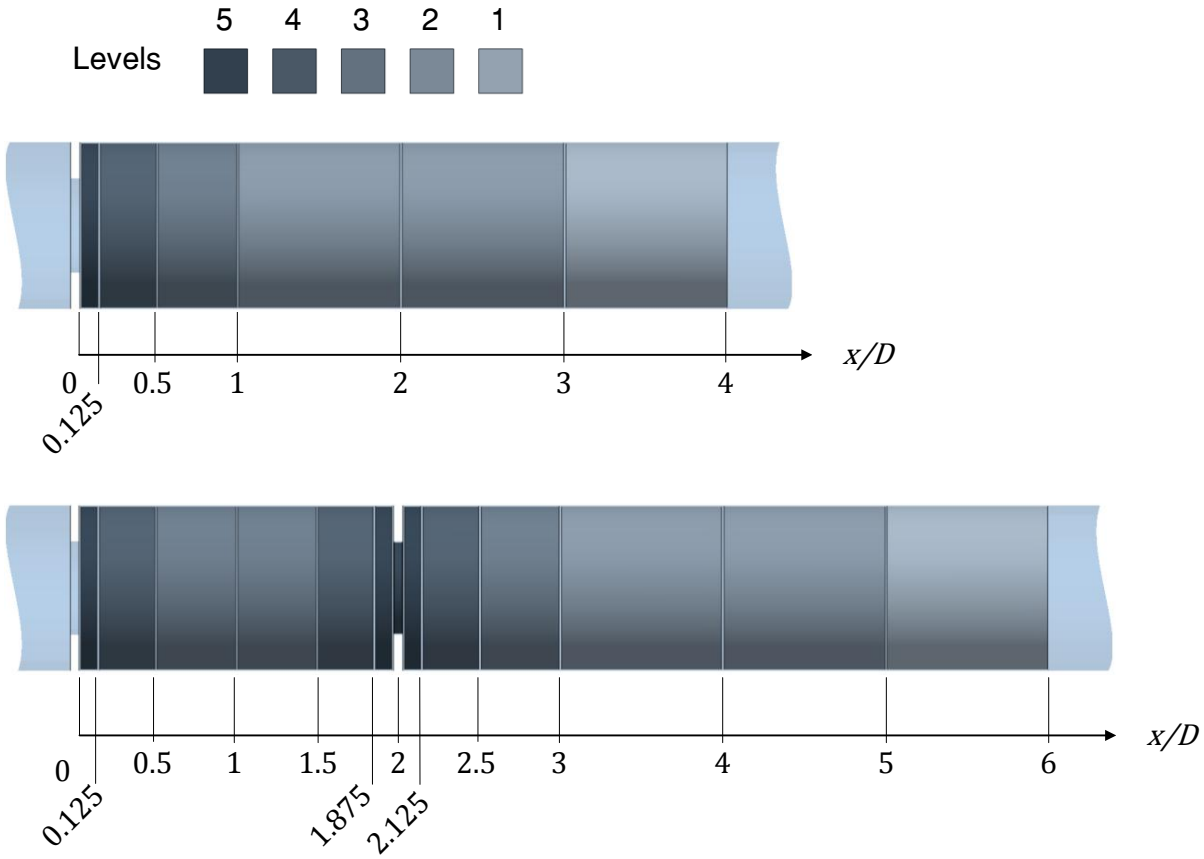

Figure 7.6: Non-dimensional limits for converged integration at each level for the single (top) and tandem (bottom) diaphragm configurations.

for higher frequencies. Beyond this frequency, the acoustic perturbations, which are very small in amplitude, are truncated by the LES solver, while the turbulent velocity fluctuations, which are used for computing the Lighthill's stress tensor, are not affected by such a truncation due to having much higher amplitudes.

The results for the tandem diaphragm case are depicted in Figure 7.10. The contamination problem for the SPL obtained from the measurements repeats for the tandem diaphragm case as well. It can again be seen that the quadrupole method satisfactorily matches the experimental results for the frequencies beyond the first cut-off. In the tandem diaphragm case, the pressure fluctuations on the downstream diaphragm significantly contribute to noise generation. This implies a better prediction of the SPL by the dipole method, which can already be observed Figure 7.10. However, it still underpredicts the SPL compared to the quadrupole method for the plane wave region, where the sound generation is expected to be dominated by the surface sources. Such an underprediction might be due to not taking into account the dipoles on the duct surfaces near the diaphragms in noise generation. For the higher order modes, the dipole method accurately predicts the peaks observed in the measurements at the mode transition frequencies despite of underestimating the sound pressure level in between those peaks. The CBF method provides a considerably better noise prediction for the overall plane wave region in the tandem diaphragm case. The 20 dB increase in the SPL, compared to the single diaphragm case, leads to ten-times-stronger acoustic perturbations, which can be more accurately captured by the LES

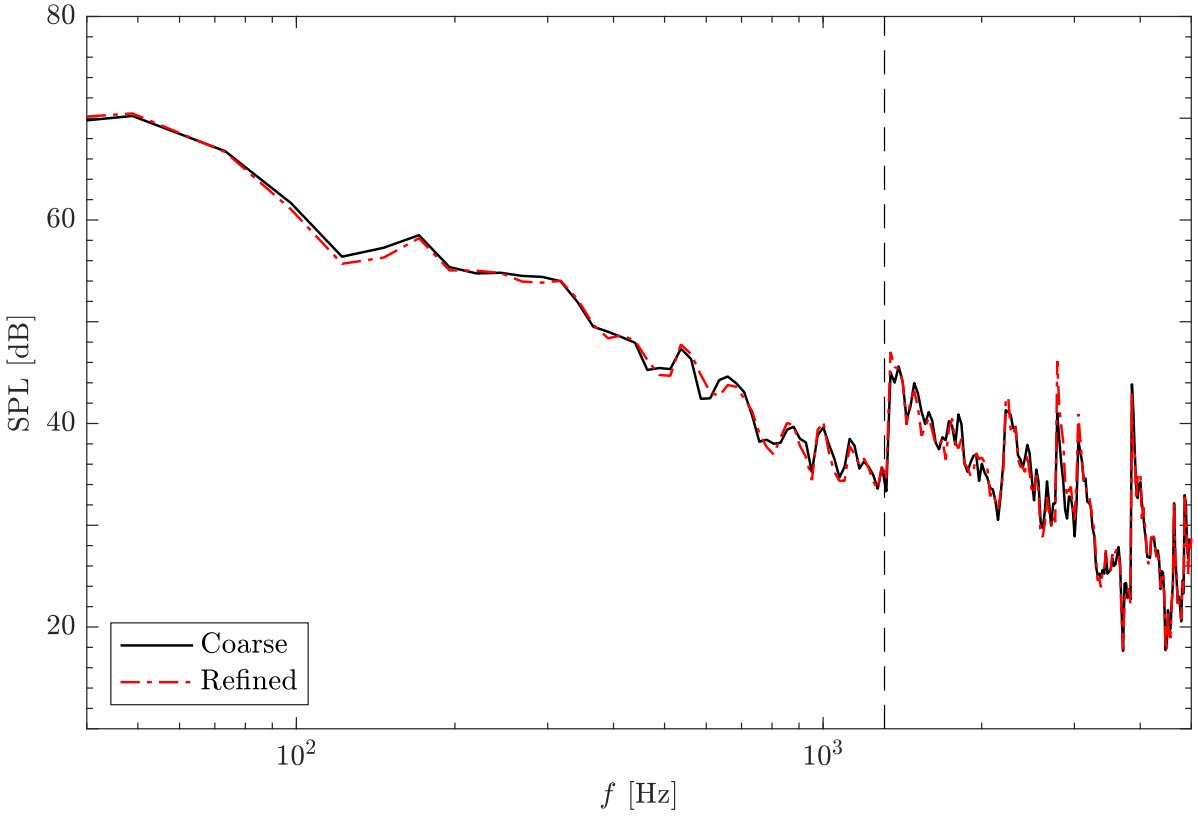

Figure 7.7: Comparison between the results of the converged grouping scheme and the refined scheme.

solver without being truncated.

7.5 Conclusions

The objective of the chapter was to assess the accuracy and robustness of the Lighthill/Curle analogy using a tailored Green's function for the duct-diaphragms system. The resulting noise predictions, compared with experimental validation data, indicate that above the first duct cut-off frequency, satisfactory results can be obtained by integrating the quadrupolar field with the new tailored Green's function. The method has the advantage of not requiring any pressure data; however, it is limited to the low Mach number applications due to not taking into account the mean flow effects. It was shown for the single diaphragm case that applying an analogy accounting only for the diaphragm unsteady forces (dipoles) underestimates the significant broadband contribution above the duct cut-off frequency. These broadband contributions were shown to be correctly predicted using distributed quadrupoles and the tailored Green's function. It is concluded that the diaphragm-distributed dipoles do not fully account for the diffraction of the quadrupoles, despite of having pressure data obtained by a compressible LES. The quadrupoles distributed inside the duct are presumed to play a non-negligible contribution as the frequency approaches the duct cut-off frequency and above.

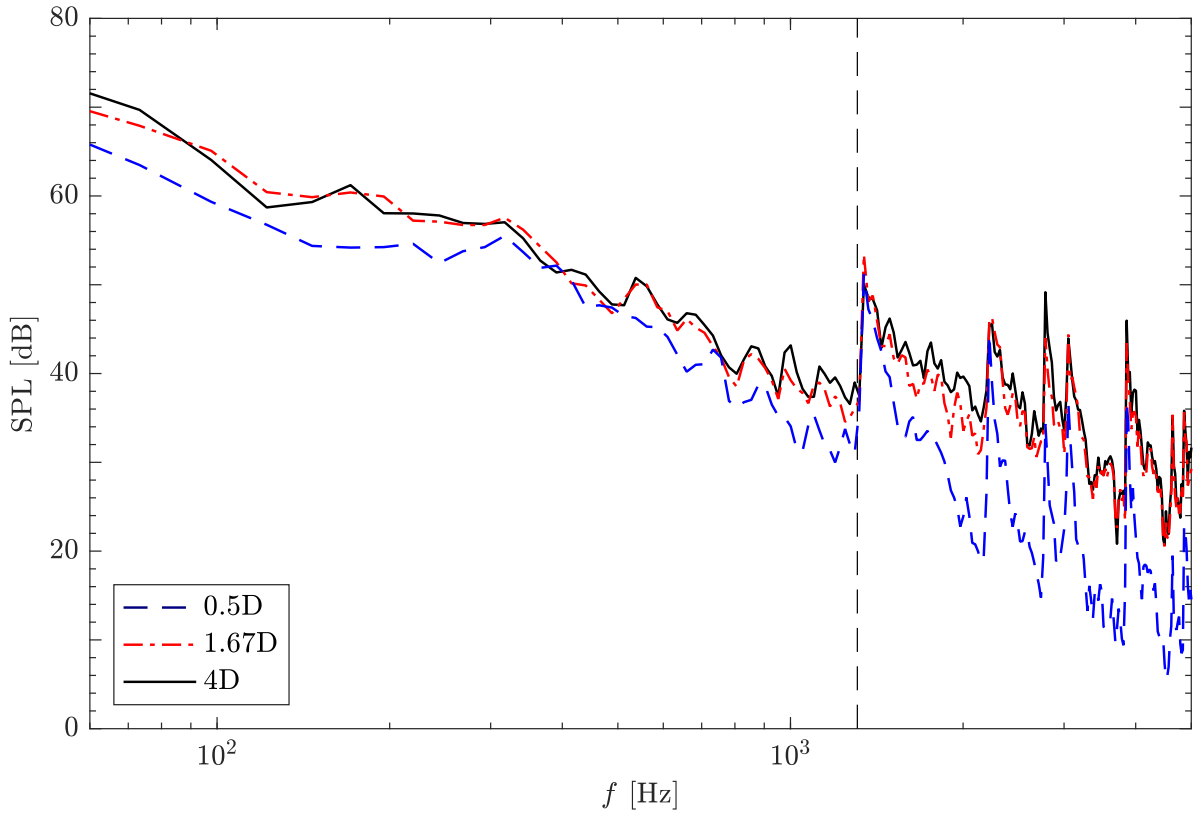

Figure 7.8: Comparison of the sound field radiated from the source regions of different lengths downstream the diaphragm.

For the tandem diaphragm case, accounting for the diaphragm-distributed dipoles yields much better agreement with the experimental and quadrupolar data. This can be explained by the much stronger hydrodynamic interactions between the two diaphragms.

Finally, the results demonstrate that even when compressible flow data are available, processing them by means of a suitable analogy with an adequate Green's function, the acoustic field can be obtained with enhanced accuracy and robustness, compared with a direct treatment of the CFD data.

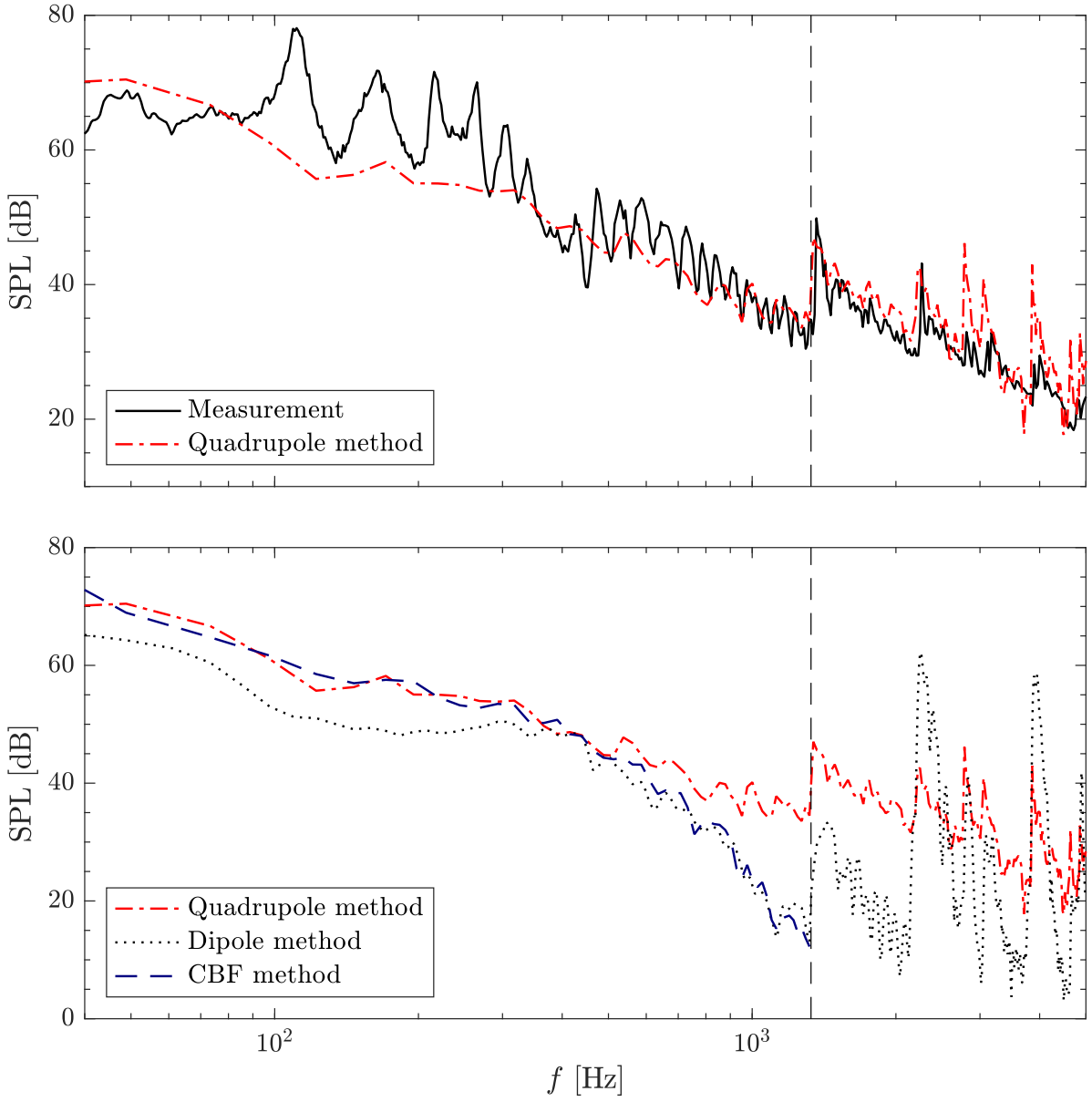

Figure 7.9: Comparison of noise spectra obtained by the measurements and different noise prediction methods at the upstream far-field for the single diaphragm case. For better readability, the quadrupole method is compared against the measurements (top), and the two other noise prediction methods (bottom) separately. The vertical dashed line indicates the first cut-off frequency.

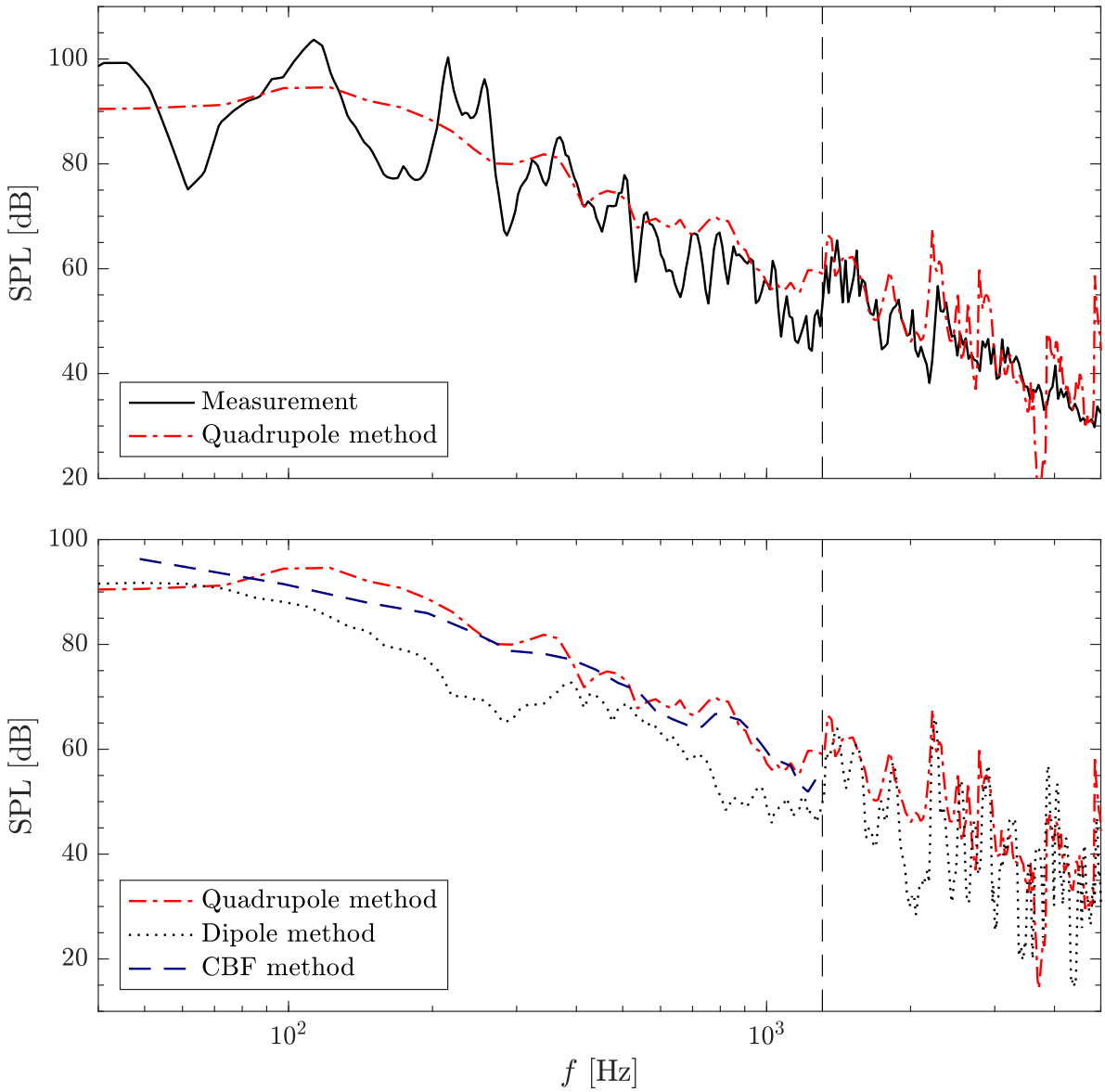

Figure 7.10: Comparison of noise spectra obtained by the measurements and different noise prediction methods at the upstream far-field for the tandem diaphragm case. For better readability, the quadrupole method is compared against the measurements (top), and the two other noise prediction methods (bottom) separately. The vertical dashed line indicates the first cut-off frequency.

8 Stochastic Noise Generation and Radiation (SNGR) method

8.1 Introduction

Methods to compute flow-induced noise commonly rely on unsteady flow data, such as Large Eddy Simulation (LES) (Gloerfelt *et* Lafon [23]), Detached Eddy Simulation (DES) or some of its variants (Shur *et al*. [86]). Quite accurate noise prediction can be obtained, but the computational costs associated with such approaches do not allow the numerous runs that are necessary for numerical optimization. As a less compute intensive alternative, stochastic approaches do not explicitly resolve the unsteady Navier Stokes equations, but are based on a generation of transient flow data satisfying statistical properties obtained by means of, for instance, Reynolds-Averaged Navier-Stokes simulations.

The use of stochastic methods to synthesize turbulence was introduced by Kraichnan *et al*. [42] to provide realistic boundary conditions for LES computations. Karweit *et al*. [38] used this concept to develop the so-called 'Stochastic Noise Generation and Radiation' (SNGR) method, where the turbulent velocity field was defined as the summation of the random Fourier modes homogeneously distributed in space. The energy level of the modes was determined using the one-dimensional von Karman-Pao energy spectrum, which is locally computed based on the mean turbulent kinetic energy and dissipation rate data obtained from a RANS solution. Bechara *et al*. [10] used this approach to predict noise generated by free turbulent flows. To introduce a temporal correlation, a band-pass filter was applied to the uncorrelated turbulent velocity data. Bailly *et al*. [8] introduced the idea of convecting the synthetic field with the mean flow and providing the temporal decorrelation by adding a time- and wavenumber-dependent phase term for each Fourier mode. They implemented the method for both confined [8] and unconfined flows [7]. Bauer *et al*. [9] applied the SGNR method to generate frozen turbulence around a flat plate to predict the trailing edge noise. Concerning the effect of the sweeping hypothesis (small eddies being carried by the most energetic eddies) on jet noise prediction [76], Lafitte *et al*. [44] modified the SNGR formulation of Bailly *et al*. [8] to include this effect. To introduce temporal decorrelation in SNGR method in a realistic and efficient way, Billson *et al*. [12] proposed a two-step method, where a simple convection equation was used to take into account the convection of the turbulence and the temporal de-correlation was achieved blending the convected velocity field with synthetic field at each time instant using an exponentially weighted filter. In a later work [13], they extended this method to take the anisotropy into account.

As an alternative stochastic approach, based on the concept introduced by Klein *et al*. [40] where the velocity fluctuations were created by filtering white noise to provide realistic inflow data for LES, Ewert *et* Emunds [21] developed the so-called Random Particle Mesh (RPM) method to

predict slat noise. They applied Gaussian filters on white noise to create stream functions from which the turbulent velocity field was obtained. The filter lengths are determined regarding the integral length scale data predicted from a RANS solution. Later, Siefert *et* Ewert [87] modified the RPM method to include the sweeping effect and implemented it for a jet noise prediction problem. In recent work, Heo *et al*. [27] implemented the RPM method using an unsteady RANS solution to predict the tonal and the broadband noise generated by a fan.

In the present thesis, SNGR approach is followed to predict the noise coming from single and double diaphragms installed in a cylindrical duct. Such configurations are frequently used in HVAC applications to balance the mass flow rate, for being very easy to manufacture and install, albeit causing significant noise. As an initial attempt to predict the ducted diaphragm noise using stochastic approaches in the present study, the SNGR method of Bailly *et al.* [8] was implemented based on a three-dimensional RANS simulation in [35]. The radiation of the acoustic sources was computed using Lighthill's analogy, implemented in a numerical acoustic solver. In parallel, Curle's analogy [18] was applied using unsteady pressure data obtained over the diaphragm surfaces by means of LES, to better understand the contribution of the diaphragm(s) to noise generation. The two numerical predictions were compared to in-duct acoustic measurements. Although the SNGR implementation showed some promising behavior, significant discrepancies remained, which were attributed to the insufficient match between the statistical properties of the RANS and LES flow fields on the one hand, and to known numerical issues that are encountered when the Lighthill sources are located too close to the acoustic mesh on the other hand. To minimize those numerical errors, a tailored Green's function was introduced in Chapter 6 and was validated using turbulent velocity field data obtained from LES in Chapter 7. In this chapter, the same methodology is followed replacing the unsteady LES data with the synthetic turbulent velocity field obtained from the SNGR method of Billson *et al*. [13].

Stochastic methods rely on a statistical description of the flow field for the generation of synthetic time-resolved velocity fields. Lighthill's approach to flow-induced noise [51] indicates the importance of two-point statistics in particular. Various studies have been published on the relation between the space-time correlation functions and the noise generation in jet or shear flows [52, 54, 70, 75]. Accordingly, stochastic noise prediction approaches are often based on the determination of the turbulent length- and time-scales from RANS k-ε or k-ω models, sometimes complemented by *ad hoc* calibration procedures to yield a satisfactory match with observations. This preliminary calculation often relies on an assumption of isotropic homogeneous turbulence. However, flow properties such as isotropy are strongly dependent on geometric details, making it difficult to develop a generic method applicable to a wide range of cases.

Thereto, an important objective of this work is to minimize the amount of input needed for the calibration of the length and time scales. The focus is placed on designing a new temporal filter, in which spectral decay is adjusted according to LES data to better represent the dissipation of turbulence. The effect of anisotropy is also investigated using a non-linear model for anisotropy correction. The noise prediction using the compressible LES data presented in Chapter 7 is taken as the reference data for comparison. For a reliable evaluation of the capability of the SNGR method in predicting the ducted diaphragm noise, the mean flow data was obtained averaging the LES field, eliminating errors due to discrepancies between the RANS and LES statistics. An aeroacoustic source grouping scheme, similar to the one introduced in Section 7.3.2, is implemented in the present study prior to the computation of the synthetic field using

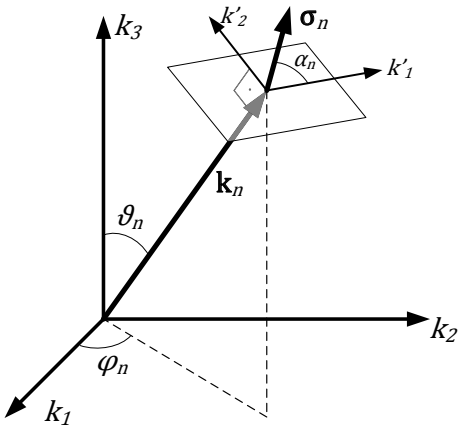

Figure 8.1: Geometric representation of a wave vector.

generic source terms to further reduce the memory requirements and computational cost of the acoustic propagation problem.

8.2 Theory

The SNGR formulation of Bechara et al. [10], where the turbulent velocity field is defined as a weighted summation of Fourier modes which are randomly and homogeneously distributed in three-dimensional space is given as follows:

$$\mathbf{u}_t(\mathbf{x},t) = 2\sum_{n=1}^{N} \hat{u}_n \cos\left(\mathbf{k}_n \cdot (\mathbf{x} - \mathbf{u}_c t) + \psi_n\right) \sigma_n \tag{8.1}$$

where $\mathbf{k}_n$ is the wavevector whose magnitude gives the wavenumber, $\mathbf{u}_c$ is the convection velocity, and $\hat{u}_n$, ψ_n, and σ_n are the amplitude, phase and direction of the n^{th} Fourier mode, respectively. σ_n is defined on a plane normal to $\mathbf{k}_n$ to obtain a solenoidal velocity field (see Figure 8.1). To achieve homogeneous distribution of the wave vectors in three-dimensional space, the following probability density functions (PDF) are used while determining the angles ϑ_n and φ_n which define the orientation of the n^{th} wave vector:

$$\mathscr{P}(\varphi_n) = (2\pi)^{-1}, \qquad -\pi \le \varphi_n \le \pi, \tag{8.2}$$

$$\mathscr{P}(\vartheta_n) = cos(\vartheta_n)/2, \qquad -\pi/2 \le \vartheta_n \le \pi/2. \tag{8.3}$$

The direction of the n^{th} Fourier mode defined by the angle α_n is expected to be randomly distributed on the plane perpendicular to the n^{th} wave vector. Therefore, the PDF corresponding to α_n is given as follows:

$$\mathscr{P}(\alpha_n) = (2\pi)^{-1}, \qquad -\pi \le \alpha_n \le \pi. \tag{8.4}$$

Similarly, the phase of the n^{th} Fourier mode, ψ_n is determined randomly with the following PDF:

$$\mathscr{P}(\psi_n) = (2\pi)^{-1}, \qquad -\pi \le \psi_n \le \pi. \tag{8.5}$$

The amplitude of the n^{th} Fourier mode is $\hat{u}_n = \sqrt{E(k_n)\Delta k_n}$, where $E(k)$ denotes the one-dimensional von Karman-Pao energy spectrum [62, 96] for isotropic turbulence given as

$$E(k) = \frac{4}{\sqrt{\pi}} \frac{\Gamma(17/6)}{\Gamma(1/3)} \frac{2K/3}{k_e} \frac{(k/k_e)^4}{\left[1+(k/k_e)^2\right]^{17/6}} e^{-2\left(\frac{k}{k_\eta}\right)^2}, \tag{8.6}$$

and Δk_n is the bandwidth of the n^{th} wave number. In Eq. (8.6), K denotes the turbulent kinetic energy, k_e and k_η are the wavenumbers corresponding to the integral and Kolmogorov length scales, respectively. These scales are locally calculated by the following two equations:

$$k_\eta = \epsilon^{1/4} \nu^{-3/4}, \tag{8.7}$$

$$k_e = \frac{9\pi}{55} \frac{\alpha}{\Lambda}, \tag{8.8}$$

where ν, ϵ and Λ correspond to the kinematic viscosity, dissipation rate and the integral length scale, respectively. The coefficient, α is used for scaling the spectrum so that the integration of the spectrum along $(0, k)$ where $k \to \infty$ yields the turbulent kinetic energy. To have such an equality, α must satisfy the following, assuming Reynolds number $\to \infty$:

$$\alpha = \frac{4}{\sqrt{\pi}} \frac{\Gamma(17/6)}{\Gamma(1/3)}. \tag{8.9}$$

The integral length scale is computed by

$$\Lambda = f_L \frac{K^{-3/2}}{\epsilon}, \tag{8.10}$$

where f_L is an adjustment parameter. The inputs in the above analysis are the mean flow velocity, the turbulent kinetic energy and the dissipation rate data. In a later work, Bailly *et al.* [8] added a time varying phase, $\omega_n t$ in Eq. (8.1) to introduce temporal de-correlation, where ω_n denoted the angular frequency of the corresponding n^{th} mode. Investigating this approach, Omais *et al.* [61] showed that any time dependent variable added to change the phase of the Fourier mode in Eq. (8.1) is to be uniformly distributed in space. This means that the time dependent terms introduced for the convection and the temporal de-correlation of turbulence cause non-physical results in case of inhomogeneous turbulence.

Alternatively, Billson *et al.* [12] proposed a two-step method for the generation of synthetic turbulence to better represent the flow de-correlation in time, which is adopted in the present study. In their approach, the turbulent velocity field, $\mathbf{v}_t^{m-1}(\mathbf{x})$ at the time step $(m-1)$ is convected through the convection equation

$$\frac{\partial\left(\overline{\rho}\mathbf{v}_t^{m-1}\right)}{\partial t} + \frac{\partial\left(\overline{\rho u_j}\mathbf{v}_t^{m-1}\right)}{\partial x_j} = 0, \tag{8.11}$$

where $\overline{\rho}$ and $\overline{\rho u_j}$ correspond to the mean density and mean momentum, respectively. Then, to obtain the turbulent velocity field at time step (m), the convected velocity field is blended with the synthetic turbulent velocity fields generated at time steps (m) and $(m-1)$ using Eq. (8.1)

with the convection term omitted from the phase of the Fourier modes. This blending operation results an exponentially weighted temporal filter equation of Holt-Winters type [29, 98]:

$$\mathbf{v}_t^m(\mathbf{x}) = a\mathbf{v}_t^{m-1}(\mathbf{x}) + b\left(\mathbf{u}_t^m(\mathbf{x}) - \mathbf{u}_t^{m-1}(\mathbf{x})\right), \tag{8.12}$$

where $a = \exp(-\Delta t/\tau_f)$ and $b = f_A\sqrt{(1-a)/2}$. The terms Δt and f_A are the time step size and the tuning parameter for the turbulent kinetic energy, while τ_f is the local dynamic time scale. Choosing a proper model for the time constant is crucial for accurate prediction of turbulent flow noise [5]. In the original work of Billson *et al.* [12], the time constant, τ_f was predicted as

$$\tau_f = f_T\frac{K}{\epsilon} \tag{8.13}$$

with an adjustment parameter, f_T. The applicability of a frequency independent time constant is to be verified for the present flow case, as the time and length scales in turbulent flows can also be frequency dependent [26] and the dependency of the scales on the frequency significantly affect flow noise generation [5]. To examine the existence of such a dependency on the frequency in the present case, the cross-power spectral density (CPSD) of velocity has been computed at each point in the flow domain for increasing time-lag values using

$$\Gamma_{uu}(\mathbf{x},\omega,\tau_i) = \mathscr{F}\{u(\mathbf{x},t)\,u(\mathbf{x},t+\tau_i)\}, \tag{8.14}$$

where $\mathscr{F}\{\cdot\}$ is the discrete Fourier Transform operator, $\tau_i = i\Delta\tau$, is the time lag at the i^{th} iteration for $i = 1, 2, \cdots, N$. The local Eulerian time scales are then calculated for each frequency:

$$L_\omega = \sum_{i=1}^{N}\Gamma_{uu}(\mathbf{x},\omega,\tau_i)\,\Delta\tau, \tag{8.15}$$

and normalized using

$$l_\omega = \frac{L_\omega U_{ref}}{\mathrm{E}\{\Lambda\}}, \tag{8.16}$$

where U_{ref} is selected to be the inflow velocity and $E\{\Lambda\}$ is the integral length scale averaged over the flow domain. The resulting normalized time scales at various points downstream of the diaphragm are plotted with respect to the Strouhal number, $St = fD/U_{ref}$ in Figure 8.2, where U_{ref} is selected to be the inflow velocity.

As seen in the figure, no strong variation is observed for the frequency range of interest. Hence the expression used for the time scale given in Eq. (8.13) has been adopted for the present study. It should be noted that all the tuning parameters faced in the above analysis have been set to be unity in the present study, as no particular tuning of the flow scales was conducted.

8.2.1 Anisotropy correction

To include the effect of the anisotropy, Billson *et al.* [13] introduced the idea of distorting the isotropic synthetic turbulent velocity field using the Reynolds stress tensor as discussed below.

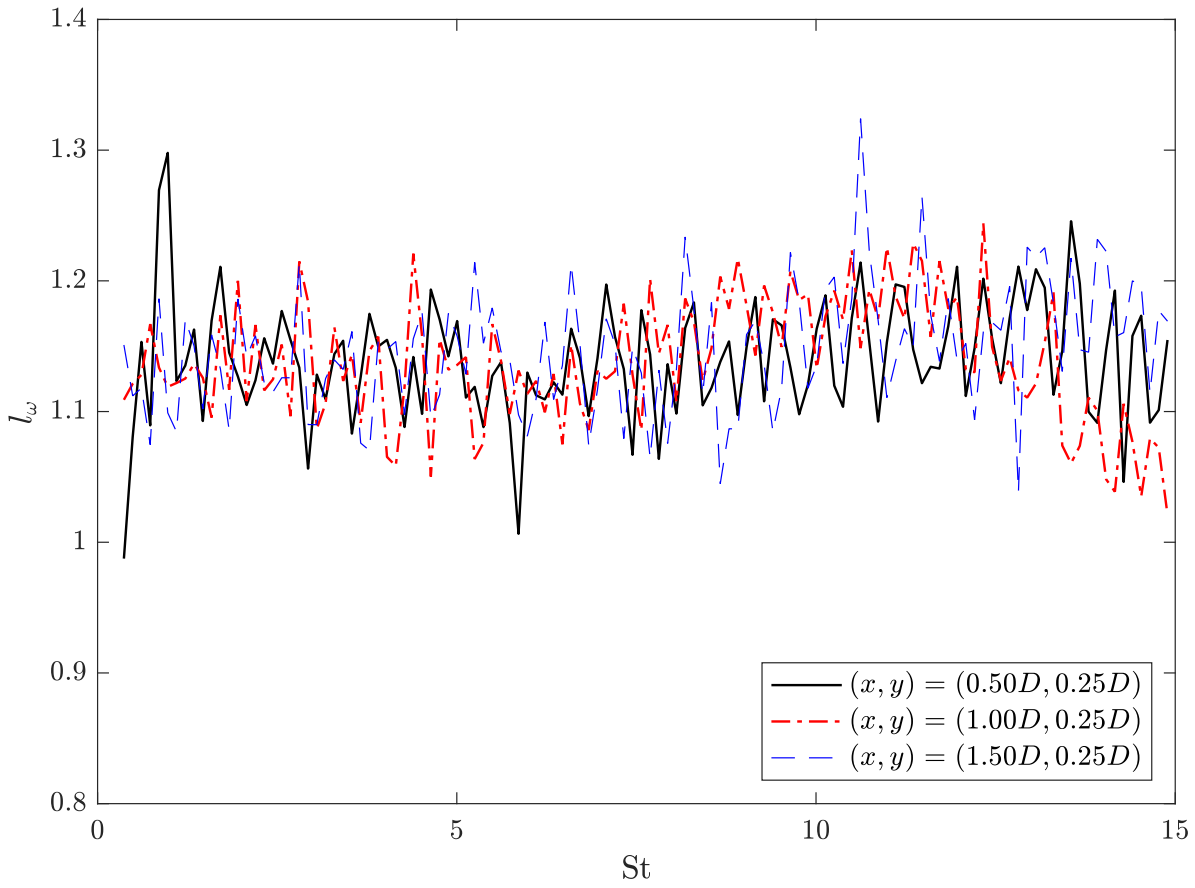

Figure 8.2: Normalized Eulerian time scales vs. Strouhal number computed at various points downstream the diaphragm for the single diaphragm case. The center of the diaphragm cross-section is taken as the origin.

Given the local Reynolds stress tensor, $\tau = \rho \mathbf{u}\mathbf{u}^\top$ normalized as

$$\mathbf{a} = -\frac{3}{2}\frac{\tau}{\overline{\rho K}}, \tag{8.17}$$

and rotated to its principal axes to yield;

$$\mathbf{a}^* = \mathscr{R}^\top \mathbf{a} \mathscr{R}, \tag{8.18}$$

where $\mathscr{R}$ is the three-dimensional rotation matrix. Anisotropy can be added to the isotropic turbulent velocity field, which is synthesized using Eq. (8.1), by rotating all the vectors to the principal axes (multiplying by $\mathscr{R}^\top$), scaling the Fourier summation with $\mathbf{a}^{*1/2}$ and rotating the resulting vector field back to the original coordinate system (multiplying by $\mathscr{R}$). To retain the divergence-free characteristic of the turbulent velocity field, the wave vector $\mathbf{k}$ is to be scaled with $\mathbf{a}^{*-1/2}$. It was shown in [13] that the stress tensor calculated from the resulting turbulent velocity field satisfies the target stress tensor τ. There are various models in the literature for predicting the anisotropy from the mean flow velocity data. In [13], a linear eddy viscosity model has been used to predict the anisotropy. Omais *et al.* [61] showed that use of a non-linear Reynolds stress model (RSM) significantly improves the prediction of the anisotropy,

and so does the accuracy of the SNGR method. Following their approach, the non-linear RSM introduced by Shih *et al*. [85] is implemented in the present study. The RSM is given by

$$\overline{u_i u_j} = \frac{2}{3}K\delta_{ij} - C_\mu \frac{K^2}{\epsilon} 2S^*_{ij} + 2C_2 \frac{K^3}{\epsilon^2}\left(-S^*_{ik}\Omega^*_{kj} + \Omega^*_{ik}S^*_{kj}\right), \tag{8.19}$$

where S^*_{ij} is the traceless strain tensor given as

$$S^*_{ij} = \frac{1}{2}\left(\frac{\partial \overline{U}_i}{\partial x_j} + \frac{\partial \overline{U}_j}{\partial x_i}\right) - \frac{1}{3}\frac{\partial \overline{U}_k}{\partial x_k}\delta_{ij}, \tag{8.20}$$

and Ω^*_{ij} is the vorticity tensor:

$$\Omega^*_{ij} = \frac{1}{2}\left(\frac{\partial \overline{U}_i}{\partial x_j} + \frac{\partial \overline{U}_j}{\partial x_i}\right). \tag{8.21}$$

with $\overline{U}_i$ representing the mean flow velocity. To satisfy the realizability in any flow condition, the coefficients C_μ and C_2 in Eq. (8.19) are defined according to the rate of deformation and the rate of rotation of the mean flow:

$$C_\mu = \frac{1}{A_0 + A^*_s \frac{U^* K}{\epsilon}}, \qquad C_2 = \frac{\sqrt{1 - 9C^2_\mu\left(\frac{S^* K}{\epsilon}\right)}}{C_0 + 6\frac{S^* K}{\epsilon}\frac{\Omega^* K}{\epsilon}}, \tag{8.22}$$

where $A_0 = 6.5$, $C_0 = 1$, $S^* = \sqrt{S^*_{ij}S^*_{ji}}$, $\Omega^* = \sqrt{\Omega^*_{ij}\Omega^*_{ji}}$, $A^*_s = \sqrt{6}\cos\left(\frac{1}{3}\arccos\left(\sqrt{6}W^*\right)\right)$, $U^* = \sqrt{S^*_{ij}S^*_{ij} + \Omega^*_{ij}\Omega^*_{ij}}$, and $W^* = \frac{S^*_{ij}S^*_{jk}S^*_{ki}}{(S^*)^3}$.

8.2.2 Computing the mean flow parameters using the LES data

The mean flow field required as input in the above analysis is usually provided by a RANS simulation in order to minimize computational costs. However, to better evaluate the accuracy of the SNGR synthesis, the mean flow parameters were first calculated using the mean LES data instead of a RANS solution, so that any ambiguities which could result from a possible difference in the RANS simulation and the mean LES data were avoided.

To obtain the turbulent kinetic energy and the dissipation rate from the LES, the conservation equation for the filtered turbulent kinetic energy has been used. Any flow variable in an LES model can be written as the summation of the filtered and the sub-grid scale parts. For the turbulent kinetic energy K, the filtered part, K_f can be directly computed using the filtered turbulent velocity field data, $\tilde{u}_i$:

$$K_f = \frac{1}{2}\tilde{u}_i\tilde{u}_i. \tag{8.23}$$

The modeled turbulent eddy viscosity, ν_t is an output of the solver. The sub-grid scale part of the turbulent kinetic energy, K_{sgs} can be predicted using

$$K_{sgs} = \left(\frac{\nu_t}{C_w \Delta}\right)^2, \tag{8.24}$$

where C_w is the model constant (=0.57 for the WALE model) and the Δ is the characteristic filter size computed as the cubic root of the volume of the corresponding mesh element. For the prediction of the dissipation rate, the conservation equation for the filtered kinetic energy, K_f as given in Pope's book [66] is considered:

$$\frac{\tilde{D}K_f}{\tilde{D}t} - \frac{\partial}{\partial x_i}\left[\tilde{u}_j\left(2\nu\tilde{S}_{ij} - \tau^r_{ij} - \frac{\tilde{p}}{\rho}\delta_{ij}\right)\right] = -\epsilon_f - \mathscr{P}_r, \tag{8.25}$$

where

$$\tilde{S}_{ij} = \frac{1}{2}\left(\frac{\partial \tilde{u}_i}{\partial x_j} + \frac{\partial \tilde{u}_j}{\partial x_i}\right) \tag{8.26}$$

represents the filtered stress tensor, and τ^r_{ij} corresponds to the residual stress computed using the linear eddy viscosity model:

$$\tau^r_{ij} = -2\nu_t \tilde{S}_{ij}. \tag{8.27}$$

The left hand side of Eq. (8.25) represents the transport of the filtered energy while the right hand side is related to viscous dissipation (ϵ_f being the viscous dissipation of the filtered field) and rate of the transfer of the kinetic energy to the sub-grid scale ($\mathscr{P}_r$). Assuming a temporarily stationary flow, i.e. the net production of the kinetic energy equals zero, the total dissipation rate, ϵ in the flow field can be found by summing these two terms:

$$\epsilon = \epsilon_f + \mathscr{P}_r, \tag{8.28}$$

where,

$$\epsilon_f \equiv \nu \tilde{S}_{ij}\tilde{S}_{ij}, \tag{8.29}$$

$$\mathscr{P}_r \equiv -\tau^r_{ij}\tilde{S}_{ij}. \tag{8.30}$$

8.3 A new temporal filter

The energy spectra of the noise sources observed in an Eulerian frame within a flow are affected by the sweeping of turbulence [75]. This is achieved with the convection operation in the present SNGR implementation. In flow regions with strong convection, the noise sources are characterized by the spatially generated synthetic velocity field. However, for the flow regions where the mean convection velocity is close to zero, such as the recirculation zone(s) downstream of the diaphragm(s) shown in Figure 8.3, the temporal de-correlation obtained by the filter given

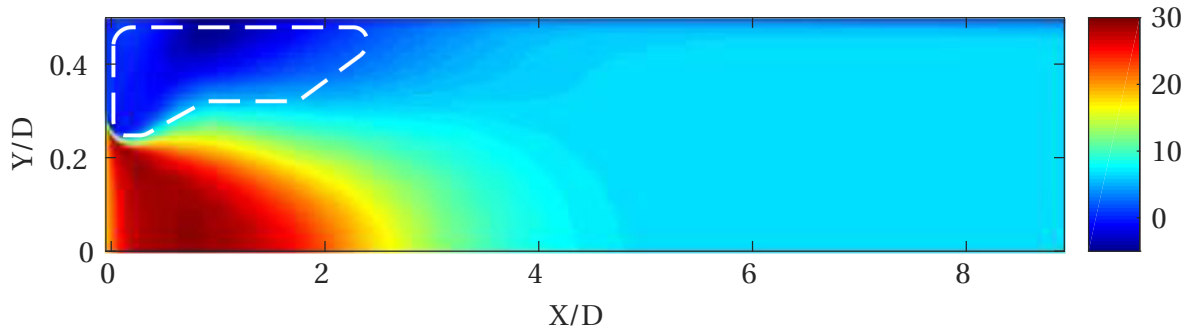

Figure 8.3: The mean u-velocity field for the single diaphragm case. The white-dashed line denotes the separation zone downstream of the diaphragm.

in Eq. (8.12) becomes also effective in defining the turbulent fluctuations in an Eulerian frame. Despite of their relatively low turbulence intensity, the acoustic sources contained within those regions may still have significant contribution, since their radiation efficiency is enhanced by the proximity of the diaphragm(s). Hence, it is important for the spectral decay of the filter to match the LES value for those regions. For the single diaphragm configuration, the energy spectra of the velocity data at randomly selected various points within the separation zone are calculated using the LES data and depicted in Figure fig:EuuSpectrum. Since the LES data includes compressibility effects, peaks in the spectra are observed at the cut-on frequencies, where new acoustic modes become propagative. It is seen that for the frequency range where the shape of the spectrum is not dominated by acoustic mode cut-on, the spectral decay can be approximated by a -4.5 slope. This spectral decay being much steeper than $-5/3$, it can be inferred that the energy spectrum corresponding to the frequency range of interest exhibits more dissipation than in isotropic homogeneous turbulence. Similar values for the spectral decay in the dissipative range were reported in various experimental studies investigating the energy spectrum in pipe flows [74, 95, 101]. The Reynolds number of the flow investigated in the present study is $Re_D = UD/\nu \cong 64{,}000$. In the work of Torbergsen *et* Krogstad [95], the closest experimental case available for comparison with $Re_D = 70{,}000$, the computed spectral decay was -4.2, fairly close to the value predicted from the present LES.

The logarithmic slope of the spectrum of the temporal filter given in Eq. (8.12) can be calculated by taking the Fourier Transform:

$$\mathbf{V}_\omega = a\mathbf{V}_\omega e^{-\frac{2\pi\omega}{N}} + b\left(\mathbf{u}_\omega + \mathbf{u}_\omega e^{-\frac{2\pi\omega}{N}}\right), \tag{8.31}$$

where $\mathbf{V}_\omega$ and $\mathbf{u}_\omega$ are the Fourier Transform of $\mathbf{v}$ and $\mathbf{u}$, respectively, and N is the number of the discrete time instants. Since the synthetic velocity field $\mathbf{u}(\mathbf{x})$ is uncorrelated in time, its Fourier Transform yields a constant, γ. Reorganizing Eq. (8.31) and taking the logarithm, one obtains:

$$\log\mathbf{V}_\omega = \log b + \log\gamma + \log\left(1 + e^{-\frac{2\pi\omega}{N}}\right) - \log\left(1 - ae^{-\frac{2\pi\omega}{N}}\right). \tag{8.32}$$

Taking the derivative of Eq. (8.32) with respect to $\log\omega$ and multiplying by 2 yields the logarithmic slope of the energy spectrum of the temporal filter:

$$slope = -\frac{4\pi\omega}{N}e^{-\frac{2\pi\omega}{N}}\left(\frac{1}{1+e^{-2\pi\omega/N}} + a\frac{1}{1-e^{-2\pi\omega/N}}\right). \tag{8.33}$$

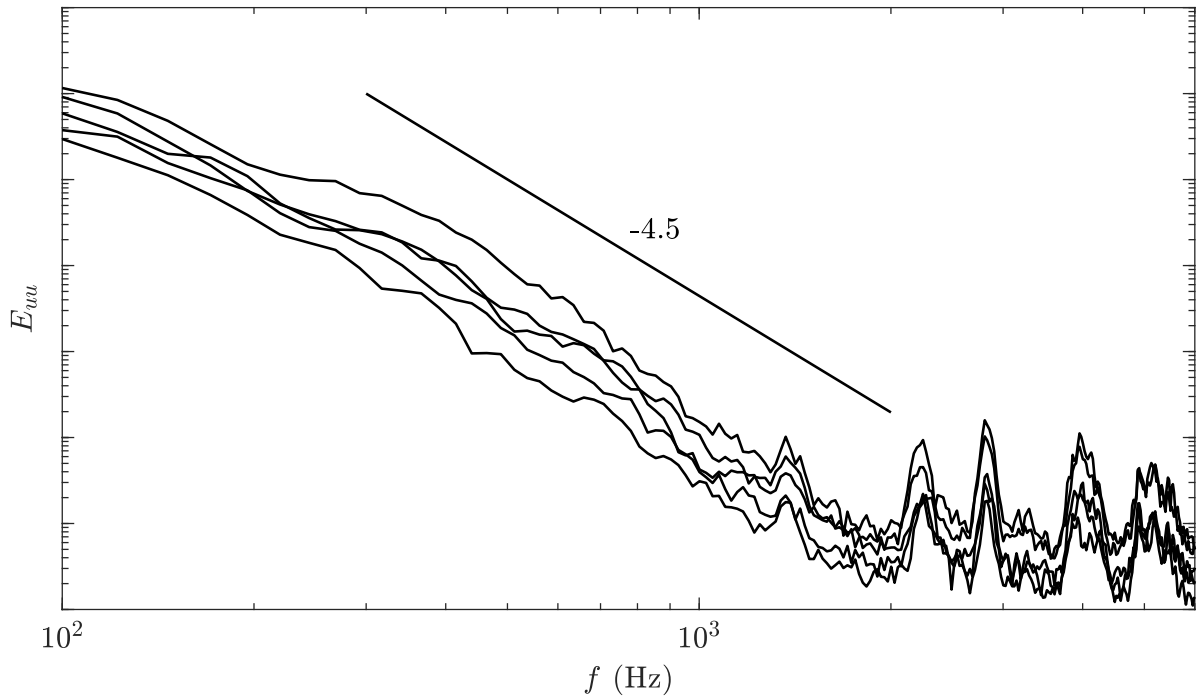

Figure 8.4: Energy spectrum of the u-velocity at various points in the separation zone.

The slope given in Eq. (8.33) is only dependent on the coefficient a, which is a function of the time step Δt, and on the time constant τ_f, neither of which are suitable for freely adjusting the slope of the filter. Given a time step satisfying the ratio, $\Delta t/\tau_f = 0.0001$, which yields a CFL value much smaller than the limit for numerical stability, the resulting slope of the spectrum in the frequency range of interest is almost constant and approximately equal to -2; while using a bigger time step makes the slope even closer to zero. This analysis implies that using the filter given in Eq. (8.12), it is not possible to obtain a velocity field with an energy spectrum matching the LES flow field. To overcome this issue, a cascaded temporal filter is proposed in the present study as follows:

$$\begin{aligned}
\mathbf{w}_t^m(\mathbf{x}) &= a_1 \mathbf{w}_t^{m-1}(\mathbf{x}) + b_1 \left(\mathbf{u}_t^m(\mathbf{x}) - \mathbf{u}_t^{m-1}(\mathbf{x})\right), \\
\mathbf{z}_t^m(\mathbf{x}) &= a_2 \mathbf{z}_t^{m-1}(\mathbf{x}) + b_2 \mathbf{w}_t^m(\mathbf{x}), \\
\mathbf{v}_t^m(\mathbf{x}) &= a_3 \mathbf{v}_t^{m-1}(\mathbf{x}) + b_3 \mathbf{z}_t^m(\mathbf{x}),
\end{aligned} \tag{8.34}$$

where $\mathbf{w}$ and $\mathbf{z}$ are auxiliary variables, a_1 and a_2 are free parameters used for tuning the slope of the resulting filter spectrum, $b_1 = \sqrt{(1-a_1)/2}$, $b_2 = \sqrt{(1-a_2)}$, $a_3 = \exp(-\Delta t/\tau_f)$, and $b_3 = \sqrt{(1-a_1)}/\sigma$. The correction factor, σ is added to ensure that the standard deviations of $\mathbf{v}$ and $\mathbf{u}$ are equal. To tune the parameters, a_1 and a_2, a random series $\mathbf{u}$ with constant spectrum is used. Setting $a_1 = 0.98$, and $a_2 = 0.7$, the logarithmic slope of the filter spectrum over the domain of interest for the single diaphragm case lies between -4.42 and -4.51, with an average equal to -4.50. The corresponding correction factor σ is numerically computed to be 8.26 by taking the ratio of the standard deviation of $\mathbf{v}$ to that of $\mathbf{u}$.

8.4 Numerical setup and synthetic flow field

The mesh used for the SNGR method has to be fine enough to minimize numerical dissipation when solving the convection equation. The SNGR mesh has been determined based on the average cell size of the LES mesh taken as reference. For both single and double diaphragm configurations, the upstream boundary of the SNGR domain has been set matching with the downstream face of the (upstream) diaphragm. Meshes of 1.67×10^6 and 2.56×10^6 elements have been created for the single and double diaphragm cases, respectively, without any particular refinement for the boundary layers. Both the inflow and outflow boundary conditions have been set to 0 m/s. A buffer layer of length $2D$ has been applied to the downstream end of the domain to avoid spurious noise generation, where the synthetic source data is weighted by a semi-Hanning decaying window function. No buffer layer is required for the inlet, as the turbulence intensity at the upstream interface of the (upstream) diaphragm is already very close to zero.

The convection equation has been solved using a first order upwind scheme with a time step of 2×10^{-5} seconds. The maximum CFL number with the given mesh and time step is 0.75, below the stability limit for the selected numerical scheme of 1. The wavenumber range has been determined through a convergence analysis. The lower bound has been taken as $0.1\min(k_e)$ where the minimum of the k_e-distribution within the domain of interest is calculated to be of order 10 m^{-1} using Eq. (8.8) for both configurations. Acoustic convergence has been achieved with the upper bound of k_e set to 200 m^{-1} and 500 m^{-1}, and the number of wavenumbers equals 50 and 125 for the single and double diaphragm configurations, respectively.

The anisotropy model investigated in the present study is compared with the anisotropy data computed from LES. The approach proposed by Lumley and Newman [53] has been adopted thereto. In their approach, the relation between the two invariants $II = -a_{ij}a_{ji}/2$ and $III = \det(a_{ij})$, with $a_{ij} = \tau_{ij}/2K - 1/3$, is used for determining the characteristics of the turbulence. $II = III = 0$ indicates isotropic turbulence, while $II > 0$ and $III \cong 0$ indicates 2-component axisymmetric turbulence. In the present SNGR data, the invariant, III is seen to be very close to zero for the entire flow domain of interest for both single and double diaphragm cases. Hence, the comparison between the anisotropy models and the LES data are made regarding the invariant, II. In Figure 8.5, the II-distribution obtained from the anisotropy model and the LES data are plotted.

The anisotropy model is seen to slightly overestimate the anisotropy for the shear zone until x/D =3.5, while it significantly underestimates the anisotropy in the boundary layer over the duct surface. Similar to the single diaphragm case, the nonlinear model shows some discrepancies in predicting the anisotropy in the shear zone for the double diaphragm configuration as seen in Figure 8.6. Once again, the anisotropy in the boundary layer over the duct surface is underestimated by the model. Another discrepancy is noticed within the region in front of the downstream diaphragm. The model indicates axisymmetric turbulence in this region, while it is close to isotropic according to the LES data. This region is known to be critical for noise generation especially within the plane wave region, hence an effect can be expected on the resulting noise predictions.

The comparison of the computational costs per CPU of a converged simulation obtained by the isotropic and anisotropic implementations of the SNGR method against the LES is given in

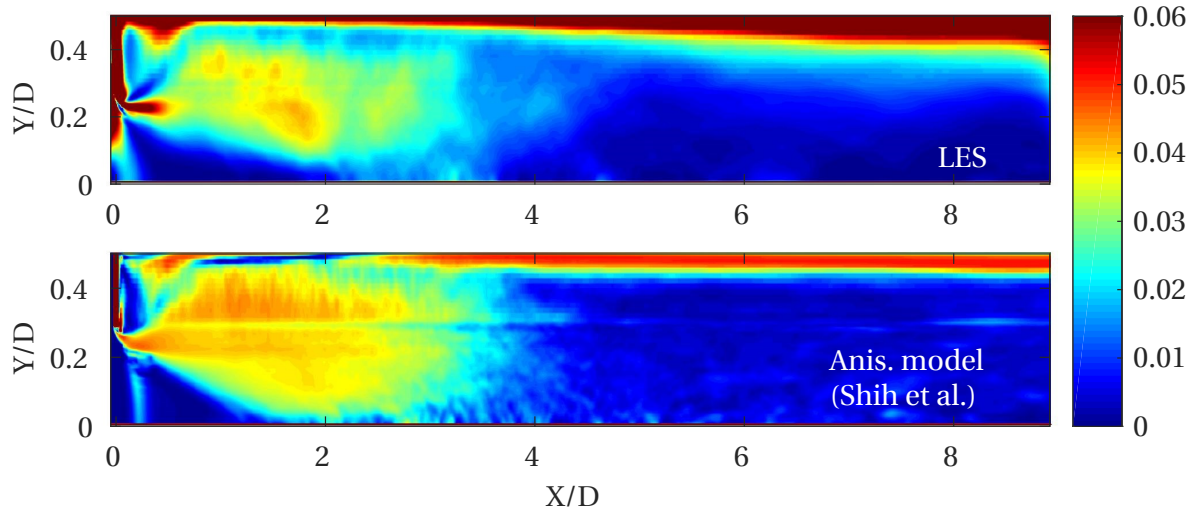

Figure 8.5: Comparison of the anisotropy tensor invariant, II for the single diaphragm case.

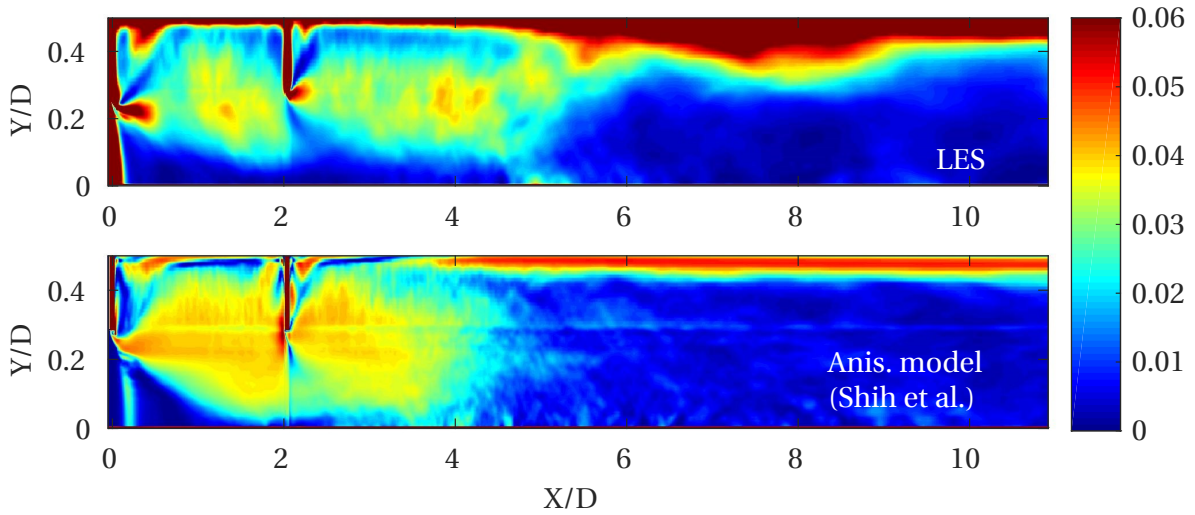

Figure 8.6: Comparison of the anisotropy tensor invariant, II for the double diaphragm case.

Table 8.1.

Table 8.1: The CPU time required per time step for the SNGR method and the LES

	SNGR - Isotropic	SNGR - Anisotropic	LES
CPU time per time step (sec)	352	480	43200

8.5 An automatic grouping scheme for effective storage of noise source data

Applying a source grouping scheme at each SNGR synthesis time step permits to considerably reduce the memory requirement. In free field conditions, the criteria to respect for such agglomeration of sources would merely be the acoustical compactness of the volume in which the sources are summed onto a single point (thereby accounting for leading-order interferential effects), and having the listener in the geometrical far-field of that volume (to neglect amplitude modulation). However, due to the presence of scattering surfaces and of the diaphragm in particular, those criteria are not necessarily sufficient in the present case, and an automatic source grouping procedure is hereby proposed to devise an optimal grouping scheme. The intention is to assess whether a convergence test performed using dummy sources remains valid when aeroacoustically meaningful sources are applied.

The dummy sources are generated over the SNGR mesh, of identical intensity for all frequencies, and locally scaled by the $\overline{u_i u_j}$ data predicted using Eq. (8.19). The phase of the dummy sources was randomly assigned. A total source region of $4D$ length downstream of the diaphragm is taken into consideration and is divided into four cylindrical blocks of $1D$ length similar to the analysis provided in Section 7.3.2. The comparison of the Sound Pressure Level (SPL) radiated at the upstream far-field by the equivalent sources grouped at different levels in each of the four level-0 blocks is depicted in Figure 8.7. It can be seen that the level-0 grouping yields convergence only for sources located at least 1D away from the diaphragm and in the plane wave regime. For frequencies above the first transverse mode cut-off frequency, and even in the plane wave regime for the closest level-0 block, significant discrepancies are observed with the level-1 grouping results.

The non-converged blocks are then octree-refined, and the analysis is repeated for each block and sub-block until convergence within 1 dB over the entire frequency range is achieved. The resulting grouping scheme is illustrated in Figure 8.8. It is then necessary to verify that the above automatic procedure leads to a source grouping scheme that is also valid when the SNGR data are used. The assessment is performed by applying the converged scheme shown in Figure 8.8 to the SNGR data, and comparing the radiated field to that obtained by applying one further refinement iteration to all sub-blocks. Figure 8.9 shows that the two SPLs satisfactorily match for the entire frequency range of interest. The number of source points to be stored in the resulting converged grouping schemes are reduced to 1,872 and 12,176 for the single and double diaphragm configurations, respectively, yielding a reduction of the memory requirement of more than 99% for both configurations.

The negligible contribution of the sources located beyond $4D$ downstream of the single diaphragm is demonstrated in Figure 8.10, where the radiated SPL (still at the same listener location) has been obtained for increasing spatial extends from $2D$ to $4D$ downstream of the diaphragm. Convergence is already obtained for a $4D$ axial extend.

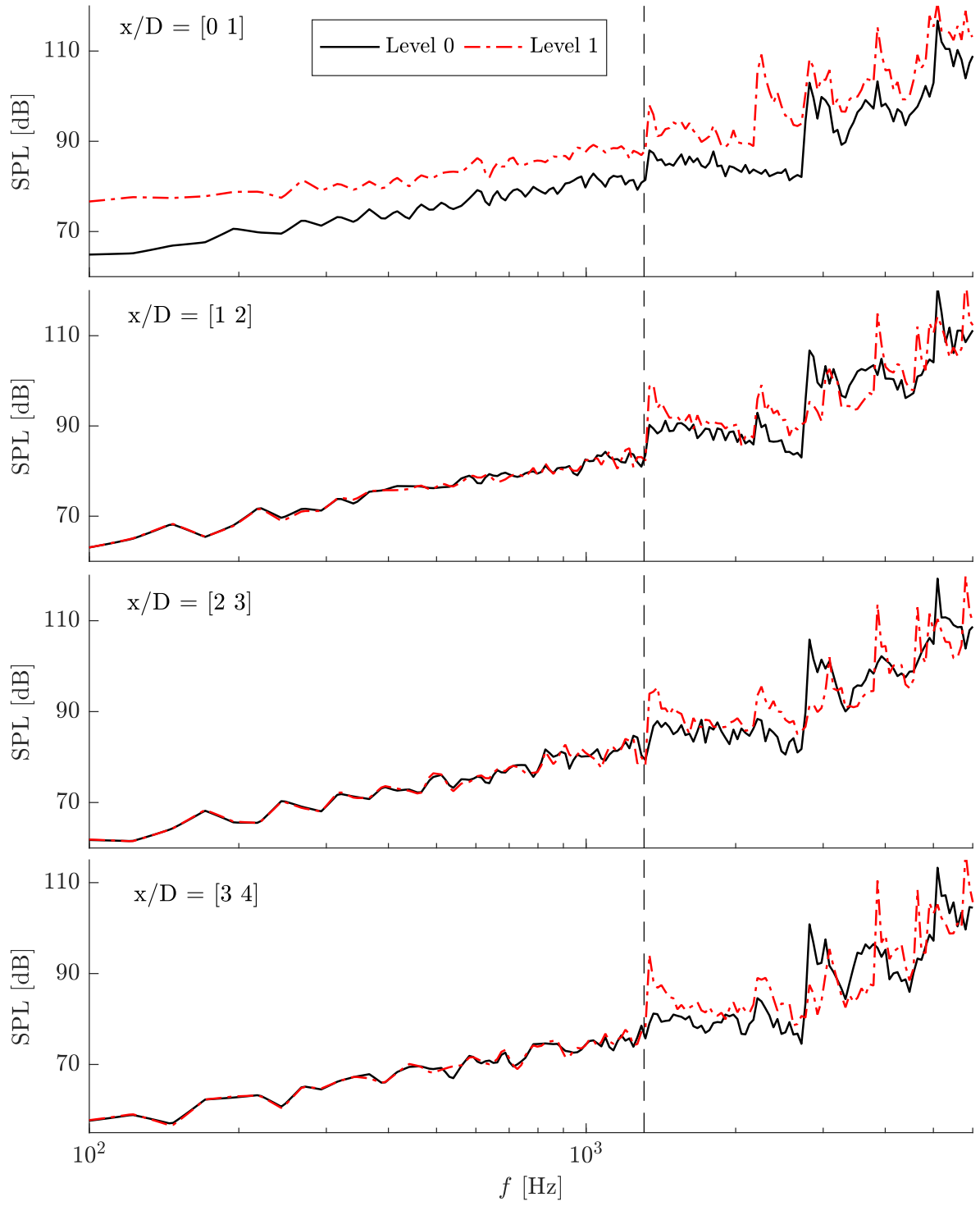

Figure 8.7: Acoustic response comparison of the four blocks grouped at levels 0 and 1. The vertical dashed lines indicate the first cut-off frequency.

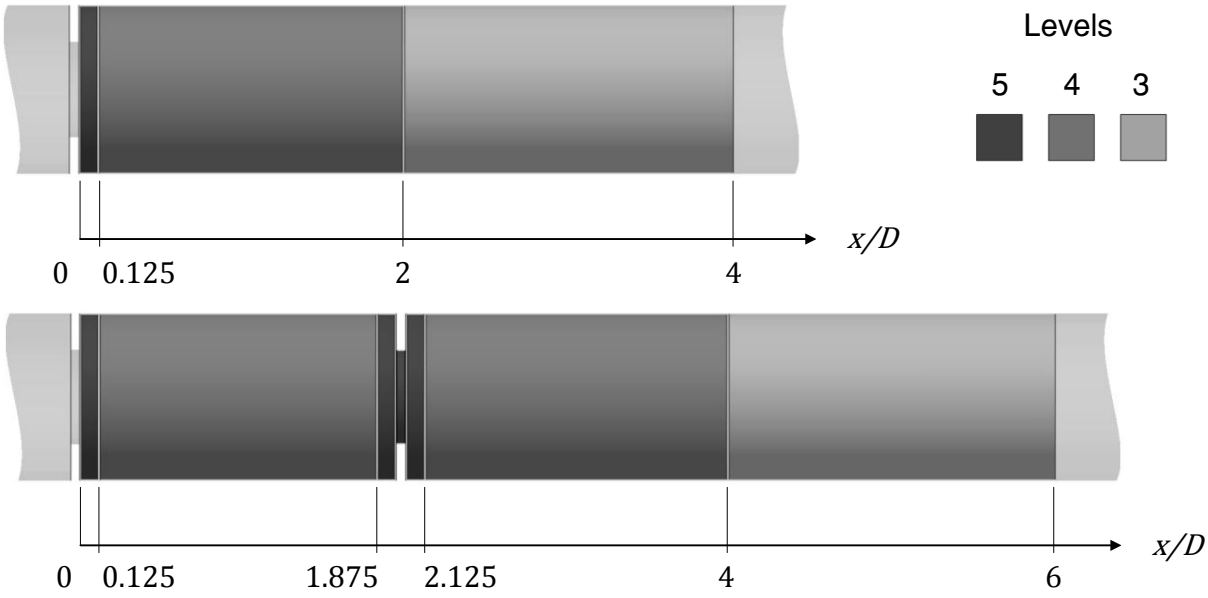

Figure 8.8: Converged grouping schemes for the single and the double diaphragm configurations.

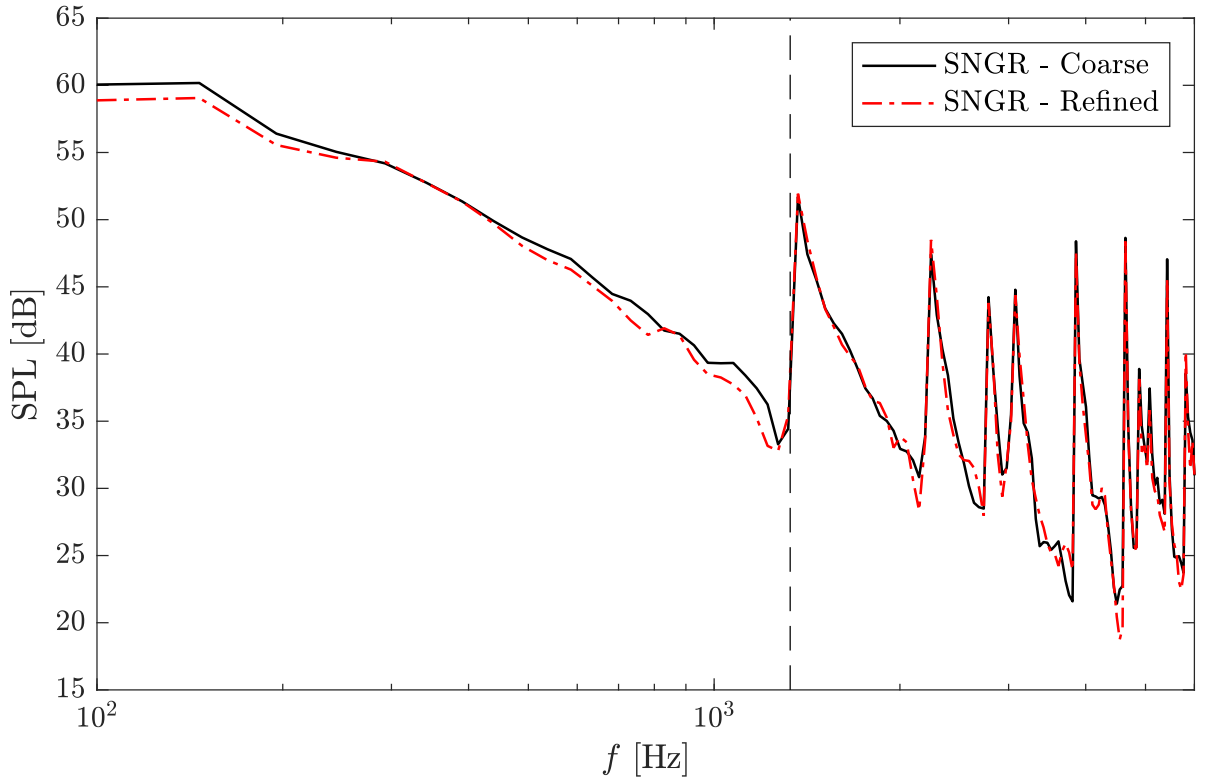

Figure 8.9: Noise predictions obtained using the coarse and refined grouping schemes.

8.6 Comparison between acoustic predictions obtained from SNGR and LES data

The LES comparisons of the SNGR results are done using the synthetic data based on the mean LES, to be able distinguish between the errors due to the method itself, and the discrepancies in

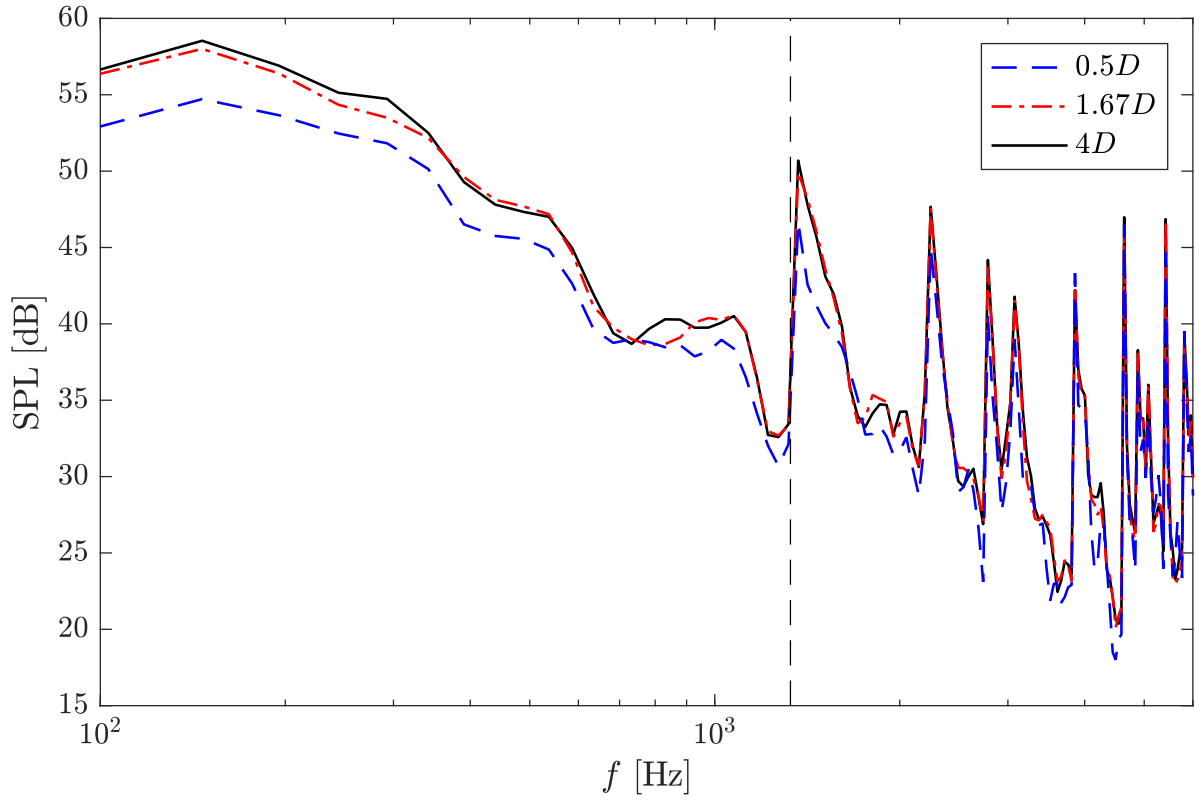

Figure 8.10: Noise predictions obtained using source regions of different axial extends for the single diaphragm case.

the mean flow data. The effects of the anisotropy correction developed in Section 8.2.1, and the temporal filter proposed in Section 8.3 are discussed respectively, in the next two subsections.

8.6.1 Effect of the anisotropy correction

A comparison of the acoustic responses obtained from the SNGR method with and without the anisotropy correction, and from the LES data, is given in Figure 8.11. Using the proposed temporal filter and the non-linear anisotropy model, a very good match between the SNGR- and LES-based predictions is observed for the single diaphragm case. In contrast, an overestimation of 20 dB, about constant over the full frequency range, is obtained without the anisotropy correction. That correction consists in reorienting and scaling the velocity vectors to meet the targeted axisymmetric anisotropic character, but without changing the invariants of Lighthill's stress tensor. It can therefore be expected that the anisotropic flow field generates less noise than the isotropic one, as the correction reduces the amplitude of the off-diagonal elements of the Lighthill's stress tensor.

For the double diaphragm configuration, the effect of the anisotropy correction is seen in Figure 8.12 to depend on the frequency. Surprisingly, it improves the match with the LES-based prediction in the high frequency range (above 3 kHz), but degrades the agreement in the low frequency range (below 400 Hz). This result is somewhat counter-intuitive considering that the

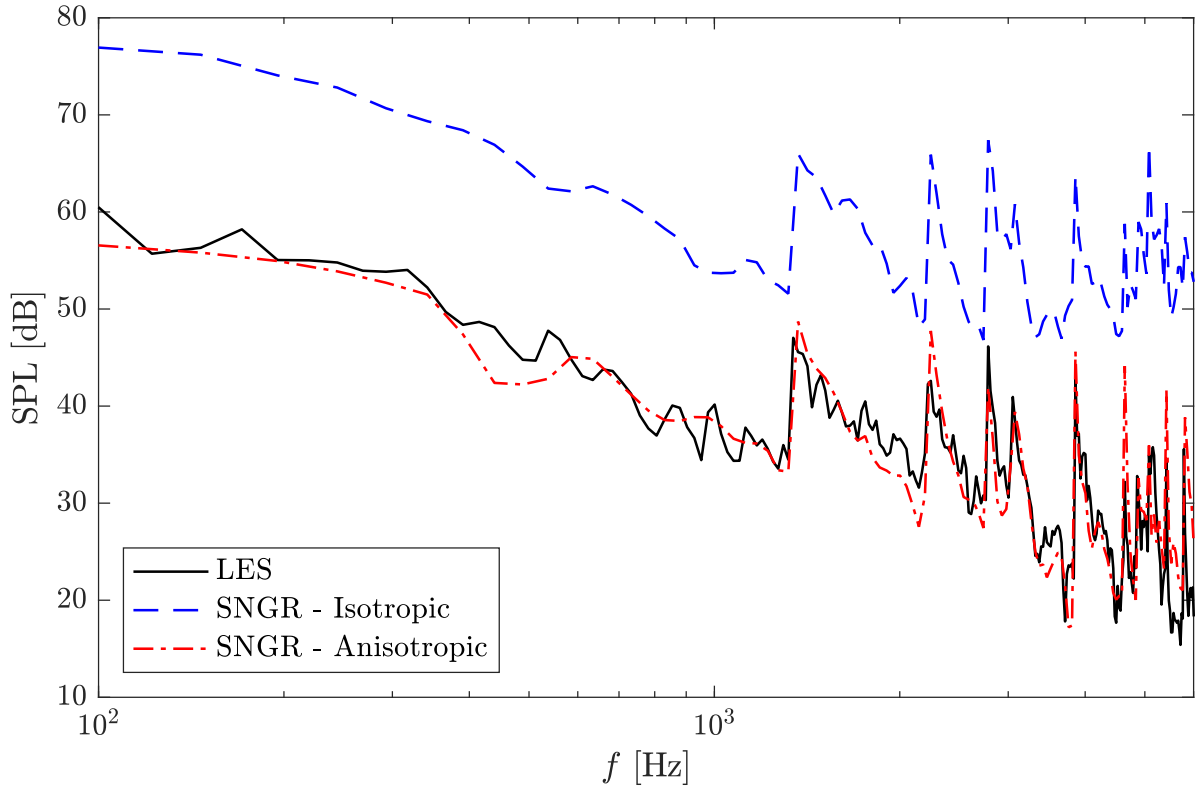

Figure 8.11: Far-field noise comparison of the SNGR implementations with or without anisotropy correction vs. LES in the single diaphragm case.

smallest turbulence scales are usually found to be more isotropic than the largest ones.

8.6.2 Effect of the temporal filter

It was mentioned in Section 8.3 that the temporal filter used in the SNGR method is expected to have a significant effect on the noise prediction for the single diaphragm case, due to possible acoustic contribution of the flow regions with almost zero convection velocity. To see this effect, the noise prediction by the SNGR method with the cascaded temporal filter is compared to that of the original method of Bilsson *et al* in Figure 8.13. The anisotropy correction is applied for both implementations. As the original temporal filter yields a shallower spectrum, a similar behavior in the resulting acoustic response is observed. It is seen in Figure 8.13 that the SNGR method of Bilsson *et al*. underestimates the far-field noise for frequencies lower than 1300 Hz, while an overestimation is observed for higher frequencies.

A similar conclusion is reached for the double diaphragm case as shown in Figure 8.14, although the effect is less pronounced. A possible reason is that the convection velocities of the dominant noise sources are larger for the double diaphragm case than for the single diaphragm case. Hence the temporal de-correlation effect is possibly less important compared with the convective effect.

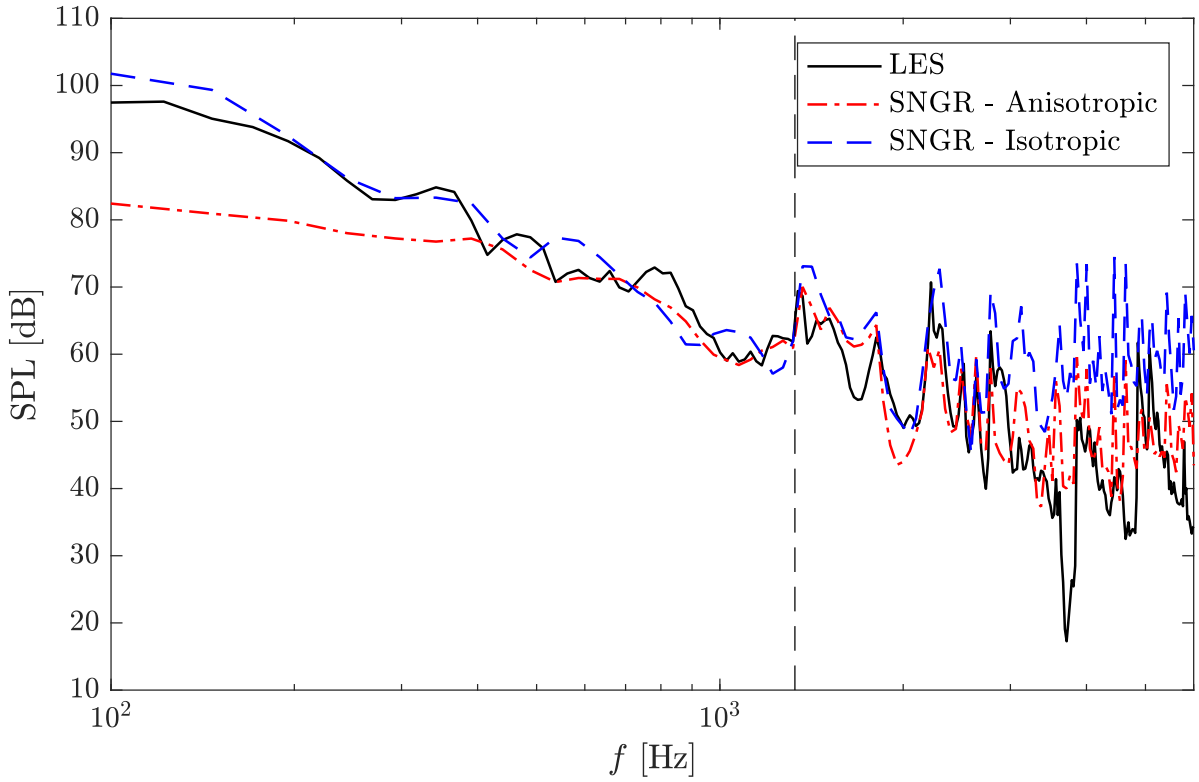

Figure 8.12: Far-field noise comparison of the SNGR implementations with or without anisotropy correction vs. LES in the double diaphragm case.

8.7 Comparison of the noise predictions obtained from the RANS-based SNGR syntheses against the LES data

Once it is verified that SNGR method is fairly reproducing the flow generated noise given the proper flow fields, the method is now implemented based on the axisymmetric RANS predictions and compared against the LES results in Figures 8.15, 8.16, 8.17 and 8.18. The SNGR predictions using the mean flow data from the first five low-Re $k-\epsilon$ models do particularly match the LES predictions for a wide range of frequency in the single diaphragm case. The standard $k-\epsilon$ and YS models underpredicts the noise which is also the case for the turbulent kinetic energy predictions. It is an expected result since the synthetic flow field is scaled with respect to turbulent kinetic energy. All the models yield poor prediction of the noise generated by the tandem diaphragms, due to not properly capturing the turbulence generation mechanisms.

8.8 Conclusions

The applicability of the SNGR method for the prediction of the noise emitted by single and double ducted diaphragms has been investigated. An analytical solution has been used for the propagation problem in order to avoid the effect of numerical propagation errors and focus

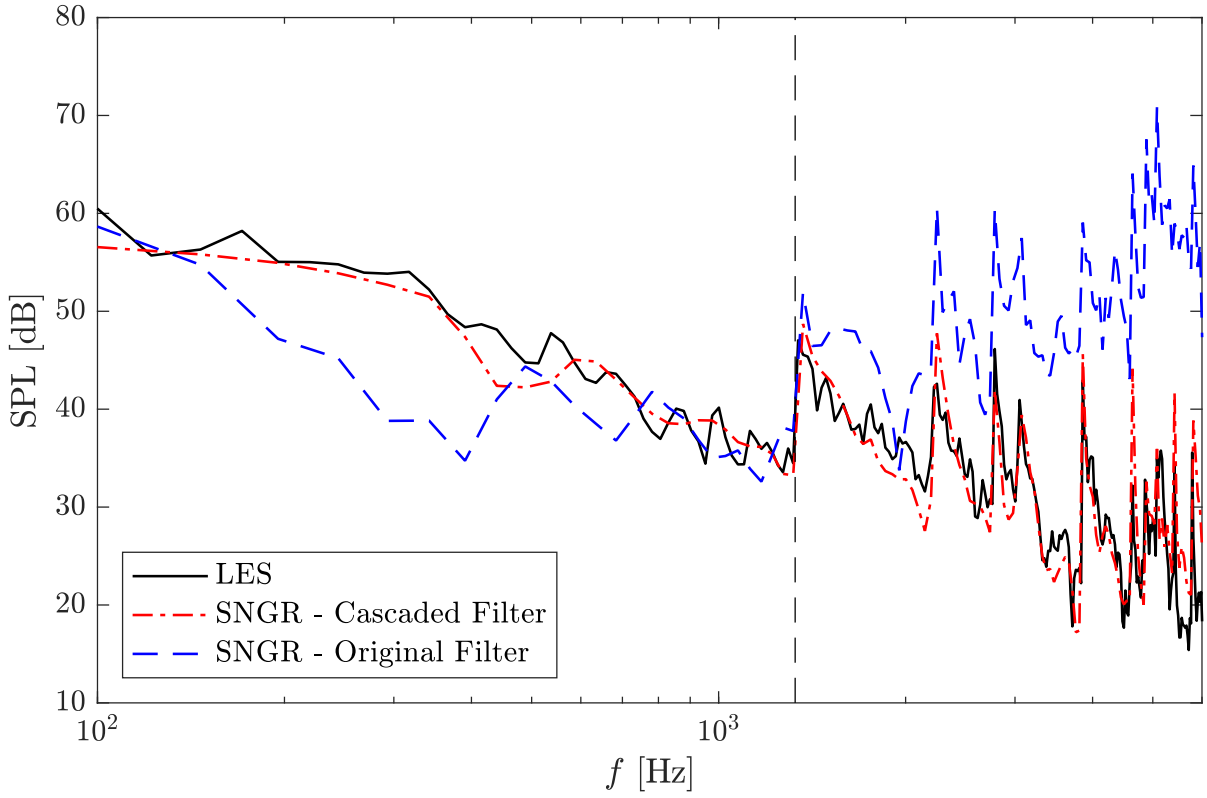

Figure 8.13: Far-field noise comparison of the SNGR implementations with different temporal filters vs. LES in the single diaphragm case.

the analysis on the accuracy of the source reconstruction. The required flow data have been obtained from LES statistics. A cascaded filter has been proposed, which was shown to yield a better match of the turbulence spectral decay with the LES data, than using the previously published temporal filter. An anisotropy correction has been implemented as well, which was shown to have a significant effect on the space-time correlation of the synthesized flow field. Lighthill's aeroacoustic analogy has been used for computing the noise sources, and the propagation problem has been solved using a tailored Green's function for ducted diaphragms. A significant reduction of the memory requirement and CPU time has been attained by applying a grouping scheme that was automatically optimized on the basis of dummy source data, and which should therefore not depend on the specific source data used in later calculations. This has been verified using the SNGR dataset. The noise generated by the ducted diaphragm(s) was proven to be quite accurately predicted through comparison with the LES-based result, provided that an accurate anisotropy model and a temporal filter with the correct spectral decay are applied. In particular, the benefit of introducing an anisotropy correction was quite clear for the single diaphragm case, but was shown to depend on the frequency range for the double diaphragm configuration. The good match between the SNGR and the LES results, where the CPU cost of the SNGR approach was about $1/50^{\text{th}}$ of the LES CPU cost, indicates that such stochastic methods are a viable option for this category of flows and could be used for optimization purposes.

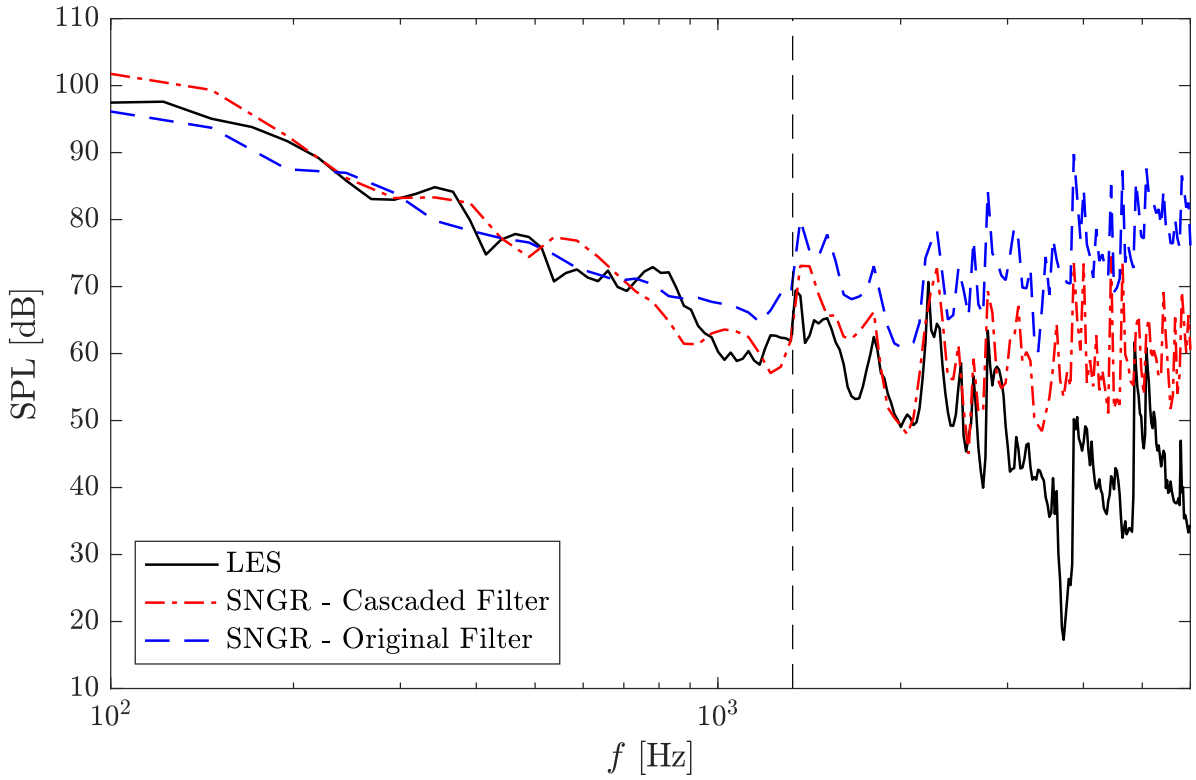

Figure 8.14: Far-field noise comparison of the SNGR implementations with different temporal filters vs. LES in the double diaphragm case.

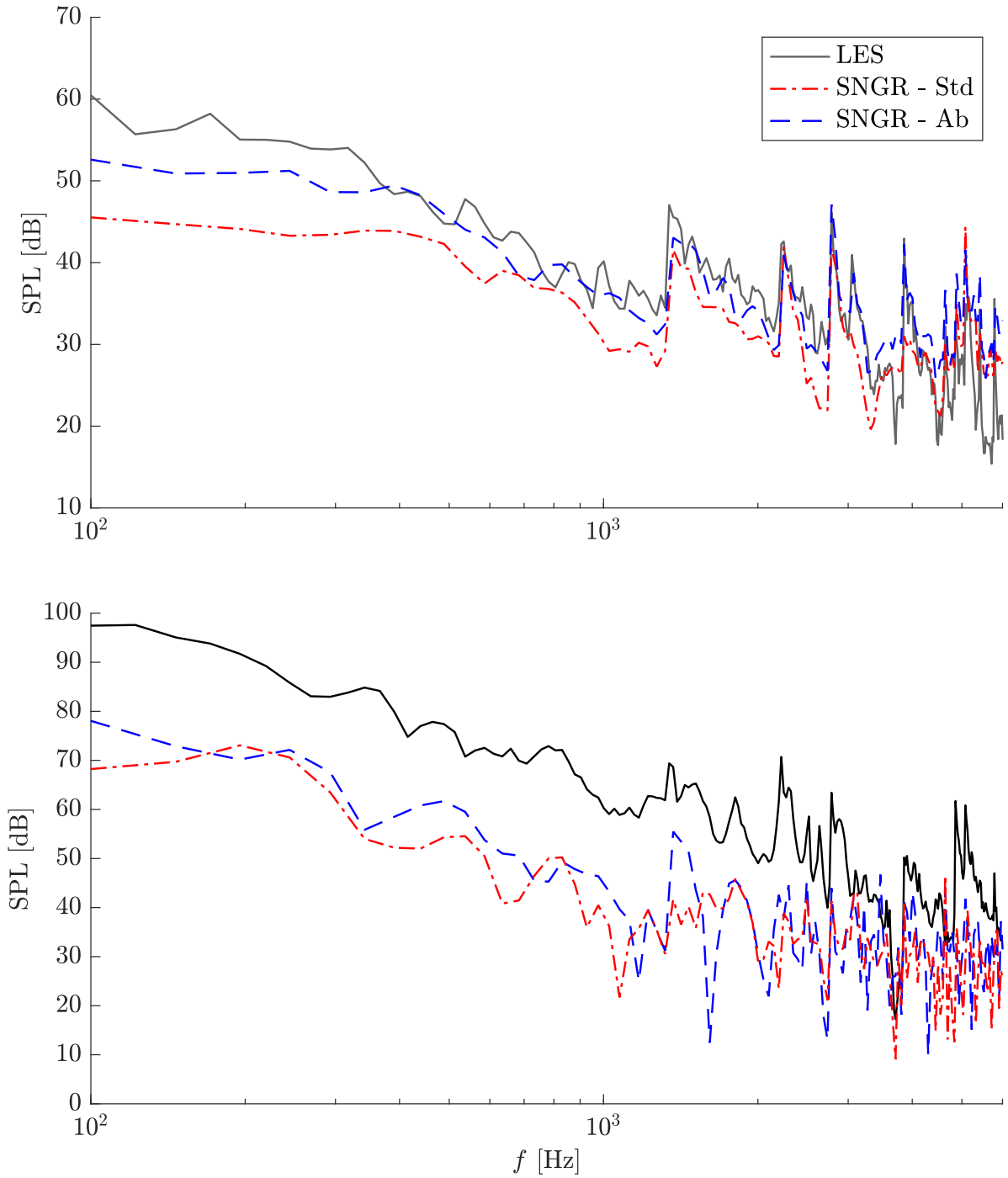

Figure 8.15: Far-field noise comparison of the SNGR implementations based on different RANS solutions vs. LES in the single (top) and double (bottom) diaphragm cases.

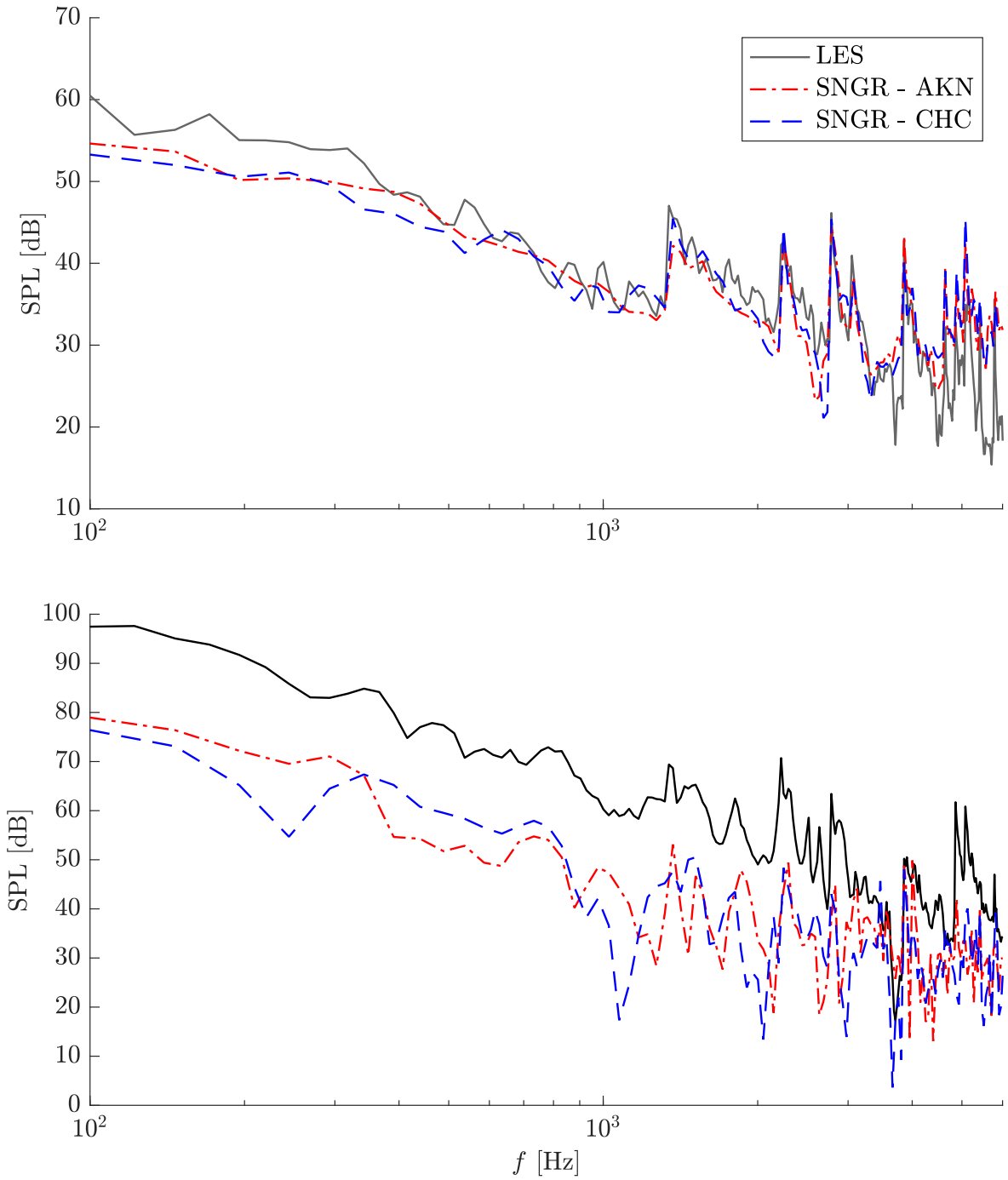

Figure 8.16: Far-field noise comparison of the SNGR implementations based on different RANS solutions vs. LES in the single (top) and double (bottom) diaphragm cases.

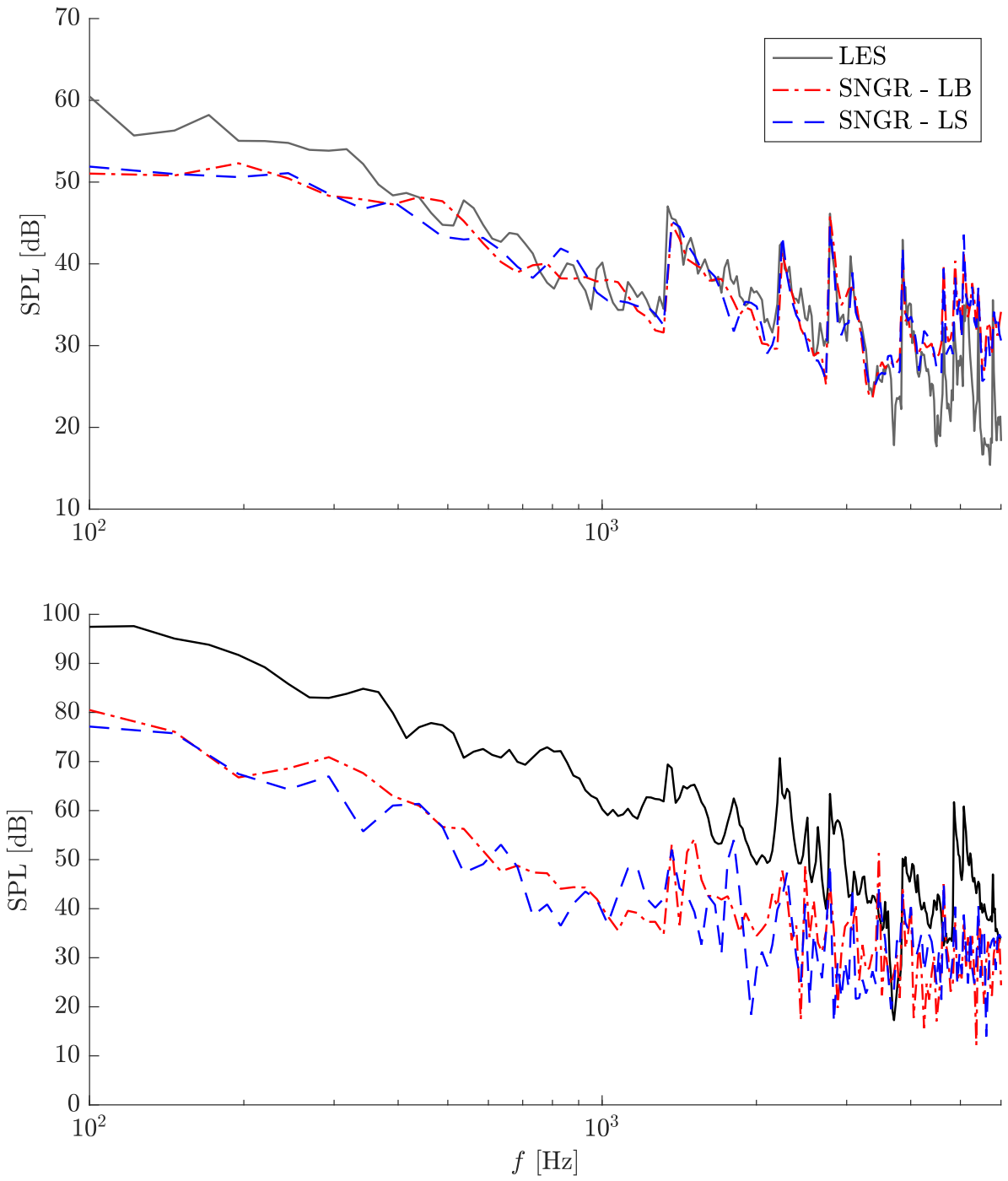

Figure 8.17: Far-field noise comparison of the SNGR implementations based on different RANS solutions vs. LES in the single (top) and double (bottom) diaphragm cases.

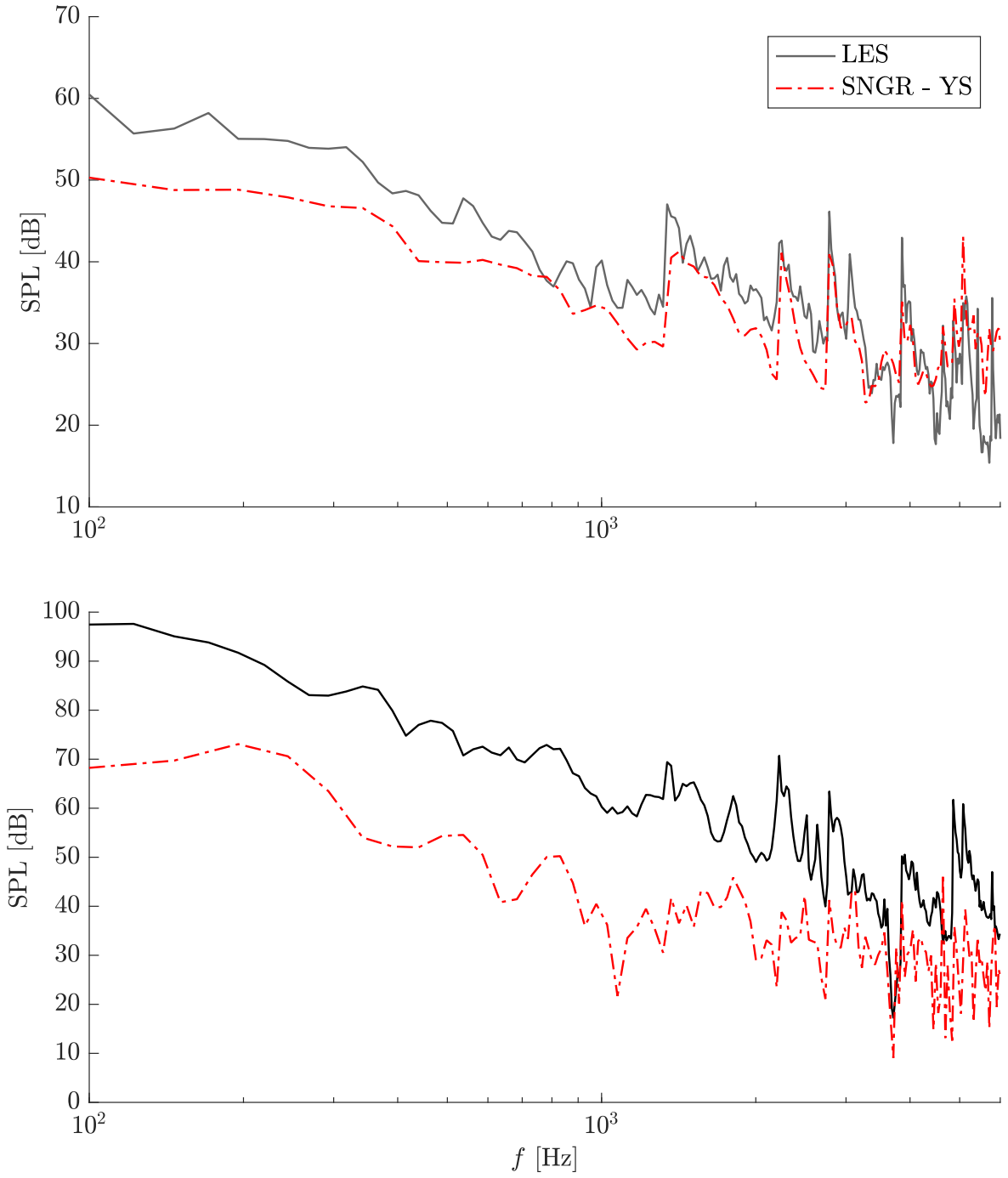

Figure 8.18: Far-field noise comparison of the SNGR implementations based on different RANS solutions vs. LES in the single (top) and double (bottom) diaphragm cases.

9 Concluding remarks

Experimental and numerical investigations of the ducted diaphragm noise were presented in this thesis. The problem of noise emitted by ducted diaphragms was considered to represent the noise generation that takes place in HVAC systems. The primary goal of the study was to develop a numerical tool providing fast and accurate prediction of ducted diaphragm noise. Development of such a tool involved bringing various analytical and numerical concepts together, and besides, a detailed experimental investigation to provide a reference solution to the problem. To meet the goal of having a 'fast' tool, a stochastic approach was adopted for the prediction of ducted diaphragm noise. The two main issues encountered in the study were lack of an existing stochastic approach yielding satisfactory predictions of duct noise, and significantly high computational costs required when numerically solving the propagation of the noise emitted by the volumetric sources inside the duct. Besides, a contamination issue was encountered in the experimental investigation. The reflections from the duct ends were observed to contaminate the measured acoustic field. The content of the thesis work was then shaped around these four issues.

The existing method of Lavrentjev *et al.* [49] for source identification in ducted flows was implemented to the ducted diaphragm cases investigated in the thesis. Some sensitivity issues related to the common approach of using the passive measurements to determine the duct termination reflection coefficients in the presence of perforated/lined duct elements were addressed. It was shown that when a lined or perforated module was installed at the duct end, the reflectivity of the duct end became highly sensitive to the acoustic conditioning, particularly at low frequencies. A plausible explanation for such a phenomenon was considered to be the non-linear interaction of the duct acoustic field with the small cavities contained on the lined/perforated surfaces, modifying the duct end reflectivity. The importance of computing the duct end reflection coefficient for every particular flow case being investigated was then pointed out. As a remedy, use of the turbulent flow noise itself for the determination of the duct end reflection coefficients was proposed, and the validity of the assumption was experimentally verified.

To overcome the excessive computational cost of numerically solving the propagation of the noise emitted by the quadrupolar sources contained within the duct, the simplicity of the axisymmetric configurations investigated in the thesis was exploited, and an analytical solution was derived. Derivation of a tailored Green's function for ducted diaphragms in the form of infinite series reduced the computational errors to the truncation level occurring due to the finite summation of the infinite series. An extension of the analytical solution to the tandem diaphragm case was introduced to increase the applicability of the approach. Despite suffering from being hard to be generalized, the proposed analytical solution provided an almost exact solution to the present problem. It can also serve as a benchmark tool to test the accuracy of various numerical approaches.

To the author, the most important factor by which the duct noise problem differ from other noise

problems is that the duct modes shape the overall spectrum of the resulting noise to a significant extent, which is not the case for un-ducted cases. This makes the noise prediction problem relatively easy by finding some other target parameters effective in noise generation. For the present case of ducted diaphragm, the vast number of numerical investigations performed throughout the thesis work revealed that the shape of the noise spectrum of a given duct flow was mainly determined by the spectral decay of the sources in the frequency domain. Besides, anisotropy acts as an important factor scaling the resultant prediction. A source field satisfying these two criteria was observed to reproduce the noise generated by a target flow field. A method controlling these two parameters was devised by using Billson's Stochastic Noise Generation and Radiation method with a modified temporal filter ensuring the synthetic field to face the same spectral decay as the actual flow. When combined with a proper anisotropy correction, very accurate noise predictions could be achieved at significantly lower costs compared to the scale-resolved approaches. The author believes that such an approach can be used to solve a range of aeroacoustic problems provided that a dataset for tabulated estimates of the key parameters affecting the noise generation is constructed for various flow configurations.

Appendices

A Comparison of the mean velocity and turbulent kinetic energy

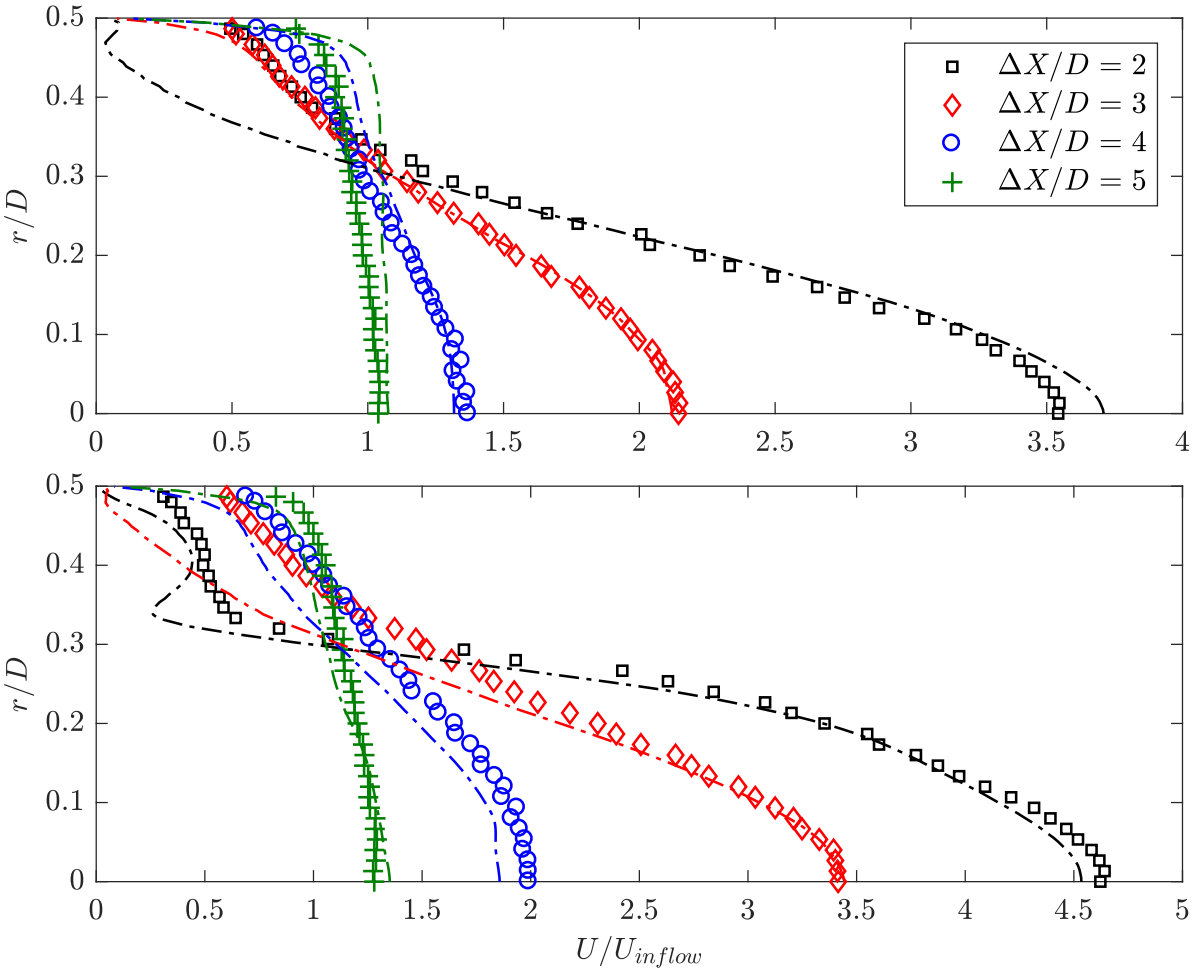

Figure A.1: Comparison of the mean velocity predicted by LES (dash-dotted) against the experimental data (markers) at cross-sections in the downstream section. $x = 0$ correspond to the upstream diaphragm.

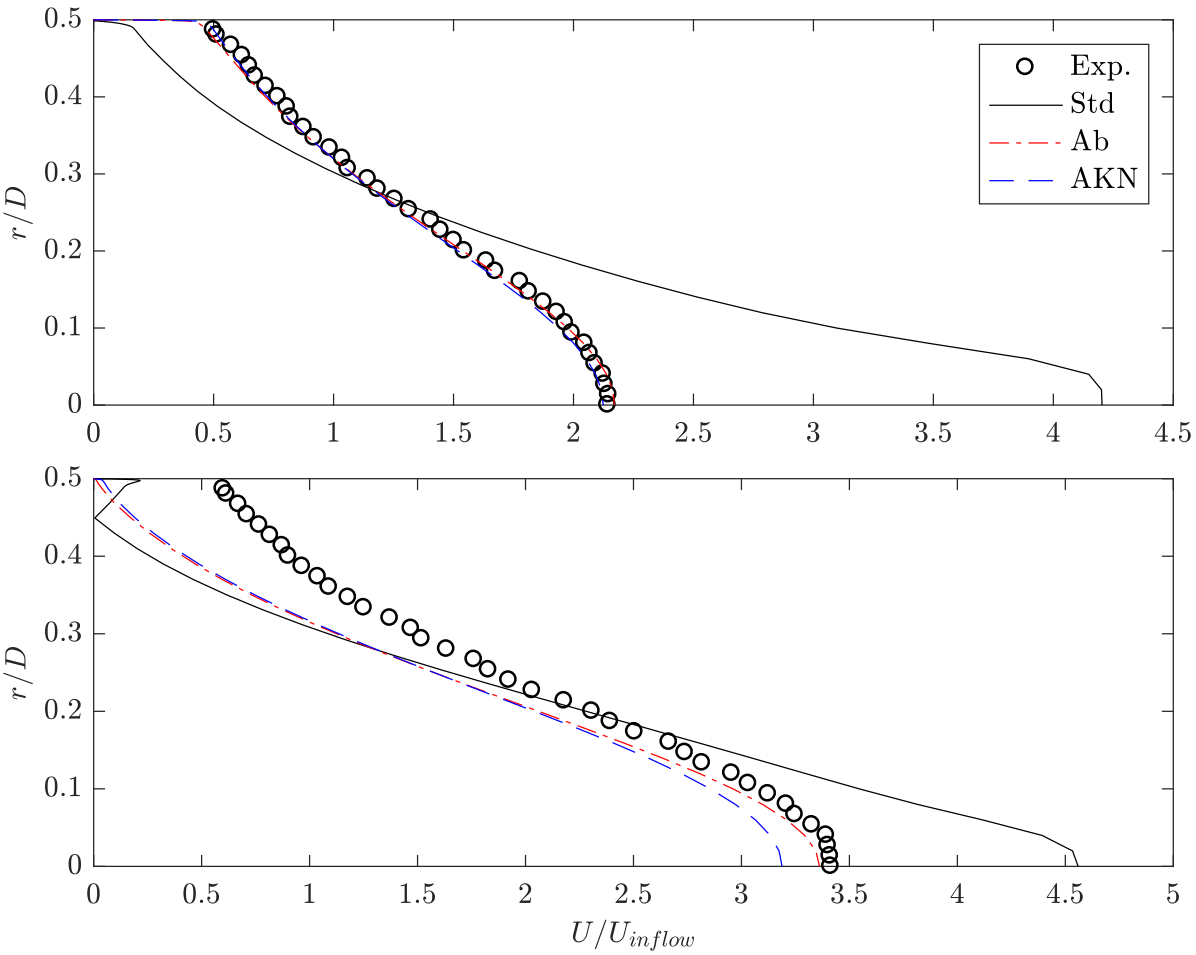

Figure A.2: Comparison of the mean velocity predicted by the standard $k-\epsilon$, Ab and AKN models against the experimental data at $x = 3D$ and $x = 1.15D$ for the single and tandem diaphragm cases, respectively.

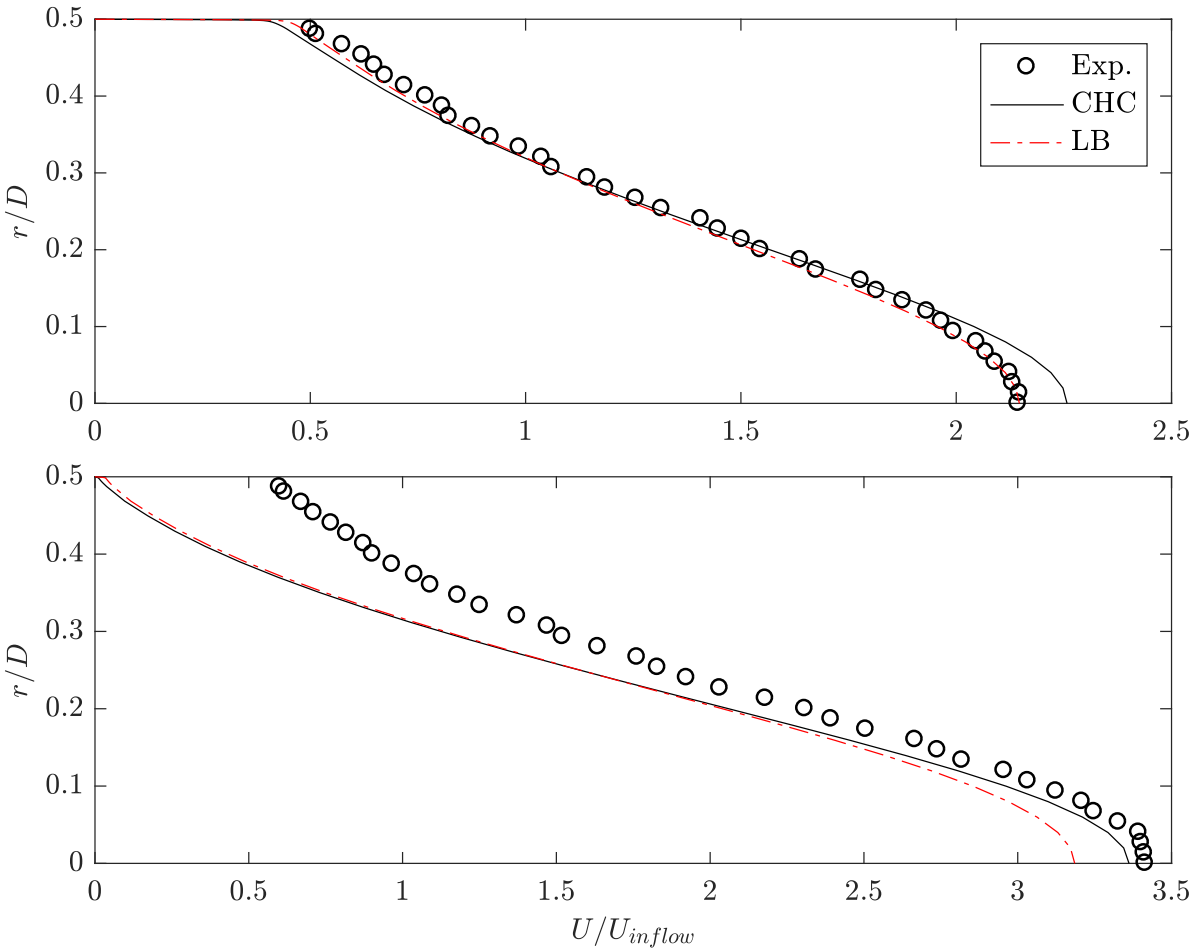

Figure A.3: Comparison of the mean velocity predicted by the CHC and LB models against the experimental data at $x = 3D$ and $x = 1.15D$ for the single and tandem diaphragm cases, respectively.

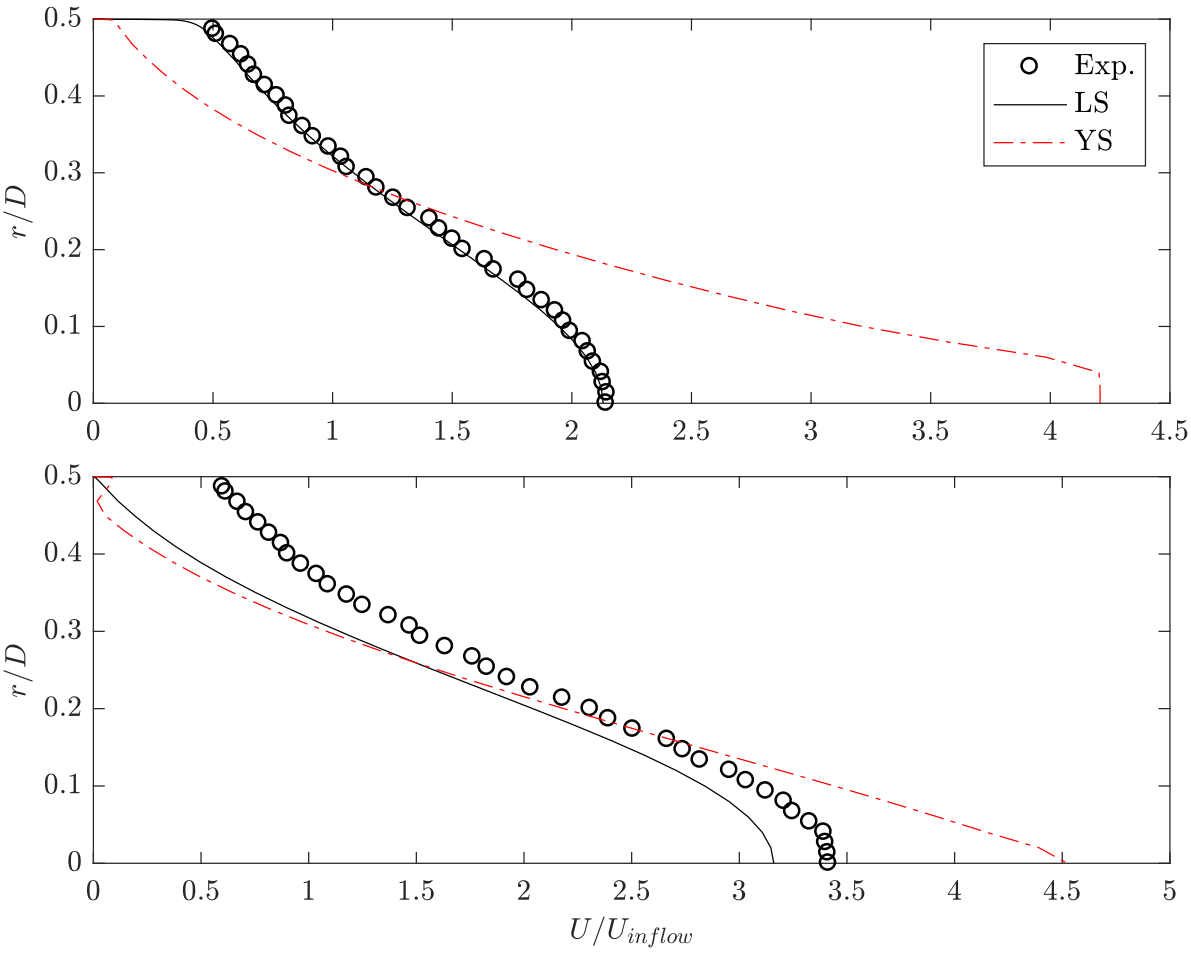

Figure A.4: Comparison of the mean velocity predicted by the LS and YS models against the experimental data at $x = 3D$ and $x = 1.15D$ for the single and tandem diaphragm cases, respectively.

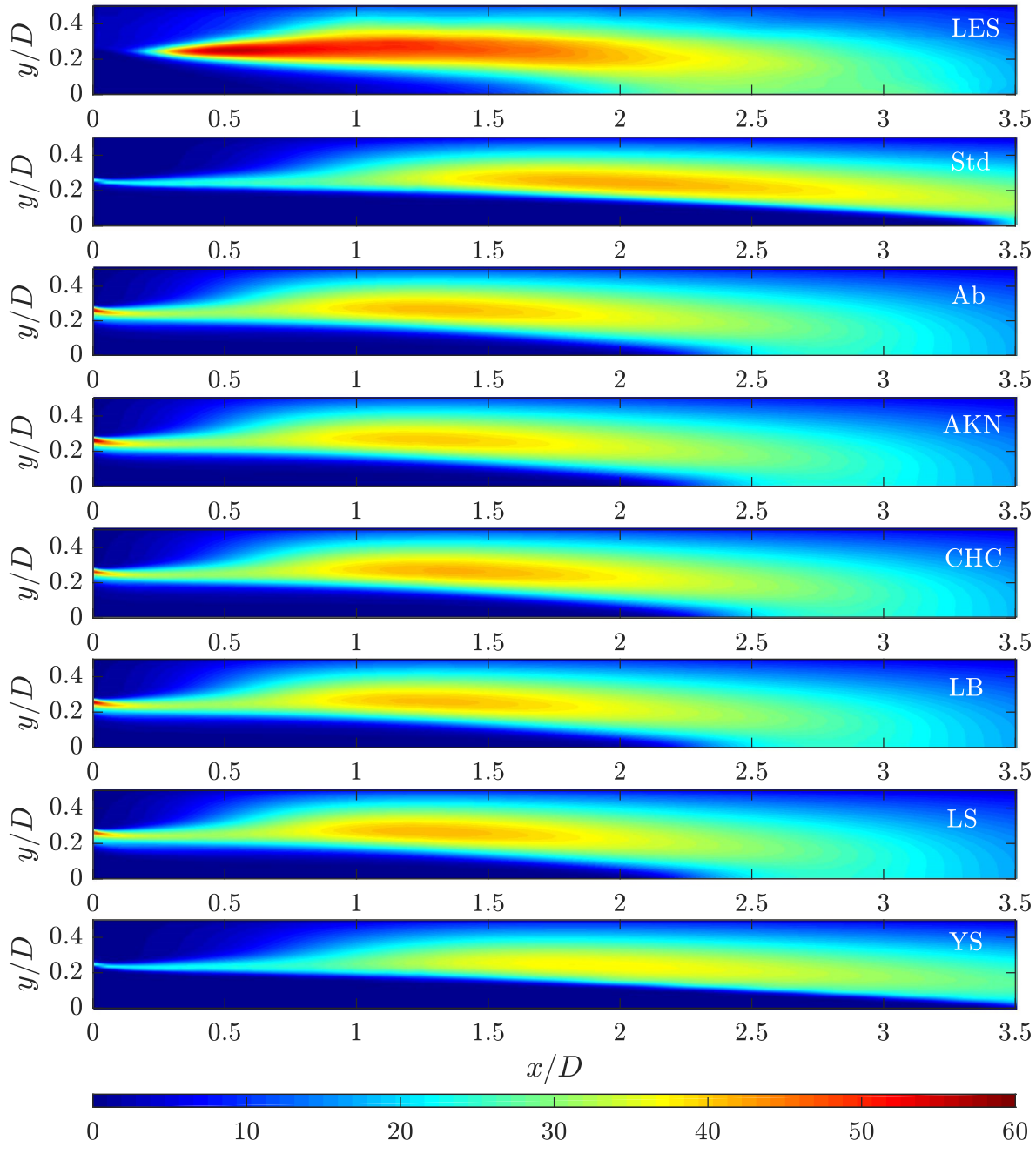

Figure A.5: Comparison of the turbulent kinetic energy distribution of the RANS models against the LES results for the single diaphragm case.

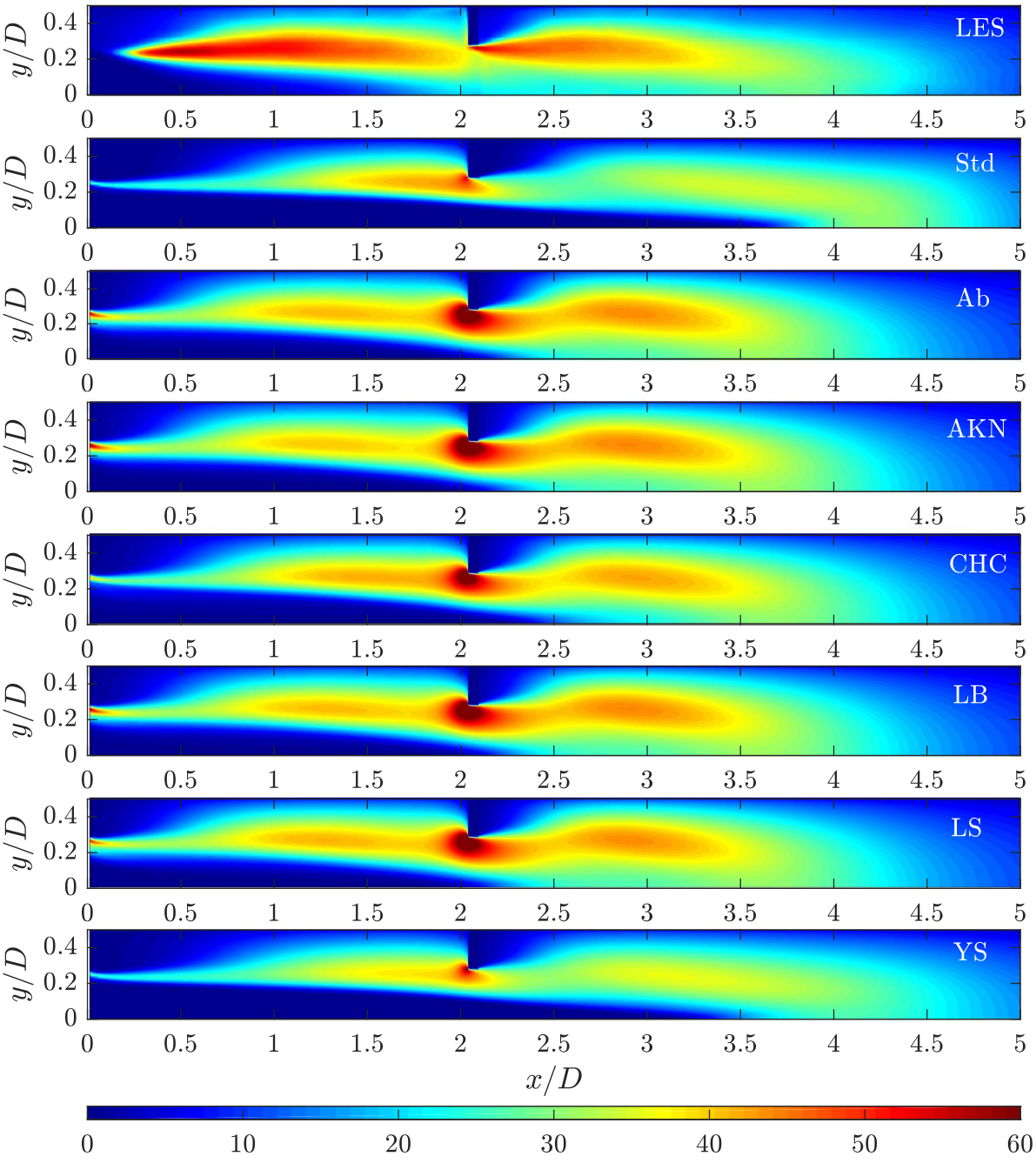

Figure A.6: Comparison of the turbulent kinetic energy distribution of the RANS models against the LES results for the tandem diaphragm case.

B Notes on tailored Green's function

B.1 Derivative Terms for Tailored Green's Function

$$F_{,x} = 0 \tag{B.1}$$
$$F_{,y} = \alpha_{m\mu}\cos(\theta_0)J'_m(\alpha_{m\mu}r_0) \tag{B.2}$$
$$F_{,z} = \alpha_{m\mu}\sin(\theta_0)J'_m(\alpha_{m\mu}r_0) \tag{B.3}$$
$$H_{,x} = \pm ik_{m\mu} \tag{B.4}$$
$$H_{,y} = -im\sin(\theta_0)/r_0 \tag{B.5}$$
$$H_{,z} = im\cos(\theta_0)/r_0 \tag{B.6}$$
$$F_{,yy} = \alpha^2_{m\mu}\cos(\theta_0)^2 J''_m(\alpha_{m\mu}r_0) + \alpha_{m\mu}\frac{\sin(\theta_0)^2}{r_0}J'_m(\alpha_{m\mu}r_0) \tag{B.7}$$
$$F_{,yz} = \alpha^2_{m\mu}\sin(\theta_0)\cos(\theta_0)J''_m(\alpha_{m\mu}r_0) - \alpha_{m\mu}\frac{\sin(\theta_0)\cos(\theta_0)}{r_0}J'_m(\alpha_{m\mu}r_0) \tag{B.8}$$
$$F_{,zz} = \alpha^2_{m\mu}\sin(\theta_0)^2 J''_m(\alpha_{m\mu}r_0) + \alpha_{m\mu}\frac{\cos(\theta_0)^2}{r_0}J'_m(\alpha_{m\mu}r_0) \tag{B.9}$$
$$H_{,xx} = 0 \tag{B.10}$$
$$H_{,xy} = 0 \tag{B.11}$$
$$H_{,xz} = 0 \tag{B.12}$$
$$H_{,yy} = 2im\sin(\theta_0)\cos(\theta_0)/r_0^2 \tag{B.13}$$
$$H_{,yz} = im\big(\sin(\theta_0)^2 - \cos(\theta_0)^2\big)/r_0^2 \tag{B.14}$$
$$H_{,zz} = -2im\sin(\theta_0)\cos(\theta_0)/r_0^2 \tag{B.15}$$

B.2 An extension to include the diaphragm thickness effects

The tailored Green's function derived in Eq. (6.13) assumes an infinitely thin diaphragm. To include the thickness effects, the sudden contraction and expansion problems are to be combined in a recursive manner. The analysis starts with derivation of a tailored Green's function for a single discontinuity inside a duct. Similar to the single diaphragm case investigated in Section 6.2, the reflected and the transmitted parts of the Green's function corresponding to a

single azimuthal mode, m and a given angular frequency ω;

$$G_{\omega m,ref} = \sum_{\mu=1}^{\infty} B_{m\mu} U_{m\mu} e^{i(\pm k_{m\mu} x - m\vartheta)} \tag{B.16}$$

$$G_{\omega m,tr} = \sum_{\mu=1}^{\infty} C_{m\mu} \hat{U}_{m\mu} e^{i(\mp k_{m\mu} x - m\vartheta)} \tag{B.17}$$

where

$$B_{m\mu} = \sum_{\nu=1}^{\infty} R_{m\mu\nu} A_{m\nu} \rightarrow \mathbf{B} = \mathbf{RA}, \tag{B.18}$$

and

$$C_{m\mu} = \sum_{\nu=1}^{\infty} T_{m\mu\nu} A_{m\nu} \rightarrow \mathbf{C} = \mathbf{TA}, \tag{B.19}$$

and $U_{m,\mu}$ and $\hat{U}_{m,\mu}$ are the orthonormal radial components for the duct sections with radii, a and b respectively. The continuity of pressure and axial velocity at the discontinuity, located at $x = D$ respectively yields;

$$\sum_{\nu=1}^{\infty} (R_{m\mu\nu} A_{m\nu} e^{ik_{m\nu}D} + A_{m\nu} e^{-ik_{m\nu}D}) U_{m\nu} = \sum_{\nu=1}^{\infty} T_{m\mu\nu} A_{m\nu} \hat{U}_{m\nu} e^{-ik_{m\nu}D}, \tag{B.20}$$

$$\sum_{\nu=1}^{\infty} k_{m\nu} (R_{m\mu\nu} A_{m\nu} e^{ik_{m\nu}D} - A_{m\nu} e^{-ik_{m\nu}D}) U_{m\nu} = \sum_{\nu=1}^{\infty} -k_{m\nu} T_{m\mu\nu} A_{m\nu} \hat{U}_{m\nu} e^{-ik_{m\nu}D}. \tag{B.21}$$

Once again, given Eqs. (B.20) and (B.21), the solution for the reflection and the transmission matrices, **R** and **T** cannot be uniquely obtained due to not defining any boundary conditions for the edge of the discontinuity. A solution on the other hand is obtained by assuming the scattering being independent of the source strength as follows:

$$\sum_{\nu=1}^{\infty} (R_{m\mu\nu} e^{ik_{m\nu}D} + e^{-ik_{m\nu}D}) U_{m\nu} = \sum_{\nu=1}^{\infty} T_{m\mu\nu} \hat{U}_{m\nu} e^{-ik_{m\nu}D}, \tag{B.22}$$

$$\sum_{\nu=1}^{\infty} k_{m\nu} (R_{m\mu\nu} e^{ik_{m\nu}D} - e^{-ik_{m\nu}D}) U_{m\nu} = \sum_{\nu=1}^{\infty} -k_{m\nu} T_{m\mu\nu} \hat{U}_{m\nu} e^{-ik_{m\nu}D}. \tag{B.23}$$

The linearity of the problem allows treating each μ-mode separately. Taking the inner product of the Eqs. (B.22) and (B.23)for the interval $0 < r < b$ using $\hat{U}_{m\lambda}$ and $U_{m\lambda}$ as the basis function respectively, the following expressions are obtained:

$$\sum_{\nu=1}^{\infty} \langle \hat{U}_{m\lambda}, U_{m\nu} \rangle_b (R_{m\nu} e^{ik_{m\nu}D} + e^{-ik_{m\nu}D}) = T_{m\lambda} e^{-ik_{m\lambda}D}, \tag{B.24}$$

$$k_{m\lambda} (R_{m\lambda} e^{ik_{m\lambda}D} - e^{-ik_{m\nu}D}) = \sum_{\nu=1}^{\infty} -\langle U_{m\lambda}, \hat{U}_{m\nu} \rangle_b k_{m\nu} T_{m\mu\nu} e^{-ik_{m\nu}D}. \tag{B.25}$$

Eqs. (B.24) and (B.25) can be written in matrix form as follows:

$$\mathbf{M}(\mathbf{RE}^{+} + \mathbf{E}^{-}) = \mathbf{TE}^{-}, \tag{B.26}$$

$$\mathbf{K}(\mathbf{RE}^{+} - \mathbf{E}^{-}) = \mathbf{M}^{\top}\mathbf{LTE}^{-}, \tag{B.27}$$

where $\mathbf{M} \equiv \langle \hat{U}_{m\lambda}, U_{m\nu} \rangle_b$, $\mathbf{E}^{\pm} \equiv \delta_{\lambda\nu} e^{\pm ik_{m\lambda}D}$, $\mathbf{K} \equiv \delta_{\lambda\nu} k_{m\lambda}$, and $\mathbf{L} \equiv \delta_{\lambda\nu} l_{m\lambda}$. Replacing $\mathbf{TE}^{-}$ in Eq. (B.27) with the expression given in Eq. (B.26);

$$\mathbf{K}(\mathbf{RE}^{+} - \mathbf{E}^{-}) = \mathbf{M}^{\top}\mathbf{LM}(\mathbf{RE}^{+} + \mathbf{E}^{-}), \tag{B.28}$$

and solving Eq. (B.28) for $\mathbf{R}$ as follows;

$$\begin{aligned}\mathbf{K}\mathbf{R}\mathbf{E}^{+} - \mathbf{M}^{\top}\mathbf{L}\mathbf{M}\mathbf{R}\mathbf{E}^{+} &= \mathbf{K}\mathbf{E}^{-} + \mathbf{M}^{\top}\mathbf{L}\mathbf{M}\mathbf{E}^{-},\\ (\mathbf{K} - \mathbf{M}^{\top}\mathbf{L}\mathbf{M})\mathbf{R} &= (\mathbf{K} + \mathbf{M}^{\top}\mathbf{L}\mathbf{M})\mathbf{E}^{2-},\\ \mathbf{R} &= (\mathbf{K} - \mathbf{M}^{\top}\mathbf{L}\mathbf{M})^{-1}(\mathbf{K} + \mathbf{M}^{\top}\mathbf{L}\mathbf{M})\mathbf{E}^{2-},\end{aligned} \tag{B.29}$$

the reflection matrix, $\mathbf{R}$ is calculated. The transmission matrix, $\mathbf{T}$ is then easily obtained via Eq. (B.26).

Given the case where a sudden contraction is followed by a sudden expansion in an infinitely long duct, the equivalent reflection and transmission matrices are calculated using the following recursive approach. For simplicity, $x = 0$ is set to match the sudden contraction. The reflection/transmission matrices for an acoustic wave generated by a point source located in the duct section with radius a are defined as $\mathbf{R}_{ab}/\mathbf{T}_{ab}$, and those generated by a point source in the duct section with radius b as $\mathbf{R}_{ba}/\mathbf{T}_{ba}$. The superscript c and e denotes whether the reflection/transmission matrices are calculated at the contraction of the expansion, respectively. The reflected wave, $\mathbf{p}^{r}$ is then written in terms of the right-going incident wave, $\mathbf{p}^{i+}$ as follows:

$$\begin{aligned}\mathbf{p}^{r} &= \Big(\mathbf{R}^{c}_{ab} + \mathbf{T}^{c}_{ba}\big((\cdots + I)\mathbf{R}^{e}_{ba}\mathbf{R}^{c}_{ba} + I\big)\mathbf{R}^{e}_{ba}\mathbf{T}^{c}_{ab}\Big)\mathbf{p}^{i+},\\ \mathbf{p}^{r} &= \big(\mathbf{R}^{c}_{ab} + \mathbf{T}^{c}_{ba}(I - \mathbf{R}^{e}_{ba}\mathbf{R}^{c}_{ba})^{-1}\mathbf{R}^{e}_{ba}\mathbf{T}^{c}_{ab}\big)\mathbf{p}^{i+}.\end{aligned} \tag{B.30}$$

Similarly, the transmitted wave, $\mathbf{p}^{t}$ is found to be as follows:

$$\mathbf{p}^{t} = \mathbf{T}^{e}_{ba}(I - \mathbf{R}^{c}_{ba}\mathbf{R}^{e}_{ba})^{-1}\mathbf{T}^{c}_{ab}\mathbf{p}^{i+}. \tag{B.31}$$

List of Figures

List of Tables

Bibliography

[1] K. Abe, T. Kondoh, and Y. Nagano. A new turbulence model for predicting fluid flow and heat transfer in separating and reattaching flow. 1: Flow field calculations. *International Journal of Heat and Mass Transfer*, 37:139–151, Jan. 1994. ISSN 0017-9310. URL http://adsabs.harvard.edu/abs/1994IJHMT..37..139A.

[2] R. Abid. Evaluation of two-equation turbulence models for predicting transitional flows. *International Journal of Engineering Science*, 31(6):831–840, June 1993. ISSN 00207225. doi: 10.1016/0020-7225(93)90096-D. URL http://linkinghub.elsevier.com/retrieve/pii/002072259390096D.

[3] M. Abom. Modal decomposition in ducts based on transfer function measurements between microphone pairs. *Journal of Sound and Vibration*, 135(1):95–114, Nov. 1989. ISSN 0022460X. doi: 10.1016/0022-460X(89)90757-8. URL http://linkinghub.elsevier.com/retrieve/pii/0022460X89907578.

[4] E. Alenius, M. ÃĚbom, and L. Fuchs. LES of Acoustic-Flow Interaction at an Orifice Plate. American Institute of Aeronautics and Astronautics, June 2012. ISBN 978-1-60086-932-7. doi: 10.2514/6.2012-2064. URL http://arc.aiaa.org/doi/10.2514/6.2012-2064.

[5] M. Azarpeyvand and R. H. Self. Improved jet noise modeling using a new time-scale. *The Journal of the Acoustical Society of America*, 126(3):1015–1025, Sept. 2009. ISSN 0001-4966. doi: 10.1121/1.3192221. URL http://asa.scitation.org/doi/10.1121/1.3192221.

[6] S. C. C. Bailey, M. Hultmark, J. Schumacher, V. Yakhot, and A. J. Smits. Measurement of local dissipation scales in turbulent pipe flow. *Physical Review Letters*, 103(1), June 2009. ISSN 0031-9007, 1079-7114. doi: 10.1103/PhysRevLett.103.014502. URL http://arxiv.org/abs/0906.1116. arXiv: 0906.1116.

[7] C. Bailly and D. Juve. A stochastic approach to compute subsonic noise using linearized Euler's equations. In *5th AIAA/CEAS Aeroacoustics Conference and Exhibit*, Bellevue, WA, U.S.A, 1999. AIAA. URL http://arc.aiaa.org/doi/abs/10.2514/6.1999-1872. DOI: 10.2514/6.1999-1872.

[8] C. Bailly, P. Lafon, and S. Candel. Computation of noise generation and propagation for free and confined turbulent flows. In *Aeroacoustics Conference*, State College, PA, U.S.A, 1996. AIAA. URL http://arc.aiaa.org/doi/abs/10.2514/6.1996-1732. DOI: 10.2514/6.1996-1732.

[9] M. Bauer, A. Zeibig, and P. Költzschc. Application of the SNGR-Model to compute trailing edge noise. Research Report, Dresden University of Technology, 2006.

[10] W. Bechara, C. Bailly, P. Lafon, and S. M. Candel. Stochastic approach to noise modeling for free turbulent flows. *AIAA Journal*, 32(3):455–463, Mar. 1994. ISSN 0001-1452, 1533-385X. doi: 10.2514/3.12008. URL http://arc.aiaa.org/doi/10.2514/3.12008.

[11] M. Bilka, J. Anthoine, and C. Schram. Design and evaluation of an aeroacoustic wind tunnel for measurement of axial flow fans. *The Journal of the Acoustical Society of America*, 130(6):3788–3796, Dec. 2011. ISSN 0001-4966. doi: 10.1121/1.3652880. URL http://asa.scitation.org/doi/10.1121/1.3652880.

[12] M. Billson, L.-E. Eriksson, and L. Davidson. Jet Noise Modeling Using Synthetic Anisotropic Turbulence. In *10th AIAA/CEAS Aeroacoustics Conference*, Manchester, 2004. AIAA. URL http://arc.aiaa.org/doi/abs/10.2514/6.2004-3028. DOI: 10.2514/6.2004-3028.

[13] M. Billson, L.-E. Eriksson, L. Davidson, and P. Jordan. Modeling of Synthesized Anisotropic Turbulence and its Sound Emission. In *10th AIAA/CEAS Aeroacoustics Conference*, Manchester, 2004. AIAA. URL http://arc.aiaa.org/doi/abs/10.2514/6.2004-2857. DOI: 10.2514/6.2004-2857.

[14] K. C. Chang, W. D. Hsieh, and C. S. Chen. A Modified Low-Reynolds-Number Turbulence Model Applicable to Recirculating Flow in Pipe Expansion. *Journal of Fluids Engineering*, 117(3):417, 1995. ISSN 00982202. doi: 10.1115/1.2817278. URL http://FluidsEngineering.asmedigitalcollection.asme.org/article.aspx?articleid=1428000.

[15] J. Y. Chung and D. A. Blaser. Transfer function method of measuring in-duct acoustic properties. I. Theory. *The Journal of the Acoustical Society of America*, 68(3):907–913, Sept. 1980. ISSN 0001-4966. doi: 10.1121/1.384778. URL http://asa.scitation.org/doi/10.1121/1.384778.

[16] J. Costa, L. Oliveira, and D. Blay. Test of several versions for the k-epsilon type turbulence modelling of internal mixed convection flows. *International Journal of Heat and Mass Transfer*, 42(23):4391–4409, Dec. 1999. ISSN 00179310. doi: 10.1016/S0017-9310(99)00075-7. URL http://linkinghub.elsevier.com/retrieve/pii/S0017931099000757.

[17] S. C. Crow. Aerodynamic Sound Emission as a Singular Perturbation Problem. *Studies in Applied Mathematics*, 49(1):21–46, Mar. 1970. ISSN 1467-9590. doi: 10.1002/sapm197049121. URL http://onlinelibrary.wiley.com/doi/10.1002/sapm197049121/abstract.

[18] N. Curle. The Influence of Solid Boundaries upon Aerodynamic Sound. *Proceedings of the Royal Society A: Mathematical, Physical and Engineering Sciences*, 231(1187):505–514, Sept. 1955. ISSN 1364-5021, 1471-2946. doi: 10.1098/rspa.1955.0191. URL http://rspa.royalsocietypublishing.org/cgi/doi/10.1098/rspa.1955.0191.

[19] I. Davids and G. J. Bennett. Novel noise-source identification technique combining acoustical modal analysis and a coherence-based noise-source-identification method. *AIAA Journal*, 2015.

[20] I. Dyer. Measurement of noise sources in ducts. *J. Acous. Soc. Am.*, 30:833–841, 1958.

[21] R. Ewert and R. Emunds. CAA Slat Noise Studies Applying Stochastic Sound Sources Based On Solenoidal Digital Filters. In *11th AIAA/CEAS Aeroacoustics Conference*, California, 2005. AIAA. URL http://arc.aiaa.org/doi/abs/10.2514/6.2005-2862. DOI: 10.2514/6.2005-2862.

[22] R. Ewert and W. Schröder. Acoustic perturbation equations based on flow decomposition via source filtering. *Journal of Computational Physics*, 188(2):365–398, July 2003. ISSN 00219991. doi: 10.1016/S0021-9991(03)00168-2. URL http://linkinghub.elsevier.com/retrieve/pii/S0021999103001682.

[23] X. Gloerfelt and P. Lafon. Direct computation of the noise induced by a turbulent flow through a diaphragm in a duct at low Mach number. *Computers & Fluids*, 37(4):388–401, May 2008. ISSN 0045-7930. doi: 10.1016/j.compfluid.2007.02.004. URL http://www.sciencedirect.com/science/article/pii/S0045793007000230.

[24] C. G. Gordon. Spoiler-generated flow noise. i: The experiment. *Journal of the Acoustical Society of America*, 43:1041–1048, 1968.

[25] J. C. Hardin and S. L. Lamkin. Aeroacoustic Computation of Cylinder Wake Flow. *AIAA Journal*, 22(1):51–57, Jan. 1984. ISSN 0001-1452, 1533-385X. doi: 10.2514/3.48418. URL http://arc.aiaa.org/doi/10.2514/3.48418.

[26] M. Harper-Bourne. Jet near-field noise prediction. In *5th AIAA/CEAS Aeroacoustics Conference and Exhibit*, Bellevue, WA, U.S.A, 1999. AIAA. URL http://arc.aiaa.org/doi/abs/10.2514/6.1999-1838. DOI: 10.2514/6.1999-1838.

[27] S. Heo, C. Cheong, and T. Kim. Unsteady Fast Random Particle Mesh method for efficient prediction of tonal and broadband noises of a centrifugal fan unit. *AIP Advances*, 5(9):097133, Sept. 2015. ISSN 2158-3226. doi: 10.1063/1.4930979. URL http://aip.scitation.org/doi/10.1063/1.4930979.

[28] F. V. Herpe and D. Crighton. Noise generation by turbulent flow in ducts. *Journal de Physique IV*, 4:947–950, 1994.

[29] C. C. Holt. Forecasting seasonals and trends by exponentially weighted moving averages. *International Journal of Forecasting*, 20(1):5–10, Jan. 2004. ISSN 01692070. doi: 10.1016/j.ijforecast.2003.09.015. URL http://linkinghub.elsevier.com/retrieve/pii/S0169207003001134.

[30] C. Hrenya, E. Bolio, D. Chakrabarti, and J. Sinclair. Comparison of low Reynolds number k-epsilon turbulence models in predicting fully developed pipe flow. *Chemical Engineering Science*, 50(12):1923–1941, June 1995. ISSN 00092509. doi: 10.1016/0009-2509(95)00035-4. URL http://linkinghub.elsevier.com/retrieve/pii/0009250995000354.

[31] F. Jacobsen. Propagation of sound waves in ducts. Technical Report 31260, Acoustic Technology, Department of Electrical Engineering, Technical University of Denmark, 2008.

[32] M. S. James. Defining the Cockpit Noise Hazard, Aircrew Hearing Damage Risk and the Benefits Active Noise Reduction Headsets Can Provide. Technical Report EN-HFM-111-05, NATO Science and Technology Organization, VA, USA, June 2005.

[33] J. P. Johnston and W. E. Schmidt. Measurement of acoustic reflection from an obstruction in a pipe with flow. *J. Acous. Soc. Am.*, 63:1455–1460, 1978.

[34] U. Karban and C. Schram. Modal identification of aeroacoustic systems using passive and active approaches. *The Journal of the Acoustical Society of America*, 142(6):3804–3812, Dec. 2017. doi: 10.1121/1.5018613.

[35] U. Karban, G. Ogus, K. Kucukcoskun, C. F. Schram, C. Sovardi, and W. Polifke. Noise Produced by a Tandem Diaphragm: Experimental and Numerical Investigations. In *20th AIAA/CEAS Aeroacoustics Conference*, Atlanta, 2014. AIAA. URL `http://arc.aiaa.org/doi/abs/10.2514/6.2014-3225`. DOI: 10.2514/6.2014-3225.

[36] U. Karban, C. Schram, C. Sovardi, and W. Polifke. Tailored Green's Functions for the Prediction of the Noise Generated by Single and Tandem Diaphragms in a Circular Duct. *Acta Acustica united with Acustica*, 102(5):779–792, Sept. 2016. ISSN 16101928. doi: 10.3813/AAA.918993. URL `http://openurl.ingenta.com/content/xref?genre=article&issn=1610-1928&volume=102&issue=5&spage=779`.

[37] U. Karban, C. Schram, C. Sovardi, and W. Polifke. Prediction of ducted diaphragm noise using a stochastic approach with adapted temporal filters. *International Journal of Aeroacoustics*, submitted.

[38] M. Karweit, P. Blanc-Benon, D. Juvé, and G. Comte-Bellot. Simulation of the propagation of an acoustic wave through a turbulent velocity field: A study of phase variance. *The Journal of the Acoustical Society of America*, 89(1):52–62, Jan. 1991. ISSN 0001-4966. doi: 10.1121/1.400415. URL `http://asa.scitation.org/doi/10.1121/1.400415`.

[39] E. J. Kerschen and J. P. Johnston. A modal separation measurement technique for broadband noise propagating inside circular ducts. *Journal of Sound and Vibration*, 76:499–515, 1981.

[40] M. Klein, A. Sadiki, and J. Janicka. A digital filter based generation of inflow data for spatially developing direct numerical or large eddy simulations. *Journal of Computational Physics*, 186(2):652–665, Apr. 2003. ISSN 00219991. doi: 10.1016/S0021-9991(03)00090-1. URL `http://linkinghub.elsevier.com/retrieve/pii/S0021999103000901`.

[41] J. Kopitz, E. Bröcker, and W. Polifke. Characteristics-based filter for identification of acoustic waves in numerical simulation of turbulent compressible flow. In *12th Int. Congress on Sound and Vibration*, Lisbon, 2005.

[42] R. H. Kraichnan. Diffusion by a Random Velocity Field. *Physics of Fluids*, 13(1):22–31, 1970. ISSN 00319171. doi: 10.1063/1.1692799. URL http://scitation.aip.org/content/aip/journal/pof1/13/1/10.1063/1.1692799.

[43] P. K. Kundu, I. M. Cohen, and D. R. D. Ph.D. *Fluid Mechanics, Fifth Edition*. Academic Press, Waltham, MA, 5 edition edition, Sept. 2011. ISBN 978-0-12-382100-3.

[44] A. Lafitte, T. L. Garrec, E. Laurendeau, and C. Bailly. A study based on the sweeping hypothesis to generate stochastic turbulence. In *17th AIAA/CEAS Aeroacoustics Conference*, Portland, OR, U.S.A, 2011. AIAA. URL http://arc.aiaa.org/doi/abs/10.2514/6.2011-2888. DOI: 10.2514/6.2011-2888.

[45] C. K. G. Lam and K. Bremhorst. A Modified Form of the k-ϵ Model for Predicting Wall Turbulence. *Journal of Fluids Engineering*, 103(3):456, 1981. ISSN 00982202. doi: 10.1115/1.3240815. URL http://FluidsEngineering.asmedigitalcollection.asme.org/article.aspx?articleid=1425367.

[46] B. Launder and B. Sharma. Application of the energy-dissipation model of turbulence to the calculation of flow near a spinning disc. *Letters in Heat and Mass Transfer*, 1 (2):131–137, Nov. 1974. ISSN 00944548. doi: 10.1016/0094-4548(74)90150-7. URL http://linkinghub.elsevier.com/retrieve/pii/0094454874901507.

[47] B. E. Launder and D. B. Spalding. The Numerical Computation of Turbulent Flows. *Comput. Methods Appl. Mech. Eng.*, pages 269–289, Sept. 1990. ISSN 0045-7825. URL http://dl.acm.org/citation.cfm?id=99300.99301.

[48] J. Lavrentjev and M. Åbom. Characterization of fluid machines as acoustic multi-port sources. *Journal of Sound and Vibration*, 197:1–16, 1996.

[49] J. Lavrentjev, M. Åbom, and H. Bodén. A measurement method for determining source data of acoustic two-port sources. *Journal of Sound and Vibration*, 183:517–531, 1995.

[50] P. Lax and B. Wendroff. Systems of conservation laws. *Communications on Pure and Applied Mathematics*, 13(2):217–237, May 1960. ISSN 00103640, 10970312. doi: 10.1002/cpa.3160130205. URL http://doi.wiley.com/10.1002/cpa.3160130205.

[51] M. J. Lighthill. On Sound Generated Aerodynamically. I. General Theory. *Proceedings of the Royal Society A: Mathematical, Physical and Engineering Sciences*, 211(1107):564–587, Mar. 1952. ISSN 1364-5021, 1471-2946. doi: 10.1098/rspa.1952.0060. URL http://rspa.royalsocietypublishing.org/cgi/doi/10.1098/rspa.1952.0060.

[52] G. M. Lilley. The radiated noise from isotropic turbulence. *Theoretical and Computational Fluid Dynamics*, 6(5-6):281–301, Oct. 1994. ISSN 0935-4964, 1432-2250. doi: 10.1007/BF00311842. URL http://link.springer.com/10.1007/BF00311842.

[53] J. L. Lumley and G. Newman. The return to isotropy of homogeneous turbulence. *Journal of Fluid Mechanics*, 82(1), June 2001.

[54] D. A. Lynch, W. K. Blake, and T. J. Mueller. Turbulence Correlation Length-Scale Relationships for the Prediction of Aeroacoustic Response. *AIAA Journal*, 43(6):1187–1197, June 2005. ISSN 0001-1452, 1533-385X. doi: 10.2514/1.2200. URL http://arc.aiaa.org/doi/10.2514/1.2200.

[55] C. M. Mak and D. J. Oldham. The Application of Computational Fluid Dynamics to the Prediction of Flow Generated Noise: Part 2: Turbulence-Based Prediction Technique. *Building Acoustics*, 5(3):201–215, Sept. 1998. ISSN 1351-010X. doi: 10.1177/1351010X9800500304. URL http://dx.doi.org/10.1177/1351010X9800500304.

[56] P. Martìnez-Lera, R. Hallez, H. Bériot, and C. Schram. Computation of sound in a simplified hvac duct based on aerodynamic pressure. In *15th AIAA/CEAS Aeroacoustics Conference*, Florida, 2009.

[57] R. Mittra and S. W. Lee. *Analytical techniques in the theory of guided waves*. The MacMillan Company, New York, 1971.

[58] C. J. Moore. Measurement of radial and circumferential modes in annular and circular fan ducts. *Journal of Sound and Vibration*, 62:235–256, 1979.

[59] P. A. Nelson and C. L. Morfey. Aerodynamic sound production in low speed flow ducts. *Journal of Sound and Vibration*, 79:263–289, 1981.

[60] F. Nicoud and F. Ducros. Subgrid-Scale Stress Modelling Based on the Square of the Velocity Gradient Tensor. *Flow, Turbulence and Combustion*, 62(3):183–200, 1999. ISSN 13866184. doi: 10.1023/A:1009995426001. URL http://link.springer.com/10.1023/A:1009995426001.

[61] M. Omais, B. Caruelle, S. Redonnet, E. Manoha, and P. Saguat. Jet Noise Prediction Using RANS CFD Input. In *14th AIAA/CEAS Aeroacoustics Conference*, Vancouver, 2008. AIAA. URL http://arc.aiaa.org/doi/abs/10.2514/6.2008-2938. DOI: 10.2514/6.2008-2938.

[62] Y.-H. Pao. Structure of Turbulent Velocity and Scalar Fields at Large Wavenumbers. *Physics of Fluids*, 8(6):1063, 1965. ISSN 00319171. doi: 10.1063/1.1761356. URL http://scitation.aip.org/content/aip/journal/pof1/8/6/10.1063/1.1761356.

[63] V. C. Patel, W. Rodi, and G. Scheuerer. Turbulence models for near-wall and low Reynolds number flows - A review. *AIAA Journal*, 23(9):1308–1319, Sept. 1985. ISSN 0001-1452, 1533-385X. doi: 10.2514/3.9086. URL http://arc.aiaa.org/doi/10.2514/3.9086.

[64] T. J. Poinsot and S. K. Lele. Boundary conditions for direct simulation of compressible viscous flows. *Journal of Computational Physics*, 101:104–129, 1992.

[65] W. Polifke, C. Wall, and P. Moin. Partially reflecting and non-reflecting boundary conditions for simulation of compressible viscous flows. *Journal of Computational Physics*, 213:437–449, 2006.

[66] S. B. Pope. *Turbulent Flows*. Cambridge University Press, Cambridge ; New York, 1 edition edition, Oct. 2000. ISBN 978-0-521-59886-6.

[67] M. Åbom. Modal decomposition in ducts based on transfer function measurements between microphone pairs. *Journal of Sound and Vibration*, 135:95–114, 1989.

[68] M. Åbom and H. Bodén. Error analysis of two-microphone measurements in ducts with flow. *J. Acous. Soc. Am.*, 83:2429–2438, 1988.

[69] M. Åbom, H. Bodén, and J. Lavrentjev. Source characterization of fans using acoustic 2-port models. In *Proceedings of Int. INCE Symposium on Fan Noise*, France, 1992.

[70] H. S. Ribner. Quadrupole correlations governing the pattern of jet noise. *Journal of Fluid Mechanics*, 38(1):1, Aug. 1969. ISSN 0022-1120, 1469-7645. doi: 10.1017/S0022112069000012. URL http://www.journals.cambridge.org/abstract_S0022112069000012.

[71] S. Rienstra and A. Hirschberg. *An Introduction to Acoustics*. Eindhoven, 2001.

[72] S. Rienstra and A. Hirschberg. An Introduction To Acoustics. IWDE, Eindhoven University of Technology, Eindhoven, May 2001.

[73] S. W. Rienstra. Acoustical detection of obstructions in a pipe with a temperature gradient. In A. v. d Burgh, editor, *Topics in Engineering Mathematics*, pages 151–179. Springer Netherlands, 1992.

[74] B. J. Rosenberg, M. Hultmark, M. Vallikivi, S. C. C. Bailey, and A. J. Smits. Turbulence spectra in smooth- and rough-wall pipe flow at extreme Reynolds numbers. *Journal of Fluid Mechanics*, 731:46–63, Sept. 2013. ISSN 0022-1120, 1469-7645. doi: 10.1017/jfm.2013.359. URL http://www.journals.cambridge.org/abstract_S0022112013003595.

[75] R. Rubinstein and Y. Zhou. Time Correlations and the Frequency Spectrum of Sound Radiated by Turbulent Flows. Technical report, Institute for Computer Applications in Science and Engineering (ICASE), 1997.

[76] R. Rubinstein and Y. Zhou. The frequency spectrum of sound radiated by isotropic turbulence. *Physics Letters A*, 267(5-6):379–383, Mar. 2000. ISSN 03759601. doi: 10.1016/S0375-9601(00)00119-5. URL http://linkinghub.elsevier.com/retrieve/pii/S0375960100001195.

[77] S. Sack and M. Åbom. Full multi-port characterization of a circular orifice-plate. In *22nd AIAA/CEAS Aeroacoustics Conference*, Lyon, 2016.

[78] S. Sack, M. Åbom, C. Schram, and K. Kucukcoskun. Generation and scattering of acoustic modes in ducts with flow. In *20th AIAA/CEAS Aeroacoustics Conference*, Atlanta, 2014.

[79] P. J. Schmid. Dynamic mode decomposition of numerical and experimental data. *Journal of Fluid Mechanics*, 656:5–28, Aug. 2010. ISSN 0022-1120, 1469-7645. doi: 10.1017/S0022112010001217. URL http://www.journals.cambridge.org/abstract_S0022112010001217.

[80] C. Schram. An Introduction to Linear Acoustics and Flow Noise at Low Mach Numbers. VKI Course Notes, von Karman Institute for Fluid Dynamics, Mar. 2012.

[81] A. Sengissen, B. Caruelle, P. Souchotte, E. Jondeau, and T. Poinsot. Les of noise induced by flow through a double diaphragm system. In *15th AIAA/CEAS Aeroacoustics Conference*, Miami, Florida, 2009.

[82] A. Sengissen, B. Caruelle, P. Souchotte, E. Jondeau, and T. Poinsot. LES of Noise Induced by Flow Through a Double Diaphragm System. In *15th AIAA/CEAS Aeroacoustics Conference*, Miami, 2009. AIAA. URL http://arc.aiaa.org/doi/abs/10.2514/6.2009-3357. DOI: 10.2514/6.2009-3357.

[83] A. F. Seybert and D. F. Ross. Experimental determination of acoustic properties using a two-microphone random-excitation technique. *J. Acous. Soc. Am.*, 61:1362–1370, 1977.

[84] M. S. Shah, J. B. Joshi, A. S. Kalsi, C. Prasad, and D. S. Shukla. Analysis of flow through an orifice meter: CFD simulation. *Chemical Engineering Science*, 71:300–309, Mar. 2012. ISSN 00092509. doi: 10.1016/j.ces.2011.11.022. URL http://linkinghub.elsevier.com/retrieve/pii/S0009250911008219.

[85] T.-H. Shih, J. Zhu, and J. L. Lumley. A new Reynolds stress algebraic equation model. *Computer Methods in Applied Mechanics and Engineering*, 125(1-4):287–302, Sept. 1995. ISSN 00457825. doi: 10.1016/0045-7825(95)00796-4. URL http://linkinghub.elsevier.com/retrieve/pii/0045782595007964.

[86] M. L. Shur, P. R. Spalart, M. K. Strelets, and A. K. Travin. A hybrid RANS-LES approach with delayed-DES and wall-modelled LES capabilities. *International Journal of Heat and Fluid Flow*, 29(6):1638–1649, Dec. 2008. ISSN 0142-727X. doi: 10.1016/j.ijheatfluidflow.2008.07.001. URL http://www.sciencedirect.com/science/article/pii/S0142727X08001203.

[87] M. Siefert and R. Ewert. A stochastic source model for turbulent noise prediction including sweeping time dynamics. *The Journal of the Acoustical Society of America*, 123(5):3129–3129, May 2008. ISSN 0001-4966. doi: 10.1121/1.2933075. URL http://asa.scitation.org/doi/10.1121/1.2933075.

[88] J. Smagorinsky. General circulation experiments with the primitive equations. *Mon. Wea. Rev.*, 91(3):99–164, Mar. 1963. ISSN 0027-0644. doi: 10.1175/1520-0493(1963)091<0099:GCEWTP>2.3.CO;2. URL http://journals.ametsoc.org/doi/abs/10.1175/1520-0493%281963%29091%3C0099%3AGCEWTP%3E2.3.CO%3B2.

[89] M. S. Sodha, A. Kumar, G. I. C., and A. K. Ghatak. Sound wave propagation in cylindrical inhomogeneus waveguides. *Acta Acustica united with Acoustica*, 41:232–237, 1979.

[90] C. Sovardi. *Identification of Sound Sources in Duct Singularities*. PhD thesis, Technicshe Universität München, June 2016.

[91] C. Sovardi, Y. Aurégan, and W. Polifke. Parametric LES/SI Based Aeroacoustic Characterization of Tandem Orifices in Low Mach Number Flows. *Acta Acustica united with Acustica*, 102(5):793–803, Sept. 2016. ISSN 16101928. doi:

10.3813/AAA.918994. URL http://openurl.ingenta.com/content/xref?genre=article&issn=1610-1928&volume=102&issue=5&spage=793.

[92] F. Tao, X. Zhang, P. Joseph, O. Stalnov, M. Siercke, and H. Scheel. Experimental study of the mechanisms of sound generation due to an in-duct orifice plate. In *21st AIAA/CEAS Aeroacoustics Conference*, Dallas, 2015.

[93] H. O. Taylor. A direct method of finding the value of materials as sound absorbers. *Physical Review*, II:270–287, 1913.

[94] P. Testud, Y. Aurégan, P. Moussou, and A. Hirschberg. The whistling potentiality of an orifice in a confined flow using an energetic criterion. *Journal of Sound and Vibration*, 325(4-5):769–780, Sept. 2009. ISSN 0022460X. doi: 10.1016/j.jsv.2009.03.046. URL http://linkinghub.elsevier.com/retrieve/pii/S0022460X09002995.

[95] L. E. Torbergsen and P. Krogstad. Axisymmetric contraction of fully developed pipe flow. In *Proceedings of the 13th Australasian Fluid Mechanics Conference*, volume 1, pages 659–662, Melbourne, Australia, Dec. 1998. Monash University. ISBN 978-0-7326-2044-8.

[96] T. von Kármán. Progress in the Statistical Theory of Turbulence. *Proceedings of the National Academy of Sciences of the United States of America*, 34(11):530–539, Nov. 1948. ISSN 0027-8424. URL http://www.ncbi.nlm.nih.gov/pmc/articles/PMC1079162/.

[97] M. Willatzen. Sound propagation in a moving fluid confined by cylindrical walls - exact series solutions for radially dependent flow profiles. *Acta Acustica united with Acoustica*, 87:552–559, 2001.

[98] P. R. Winters. Forecasting Sales by Exponentially Weighted Moving Averages. *Management Science*, 6(3):324–342, Apr. 1960. ISSN 0025-1909, 1526-5501. doi: 10.1287/mnsc.6.3.324. URL http://pubsonline.informs.org/doi/abs/10.1287/mnsc.6.3.324.

[99] Z. Yang and T. H. Shih. New time scale based k-epsilon model for near-wall turbulence. *AIAA Journal*, 31(7):1191–1198, 1993. ISSN 0001-1452. doi: 10.2514/3.11752. URL https://arc.aiaa.org/doi/abs/10.2514/3.11752.

[100] P. Yardley. *Measurement of noise and turbulence generated by rotating machinery*. PhD thesis, University of Southampton, 1974.

[101] C. Zuniga Zamalloa. *Experiments on turbulent flows in rough pipes: spectral scaling laws and the spectral link*. PhD thesis, University of Illinois at Urbana-Champaign, Sept. 2012. URL https://www.ideals.illinois.edu/handle/2142/34359.